# Etude de la radioactivité deux-protons de 67Kr et développement d'une chambre à projection temporelle

Thomas Goigoux

# université
## de BORDEAUX

THÈSE PRÉSENTÉE

POUR OBTENIR LE GRADE DE

## DOCTEUR DE

## L'UNIVERSITÉ DE BORDEAUX

ÉCOLE DOCTORALE DES SCIENCES PHYSIQUES ET DE L'INGÉNIEUR

SPÉCIALITÉ ASTROPHYSIQUE, PLASMAS, NUCLÉAIRE

Par Thomas GOIGOUX

## Etude de la radioactivité deux-protons de $^{67}$Kr et développement d'une chambre à projection temporelle

Sous la direction de : Jérôme GIOVINAZZO

Soutenue le 23 octobre 2017

Membres du jury :

| | | |
|---|---|---|
| M. PIQUEMAL, Fabrice | Directeur de recherche, CENBG | Président |
| Mme KORICHI, Amel | Directrice de recherche, CSNSM | Rapporteur |
| M. DE OLIVEIRA SANTOS, François | Directeur de recherche, GANIL | Rapporteur |
| M. ALGORA, Alejandro | Directeur de recherche, IFIC | Examinateur |
| Mme MATEA MACOVEI, Iolanda | Maîtresse de conférences, IPNO | Examinatrice |
| M. BLANK, Bertram | Directeur de recherche, CENBG | Examinateur |
| M. GIOVINAZZO, Jérôme | Directeur de recherche, CENBG | Directeur de thèse |

**Titre : Étude de la radioactivité deux-protons de $^{67}$Kr et développement d'une chambre à projection temporelle**

**Résumé :** La radioactivité deux-protons est un mode de décroissance du noyau atomique ne se produisant que pour des noyaux extrêmement riches en protons, situés au-delà de la limite de cohésion proton des noyaux (drip line). Prédit dans les années 1960, ce phénomène n'a été mis en évidence expérimentalement qu'en 2002 avec l'observation de la décroissance de $^{45}$Fe. Jusqu'à maintenant, seuls quatre noyaux se désintégrant par radioactivité deux-protons étaient connus : $^{45}$Fe, $^{48}$Ni, $^{54}$Zn et $^{19}$Mg. La recherche de nouveaux émetteurs a été menée lors d'une expérience avec le dispositif EURICA-WAS3ABi au centre RIKEN Nishina en 2015. La décroissance de $^{59}$Ge, $^{63}$Se, $^{67}$Kr et $^{68}$Kr a été observée pour la première fois. La radioactivité deux-protons de $^{67}$Kr a pu être etudiée ainsi que la décroissance bêta et l'émission retardée de protons de noyaux exotiques de la région. Une chambre à projection temporelle ou TPC (Time Projection Chamber) conçue par le CENBG (2004-2011) a permis d'étudier les corrélations entre les protons pour $^{45}$Fe et $^{54}$Zn. Une deuxième génération de TPC est développée au sein de la collaboration ACTAR TPC (ACtive TARget for TPC). Ce détecteur doit permettre une vraie reconstruction tridimensionnelle de l'énergie déposée par les particules dans le volume actif, afin d'obtenir une reconstruction des traces plus performantes que l'ancienne TPC. L'électronique générique GET (General Electronics for TPCs) gère le traitement et l'acquisition des signaux. La caractérisation de l'électronique GET ainsi que du démonstrateur de la TPC au CENBG est le deuxième aspect de ce travail de thèse.

**Mots clés :** radioactivité, deux-protons, ACTAR TPC, nucléaire, structure

---

**Title: Study of $^{67}$Kr two-proton radioactivity and development of a time projection chamber**

**Abstract:** Two-proton radioactivity is a decay mode of proton-rich nuclei located beyond the proton nuclear existence limit (drip line). Predicted in the 1960s, this process was observed for the first time in 2002 in the $^{45}$Fe decay study. Only four two-proton emitters were known so far: $^{45}$Fe, $^{48}$Ni, $^{54}$Zn and $^{19}$Mg. A search for new emitters was performed with the EURICA-WAS3ABi setup at the RIKEN Nishina center in 2015. The decay of $^{59}$Ge, $^{63}$Se, $^{67}$Kr and $^{68}$Kr was observed for the first time. Two-proton radioactivity of $^{67}$Kr together with the beta and delayed proton decay of exotic nuclei in the region were studied. A time projection chamber (TPC) developed at the CENBG (2004-2011) enabled the study of the correlations between the protons for $^{45}$Fe and $^{54}$Zn. A second generation of TPC is under construction within the ACTAR TPC (ACtive TARget for TPC) collaboration. This detector enables a reconstruction in three dimensions of the energy deposited in the active volume which allows a more efficient reconstruction of the tracks as compared to the previous TPC. The generic electronics GET (General Electronics for TPCs) manages the processing and acquisition of the signals. The characterisation of the GET electronics and the TPC demonstrator at CENBG is devoted to the second aspect of this PhD work.

**Keywords:** radioactivity, two-proton, ACTAR TPC, nuclear, structure

---

# Résumé en français

La physique nucléaire est un domaine vieux d'un peu plus d'un siècle. La radioactivité fut observée pour la première fois en 1896 par Henri Becquerel. Les désintégrations $\alpha$ et $\beta^-$ ont été mises en évidence en 1899 par Rutherford, la radioactivité $\beta^+$ en 1934 par les Joliot-Curie. Le processus le plus exotique d'émission de proton a été observé pour la première fois dans les années 1980 avec la radioactivité un-proton. La dernière découverte d'une radioactivité remonte à 2002 avec la radioactivité deux-protons de $^{45}$Fe. Cette dernière fut mise en évidence par une observation indirecte, ne permettant pas de dinstiguer individuellement les deux protons. Les découvertes de $^{48}$Ni, $^{54}$Zn et $^{19}$Mg complétèrent notre connaissances des émetteurs deux-protons. L'utilisation de chambres à projection temporelle (TPC ou Time Projection Chamber) permit d'étudier les corrélations en angle et énergie entre les protons émis par ces noyaux. La comparaison de ces mesures expérimentales avec les modèles théoriques permet l'étude de la structure de ces noyaux qui sont situés au-delà de la limite de cohésion proton (drip line). Un nouveau pas a été franchi avec la découverte du noyau de $^{67}$Kr et de sa décroissance deux-protons, reporté dans cette thèse. Il s'agit de l'émetteur deux-protons le plus lourd jamais observé.

Les noyaux riches en protons décroissent principalement par radioactivité $\beta^+$. En s'éloignant de la vallée de la stabilité, l'énergie $Q_\beta$ de décroissance $\beta^+$ augmente et l'énergie de séparation un-proton $S_p$ diminue. Il devient alors possible de peupler par décroissance $\beta$ des niveaux instables proton qui se désexcitent par l'emission de protons : l'émission retardée de protons ($\beta p$). Lorsque l'énergie de séparation proton devient négative, ce que l'on appelle la drip line proton est franchie. Au delà, l'émission directe de protons depuis l'état fondamental est autorisée : la radioactivité un-proton pour la drip line un-proton ($S_p < 0$), la radioactivité deux-protons pour la drip line deux-protons ($S_{2p} < 0$).

Les prédictions de $Q_p$ et $Q_{2p}$ pour la recherche de candidats reposent sur des modèles locaux de masse : IMME (Isobaric Multiplet Mass Equation) et Garvey-Kelson. En effet aucune masse n'est connue expériementalement pour ces noyaux loin de la stabilité et les prédictions des modèles globaux de masse sont trop imprécis. Les durées de vie deux-protons théoriques peuvent quand à elles être estimées par des calculs de pénétration de la barrière coulombienne. Ces calculs reposent sur le formalisme matrice R ou le modèle en couches. Un modèle dynamique de la radioactivité deux-protons, le modèle à trois corps de Grigorenko, a également été mis au point pour calculer les corrélations angulaires et énergétiques entre les deux protons en fonction de la structure du noyau. L'observation de ces corrélations par un détecteur tel qu'une TPC, permet de faire des études spectroscopiques des émetteurs deux-protons.

Après $^{45}$Fe, $^{48}$Ni et $^{54}$Zn dont la radioactivité deux-protons est connue, les modèles locaux de masse désignent $^{59}$Ge, $^{63}$Se et $^{67}$Kr comme les meilleurs candidats du domaine de masse A $\sim 70$. Ces trois candidats ont été produits et identifiés sur la ligne de faisceau BigRIPS du RIKEN Nishina Center en 2015, lors de l'expérience RIBF4R1. La production des candidats deux-protons a été possible grâce à la fragmentation d'un faisceau de $^{78}$Kr (345 MeV/u et 250 pnA) sur une cible de béryllium de 5 mm d'épaisseur. Les fragments sont sélectionnés en masse et identifiés par le séparateur BigRIPS et ses divers détecteurs pour être ensuite implantés dans les détecteurs silicium (DSSSD ou Double-Sided Strip Silicon Detector) de WAS3ABi, mesurant l'energie déposée par les particules chargées émises suite aux décroissances (protons et particules $\beta$ ici). WAS3ABi est entouré par les détecteurs germanium EURICA pour détecter les rayons $\gamma$ issus des désexcitations nucléaires.

Les DSSSDs de WAS3ABi permettent de corréler en temps et en position les évènements d'implantation (noyaux) qui ont une énergie élevée, à ceux de décroissance qui ont une énergie

plus faible (émission retardée ou directe de protons, décroissance $\beta$). La comparaison des times-tamps des acquisitions BigRIPS et WAS3ABi permet d'identifier les noyaux implantés. Pour chaque DSSSD, les implantations sont corrélées avec toutes les décroissances détectées dans la même strip sur une fenêtre en temps définie. Cela permet d'obtenir les spectres en énergie et temps des décroissances corrélées pour chaque type de noyau identifié. La soustraction des spectres en energie des temps de corrélation positifs et négatifs permet de nettoyer les spectres en énergie d'associations fortuites d'évènements. Ensuite les spectres nettoyés sont utilisés pour déterminer les rapports d'embranchement et énergies des transitions protons. Les spectres en temps donnent eux la durée de vie d'un noyau en tenant compte des filiations. Pour cela, il a été nécessaire de déterminer l'efficacité de détection $\beta$ (probabilité de détecter dans le DSSSD d'implantation la particule $\beta$ issu de la décroissance du noyau) pour prendre en compte correctement les différentes décroissances possibles pour le noyaux père.

Les noyaux $^{63}$Se, $^{67}$Kr et $^{68}$Kr ont été identifiés pour la première fois lors de l'expérience RIBF4R1. Leurs décroissances avec celle de $^{59}$Ge ont été observées. Aucune indication de radioactivité deux-protons n'a été vue pour $^{59}$Ge et $^{63}$Se. Leur spectre en énergie est dominé par des protons observés en coincidence avec des particules $\beta$ montrant que l'émissions retardées de protons est dominante et l'émission deux-protons, si elle existe, est très faible avec un rapport d'embranchement inférieur à 1%. Au contraire, un pic proton sans particule $\beta$ détectée en coincidence a été observé pour $^{67}$Kr. Ce dernier, d'une énergie de 1690(17) keV et un rapport d'embranchement de 37(14)%, est issu de la radioactivité deux-protons. La durée de vie de $^{67}$Kr a été estimée à 7.4(30) ms. L'énergie deux-protons estimée dans ce travail est en accord avec les modèles locaux de masse, mais la durée de vie est en fort désaccord avec les calculs modèles en couches et trois corps. Suite à ce désaccord, de nouveaux calculs théoriques ont été réalisés par Grigorenko grâce à une nouvelle amélioration du modèle à trois corps : l'IDDM (Improved Direct Decay Model). Ces calculs montrent une possible explication à ce désaccord. En effet les résultats expérimentaux (demi-vie et énergie de décroissance deux-protons) sont compatibles avec une dynamique d'émission qui se situe à la limite entre l'émission séquentielle de protons et la radioactivité deux protons (émission de protons corrélés), et dépend de la position de l'état fondamental de $^{66}$Br, qui n'est pas connue expérimentalement. D'après les calculs IDDM, la distribution du partage d'énergie entre les deux protons diffère selon le type d'émission deux-protons. Une observation de cette distribution avec une TPC pourrait valider cette hypothèse.

L'expérience RIBF4R1 a également permis de mesurer pour la première fois les durées de vie des émetteurs retardés de protons $^{59}$Ge $^{63}$Se et $^{68}$Kr. Des mesures plus précises des rapports d'embranchement proton et durées de vie des émetteurs $\beta p$ $^{65}$Se, $^{61}$Ge et $^{57}$Zn ont été réalisées. Les durées de vie des émetteurs $\beta$ $^{55}$Cu, $^{64}$As, $^{60}$Ga, $^{56}$Cu, $^{65}$As et $^{63}$Ge ont pu être mesurées avec une meilleure précision. Les nouvelles données sur ces noyaux du chemin du processus $rp$ peuvent être utilisées pour améliorer la précision des calculs astrophysiques.

La cas de $^{67}$Kr pourra être clarifié par une observation avec une TPC. Le projet ACTAR TPC (ACtive TARget TPC) permettra d'observer individuellement les protons de la décroissance deux-protons de ce noyau. Ce projet fait suite à l'ancienne génération de TPC pour la physique nucléaire en France : MAYA et la TPC du CENBG. Le plan de détection de MAYA est composée de pads hexagonals. Elle est utilisée comme cible active avec éventuellement des détecteurs auxiliaires (détecteurs silicium). Ce détecteur ne fourni pas d'information temporelle au niveau des pads. La TPC du CENBG a été utilisée pour l'étude de la radioactivité deux-protons. Elle est composée d'un plan de détection avec des strips horizontales (X et Y), elle ne mesure pas la projection en deux dimensions de l'énergie déposée dans le gaz mais deux projections unidimensionnelles (X et Y). De plus cette TPC souffre d'un temps mort élevé de 1.4 ms qui implique des pertes d'évènements non négligeables pour les émetteurs deux-protons dont la durée de vie est de quelques ms. Le détecteur ACTAR TPC est composé d'un plan de 16384 pads de $2 \times 2$ mm$^2$ chacun avec une électronique numérique dédiée : GET (General Electronics for TPCs). Le signal de chaque pad est numérisé puis stocké. Cela permet une meilleure résolution en temps sur les signaux contrairement à l'ancienne TPC qui codait seulement la position du maximum du signal en énergie. De plus GET possède un mode dédié aux décroissances à durées de vie courtes qui permet d'atteindre un temps mort de quelques $\mu$s entre l'implantation du noyau dans le volume de gaz et sa décroissance. Ce mode divise la mémoire analogique associée à chaque

pad en deux : la première partie pour l'implantation, la deuxième pour la décroissance. Le temps de basculement entre les deux mémoires est très court et diminue ainsi le temps mort.

Un démonstrateur de la TPC a été construit au CENBG pour réaliser des tests du plan de pads et de l'électronique. Un plan de 2048 pads a été construit pour tester la technologie développée pour le plan de pads. Le plan de pads utilise un bulk micromegas pour l'amplification. Le PCB (Printed Circuit Board) qui supporte les pads et le micromegas est habituellement collé sur un support métallique (bride de la TPC). Cette solution nécessite de faire passer les connectiques à travers la plaque métallique ce qui augmente la déformation lors de différences de pression. La solution développée par le service électronique du CENBG avec le CERN (PCB workshop) et l'entreprise Fedd (Fabrique électronique de Dordogne) consiste à concevoir un PCB à coeur métallique qui fait aussi office de bride pour une meilleure robustesse et une connexion plus simple des pads à l'électronique. Des tests en sources X ($^{55}$Fe) et $\alpha$ (Pu/Am/Cm) ont montré que ce procédé permet d'obtenir une résolution classique pour un micromegas. Le plan test du CENBG (2048 pads) a une résolution (FWHM) de 21.5(5)% à 5.9 keV (source rayons X) et de 3.1(1)% à 4.8 MeV (source $\alpha$).

La deuxième caractérisation du démonstrateur concerne l'électronique GET. Le traitement des signaux par cette dernière induit trois sources de distorsion. Les première et dernière valeurs du signal sont systématiquement aberrantes. Ensuite le signal est déformé par la baseline qui est un offset non constant, induit par la lecture de la mémoire. Le dernier effet constaté est l'effet de phase qui est une déformation du signal dû à la position physique des échantillons du signal dans la mémoire analogique de GET. La correction de ces effets permet de réduire de 20 à 30 % les distorsions des signaux. Après cette étape de correction, le signal d'entrée est reconstruit grâce à la fonction transfert du système. Cette fonction transfert est calculée à partir de signaux obtenus en sortie avec des signaux pulser en entrée.

Le démonstrateur assemblé au CENBG est composé d'un plan de détection de 2048 pads et de l'électronique GET pour la lecture des voies. Les premiers tests ont été réalisés avec une source alpha. La prochaine étape sera d'appliquer la procédure de reconstruction des signaux mise en place dans ce travail pour permettre de renconstruire en trois dimensions les trajectoires des particules chargées dans la TPC. Le détecteur final ACTAR TPC sera construit fin 2017 avec une première expérience test sur la radioactivité deux-protons de $^{48}$Ni ou $^{54}$Zn en 2018.

Le détecteur final sera également utilisé pour réaliser une mesure directe de la décroissance deux-protons de $^{67}$Kr. En effet, la proposition d'expérience avec ACTAR TPC à RIBF a été acceptée. La mesure de la distribution de la répartition en énergie entre les deux protons permettra de tester l'hypothèse de Grigorenko sur la nature de l'émission deux-protons de $^{67}$Kr.

# Acknowledgements

Tout d'abord, je remercie mon jury de thèse pour les nombreuses remarques pertinentes apportées au manuscrit, particulièrement de la part de mes deux rapporteurs Amel (merci pour sa correction de l'anglais) et François. Ils m'ont grandement permis d'améliorer la qualité du manuscrit pour cette version finale.

Pendant ces trois ans de thèse, j'ai pu profiter du cadre bucolique du CENBG, loin de toute civilisation à Gradignan. Un laboratoire doté d'une sécurité informatique infaillible et d'un webmail d'une grande ergonomie (qui m'a accompagné dans tous mes déplacements).

Merci au groupe Noyaux Exotiques - NEX pour les intimes - qui m'a accueilli pendant ces trois ans et m'a fait profiter de son ambiance très sympathique, surtout lors de nos pauses cafés. Je remercie donc Pauline, Teresa, Mathias et Stéphane. Je finis par les deux membres avec qui j'ai le plus travaillé dans ce groupe : Jérôme et Bertram. Cela a été un honneur d'être ton premier doctorant officiel, Jérôme, j'ai eu la chance de pouvoir discuter avec toi que ce soit au labo ou dans la vie personnelle. Tes programmes C++ m'ont simplifié les fits de ROOT même si j'ai pu avoir des problèmes de compatibilité (et de patience) selon la version de ROOT, gcc ou de Scientific Linux :o Bertram, ton aide sur l'analyse du $^{67}$Kr m'a été précieuse et j'ai pu profiter de ton immense savoir, de ton calme (germanique ?) en toute circonstance mais aussi des discussions lors des repas de midi au labo. Même si j'ai du subir l'odeur de ton thé aux fruits rouges sur les derniers mois de la thèse, cette odeur ne m'a pas gêné contrairement à certains de mes prédécesseurs ;)

Pour rester sur la nourriture, cette thèse fut agrémentée des pauses repas au labo (souvent dehors) les autres doctorants, stagiaires, et Ludo avec qui l'on pouvait avoir des discussions de jeux vidéos, notamment Minecraft :)

La majeure partie de cette thèse a été faite dans le bureau 113, LE bureau des thésards avec Arnaud, Mehdi (alias M. JSB), Maxime, mais aussi Jean et Nicolas ce qui permettait d'avoir toujours une bonne ambiance et de bien discuter ! (on travaillait quand même). J'ai aussi eu la chance de cotoyer les autres thésards de NEX, Mehdi, Antoine (qui m'a convaincu de faire de l'escalade) et Cécile, avec qui j'ai beaucoup ri et parlé aussi. Je remercie tous les autres thésards des pauses midi et autres : Ricardo, Xavier, et tous les autres que j'ai pu oublier. Je remercie aussi le groupe Neutrinos, Christine, Fred, Manu et Fabrice avec qui j'ai aussi partagé de nombreux moments.

Le fonctionnement du détecteur ACTAR TPC doit beaucoup au service électronique, je les remercie pour l'aide qu'ils m'ont apportés, particulièrement Jérôme avec qui j'ai travaillé sur les tests du détecteur et de l'électronique, et profité de son humour et de sa bonne humeur.

Mes remerciements vont aussi à Nadine, secrétaire du groupe NEX pour son aide : sa gestion des missions, mais surtout l'organisation du pot de thèse. Pour les missions, sans l'aide de Sylvie je n'aurais pas pu avoir d'assurance pour partir en conférence en Russie, je la remercie grandement. Je remercie également Aziz, du service informatique, pour sa gentillesse et son aide. Je remercie égelement tous ceux du labo que j'aurais pu oublier.

Je remercie tous mes amis que je connais depuis très longtemps pour certains : Alexandre, Julien (bon courage, plus qu'un an de thèse !), Loïc, Yujuan et aussi tous ceux que j'ai pu croiser à Bordeaux. Pour ceux qui ont lu ce manuscrit, ils auront remarqué que j'en arrive aux étoiles à neutrons, comme quoi j'ai réussi à me raccorder (un peu) à ton sujet Franck ! Les pulsars sont vraiment partout ˆˆ

Pour finir, je remercie ma famille, tout d'abord mes parents pour être venu à ma soutenance et m'avoir soutenu pendant les études, il a fallu d'ábord emménager en Alsace puis en Essonne et

enfin Bordeaux pour cette thèse. Je remercie ma grand-mère pour être venu m'apporter soutien et me voir défendre mon travail de thèse, également mes deux grand-pères qui ne sont plus là, et ma grand-mère qui n'a pas pu venir mais m'a accompagné au jour le jour lors du tout début de mes études.

Cette thèse à Bordeaux m'a permis de te rencontrer Marie, ta présence a beaucoup contribué à l'écriture de cette thèse. En effet, comme tu préparais ardemment le CRFPA, je me serais senti trop coupable de céder à la fénéantise au lieu de rédiger ;) Par bien des aspects tu m'as accompagné dans cette dernière année de thèse.

虎穴に入らずんば虎子を得ず。

# Contents

# List of Figures

# List of Tables

# Introduction

Nuclear physics is a relative recent domain, aged of one century. Indeed the radioactivity was discovered by Henri Becquerel in 1896. Later, all the most common kinds of radioactivity were discovered in the beginning of the twentieth century: the $\alpha$ and $\beta^-$ decays in 1899 by Rutherford, the $\beta^+$ decay in 1934 by the Joliot-Curie. The same decade, the first cyclotron is designed, opening the era of particle accelerators. After the second world war, the first nuclear reactors and the discovery of the neutrino opened new perspectives of study nuclear processes. With even more powerful accelerators, new exotic decays could be produced and discovered such as the one-proton radioactivity in the 1980s. The last discovery of a new radioactivity, even more exotic, took place in 2002, with the first indirect observation of the two-proton radioactivity of $^{45}$Fe.

With the particle physics evolution in the second half of the twentieth century, new detectors were developed such as time projection chamber in the 1970s. Such a device allows a full three-dimensional measurement of charged particles tracks. Time projection chambers are being more and more used in nuclear physics. In the 2000s, a TPC was developed at CENBG to observe directly the two-proton radioactivity. The tracks of the two protons of $^{45}$Fe were successfully observed in 2007. By comparing theoretical calculations of two-proton radioactivity models with the experimental angular correlations of the protons, it is possible to describe the structure of such exotic nuclei. Four two-proton emitters were known until 2015: $^{45}$Fe, $^{48}$Ni, $^{54}$Zn and $^{19}$Mg.

A new step forward in the study of two-proton radioactivity is completed, as a new emitter, $^{67}$Kr, is observed in this work. It was successfully produced and identified by the BigRIPS fragment separator at the RIKEN Nishina centre at Tokyo in 2015. The experiment, named RIBF4R1, was performed with the EURICA-WAS3ABi setup coupling gamma-ray and charged-particle measurements associated to the decays of nuclei of interest. These results are reported in this PhD thesis.

A presentation of the main decays observed for proton-rich nuclei near the drip line is reported in chapter 1 together with a description as beta-delayed emission of protons and the two-proton radioactivity. The theoretical models and main milestones of the two-proton study are also presented.

Chapter 2 describes the RIBF4R1 experiment including a presentation of the BigRIPS fragment separator, the identification procedure and the EURICA-WAS3ABi setup dedicated to the study of gamma-ray deexcitation and decay by charged-particle emission (beta and beta-delayed decay, two-proton radioactivity).

The analysis procedure detailed in chapter 3, allowed to identify the nuclei and study the two-proton radioactivity of $^{67}$Kr and the beta and beta-delayed proton decays of other exotic nuclei produced during the same experiment.

The results are summarised in chapter 4. The first observation of the decay of $^{67}$Kr (two-proton radioactivity), $^{68}$Kr, $^{63}$Se and $^{59}$Ge (beta-delayed proton emission) is reported. The new measurements of the properties of the $T_z = -\frac{3}{2}$ nuclei $^{69}$Kr, $^{65}$Se, $^{61}$Ge, $^{57}$Zn are presented. New half-life measurements of the $\beta$ decay of $^{55}$Cu, $^{56}$Cu, $^{60}$Ga, $^{63}$Ge, $^{64}$As and $^{65}$As were also performed. These new data improve the precision of the existing ones and can be used in future calculations of $rp$ process. Some of them bring a new insight into the contradictory literature data.

The observation of $^{67}$Kr two-proton radioactivity was indirect. A new time projection chamber, more efficient than the previous chamber, is under development in the ACTAR TPC collaboration. It will be used for new studies on two-proton radioactivity, especially $^{67}$Kr. A

demonstrator is installed at CENBG, the characterisation of this detector and the tests of the dedicated electronics (GET) are reported in chapter 5.

# Chapter 1

# Physics of proton-rich nuclei

The processes presented in this chapter are only those observed for proton-rich nuclei for which the proton number is higher than the neutron one. The proton excess induces an instability of the nucleus and the most usual decay mode for such nuclei occurs via the $\beta^+$ radioactivity. Besides, proton emissions are observed when the proton excess increases: $\beta$-delayed one-, two- and three-proton decays or one- and two-proton radioactivities.

After a presentation of the $\beta$ decay theory, the exotic $\beta$-delayed proton emissions are discussed. Beyond the proton drip line, direct emission of protons can also be observed: one- and two-proton (2p) radioactivities. The 2p radioactivity will be explained precisely with the existing emission models and the prediction of candidates by local mass models. Finally, the experimental discovery of 2p radioactivity together with the main achievements so far are presented here.

## 1.1 The nucleus and its decay modes

The nuclear physics playground is infinitely smaller than our scale, invisible to our eyes. As Democritus postulated four centuries before our era, the matter is composed of vacuum and atoms. The existence of the nucleus in the atom was proven in 1911 by the Rutherford experiment of alpha particle scattering on gold foils. The atomic size is of the order of $10^{-10}$ m (see figure 1.1). The atomic nucleus is $10^4$ to $10^5$ smaller than the atom. The nucleus is composed of
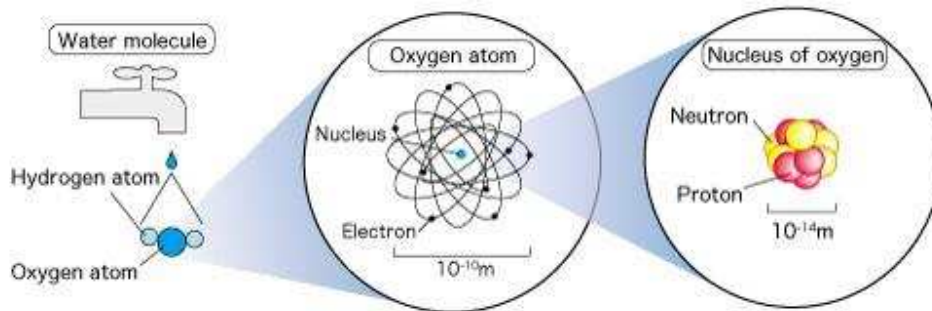


Figure 1.1: Typical size of the nucleus. An atom is ten orders of magnitude smaller than human scale, a nucleus is even four orders of magnitudes smaller. Taken from [Rik17].

nucleons: the protons which are positively charged and the neutrons with a neutral electric charge. These nucleons are in cohesion according to the fundamental interactions involved at this scale: the nuclear weak force responsible for nucleon decay, the strong interaction keeping all nucleons bound together inside the nucleus and the electromagnetic interaction.

All nucleons composing the nucleus interact with a potential created by themselves. The strong interaction Hamiltonian of a nucleon is obtained by superposition principle. It is the sum of the kinetic energy operator, one-body strong interaction potential, two-body, etc until (A-1)-body potential. For evident issues of N-body potential calculations, the strong interaction with

the other nucleons is simplified by a nuclear mean field. The Woods-Saxon potential [Woo54] is a convenient phenomenological choice for the one-body potential:

$$V(r) = \frac{-V_0}{1 + e^{\frac{r-R}{a}}} \tag{1.1}$$

$a$ is the diffusivity and its value is between 0.5 and 2.2 fm. $R$ is the nuclear radius parametrized by $R = R_0 A^{1/3}$ with $R_0$ between 1.1 and 1.5 fm. The amplitude $V_0$ also depends on the nucleus (usually $\simeq 50$ MeV). This expression is the central part of the interaction potential (it is spin-independent) and does not take into account the spin-orbit coupling.

For the proton, one has to consider the potential due to the positive charges of the other protons: the Coulomb potential. This latter is added to the Woods-Saxon potential and has the expression:

$$V_{\text{Coulomb}}(r) = \begin{cases} \frac{Ze^2}{4\pi\varepsilon_0 R_c}\left(\frac{3}{2} - \frac{1}{2}\left(\frac{r}{R_c}\right)^2\right) & \text{if } r < R_c \\ \frac{Ze^2}{4\pi\varepsilon_0 r} & \text{else.} \end{cases} \tag{1.2}$$

with $e$ the electron charge magnitude in absolute value, $\varepsilon_0$ the permittivity of free space, $Z$ the charge number of the nucleus and $R_c$ its charge radius. These potentials are represented in figure 1.2.
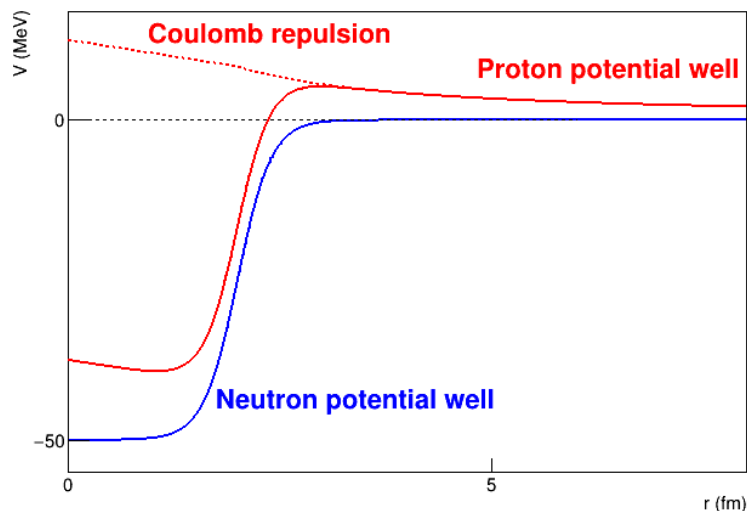


Figure 1.2: The nuclear potential well of Woods-Saxon. The central potential well for the neutrons is represented in blue, in red for the protons. The potential of the protons is the sum of the Woods-Saxon (blue solid line) and the Coulomb potential (red dashed line) because of their electric charge.

The potential seen by a nucleon is modelled by a quantum harmonic oscillator. Calculations with the Woods-Saxon central potential and the spin-orbit coupling give the energy levels accessible by the neutrons (or protons) and the energy gaps between these levels. This approach called "shell model" [May48] gives results very close to the observations. This model predicts higher energy gaps for a number of protons (neutrons) $Z(N) = 2, 8, 20, 28, 50, 82$ and $126$. These numbers are called "magic numbers" and they are associated with the spherical shell closures. Nuclei close to these numbers are more stable. In practice, one observes a higher proton/neutron separation energy for a magic number. It gives consequently more stability to the nucleus because one has to inject much more energy to remove a proton/neutron.

More than 3200 nuclei are known nowadays, but only about 250 are stable. The unstable nuclei have various decay modes according to their degree of "exoticity". These decay modes are distinguishable by the coloured squares on the nuclide chart in figure 1.3, details are given in table 1.1.
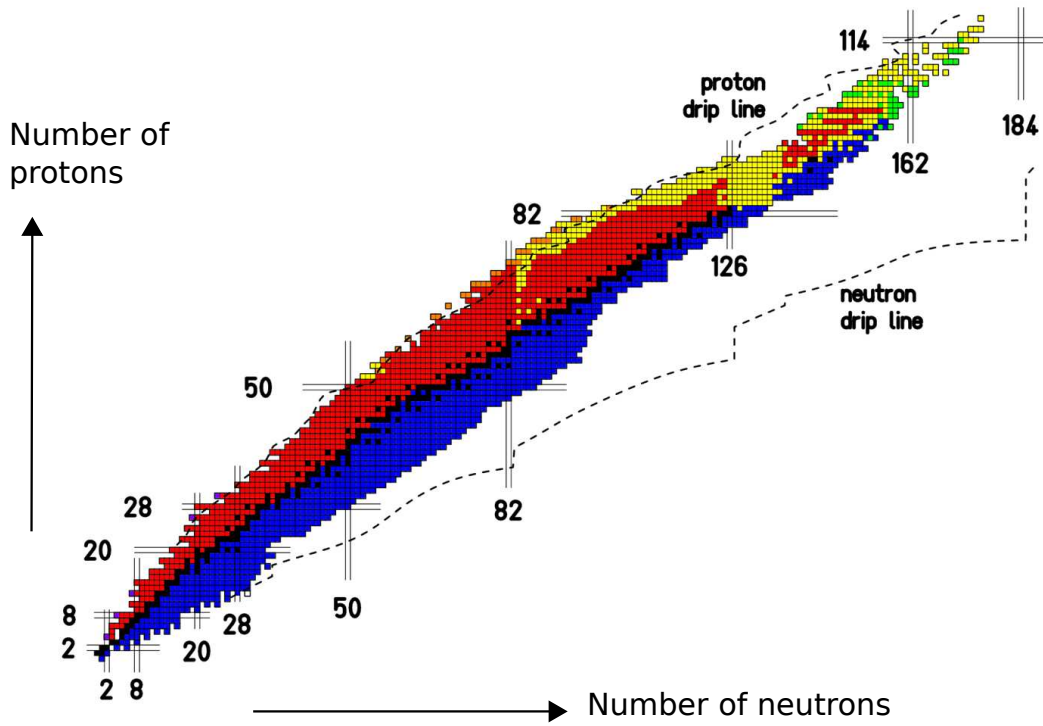
Figure 1.3: The chart of nuclides. All the known nuclei are represented as a function of their number of neutrons (N) and protons (Z). The black squares are the stable nuclei, the red ones decay by $\beta^+$/EC decay, the blue ones by $\beta^-$ decay, the yellow ones by $\alpha$ decay and the green nuclei by spontaneous fission. The proton and neutron nuclear existence limits called "drip lines" are drawn, and also the magic numbers of protons and neutrons matching the shell closures.

The stable nuclei constitute what we call the "valley of stability". The other nuclei, the radioactive nuclei, have an unstable proton-neutron ratio. They tend to get closer to stability by spontaneous transformation. Most proton-rich nuclei decay via $\beta^+$ radioactivity or electron capture. For $\beta^+$ radioactivity, a proton decays to a neutron with a positron and an electronic neutrino which are emitted. In the case of electron capture (EC), an electron of the atom is captured by a proton of the nucleus. This proton decays to a neutron by weak interaction with this electron. Most neutron-rich nuclei decay by $\beta^-$ radioactivity, which is the inverted process: a neutron decays to a proton with the emission of an electron and an electronic anti-neutrino. The heaviest nuclei (such as uranium) decay by the emission of an $\alpha$ particle (helium nucleus) or spontaneous fission.

| $\beta^+$ radioactivity | $^A_Z X_N \to ^A_{Z-1} Y_{N+1} + e^+ + \nu_e$ |
|---|---|
| $e^-$ capture (EC or $\varepsilon$) | $^A_Z X_N + e^- \to ^A_{Z-1} Y_{N+1} + \nu_e$ |
| $\beta^-$ radioactivity | $^A_Z X_N \to ^A_{Z+1} Y_{N-1} + e^- + \overline{\nu}_e$ |
| $\alpha$ radioactivity | $^A_Z X_N \to ^{A-4}_{Z-2} Y_{N-2} + ^4_2 \text{He}_2$ |
| Spontaneous fission | $^A_Z X_N \to ^{A'}_{Z'} Y_{N'} + ^{A''}_{Z''} Y_{N''} + xn$ |

Table 1.1: Enumeration of the common decay processes.

The stability of a nucleus, according to the strong interaction, is linked to the binding energy between its nucleons. It represents the average energy to rip one nucleon away from the nucleus. A high value induces more stability of the nucleus. The binding energy $B(A, Z)$ of a nucleus is related to its nuclear mass by

$$M_{\text{nucl}}c^2 = Zm_pc^2 + (A - Z)m_nc^2 - B(A, Z) \tag{1.3}$$

with $m_p$ the proton mass and $m_n$ the neutron mass. In the same manner, the atomic mass is

$$M_{\text{at}}c^2 = M_{\text{nucl}}c^2 + Zm_ec^2 - B_{el}(Z) \tag{1.4}$$

with $m_e$ the mass of the electron and $B_{el}(Z)$ the binding energy of the electrons. The best approximation for the electrons binding energy is given by [Lun03]

$$B_{el}(Z) = 14.4381 Z^{2.39} + 1.55468 \times 10^{-6} Z^{5.35} \text{ eV} \tag{1.5}$$

This value ranges from 13.6 eV for H up to 700 keV for U, negligible compared to the atomic mass unit. The nuclear and atomic masses can hence be assumed to be the same.

The difference of nuclear binding energies between two nuclei with one nucleon difference is the proton/neutron separation energy:

$$\begin{cases} S_n = B(^A_Z X_N) - B(^{A-1}_Z Y_{N-1}) \\ S_p = B(^A_Z X_N) - B(^{A-1}_{Z-1} Y_N) \end{cases} \tag{1.6}$$

When the proton or neutron separation energy becomes negative, we cross the proton (respectively neutron) drip line. Beyond this frontier, the nuclei are unbound according to the strong interaction and the direct emission of neutrons (for neutron drip line) or protons (for proton drip line) is possible: proton radioactivity as an example. Near the proton (neutron) drip line, $\beta$-delayed emission of protons (neutrons) is observed. The proton emission is a slower process than the neutron emission because the protons have to tunnel the Coulomb barrier. If the two-proton separation energy $S_{2p} = B(^A_Z X_N) - B(^{A-2}_{Z-2} Y_N)$ is negative, the two-proton drip line is crossed allowing the direct emission of two protons (2p radioactivity).

In the following, the decays of proton-rich nuclei are explained, from the $\beta^+$ decay to $\beta^+$-delayed and direct emission of protons for very exotic nuclei near the proton drip line.

## 1.2  Beta radioactivity

The $\beta$ radioactivity is the most observed decay process for unstable nuclei. The most common $\beta$ radioactivity, named $\beta^-$ radioactivity, is observed for neutron-rich nuclei and is known since 1899. In the 1920s, the emission spectrum of electrons from this radioactivity was a controversial subject. This spectrum is continuous, in contradiction with energy conservation, because a sharp peak was expected, as observed in $\alpha$ decay. In 1931, Pauli proposed an answer to this missing energy by assuming the emission of a second particle, without electric charge, the neutrino. This latter was discovered by Clyde Cowan and Fred Reines in 1956 [Cow56]. The other types of $\beta$ radioactivities were observed later than the $\beta^-$ decay. The $\beta^+$ radioactivity, common process for proton-rich nuclei, was discovered in 1934 by Joliot-Curie through the observation of the emission of positrons by nuclei. The electron capture was discovered in 1938 by Alvarez [Alv38] who detected X rays emitted in the filling of the vacancy left by the captured electron.

Regarding the region of interest in this PhD thesis, the unstable proton-rich nuclei decay by $\beta^+$ radioactivity or electron conversion. The $\beta^+$ decay is the conversion of a proton to a neutron with the emission of a positron (also called $\beta^+$ particle) and an electronic neutrino:

$$p \rightarrow n + e^+ + \nu_e \tag{1.7}$$

A similar decay for the same nuclei is the electron capture (abbreviated EC or $\varepsilon$). An electron is captured by the nucleus producing also a neutron:

$$p + e^- \rightarrow n + \nu_e \tag{1.8}$$

The released energy by the $\beta^+$ decay is

$$Q_{\beta^+} = \left( M(^A_Z X) - M(^A_{Z-1} Y) - 2m_e \right) c^2 \tag{1.9}$$

with $M$ the atomic masses of the mother and daughter nuclei, $m_e$ the mass of the electron.

The $Q$ value for the electron capture is

$$Q_{EC} = M(^A_Z X)c^2 - M(^A_{Z-1} Y)c^2 - B_{e^-} \tag{1.10}$$

with $B_{e^-}$ the binding energy of the captured electron. One has $Q_{EC} - Q_{\beta^+} \sim 2m_e = 1.022$ MeV by neglecting the binding energy of the captured electron. Note that, nuclei for which $\beta^+$ decay is energetically possible, can also undergo EC but the reverse is not necessarily true. Indeed, it is possible to have $Q_{EC} > 0$ while $\beta^+$ decay is energetically forbidden ($Q_{\beta^+} < 0$). The values of $Q_{EC}$ for the nuclei studied in this thesis are in the 9 to 15 MeV range.

The first successful model of the $\beta$ decay is the Fermi theory. Moreover, different types of transitions can be observed with their own selection rules. Theory of $\beta$ decay gives a relation between the half-life and the properties of the transition. It is therefore not possible to estimate the half-life because one does not precisely know the value of the matrix element of the transition. However a theory was elaborated, the "Gross theory", which enables half-life predictions by estimating this matrix element.

### 1.2.1 Fermi theory of beta decay

Fermi introduced for the first time in 1934 a successful theory of $\beta$ decay [Fer34], including Pauli's neutrino hypothesis. This approach is derived from the expression of the transition probability to a continuum of states. This value is given by Fermi's golden rule. The transition rate between an initial state $|\psi_i\rangle$ and a final state $|\psi_f\rangle$ is given by:

$$\lambda = \frac{2\pi}{\hbar}|\langle\psi_f|U|\psi_i\rangle|^2\rho(E_f) \tag{1.11}$$

with $\hbar = \frac{h}{2\pi}$ the reduced Planck constant, $\rho(E_f)$ the density of final states (per energy unit) and $U$ the interaction between the two states. Precisely the final state of the system is a combination of the $\beta$ particle, neutrino and nucleus states. The transition matrix element $\langle\psi_f|U|\psi_i\rangle$ between the initial and final states of the nucleus $|\psi_{i(f)}\rangle$ must take into account the $\beta$ particle state $|\varphi_e\rangle$ and the neutrino state $|\varphi_\nu\rangle$. A more realistic expression of the transition matrix element is:

$$g\langle\psi_f\varphi_e\varphi_\nu|O_X|\psi_i\rangle \tag{1.12}$$

The mathematical operator $O_X$ of the interaction can have five forms consistent with special relativity: V (vector), A (axial vector), S (scalar), P (pseudo-scalar) and T (tensor). The constant $g$ defines the strength of the interaction.

The density of states determines the shape of the energy spectrum of the emitted $\beta$ particles. If we consider the emission of a positron/electron of momentum $p$ and a neutrino of momentum $q$ confined in a volume $V$, the densities of final positron/electron and neutrino states are

$$dn_e = \frac{4\pi p^2 dp V}{h^3} \text{ and } dn_\nu = \frac{4\pi q^2 dq V}{h^3} \tag{1.13}$$

(normalised by $h^3$ because it is a six dimensional space: three for position and three for the momentum vector). Both neutrino and positron/electron have a free-particle wave function $\varphi(r) = \frac{1}{\sqrt{V}}e^{\frac{i\vec{p}.\vec{r}}{\hbar}}$. In first order approximation ($\vec{p}.\vec{r} \ll 1$), one has $\varphi(r) \sim \frac{1}{\sqrt{V}}$. This approximation is called the *allowed* approximation.

By applying Fermi's golden rule (equation 1.11) with the matrix element of equation 1.12, one obtains the partial decay rate as:

$$d\lambda = \frac{2\pi}{\hbar}g^2|M_{fi}|^2\frac{dn_e dn_\nu}{V^2 dE_f} \tag{1.14}$$

where

- $\frac{dn_e dn_\nu}{dE_f} = (4\pi)^2\frac{V^2 p^2 dp q^2 dq}{h^6 dE_f}$,

- $M_{fi} = \langle\psi_f\varphi_e\varphi_\nu|O_X|\psi_i\rangle$ the transition matrix element,

- $E_f = E_e + E_\nu \sim E_e + qc$ thus $\frac{dq}{dE_f} = \frac{1}{c}$ with $E_e$ the energy of the $\beta$ particle. One assumes the neutrino mass is null, consequently its total energy is $E_\nu \sim qc$.

One has the number of $\beta$ particles between $p$ and $p + dp$:

$$N(p)dp = d\lambda = \frac{g^2|M_{fi}|^2}{2\pi^3\hbar^7 c}p^2 q^2 dp = \frac{g^2|M_{fi}|^2}{2\pi^3\hbar^7 c^3}p^2(Q_\beta - T_e)^2 dp \qquad (1.15)$$

with $Q_\beta = T_e + qc$ the energy released by the process. The relation $c^2 p dp = (T_e + m_e c^2)dT_e$, that leads to the number of emitted $\beta$ particles with a kinetic energy $T_e$ :

$$N(T_e) = \frac{g^2|M_{fi}|^2}{2\pi^3\hbar^7 c^6}\sqrt{T_e^2 + 2T_e m_e c^2}(Q_\beta - T_e)^2(T_e + m_e c^2) \qquad (1.16)$$

With this simplified approach, one obtains a good approximation of the $\beta$ particle emission spectrum, vanishing at $T_e = Q_\beta$, the end-point of the energy spectrum. The shape of the spectrum as obtained with equation 1.16 is illustrated in figure 1.4.
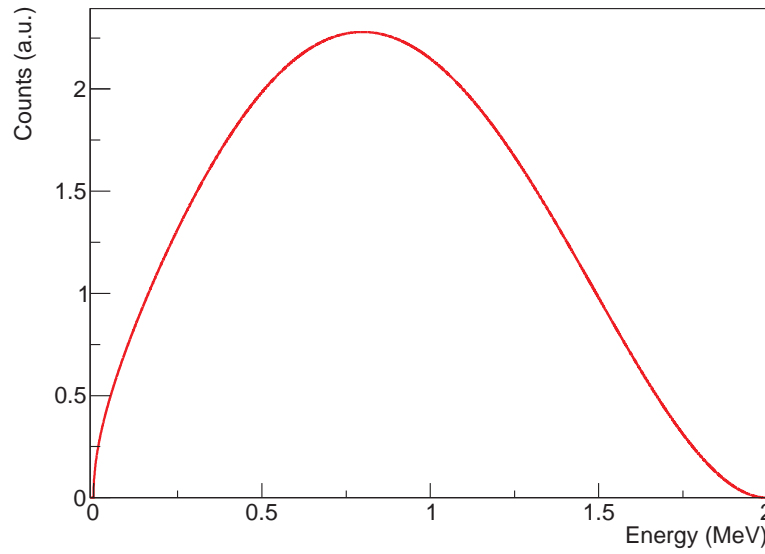


Figure 1.4: Shape of the $\beta$ particle energy spectrum deviated from equation 1.16 for a $Q_\beta$ value of 2 MeV.

The shape of the $\beta$ particle spectrum is well reproduced but the equation 1.16 is divergent for $T_e > Q_\beta$. One has to keep in mind that this function is a first order approximation of Fermi's golden rule and is only suitable to give an idea of the shape of the $\beta$ particle spectrum. Moreover the charge of the $\beta$ particle is not taken into account (electron or positron). In practice, one observes a change of the shape. The number of accessible final states $N(p)$ is modified by the Fermi function $F(Z_{\text{daughter}}, p)$. It models the influence of the Coulomb field originating from the nucleus and takes into account the charge of the emitted electron or positron:

$$N(p) = \frac{g^2|M_{fi}|^2}{2\pi^3\hbar^7 c^3}p^2(Q_\beta - T_e)^2 F(Z_{\text{daughter}}, p) \qquad (1.17)$$

By rewriting equation 1.15 using equation 1.17, one has:

$$\lambda = \frac{g^2|M_{fi}|^2}{2\pi^3\hbar^7 c^3}\int_0^{p_{max}} F(Z_{\text{daughter}}, p)p^2(Q_\beta - T_e)^2 dp \qquad (1.18)$$

From equation 1.18, the Fermi integral can be expressed as:

$$f(Z_{\text{daughter}}, p) = \frac{1}{(m_e c)^3(m_e c^2)^2}\int_0^{p_{max}} F(Z_{\text{daughter}}, p)p^2(Q_\beta - T_e)^2 dp \qquad (1.19)$$

### 1.2.2 Selection rules and types of transition

Calculations presented before are performed in the allowed approximation where wave functions $\varphi(r) = \varphi(0)$ are assumed. However, this scheme does not correspond to all emitted transitions and hence different approximations are needed. Besides this, two types of transitions are observed depending on the configurations of the $\beta$ particle and the neutrino: Fermi and Gamow-Teller. Each type has its own selection rules according to the spin, isospin and parity of the nucleus.

The total spin $J = L + S$ is the sum of the quantum numbers $S$ (spin) and $L$ (angular momentum).

The isospin $(T)$ is a fictive spin formalism introduced in 1932 by Heisenberg [Hei32] in order to distinguish protons and neutrons with their charge state. Each nucleon has the same isospin $\frac{1}{2}$ with a projection $T_z = -\frac{1}{2}$ for protons and $T_z = +\frac{1}{2}$ for neutrons. The isospin projection of a nucleus is given by $T_z = \frac{N-Z}{2}$.

The parity of a nucleus is defined as $\pi = (-1)^L$ with $L$ the angular momentum of the nucleus. $L = L_{\text{protons}} + L_{\text{neutrons}}$ is the sum of the angular momenta of the protons and neutrons, depending on the occupied shells. According to the Pauli exclusion principle, the angular momentum is given by the single nucleon filling the highest energetic shell in the case of an odd number of proton or neutron. With an even number of proton/neutron, $L_{\text{protons(neutrons)}}$ is equal to zero. As an example, an even-even nucleus has $L = 0$ and $\pi = 1$.

The electron (or positron) and the neutrino configurations define the type of the $\beta$ decay transition. The spins of the electron (positron) and the neutrino can be parallel (spin of the electron-neutrino system $S = 1$) or anti-parallel $(S = 0)$. For a Fermi decay, the spin is $S = 0$ (anti-parallel). In the allowed approximation, the nuclear spin is not changed resulting in $\Delta J = \Delta T = 0$.

In opposite, the Gamow-Teller decay involves spin $S = 1$ (parallel). For a decay between two states $(J_i, \pi_i, T_i)$ and $(J_f, \pi_f, T_f)$, their nuclear spins are defined by $J_i = J_f + 1$ (except for $J_i = J_f = 0$). We therefore have to consider $\Delta J = 0, 1$ in the allowed approximation.

For both types of allowed transitions, Fermi and Gamow-Teller, the parity is conserved $\pi_f = \pi_i$ and $l = 0$.

Less probable $\beta$ decays violate these selection rules. They are named *forbidden* decays and can be of Fermi $(S = 0)$ or Gamow-Teller $(S = 1)$ type. This results in $\Delta J = 0, 1$ for Fermi and $\Delta J = 0, 1, 2$ in the case of Gamow-Teller decays. If $l = 1$, the parity conservation is violated and the transition is a 1st forbidden decay. If $l = 2$, the parity is conserved and $\Delta J = 2, 3$. This is a 2nd forbidden decay. For $l = 3$, $\pi_f \neq \pi_i$ and $\Delta J = 3$, this is a 3rd forbidden decay. If $l = 4$, $\pi_f = \pi_i$ and $\Delta J = 4, 5$, it is a 4th forbidden decay.

If the initial and final state quantum numbers are identical, the final state is called "Isobaric Analogue State" (IAS). This state has the same isospin $T$ as the precursor but a different $T_z$ projection. The IAS is so similar to the precursor state that it is populated by the majority of the $\beta$ decays (Fermi transition).

In the case of a pure Fermi or Gamow-Teller transition, the decay rate in the allowed configuration is given by equation 1.18. With $\lambda = \frac{\ln(2)}{t_{1/2}}$, this leads to the definition of the transition strength

$$ft_{1/2} = \frac{2\pi^3\hbar^7\ln(2)}{m_e^5 c^4} \frac{1}{g^2|M_{fi}|^2} \tag{1.20}$$

$G$ is the coupling constant of the transition. For a Fermi transition, it is $g_V$ (vector coupling constant) since the Fermi theory takes into account only the vector interaction of the transition. The coupling constant of Gamow-Teller transitions is $g_A$ (axial vector coupling constant). $M_{fi}$ is the matrix element of the transition.

The $\beta$ decay of a nucleus is most of the time a mixing between Fermi and Gamow-Teller transitions. Equation 1.20 is therefore rewritten:

$$ft_{1/2} = \frac{2\pi^3\hbar^7\ln(2)}{m_e^5 c^4} \frac{1}{g_V^2|M_F|^2 + g_A^2|M_{GT}|^2} \tag{1.21}$$

where $M_F$ and $M_{GT}$ correspond to the interaction matrix elements of the pure Fermi (vector) and Gamow-Teller (axial vector) interaction, respectively. The Fermi/Gamow-Teller transition mixing is expressed by the amplitude ratio $\frac{g_V M_F}{g_A M_{GT}}$. The value of $log(ft)$ is different according to the transition type. For the shortest comparative half-lives, the transition is *super-allowed*, then the $log(ft)$ value increases because transitions of higher orders are less probable:

- 3 to 4: super-allowed

- 3 to 7: allowed

- 6 to 9: 1$^{st}$ forbidden

- 10 to 13: 2$^{nd}$ forbidden

- 14 to 20: 3$^{rd}$ forbidden

- 20 to 24: 4$^{th}$ forbidden

### 1.2.3   The Gross theory

The Gross theory was developed by Takahashi and Yamada in 1969 [Tak69] to perform quantitative calculations of the half-lives of the $\beta^{+/-}$ decay and electron capture. This theory evaluates the Fermi and Gamow-Teller matrix elements $|M_\Omega(E)|^2$ as shown in equation 1.21 for a $\beta$ decay of energy $E$ (difference between the final and initial states). It supposes the existence of a single-nucleon energy $\varepsilon$ (proton for $\beta^+$/EC decay and neutron for $\beta^-$ decay) with a transition probability $D_\Omega(E,\varepsilon)$. The following expression is assumed for the transition matrix element:

$$|M_\Omega(E)|^2 = \int_{\varepsilon_{min}}^{\varepsilon_{max}} D_\Omega(E,\varepsilon)W(E,\varepsilon)\frac{dn}{d\varepsilon}d\varepsilon \qquad (1.22)$$

$\Omega$ is the type of transition (Fermi or Gamow-Teller). $\varepsilon$ is the sum of the neutron-proton mass difference, the kinetic energy and the potential energy of the nucleon. $W(E,\varepsilon)$ is the weight function to take into account the degree of vacancy of the final states. The single-nucleon distribution $\frac{dn}{d\varepsilon}$ is calculated from the Fermi gas model. In the Gross theory, the properties of the decay are averaged over the transition possibilities which depend on the number of different final states.

An improvement of the theory was performed in 1985 [Kon85] to include the pairing effect and the non-energy-weighted sum rule of the Fermi transition. A second improvement came out in 1990 [Tac90] with a modification of the one-particle strength function.

## 1.3   Beta-delayed proton emission

The $\beta$-delayed emission of particles is a more exotic decay mechanism compared to the $\beta$ radioactivity. It is observed when the $\beta$ decay populates nuclear states unstable against the emission of one or more nucleons. The $\beta$-delayed emission of proton, neutron or alpha particle are possible. The first indication of the $\beta$-delayed emission of particles was observed for the first time in 1916 by Rutherford [Rut16]. He reported the observation of two different groups of $\alpha$ particles from the disintegration of $^{212}$Bi. The "long-range" $\alpha$ particles were emitted by the $\alpha$ decay to $^{208}$Tl whereas the "short-range" ones by $\beta$-delayed $\alpha$ emission to $^{208}$Pb. Near the neutron drip line, $\beta$-delayed neutron emission is observed, a nucleus decays by $\beta^-$ process to an excited state which emits a neutron. Near the proton drip line, emission of protons is observed following a $\beta^+$/EC decay.

In the $\beta^+$-delayed proton emission process, a precursor decays by $\beta^+$ emission to an excited state of an emitter (see figure 1.5). If the excitation energy is above the proton separation energy $S_p$, this nucleus de-excites by emitting a proton ($\beta p$ decay). If the excitation energy is above the two-proton separation energy $S_{2p}$, it emits two protons ($\beta 2p$ decay), three protons for an excitation energy above $S_{3p}$ ($\beta 3p$ decay). Emission of more than three protons is very unlikely because the energy of the potential levels to be populated is too high. Nuclei can also decay by
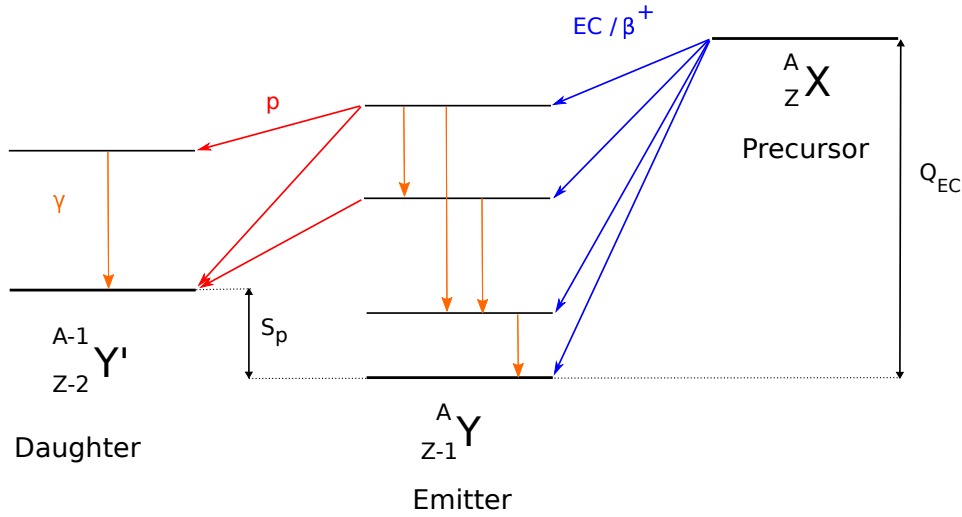
Figure 1.5: Schematic level schemes of $\beta$ decay and $\beta$-delayed proton emission for a proton-rich nucleus. The precursor $^{A}_{Z}X$ decays by $\beta^{+}$ decay or electron conversion (EC) to an excited state of the daughter $^{A}_{Z-1}Y$ called "emitter". This latter de-excites by $\gamma$ emission, or by proton emission to the daughter $^{A-1}_{Z-2}Y'$ if the excitation energy is above the proton separation energy $S_p$. If the level energy is above $S_{2p}$ the emitter can also emit two protons, or even three if the energy is above $S_{3p}$. The emitter can also decay by emitting an $\alpha$ particle from the excited state if it is above $S_{\alpha}$.

emitting an $\alpha$ particle from the excited state if it is above $S_{\alpha} = B(^{A}_{Z}X) - B(^{A-4}_{Z-2}Y)$. Only the $\beta$-delayed proton emission is discussed in this section.

### 1.3.1 Beta-delayed one-proton emission

The first observation of $\beta$-delayed one-proton emission was performed for $^{25}$Si in 1963 [Bar63]. Currently, more than 160 emitters are known from $^{8}$B to $^{163}$Hg [Bla08a] (2008 review).

The released energy by the $\beta p$ decay is:

$$Q_{\beta p} = \left( M(^{A}_{Z}X) - M(^{A-1}_{Z-2}Y') - m(^{1}H) - 2m_e \right) c^2 \tag{1.23}$$

with $m(^{1}H)$ the hydrogen mass. This formula is given with atomic masses. That leads to the relation with the $Q_{\beta}$:

$$Q_{\beta p} = Q_{\beta} - S_p \tag{1.24}$$

$S_p = \left( M(^{A-1}_{Z-2}Y') - M(^{A}_{Z-1}Y) + m(^{1}H) \right) c^2$ is the proton separation energy expressed in atomic masses. Figure 1.5 shows that the emission of the proton is possible only if $Q_{\beta} > S_p$.

For a level of energy $E_i$ populated by $\beta$ decay, the energy of the emitted proton is given by the energy $E_f$ of the final state and the separation energy $S_p$:

$$E_p = E_i - (E_f + S_p) \tag{1.25}$$

The precursors studied in this work populate emitters with a low density of excited states. The proton energy spectrum is composed of sharp peaks corresponding to each state populated by $\beta$ decay. On the contrary, the $\beta$-particle energy is a broad distribution. From the relative probability of proton emission from each excited state, one can deduce the relative population of these levels by $\beta$ decay.

The emission probability of a proton from an excited state will depend on the barrier height and the proton separation energy of the emitter. The greater the level energy is, the shorter is the half-life of the emitting state.

### 1.3.2 Beta-delayed two-proton emission

For more exotic nuclei, closer to the proton drip line, the two-proton separation energy $S_{2p}$ decreases. Reaching a state of energy above $S_{2p}$ by $\beta$ decay becomes more likely and the $\beta 2p$ emission becomes possible.

The $Q$ value of this reaction is:

$$\begin{aligned} Q_{\beta 2p} &= \left( M(^A_Z X) - M(^{A-2}_{Z-3} Y') - 2m(^1H) - 2m_e \right) c^2 \\ &= Q_\beta - S_{2p} \end{aligned} \tag{1.26}$$

where $S_{2p} = \left( M(^{A-2}_{Z-3} Y') - M(^A_{Z-1} Y) + 2m(^1H) \right) c^2$ is the two-proton separation energy.

The total energy of the two protons is equal to the difference between the state $E_i$ populated by $\beta$ decay and the final state $E_f$:

$$E_{2p} = E_i - (E_f + S_{2p}) \tag{1.27}$$

The $\beta 2p$ decay was observed for the first time in 1983 with $^{22}$Al [Cab83]. The other known emitters are $^{23}$Si, $^{26}$P, $^{27}$S, $^{31}$Ar, $^{35}$Ca, $^{39}$Ti, $^{43}$Cr, $^{45}$Fe, $^{50}$Ni [Bla08a] (2008 review), $^{51}$Ni [Aud12] (2012) and $^{46}$Fe [Pom14] (2014).

### 1.3.3 Beta-delayed three-proton emission

This process is the most exotic $\beta$-delayed proton emission. The $\beta$ decay has to populate an excited state above the three-proton separation energy $S_{3p}$. The $Q_{\beta 3p}$ value is similar to equation 1.26 and the total energy is similar to equation 1.27 but considering $S_{3p}$ instead. Thus one has:

$$\begin{aligned} Q_{\beta 3p} &= \left( M(^A_Z X) - M(^{A-3}_{Z-4} Y') - 3m(^1H) - 2m_e \right) c^2 \\ &= Q_\beta - S_{3p} \end{aligned} \tag{1.28}$$

and

$$E_{3p} = E_i - (E_f + S_{3p}) \tag{1.29}$$

The first observation came out from an experiment using a time projection chamber, a gaseous detector providing a three-dimensional reconstruction of the tracks of the protons, in which $^{45}$Fe was studied in 2007 [Mie07a]. This was followed by the observation of $\beta 3p$ decays in the $^{43}$Cr [Pom11b, Aud12] and $^{31}$Ar [Lis15] nuclei resulting small branching ratios: 0.07(2)% for $^{31}$Ar [Lis15] and 0.30(4)% for $^{45}$Fe [Mie07a].

## 1.4 Two-proton radioactivity

The prediction and the first calculations of the proton radioactivities (one- and two-proton) were performed by Goldansky [Gol60] in 1960. The one-proton radioactivity was discovered in 1982 with $^{151}$Lu [Hof82] and $^{147}$Tm [Kle82]; now around 30 emitters are known [Bla08a]. The 2p radioactivity was discovered only forty years after the first predictions with the $^{45}$Fe observation in 2002 [Pfü02, Gio02]. Only four other emitters are known: doubly-magic $^{48}$Ni [Dos05, Pom11a], $^{54}$Zn [Bla05], $^{19}$Mg [Muk07] and recently $^{67}$Kr [Goi16] which is discussed in this thesis.

The protons are emitted by crossing the Coulomb barrier (see left scheme in figure 1.6). The process depends on the available energy $Q_{2p}$:

$$\begin{aligned} Q_{2p} &= -S_{2p} \\ &= B(^{A-2}_{Z-2} Y) - B(^A_Z X) \\ &= \left( M(^A_Z X) - M(^{A-2}_{Z-2} Y) - 2m(^1H) \right) c^2 \end{aligned} \tag{1.30}$$

Its value has to be high enough to have a time to cross the barrier which is competitive compared to $\beta$ decay half-life. Similarly to the Gamow model for $\alpha$ decay, simple 2p emission models
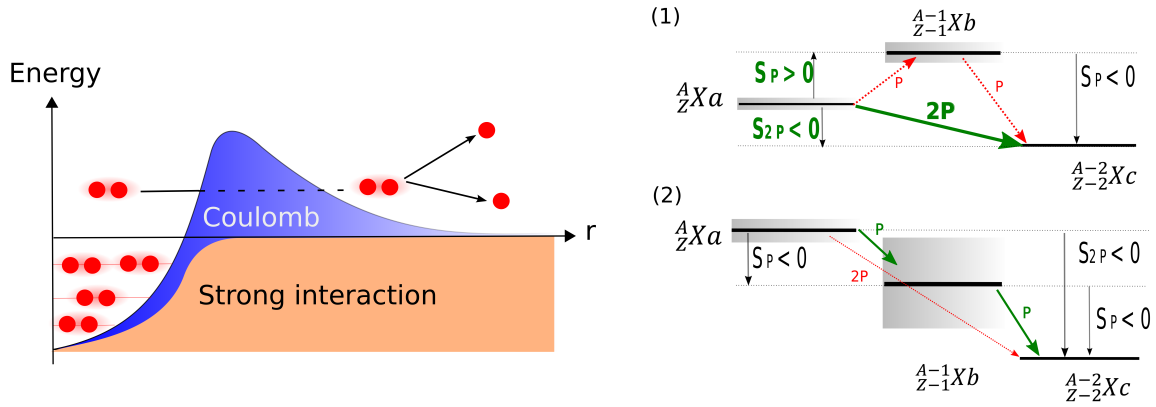
Figure 1.6: Left: illustration of the tunnelling process of two-proton radioactivity. The nucleus has an even number of protons. The protons are quasi bound by the strong interaction potential and the Coulomb barrier. Two valence protons have a high enough energy to not be bound by the strong interaction and can be emitted by tunnelling the Coulomb barrier. The pairing effect forbids the emission of a single proton. Right: cases of direct proton emission from a ground-state. A negative value of $S_{2p}$ is necessary to allow the emission of two protons. In case (1), $S_p$ is positive because of the pairing effect, so the one-proton decay is energetically forbidden. This case is the 2p radioactivity. In case (2), $S_p$ is also negative and an intermediate state can be reached by one-proton decay. The 2p decay can be interpreted as a sequential emission.

suppose that the di-proton system pre-exists in the nucleus and the 2p radioactivity is the tunnelling through the Coulomb potential barrier by this system.

To observe 2p radioactivity, the nucleus needs to have an even number of protons. Because of the pairing effect, $S_p > 0$ and the emission of one proton is forbidden. This case is represented on the inset (1) of figure 1.6. For this configuration, the two protons are emitted simultaneously from a ground-state with a long lifetime. Indeed Goldansky defined in his model the lifetime limits of the 2p radioactivity with a 2p region above $10^{-12}$ s [Gol66]. He also assumes that the observation of 2p radioactivity is impossible above 100 s because of the competition of the $\beta$ decay. The nuclei $^{19}$Mg, $^{45}$Fe, $^{48}$Ni and $^{54}$Zn follow the 2p radioactivity scheme represented on the inset (1) of figure 1.6 and half-lives greater than the ps (a few ps for $^{19}$Mg, ms for the $^{45}$Fe, $^{48}$Ni and $^{54}$Zn). The case of $^{67}$Kr is discussed in section 4.2. The inset (2) of figure 1.6 illustrates a nucleus with negative $S_{2p}$ and $S_p$. Thus a very short-lived intermediate state is reachable by one-proton decay and the 2p decay consists in sequential two proton emissions. This configuration is similar to a decay from an excited initial state, as for a $\beta 2p$ decay. The intermediate energy state can also be too large to distinguish simultaneous 2p emission from sequential. These nuclei do not fulfil the Goldansky criterion of 2p radioactivity because of their very short half-life below $10^{-12}$ s. $^6$Be [Gee77], $^{12}$O [Kry95], $^{16}$Ne [Muk08] and $^{30}$Ar [Muk15] follow this decay scheme with upper half-life limits from $10^{-21}$ to $10^{-15}$ s.

In this section we will focus on the theory of 2p radioactivity since the first predictions of Goldansky with the description of the different emission models. Another important question is the prediction of new emitters. To achieve this, one needs mass estimate of the potential emitters. Because these masses are not experimentally known, local mass models are used by extrapolating nuclei properties in the vicinity of the nucleus of interest. Then a brief history of the experimental milestones of the 2p radioactivity study will be presented.

## 1.4.1 Emission models

The first calculations were performed by Goldansky in 1960. He used a square potential well for the strong interaction. A di-proton system ($^2$He) crosses the Coulomb barrier of the nucleus defined by equation 1.2. Then this di-proton system breaks after crossing the barrier. The probability of crossing the barrier is the product of the two usual barrier factors of each proton,

giving the total factor [Gol60]

$$w(E) = exp\left(\frac{-2\pi(Z-2)e^2\sqrt{m_p}}{\hbar\sqrt{E_{pp}}}\left[\frac{1}{\sqrt{x}} - \frac{1}{\sqrt{1-x}}\right]\right) \tag{1.31}$$

with $e$ the absolute value of the electric charge of the electron, $m_p$ the proton mass, $E_{pp}$ the total energy of the two protons and $x$ the energy division between the two protons ($E = xE_{pp}$ or $(1 - x)E_{pp}$). This distribution is maximum for $x = 0.5$ i.e. for an equal energy division between the two protons.

Three emission models were then developed to describe the $2p$ radioactivity and compute the half-lives. Two of them are di-proton approaches: the R-matrix formalism and the SMEC (Shell Model Embedded in the Continuum). The third approach, the three-body model, describes the whole dynamics of the emission.

**R-matrix formalism**

The simplest approach of the 2p radioactivity, as proposed by Goldansky, considers a di-proton system crossing the Coulomb barrier. Otherwise the emission has to be treated as a three-body problem, more difficult to solve analytically. A possible formalism to estimate the half-life of a 2p emitter relies on the R-matrix theory defined by Lane and Thomas in 1958 [Lan58]. Only two-body phenomena are considered with the interactions between the di-proton and the core (the remaining nucleons). This method supposes the existence of a channel radius $R_0$ beyond which the strong interaction is null and results in a 2p decay width expression:

$$\begin{aligned} \Gamma &= \frac{\hbar \ln 2}{T_{1/2}} \\ &= 2\theta^2 \gamma^2 P_L(Q_{2p}) \end{aligned} \tag{1.32}$$

The spectroscopic factor $\theta^2$ is extracted from shell-model calculations. The usual probability of crossing the Coulomb barrier $P_L(Q_{2p})$ (penetrability) is calculated as Goldansky with equation 1.31. The penetrability depends on the orbital momentum $L$ of the protons. $\gamma^2$ is the Wigner reduced width:

$$\gamma^2 = \frac{3\hbar^2 c^2}{2\mu R_0^2} \tag{1.33}$$

where $\mu = \frac{m_p m_p}{m_p + m_p}$ is the reduced mass of the di-proton system and $R_0$ the channel radius.

The R-matrix formalism was used by Brown [Bro91], Ormand [Orm96, Orm97] or Barker [Bar01] to predict the half-lives of 2p emitters. Examples of half-lives obtained for $^{45}$Fe and $^{48}$Ni with this formalism are summarised in table 1.2.

| Nucleus | $T_{1/2}$ (ms) | | |
|---|---|---|---|
| | [Bro91] | [Orm96] | [Orm97] |
| $^{45}$Fe | $0.002 - 0.3$ | $10^{-5} - 10^{-1}$ | - |
| $^{48}$Ni | $0.001 - 0.2$ | $0.01 - 3660$ | $5 \times 10^{-6} - 90$ |

Table 1.2: Half-life calculations from R-matrix formalism [Bro91, Orm96, Orm97] for the 2p emitters $^{45}$Fe and $^{48}$Ni. The spectroscopic factor is assumed to be $\theta^2 = 1$.

Following the discovery of 2p radioactivity in 2002, improvements of R-matrix calculations were proposed by Brown and Barker [Bro03]. The most recent half-lives of the medium-mass emitters calculated from the experimental $Q_{2p}$ values are summarised in table 1.3.

**Shell model embedded in the continuum**

The standard shell model does not take into account the continuum. Thus to describe the emission of particles by the nucleus, one needs to establish the coupling of the shell model to the continuum. The SMEC (Shell Model Embedded in the Continuum) [Rot05a, Rot05b, Rot06] is an extension of the shell model which was briefly introduced in section 1.1.

It describes the behaviour of the nucleons inside the potential well. The nucleus is divided in three spaces:

| Nucleus | $T_{1/2}$ (ms) |
|---------|----------------|
| $^{45}$Fe | $46^{+25}_{-16}$ [Dos05] |
| $^{48}$Ni | $16^{+10}_{-4}$ [Dos05] |
| $^{54}$Zn | $10^{+7}_{-4}$ [Bla05] |

Table 1.3: Half-life calculations of $^{45}$Fe, $^{48}$Ni and $^{54}$Zn (Brown and Barker R-matrix) from experimental $Q_{2p}$ values of [Dos05] and [Bla05].

- The core composed of nucleons, without possible rearrangement of them.

- The valence space with the nucleons of the outer shells. This space determines the energy level of the nucleus.

- The continuum which is the outside of the nucleus. Here the nucleons are not bound to the nucleus.

The first model of open system coupling to the continuum was established by Fano in 1960 [Fan61]. The continuum is divided in two sub-spaces: one for bound states, another for energy dispersion states.

In SMEC, a third sub-space of the continuum is defined. It is composed of the two-particle states in the continuum. Calculations within this sub-space show the different possibilities of coupling between the two protons. The 2p decay width is expressed in function of the Hamiltonian of the proton states coupling to the continuum and depends on the available energy $Q_{2p}$.

Calculations are performed with effective shell model Hamiltonian as GXPF1 [Hon05]. Example of half-lives, calculated with SMEC model, are presented in table 1.4.

| Nucleus | $T_{1/2}$ (ms) |
|---------|----------------|
| $^{48}$Ni | $7.4^{+4.9}_{-2.9}$ |
| $^{54}$Zn | $13.8^{+8.4}_{-5.1}$ |

Table 1.4: Half-life calculations of $^{48}$Ni and $^{54}$Zn from SMEC with a GXPF1 Hamiltonian. Values taken from [Rot06].

**Three-body model**

In the 2000s, Grigorenko developed a new approach of the 2p radioactivity based on solving the three-body problem. After first calculations on $^{19}$Mg [Gri00], he developed widely the basis of his three-body model [Gri01, Gri03, Gri07a, Gri07b, Gri10]. The system is composed of three interacting objects: the two protons and the core (the remaining nucleons). The strong interaction potential used is the Woods-Saxon function (cf. equation 1.1).

In order to solve the Schrödinger equation of this three-body system, Grigorenko uses the hyperspherical harmonics method. This latter was introduced by Zernike and Brinkman in 1935 [Zer35]. The harmonics are polynomials in a N-dimensional spherical space, they are thus a generalisation of the classical three-dimensional spherical harmonics functions. They are expressed in the hyperspherical coordinates, reducing the number of metric coordinates of a N-dimension system. The hyperspherical system is composed of only one metric coordinate called hyper-radius ($\rho$) and angular coordinates called hyper-angles ($\Omega_k$). For our three-body system, the hyperspherical coordinates are composed of the hyper-radius and one hyper-angle:

$$\begin{cases} \rho = \sqrt{x^2 + y^2} \\ \Omega = \arctan(x/y) \end{cases} \tag{1.34}$$

with $x$ and $y$ the scaled vectors

$$x = \sqrt{\frac{A_1 A_2}{A_1 + A_2}} X \ , \ y = \sqrt{\frac{(A_1 + A_2)A_3}{A_1 + A_2 + A_3}} Y \tag{1.35}$$

$X$ and $Y$ are the Jacobi vectors of the system. For three bodies of mass number $A_i$, these vectors are:

$$\begin{cases} X = r_1 - r_2 \\ Y = \frac{A_1 r_1 + A_2 r_2}{A_1 + A_2} - r_3 \end{cases} \tag{1.36}$$

with $r_i$ the position vector of the $i^{th}$ particle.

**(a) Shell model "V"**    **(b) Jacobi "T"**    **(c) Jacobi "Y"**
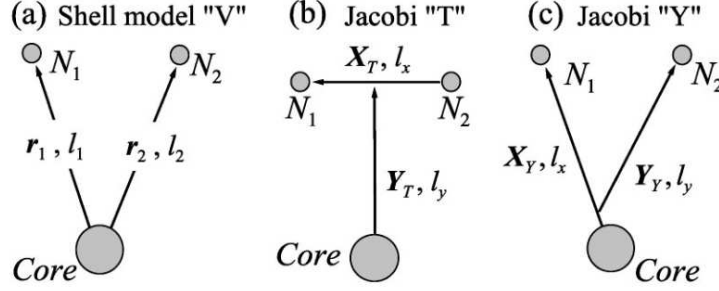
Figure 1.7: Hyperspherical tree diagrams of the three representations of 2p emission. The system is composed of three bodies: the core and the two protons $N_1$, $N_2$. In the first case (a), the emission is simultaneous and there is no need to calculate the Jacobi coordinates, it is a simple shell model approach. Each proton has a position $r_i$ and an angular momentum $l_i$. For the case (b), named Jacobi "T", it is a di-proton emission. There is a correlation between the two protons and we have the two Jacobi coordinates $X_T$, $Y_T$. The last representation (c), Jacobi "Y", considers the core-proton system with the two Jacobi coordinates $X_Y$ and $Y_Y$. Taken from [Gri01].

With this representation, we can draw the system in a "tree" diagram as shown in figure 1.7. Each Jacobi coordinate corresponds to a leaf, the root of the tree is associated with the hyper-radius $\rho$ and each junction with a hyper-angle. A hyperspherical representation of the system is fixed by a path from the root to the leaf. The number of paths defines the number of possible representations. In the case of 2p emission, three diagrams are represented in figure 1.7. In case (a), the protons are simultaneously emitted. This type is a direct decay to the continuum. Here one can simply keep the classical coordinates. The case (b) is the emission of a di-proton with a correlation between the protons. The studied two-body system is the p-p system. The last case (c) corresponds to a configuration where the two-body system to study is core+p . The Jacobi coordinate systems of the two last cases are named "T" and "Y". The hyperspherical coordinates for these two systems are [Gri01]:

$$\text{Jacobi T} \begin{cases} \theta = \arctan\left(\sqrt{\frac{A_{\text{core}}+2}{4A_{\text{core}}}} \frac{X_T}{Y_T}\right) \\ \rho^2 = \frac{X_T^2}{2} + \frac{2A_{\text{core}}}{A_{\text{core}}+2} Y_T^2 \end{cases} \tag{1.37}$$

$$\text{Jacobi Y} \begin{cases} \theta = \arctan\left(\sqrt{\frac{A_{\text{core}}(A_{\text{core}}+2)}{(A_{\text{core}}+1)^2}} \frac{X_Y}{Y_Y}\right) \\ \rho^2 = \frac{A_{\text{core}}}{A_{\text{core}}+1} X_Y^2 + \frac{2A_{\text{core}}+1}{A_{\text{core}}+2} Y_Y^2 \end{cases} \tag{1.38}$$

For these two Jacobi configurations, the wave function $\Psi(\rho, \Omega)$ of the protons is expanded in the hyperspherical space basis thanks to the hyperspherical harmonics. The solving of the Schrödinger equation in the hyperspherical space is more convenient.

The $Q_{2p}$ value and the wave function solutions allow to calculate the decay width $\Gamma_{2p}$ but also the kinematic properties of the protons: angle between the two emission trajectories and kinetic energy of each proton. An example of calculation is illustrated in figure 1.8 ($^{45}$Fe case). The energy and angle distributions depend on the wave function configuration of the protons ($pf$ shell mixing for $^{45}$Fe) and the Jacobi systems "Y" and "T".

### 1.4.2   The prediction of two-proton emitters: the local mass models

All the emission models presented previously need the $Q_{2p}$ value to predict the half-life $T_{1/2}$. This value is directly linked to the two-proton separation energy and thus the masses (or mass
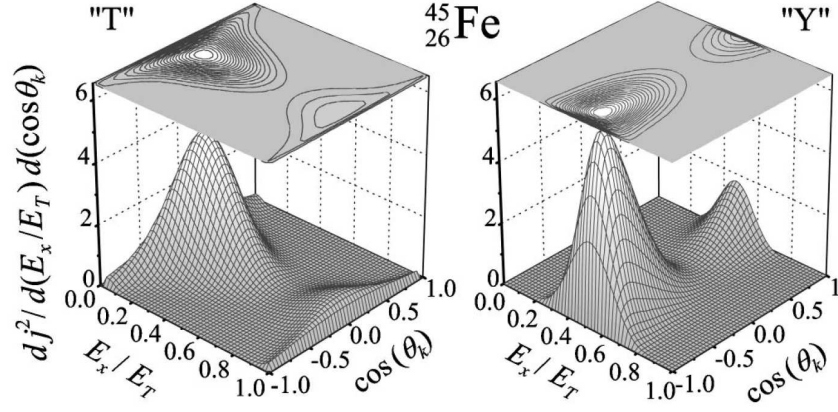
Figure 1.8: Energy and angular correlations for $^{45}$Fe. The distributions for the two Jacobi systems "T" and "Y" are computed. Case of a $pf$ shell mixing with a $f$-wave domination (75%) and a total decay energy $E_T = 1140 keV$. $E_x/E_T$ is the energy fraction of one proton with $E_T$ the 2p decay energy. Taken from [Gri03].

excess) of the parent and daughter nuclei (cf. equation 1.30). The 2p emitters are very exotic, located beyond the drip line. Most of the time, the first observation of 2p radioactivity coincides with the first production and identification of the nucleus, consequently masses are not available.

Empirical mass models are used for predictions. The usual global mass model is the Bethe-Weizsäcker one [Wei35, Bet36] based on the liquid drop model. The nucleus, assumed to behave as an incompressible drop of liquid, has a binding energy

$$B = a_v A - a_s A^{\frac{2}{3}} - a_c Z(Z-1) A^{-\frac{1}{3}} - a_{sym} \frac{(A-2Z)^2}{A} + \delta \tag{1.39}$$

$a_v$ is the volume term giving to each nucleon the same contribution. $a_s$ is the surface term to compensate the over-estimation of $B$ because nucleons near the surface have less neighbours to interact. $a_c$ is the Coulomb term to take into account the Coulomb repulsion by considering the nucleus as a uniformly charged sphere. The symmetry term $a_{sym}$ takes into account the fact that stable light nuclei are near $Z \sim A/2$. The pairing term $\delta$ adjusts $B$ according to the pairing effect.

Nevertheless global mass models based on this approach, as the Finite-Range Droplet Mass Model (FRDM) [Möl12], are not enough accurate near the limits of stability. Estimates of $S_{2p}$ are thus performed from local mass model predictions, providing lower uncertainties. They calculate the masses from known nuclei in the vicinity of the nucleus of interest. They are based on the study of the isobaric multiplets (nuclei of same isospin $T$).

Two local models are used for the 2p predictions: the IMME (Isobaric Multiplet Mass Equation) and the Garvey-Kelson formula. The estimated $Q_{2p}$ values of the known 2p emitters are summarised in section 1.4.4.

**The isobaric multiplet mass equation**

According to the projection rules of a quantum operator, an isospin $T$ has $(2T + 1)$ projections $T_z = \frac{N-Z}{2}$. A multiplet of $(2T + 1)$ nuclei of same isospin can be parametrized in mass or binding energy by:

$$\begin{cases} M(A, T_z) = a + bT_z + cT_z^2 \\ B(A, T_z) = a' + b'T_z + c'T_z^2 \end{cases} \tag{1.40}$$

The difference between the binding energies of two nuclei of opposite isospin projection $T_z$ according to the equation 1.40, is given by:

$$B(A, T_z = -T) - B(A, T_z = T) = -2b'T \tag{1.41}$$

Thus we obtain the relation linking the nucleus of interest $T_z = -T$ with its neutron-rich mirror nucleus $T_z = T$ ($T > 0$).

The mass of the neutron-rich mirror nucleus is deduced from experimental values. The $b'$ parameter can be deduced by a fit of experimental masses. There are few multiplets for which three or more masses are known accurately enough. The mass uncertainties for our multiplets of interest are not lower than a few hundreds keV [Bro91]. The estimation of the displacement energy $\Delta E = 2b'T$ gives better results than the fit of the multiplet masses and is better known with an uncertainty of a few tens keV [Bro91].

Brown [Bro91, Bro02] and Ormand [Orm96, Orm97] compute $S_{2p}$ by estimating the displacement energy from shell model calculations. As an example, the 2p separation energy of $^{45}$Fe calculated by [Orm96] is:

$$S_{2p} = B\left(^{45}_{26}\text{Fe}\right) - B\left(^{43}_{24}\text{Cr}\right) \tag{1.42}$$

$^{45}$Fe belongs to the $T = \frac{7}{2}$ multiplet and $^{43}$Cr to the $T = \frac{5}{2}$ multiplet, their binding energies are not known experimentally. With the equation 1.41, one has for these nuclei:

$$\begin{cases} B(^{45}_{26}\text{Fe}) = B(^{45}_{19}\text{K}) - 2b'_{\frac{7}{2}}\frac{7}{2} \\ B(^{43}_{24}\text{Cr}) = B(^{43}_{19}\text{K}) - 2b'_{\frac{5}{2}}\frac{5}{2} \end{cases} \tag{1.43}$$

The binding energies of $^{45}$K and $^{43}$K are calculated from their experimental masses. The displacement energies $2b'_{\frac{7}{2}}\frac{7}{2}$ and $2b'_{\frac{5}{2}}\frac{5}{2}$ are evaluated from shell model calculations.

Another method to estimate the $2b'T$ term is the parametrization of the Coulomb displacement energy. The binding energies of the two mirror nuclei should only differ by their Coulomb energy according to the liquid drop model. The Coulomb displacement energy is supposed to be equal to $2b'T$. Cole [Col96, Col97, Col99] parametrized the Coulomb energy displacement in the mass region of interest from experimental data. Pape and Anthony proposed a global parametrization for $9 \leq A \leq 60$ [Ant86, Pap88]. An extension was then done for $3 \leq A \leq 239$ [Ant97].

### The Garvey-Kelson relation

This phenomenological relation between masses of mirror nuclei derives from the IMME and was introduced by Garvey and Kelson in 1966 [Gar66, Kel66].

The nuclear forces are charge-symmetric and the difference between binding energies of mirror nuclei is mainly due to their Coulomb energies as it was previously explained. As the other models presented here, the Garvey-Kelson approach allows to calculate the mass difference between a proton-rich nucleus and its neutron-rich mirror nucleus. This relation connects the mirror nuclei along the $Z = N$ line [Kel66]:

$$M(A, T_z = -T) - M(A, T_z = T) = \sum_{i=-(2T-1)}^{2T-1} M(A+i, T_z = -\frac{1}{2}) - M(A+i, T_z = \frac{1}{2}) \tag{1.44}$$

The summation is performed for odd values of $A + i$. The difference between the most proton-rich and the most neutron-rich nuclei is estimated from known mass differences between $T = \frac{1}{2}$ mirror nuclei. This equation is schematised in figure 1.9.

Approximately 5600 mass-excess values were evaluated with this method by Jänecke [Jän88].

### 1.4.3   Experimental prospects for two-proton radioactivity

As already mentioned, the first observation of 2p radioactivity was performed in 2002. The study of this exotic decay was possible due to the development of radioactive beams and production methods based on fragmentation, providing acceptable production rates.

The main experimental facts on the 2p radioactivity will be briefly presented here, with a focus on medium-mass nuclei $^{45}$Fe, $^{48}$Ni and $^{54}$Zn with half-lives of the order of ms. The last discovery of $^{67}$Kr is detailed in section 4.2. The first observations of the 2p radioactivity were
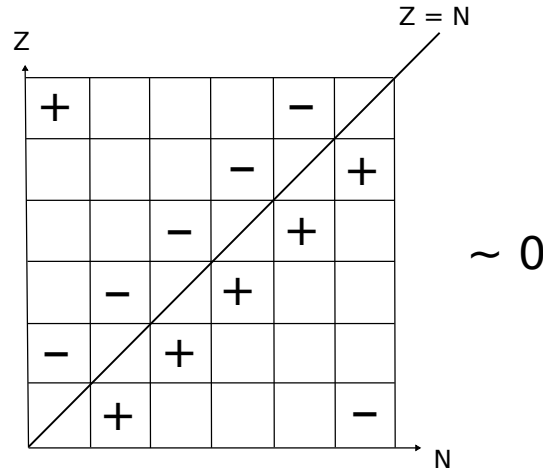
Figure 1.9: Nuclide chart illustrating the charge symmetry of the Garvey-Kelson equation for a nucleus of isospin $T = \frac{5}{2}$. One sums the mirror masses along the $Z = N$ line with the sign written in the boxes, and the mass difference between the most proton-rich and neutron-rich nucleus.

performed with silicon detectors (indirect observation). Then, proton-proton correlation studies followed with time projection chambers, measuring the energy and angle correlation between the protons (direct observation).

**First indirect observations**

The most favourable region for 2p radioactivity is the A $\sim$ 50 region according to the mass models. They pointed out $^{39}$Ti, $^{42}$Cr, $^{45}$Fe , $^{48,49}$Ni and $^{54}$Zn as the best candidates according to the $S_{2p}$ calculations [Bro91, Orm96, Col96, Bro02]. Most of these calculations were done in the 1990s. At this time, the A $\sim$ 50 region was investigated for the first time at GANIL and GSI with the observation of these candidates. Only three observations were successful.

$^{45}$Fe was observed for the first time in 1996 [Bla96] without any information about its decay. Its 2p radioactivity was observed in 2002 at GANIL [Gio02] and GSI [Pfü02]. The same experiment was re-conducted at GANIL in 2005 [Dos05].

Similarly, the doubly-magic $^{48}$Ni was identified for the first time in 2000 at GANIL [Bla00] but the first indication of its 2p radioactivity was established in a follow-up experiment in 2005. Only one event could be correlated to a 2p radioactivity in this experiment [Dos05].

$^{54}$Zn was produced and observed in 2004 at GANIL [Bla05]. The last discovery was performed in 2015 at the RIKEN Nishina Center with the first production of $^{67}$Kr [Bla16] and the observation of its 2p radioactivity [Goi16]. It is the heaviest known 2p emitter so far.

All discoveries of 2p radioactivity were performed with a measurement of the released decay energy in silicon detectors as the setup illustrated in figure 1.10. The nuclei are produced by fragmentation, identified and implanted in a segmented silicon detector DSSSD (Double-Sided Silicon Strip Detector) with a typical depth of a few hundreds of $\mu$m. Thanks to the strips, the decay events (low energy) are correlated in position with the implantation events (high energy). The correlation over a defined time window gives the energy and time spectra which are displayed in figure 1.11 for the $^{45}$Fe. The proton emission provides a narrow peak. On the contrary, the $\beta$ particles have a broad energy distribution as it is shown in section 1.2.

The direct 2p emission is discriminated from $\beta$-delayed proton decay by the shape of the spectrum. The peak is broaden because it is the sum of the two energy deposits ($\beta$ particle and proton). Moreover a proton of the expected energies (below 2-3 MeV) has a short range compared to the DSSSD thickness (47 $\mu$m at 2 MeV [Sup09]) and a $\beta$ particle has a longer range (1 mm for 520 keV [Sup09]).

The silicon detector behind the DSSSD is used as a veto. The signature of a 2p radioactivity is related to the observation of a narrow peak without any $\beta$ particle in the veto detector. Additional evidence for 2p radioactivity is based on the measurement of the daughter half-
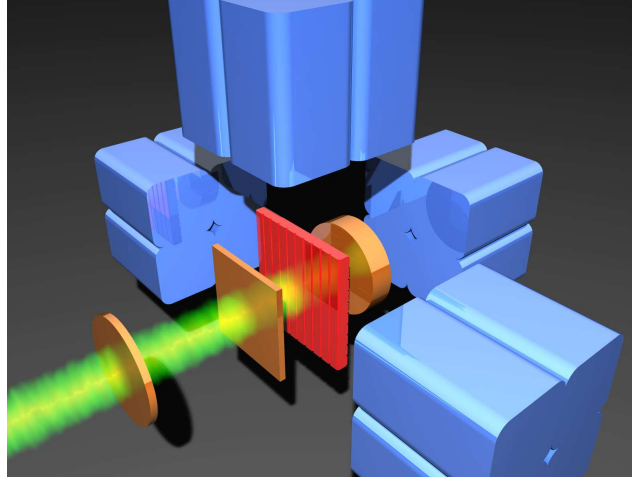
Figure 1.10: Setup used for the discovery of the 2p radioactivity of $^{45}$Fe during the GANIL experiment [Gio02]. The nuclei are implanted in a double-sided silicon strip detector or DSSSD (in red in figure). Behind and in front of the DSSSD are located silicon detectors (in orange) to detect charged particles escaping from the DSSSD. The setup is surrounded by germanium clusters (in blue) to detect $\gamma$ rays.

life. The half-life of events subsequent to the decay peak is compared with the possible decay processes (see figure 1.12 for $^{45}$Fe). If the compatible half-life is the 2p daughter one, it confirms the observation.
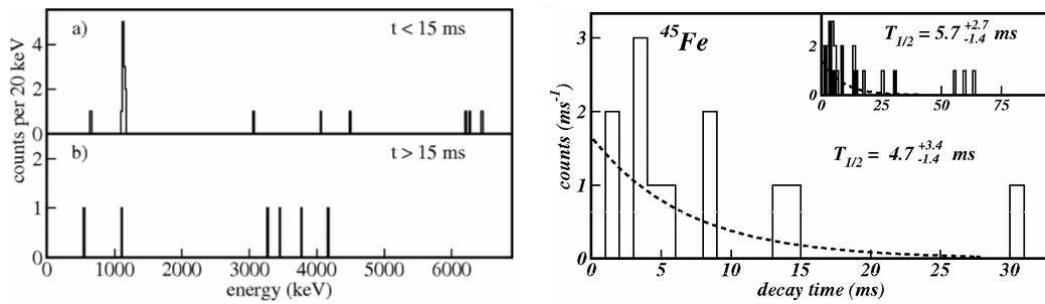


Figure 1.11: First results of $^{45}$Fe obtained in the GANIL experiment. Left: energy spectra for two different time-correlation windows between the implantation and the decays. The narrow peak at 1.14(4) MeV for short times indicates the 2p radioactivity. Right: distribution of the correlated decay events in time for half-life calculation. Taken from [Gio02].

This method has some limitations. One measures overall characteristics of the decay: the half-life, the released energy $Q_{2p}$ and the 2p branching ratio. However, the individual properties of the protons (energy and angles) are not known.

**Direct observations**

To observe the real dynamics of the 2p decay and compare with the three-body model emission distributions, a Time Projection Chamber (TPC) which tracks the decay is an ideal setup. The ions are implanted in a gas volume. The ionisation electrons along the charged-particle track are drifted into a segmented detection plane. One has a three-dimensional reconstruction of the proton trajectories. Two TPCs were developed to study 2p radioactivity (cf. figure 1.13): one at the Centre d'Etudes Nucléaires de Bordeaux Gradignan (CENBG) and another at the Institute of Experimental Physics of Warsaw.

The first TPC [Bla08b, Bla10] has a detection plane composed of XY strips giving the X and Y projections of the horizontal projection of the trajectories. The Z dimension is extracted from the timing information. The PhD theses of Audirac [Aud11] and of Ascher [Asc11a] explain in
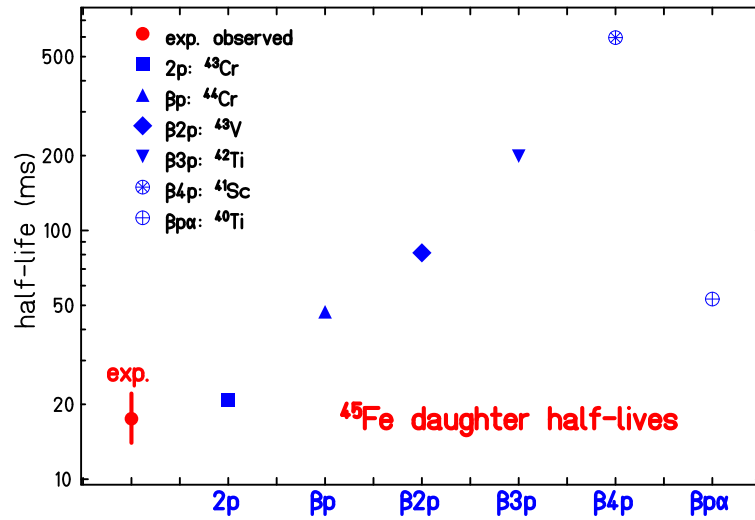
Figure 1.12: Experimental half-life of the daughter of $^{45}$Fe in the GANIL experiment [Gio02] compared to the theoretical half-lives of the possible decay processes. The experimental value is compatible with the $^{43}$Cr half-life. This shows the 2p decay of $^{45}$Fe.
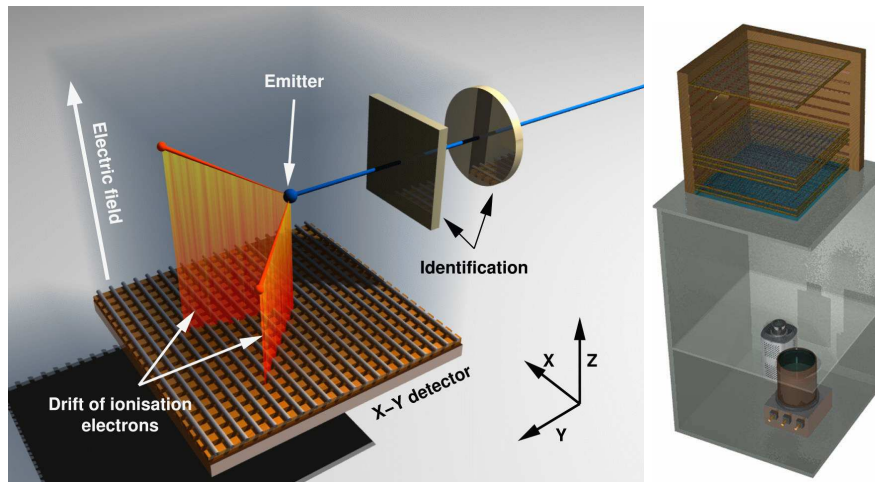


Figure 1.13: Schemes of the two TPC used for the 2p radioactivity study (CENBG TPC on the left and optical TPC from Warsaw on the right). The basic principle is the same for both. The charged particles ionise the gas producing electrons which are drifted by an electric field to a detection plane. The detection plane of the CENBG TPC [Bla08b] (left) is composed of X and Y strips to have a projection of the trajectories in the horizontal plane. The TPC from Warsaw [Mie07b] (right) has a scintillation material producing light from the ionisation electrons. A CCD camera takes pictures of the trajectory projections on the XY plane.

detail the reconstruction procedures of the 2p decay events.

The second TPC is optical [Mie07b]. The ionisation electrons produce light with a scintillation material and the trajectory projection on the plane defined by this material is recorded by a CCD camera. This TPC gives literally a picture of each event. A photo-multiplier is placed behind the scintillator to measure the collected charges. Its timing information provides the third dimension of the tracks and its charge information the decay energy measurement.

The observation with a TPC began in 2006 with the first three-dimensional (or direct) observation of the 2p radioactivity of $^{45}$Fe at GANIL [Gio07]. An experiment was also performed with the optical TPC at the NSCL [Mie07c, Mie09]. The first direct observation of the 2p radioactivity of $^{48}$Ni was done in 2011 [Pom11a] (only four 2p decays observed) and confirmed the indication of [Dos05]. The direct observation of $^{54}$Zn was performed in 2011 [Asc11b, Asc11a].
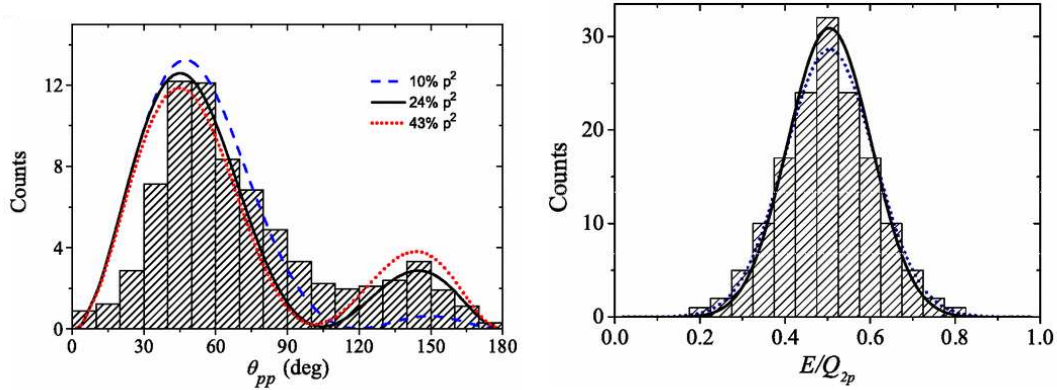


Figure 1.14: Results of $^{45}$Fe obtained with the optical TPC at NSCL. The angular distribution of the proton emission is compared with different shell mixing calculations of the three-body model: 10%, 24% and 43% of the proton wave function originating from the $p$ shell. The energy distribution between the two protons is also measured on the right. Taken from [Mie07c].

The angular and energy distributions of $^{45}$Fe are the best known ones. The results are given in figure 1.14. The energy sharing centred on 0.5 confirmed the original assumption of an equitable energy sharing between the protons to optimise the crossing of the Coulomb barrier. It is in agreement with the three-body model and the predictions of Goldansky. The angle between the two proton trajectories is calculated for different orbital configurations of the valence protons. For all the known medium-mass 2p emitters, the valence shells involved in the 2p radioactivity are $p$ and $f$ shells. The possible configurations are a pure $f^2$, a pure $p^2$ or a $pf$-shell mixing. The experimental angular distribution is compared to the theoretical one for different mixing configurations of three-body model calculations.

### 1.4.4   The study of heavier candidates

Until now, our knowledge about 2p radioactivity was limited to three medium-mass emitters with half-lives of the order of ms. There measured properties are summarised in table 1.5.

| Nucleus | $Q_{2p}$ (MeV) | Half-life (ms) | 2p BR (%) |
|---|---|---|---|
| $^{45}$Fe [Gio02, Pfü02, Dos05, Mie07a, Aud12] | 1.156(14) | $2.45^{+19}_{-17}$ | $67.8^{+34}_{-35}$ |
| $^{48}$Ni [Dos05, Pom11a] | 1.26(12) | $2.1^{+12}_{-5}$ | $52^{+17}_{-14}$ |
| $^{54}$Zn [Bla05, Asc11b] | 1.48(2) | $1.8^{+6}_{-3}$ | $90^{+5}_{-10}$ |

Table 1.5: Most recent $Q_{2p}$ values, half-lives and 2p branching ratios of the known medium-mass 2p emitters.

The increasing possibilities of high-intensity beam-line of the RIBF facility in Tokyo (RIKEN Nishina Center), presented in chapter 2, make possible to reach heavier 2p radioactivity candidates. The mass models presented in section 1.4.2 shows that the best candidates in heavier

mass domain are $^{59}$Ge, $^{63}$Se and $^{67}$Kr. Indeed their theoretical $S_p$ is positive and $S_{2p}$ is negative.

Because the $Q_{2p}$ is the energy needed to cross the Coulomb barrier seen by the two protons, it is supposed to grow proportionally to $(Z-2)$ as the barrier height. This tendency is visible in figure 1.15, gathering all the known experimental and theoretical values of the candidates and known emitters. One sees that the $Q_{2p}$ value of $^{67}$Kr correspond the best to the tendency if one extrapolates a line from the of the last known emitters ($^{45}$Fe, $^{48}$Ni and $^{54}$Zn).
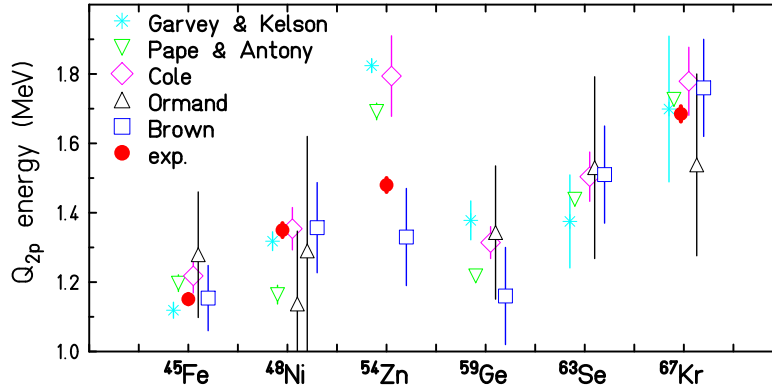


Figure 1.15: Comparison of the $Q_{2p}$ values between model calculations of [Jän88, Ant97, Orm96, Orm97, Col96, Col99, Bro91, Bro02] and the experimental average values of the known emitters (table 1.5). The last known emitter $^{67}$Kr is discussed in this PhD work.

An experiment at RIBF confirmed this tendency with the discovery of the 2p radioactivity of $^{67}$Kr in 2015. The details of this experiment are reported in chapter 2. The method used to analyse the data is described in chapter 3 and the results of this analysis are given in chapter 4. This represents an indirect observation with only a silicon detector (DSSSD) but a measurement using a TPC is foreseen in the coming years. Indeed, the ACTAR TPC device, as described in chapter 5, will be used to firmly establish the 2p radioactivity in $^{67}$Kr.

# Chapter 2

# The RIBF4R1 experiment

A new 2p investigation in the mass A $\sim$ 70 region ($^{59}$Ge, $^{63}$Se and $^{67}$Kr) was conducted in May 2015 at the BigRIPS fragment separator, located at RIBF (Radioactive Isotope Beam Factory) of the RIKEN Nishina Center. The RIBF4R1 experiment was possible thanks to the development of a new beam of $^{78}$Kr at the facility.

After a selection in mass and charge by the BigRIPS magnetic separator and the ZeroDegree Spectrometer (ZDS), nuclei produced by fragmentation of the $^{78}$Kr primary beam were implanted in the decay study setup WAS3ABi composed of three contiguous DSSSDs (Double-Sided Silicon Strip Detector). A set of germanium detectors (EURICA) covered a large solid angle around the DSSSDs and enabled the detection of $\gamma$ rays in coincidence with protons and $\beta$ particles emitted during the decay of radioactive fragments.

The RIBF facility, the production of the beam and the detectors of the beam line are presented in this section. The EURICA-WAS3ABi decay setup and the run conditions of the experiment are also discussed.

## 2.1 Overview of the RIBF facility

Created in 1986, the RIBF facility was composed at this time of the RRC (RIKEN Ring Cyclotron) and two injectors (cf. figure 2.1): the variable frequency linear accelerator RILAC (RIKEN heavy Ion LINear ACcelerator) and the AVF (Azimuthally Varying Field) cyclotron. After this latter, the beam was injected in the fragment separator RIPS (RIKEN Projectile Fragment Separator). The facility produced beams of nuclei from hydrogen to bismuth with an energy up to 135 MeV/u at the exit of RRC.
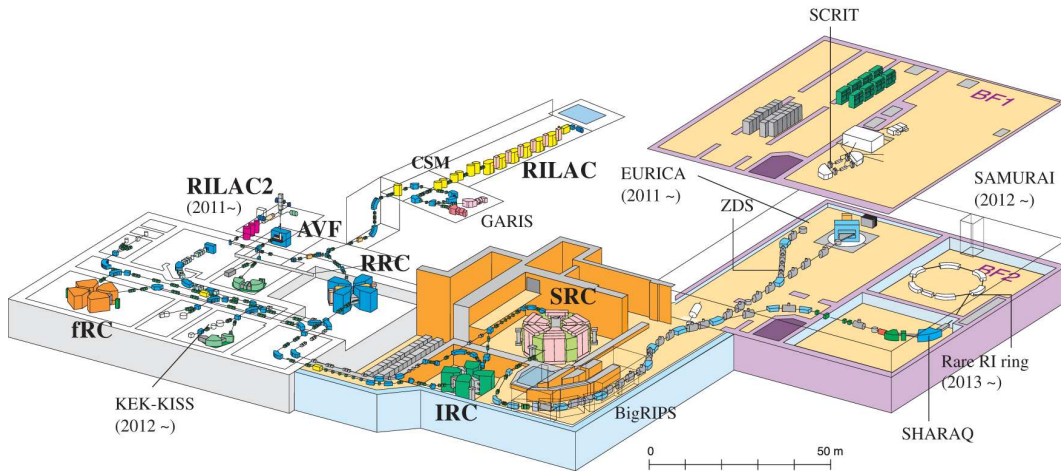


Figure 2.1: Overview of the Radioactive Isotope Beam Factory (RIBF) with its five cyclotrons, its two linear accelerators, its separator-spectrometer set BigRIPS-ZDS and its various experimental areas. Taken from [Oku12].

Facility capabilities increased with the addition of three new cyclotrons: the fRC (Fixed-

frequency Ring Cyclotron), IRC (Intermediate Range Cyclotron) and the SRC (Superconducting Ring Cyclotron). Coupled to the former injectors, they provide higher energy beams, up to 350 MeV/u, from hydrogen/deuterium to $^{238}$U. Since 2007, a new facility is operational with the new fragment separator BigRIPS [Kub12]. It makes possible the production and separation of secondary beams produced by fragmentation reaction or in-flight fission. Since 2008, the ZDS (ZeroDegree Spectrometer) [Kub12], composed of similar magnets and detectors as the BigRIPS beam-line, is operational.

A new injector called RILAC2 is available since 2011. It is coupled with the new SC-ECRIS source of 28 GHz to increase the variety of beam types, including $^{78}$Kr since 2015. With a fragmentation reaction on a beryllium target, this new beam enabled the production of new nuclei beyond the proton drip-line such as $^{67}$Kr, $^{63}$Se and $^{59}$Ge.

### 2.1.1   Primary $^{78}$Kr beam production

RIBF provides a large variety of primary beams ranging from proton to $^{238}$U depending on the used injectors (RILAC, RILAC2 or AVF) and the ion sources coupling to these injectors. Then different combinations of cyclotrons and strippers accelerate the beam (the different settings are illustrated in figure 2.2). Each possibility of injector-cyclotrons-strippers set is called a mode. Three are available at RIBF. The AVF injection mode required the AVF cyclotron and produces light beams up to oxygen at 250 MeV/u. The variable-energy mode uses a SC-ECRIS source (SuperConducting Electron Cyclotron Resonance Ion Source) coupled to the historical linear accelerator RILAC to produce beams up to $^{86}$Kr at 345 MeV/u maximum.

We focus on the fixed-energy mode (in orange in figure 2.2) producing the $^{78}$Kr beam, used during our experiment. This latter uses the new injector RILAC2. The upcoming ions from the SC-ECRIS source and RILAC2 are accelerated by the RRC. Then there is an electron stripping on the first stripper before being accelerated again by the fRC. A second stripping is performed after the fRC. At the last cyclotron exit, the SRC, a continuous beam of fully stripped $^{78}$Kr$^{36+}$ is delivered with an energy of 345 MeV/u and a maximum intensity of 350 pnA.

This beam could not be delivered by the RILAC injector because of the short lifetime of the stripper located behind RILAC, a few hours when the intensity reaches 100 pnA, even for nuclei lighter than zinc. The stripper after the RRC (ST3) is not necessary because of the last upgrade of the fRC. The fixed-energy mode has also the advantage of using the new high-intensity source (SC-ECRIS) of 28 GHz.
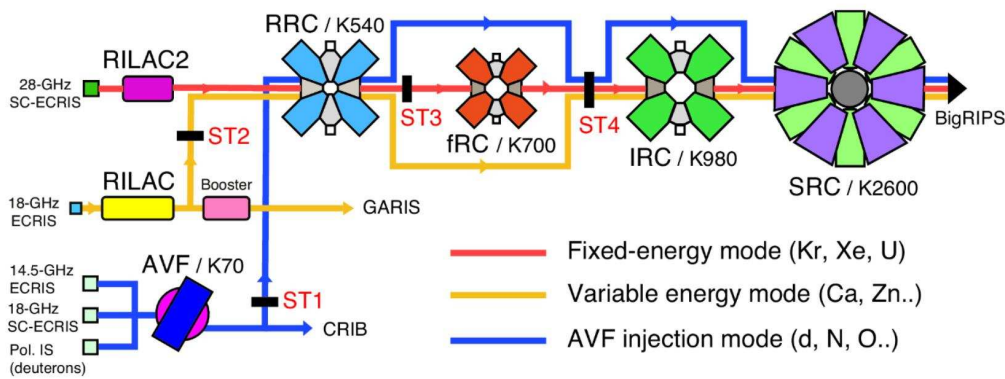


Figure 2.2: Different primary beam settings with the three injectors used at RIBF: AVF, RILAC and RILAC2. The orange line corresponds to the fixed-energy mode ($^{78}$Kr, Xe, U beams), the yellow one to the variable energy mode (Ca, Zn beams) and the blue one to the AVF injection mode (d, N, O beams). The available strippers are ST1, ST2, ST3 and ST4. Taken from [Kam16].

After its production, the $^{78}$Kr$^{36+}$ primary beam is sent on a 5-mm thick beryllium target. Fragmentation reaction products are then selected and identified by the BigRIPS separator.

### 2.1.2 Separation and identification

The experimental setup is located at the focal point F11 of the ZDS spectrometer (overview in figure 2.3).
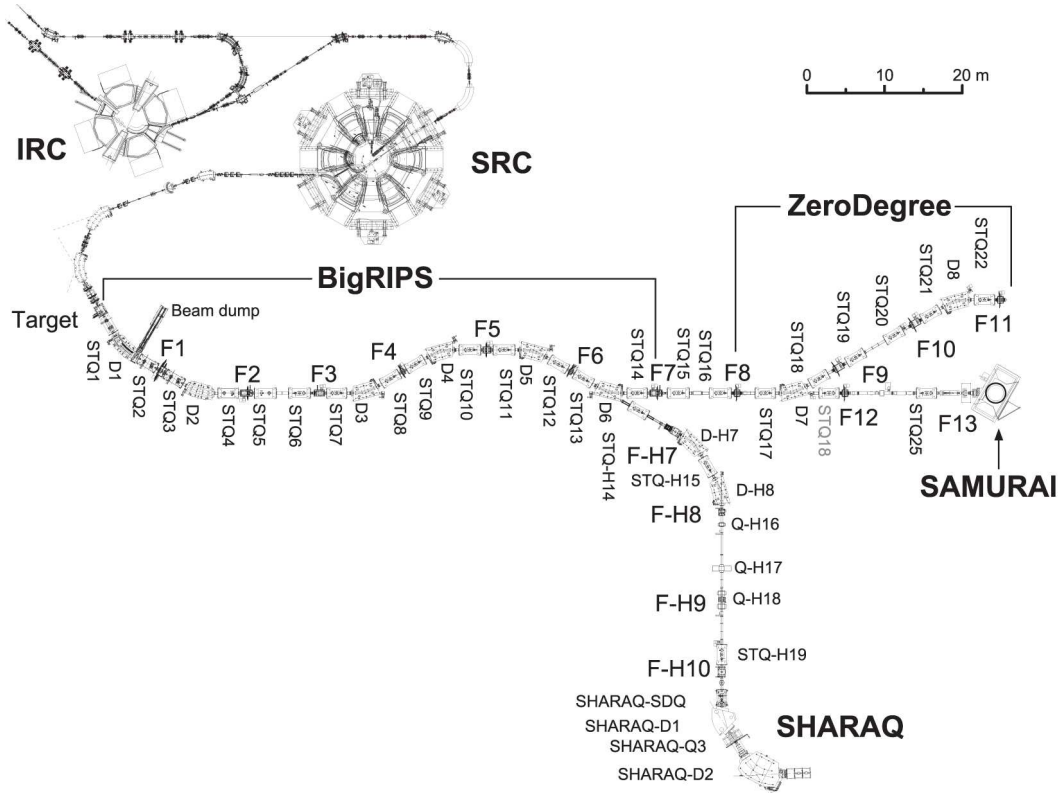


Figure 2.3: Beam line after the last cyclotron (SRC). The BigRIPS-ZDS couple performs a selection and identification of nuclei for various experiences situated in F10, F11 and F13. Taken from [Kub12].

With a total length of 77 m, BigRIPS is organised in two sections. The first section located between the target (F0) and F2 is a two-bend achromatic spectrometer composed of four superconducting quadrupole triplets (STQ), and two room-temperature dipoles (RTD) with a bending angle of 30 degrees. The focal point F1 is a momentum dispersive: the D1 dipole deviates trajectories proportionally to their momentum. F2 is achromatic focusing the beam horizontally and vertically with two quadrupoles, but spreading the momentum distribution. The second section located between F3 and F7 is composed of eight STQ and four RTD making a four-bend achromatic spectrometer. The focal point F3 is achromatic but F4, F5 and F6 are momentum dispersive and F7 is doubly achromatic. The BigRIPS angular acceptance is 80 mrad horizontally and 100 mrad vertically. Aluminium degraders are located in F1, F4, F5 and F6.

The ZeroDegree spectrometer (ZDS), situated after the BigRIPS separator, is 36 m long (from F8 to F11) and composed of two dipoles with the associated STQ. Its magnets have the same properties as those of BigRIPS. The ZDS can be configured in achromatic or dispersive mode with medium and high resolution settings for each. The dispersive mode has a better momentum resolution and a higher magnetic rigidity value for a better separation of the nuclei. The achromatic mode has a higher angular acceptance but a poorer resolution. The ZDS can be used to identify the ions similarly to the BigRIPS separator, or to study decays with a secondary target and a $\gamma$-ray detector (NaI or Ge) at F8. In achromatic mode, it enables the measurement of the total kinetic energy of the beam with a NaI or CsI detector at F11. More details about BigRIPS and the ZDS can be found in [Kub12].

The corresponding beam line used for our experiment, includes the elements between the F0 and F11 focal points with a series of eight dipoles. The quadrupole triplet (STQ) following the exit of each dipole is dedicated to re-focalise the beam. The BigRIPS separator functions in two

steps: the ion separation between F0 and F3 followed by the identification between F3 and F7.

### Separation

A first selection is performed after the target by a magnetic dipole. The ion trajectories are bent under a constant vertical magnetic field $\overrightarrow{B}$ because of the Lorentz magnetic force $q\overrightarrow{v} \times \overrightarrow{B}$. Their deviation through the dipole is quantified by their magnetic rigidity, which is defined as:

$$B\rho = \frac{\|\overrightarrow{p}\|}{Q} = \frac{\beta\gamma u}{c}\frac{A}{Q} \tag{2.1}$$

where

- $\overrightarrow{p}$ is the momentum of the ion,

- $c$ the velocity of light in free space,

- $A$ the ion mass number

- $Q$ the ion charge,

- $u$ the atomic mass unit,

- $\gamma = \frac{1}{\sqrt{1-\beta^2}}$ and $\beta = \frac{v}{c}$ with $v$ the velocity of the ion.

The tuning of the magnetic dipole and its curvature gives a reference value for the magnetic rigidity $B\rho_0$, and thus a reference $A/Q$ ratio for ion selection. The maximum bending of the dipoles is 9 Tm. It was around 3-5 Tm during the experiment. The nuclei having too low or too high $A/Q$ deviation from the reference are lost between the two successive focal points. One notices that the dipole selection is $A/Q$-depended (or $A/Z$) according to the equation 2.1. A lot of different isotopes are also selected by the dipole.

A second selection, only $Z$-dependent, is performed to select the nuclei in a narrower area near the ions of interest. An achromatic wedge-shaped degrader is put in F1 to perform this selection. This 2-mm thick target of aluminium slows down the ions and thus performs a selection with their energy loss (i.e. $Z$), according to the Bethe-Bloch formula [Bet30]. The slowing down of charged particles in matter at intermediate energies $0.1 < \beta\gamma < 1000$ is expressed as [Pat16]:

$$-\frac{dE}{dx} = \frac{4\pi e^4 N}{m_e v^2}Z^2 \left[ \ln\left(\frac{2m_e v^2}{I}\right) - \ln(1 - \beta^2) - \beta^2 \right] \tag{2.2}$$

where

- $N$ is atomic density of the stopper,

- $e$ the electron charge,

- $m_e$ the electron mass,

- $Z$ the atomic number of the ion,

- $I$ the mean ionisation potential.

A second dipole performs a $B\rho$ compensation after F1 in order to have a dispersion close to zero between F1 and F3 (same trajectory position at F1 and F3). A quadrupole pair is located at F3 to refocus the beam before the identification stage.

**Identification**

The ions are identified between the F3 and F7 focal points by the $\Delta E$-$B\rho$-$ToF$ method [Fuk13]. It gives an identification matrix in $Z$ and $A/Q$. A similar degrader as the F1 one is located in F5 in order to improve the BigRIPS selectivity.

Many detectors are arranged along the beam line between F3 and F7 for the identification (they are more precisely detailed in section 2.2):

- plastic scintillators: time of flight (ToF) measurement,

- a MUlti-Sampling Ionisation Chamber (MUSIC): energy loss measurement,

- Parallel Plate Avalanche Counters (PPAC): ion trajectories measurement.
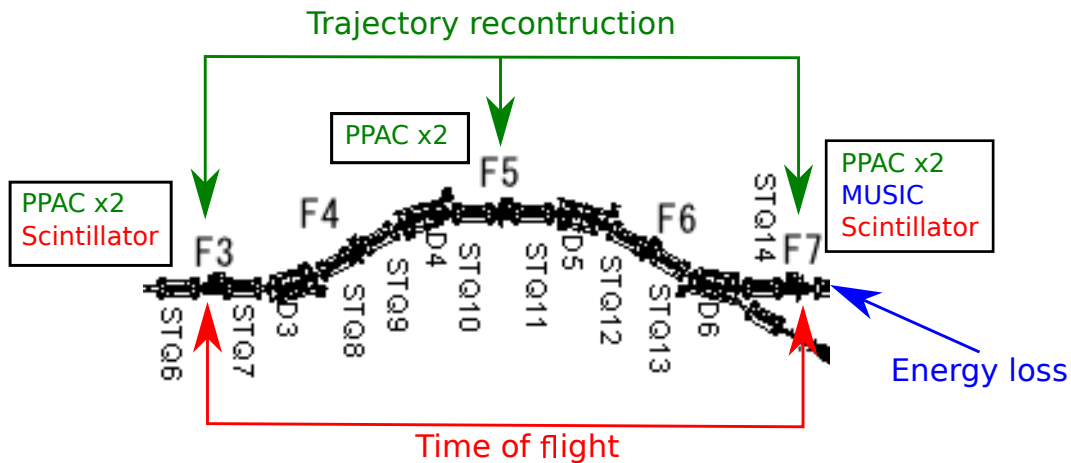


Figure 2.4: Identification method between F3 and F7 on the BigRIPS separator. The PPAC detectors located at F3, F5 and F7 perform the trajectories reconstruction for the $B\rho$ calculation over the F3-F5 and F5-F7 paths. The plastic scintillators at F3 and F7 measure the time of flight and thus the velocities of the ions. The MUSIC at F7 measures the energy loss to obtain $Z$ with the velocity at the chamber entrance.

The particle identification procedure is illustrated in figure 2.4. Two magnetic rigidity measurements are performed between F3, F5 and F5, F7. PPAC pairs located at F3, F5 and F7 give the ion trajectories at these focal points. These detectors allow to reconstruct trajectories inside the dipoles and compute the magnetic rigidity $B\rho$ on F3-F5 and F5-F7 separately. The $A/Q$ ratio comes straightforward out of the F3-F7 time of flight measurement (i.e. velocity). $Z$ is given by the energy loss inside the F7 MUSIC, proportional to $Z^2$ (cf. Bethe-Bloch equation 2.2), and the velocity at the entrance of the chamber (calculated from the time of flight). Details of the reconstruction procedure are given in section 3.1 in the next chapter dedicated to the analysis procedures.

The ZDS can also perform an identification as BigRIPS with a similar procedure, or a complementary analysis of the beam. In the presented experiment, these functions were not used. The task of the ZDS was only to deliver the beam to the experimental setup at F11. For this purpose the ion optics is tuned for an optimisation of the transmission efficiency between F7 and F11.

## 2.2 Beam-line detectors

The detectors located at the different focal points of BigRIPS (and ZDS) allow to measure the $A/Q$ and $Z$ of the fragments for their identification. Three types are situated along the beam line: plastic scintillators, ionisation chambers (MUSIC) and PPAC detectors.

## 2.2.1   Plastic scintillator

The plastic scintillator (see picture in figure 2.5) is composed of a plastic material EJ-212 based on polyvinyltoluene polymer. This latter is connected to two photo-multiplier tubes (PMT) on each side (left and right). They measure the time and charge collected on both sides with respectively two TDC (Time-to-Digital Converter) and QDC (Charge-to-Digital Converter) coders.

Each scintillator gives left and right timing signals. By averaging these two times we obtain the time of the event. Two plastic scintillators are used in this analysis procedure to estimate the time of flight: those in F3 and F7 to measure the time of flight between these two focal points (46.976 m length).
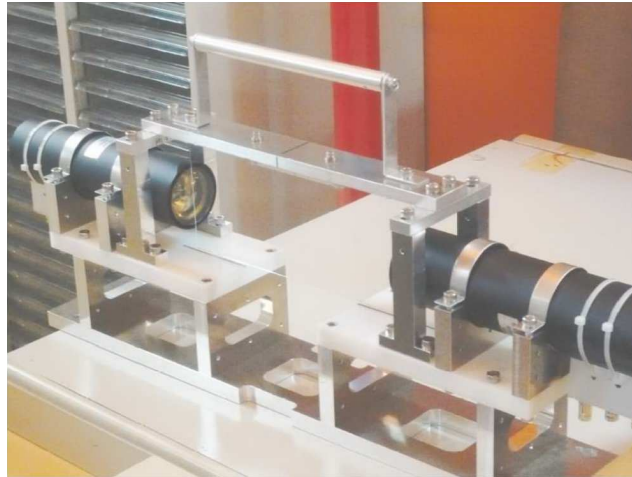


Figure 2.5: Photograph of a plastic detector of the BigRIPS beam-line. The plastic material (center) is used with two photo-multiplier tubes (PMT), one on its left and another on its right. Taken from [Rik17].

## 2.2.2   MUSIC

The Multi-Sampling Ionisation Chamber (MUSIC) [Kim05] is a gaseous detector with a 480-mm long active volume filled of Ar-CH$_4$ (90%-10%) at a pressure of 740 Torr. The entrance and exit of the chamber are each made of a kapton foil. The inside is composed of twelve anodes and thirteen cathodes disposed alternatively (cf. figure 2.6). Each electrode is made of two aluminised mylar foils. They are tilted with an angle of 30 degrees with respect to vertical. This detector is referred as a tilted electrode gas ionization chamber (TEGIC). The tilting avoids recombinations between ionisation electrons and positive ions by drifting them away in opposite directions. Each electrode is 20 mm distant from the previous one. Anodes are connected by pairs via ADC coders (Analog-to-Digital Converter), thus six energy signals are read on MUSIC outputs.

Energy loss of ions crossing the MUSIC is computed by averaging the signals of the six anode pairs:

$$\Delta E = \sqrt[6]{\prod_{i=1}^{6} \Delta E_i} \tag{2.3}$$

with $\Delta E_i$ the energy loss signal of the $i^{th}$ pair.

The MUSIC located at F7 is used for the identification procedure performed between F3 and F7.

## 2.2.3   PPAC

A Parallel Plate Avalanche Counter (PPAC) [Kum01, Kum13] is composed of an anode plate between two cathodes distant by 4 mm. Each cathode is a set of fourty 2.4-mm-width strips
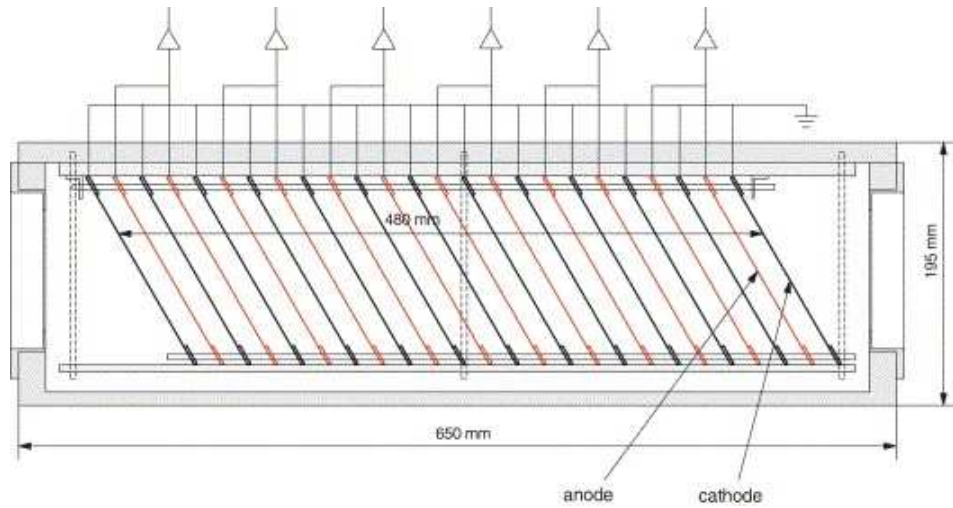
Figure 2.6: Transversal scheme of MUSIC (Multi-Sampling Ionisation Chamber) as used on the BigRIPS line. The anodes (in orange) are connected two-by-two to ADCs. Each ADC provides the collected charge (and the energy loss) between the two subsequent anodes. The cathodes (in black) are connected to the ground. Taken from [Kim05].

separated by a 150-$\mu$m interstice. Vertical strips give a measurement of the X position and horizontal strips give the Y position. These electrodes are made of aluminium or gold evaporated on mylar. A PPAC has an active area of $240 \times 150$ mm$^2$. The volume is filled with gaseous perfluoropropane ($C_3F_8$) at a pressure of 30 Torr. The entrance and exit windows are made with aluminised mylar foils. A high voltage of 2000 Volts is applied on each anode. A PPAC works as a multi-wire proportional counter even if it is not composed of wires. As one can see
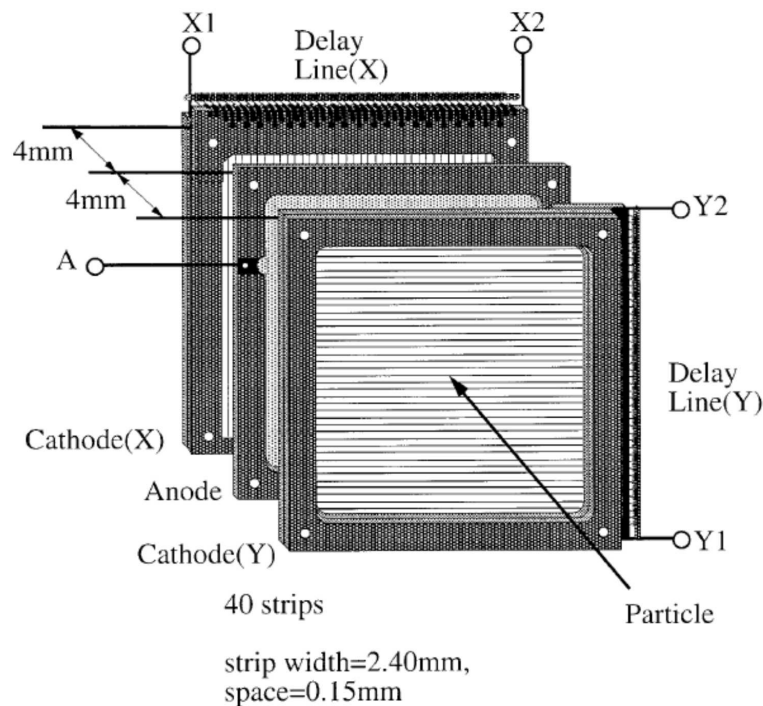


Figure 2.7: PPAC (Parallel Plate Avalanche Counter) scheme view. Taken from [Kum01].

in figure 2.7, the strips are connected to delay lines. Each side of the line is processed by a CFD (Constant Fraction Discriminator) and coded by a TDC.

As illustrated in figure 2.8, when a charged particle crosses a cathode plate composed of vertical strips (X), an electron avalanche occurs in the nearest wires. These wires are connected to LC circuits which are themselves connected in series: the delay line. The maximum signal
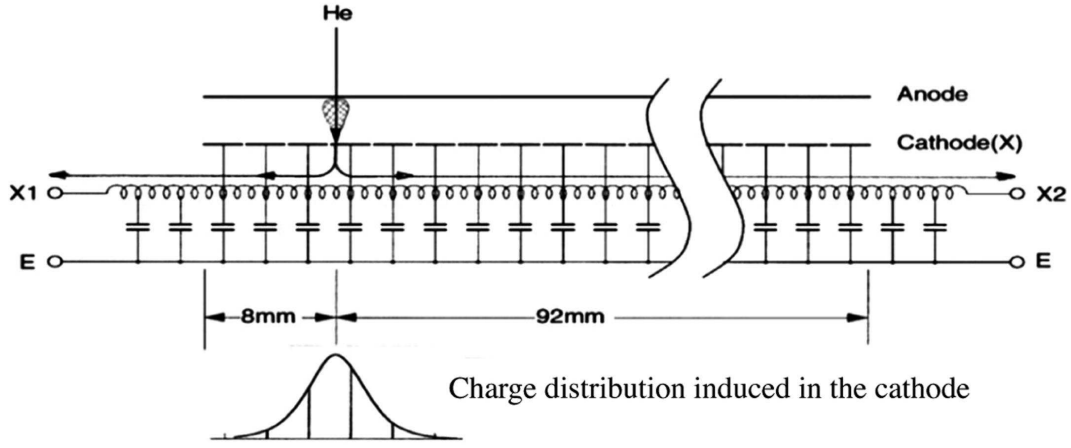
Figure 2.8: Equivalent circuit of the delay line of a PPAC (vertical X strips) and the distribution of the deposited charge on the cathodes by an $\alpha$ particle. The connection of LC circuits in series splits the signal induced in the cathode. One measures an output on each end of the line ($X_1$ and $X_2$). Taken from [Kum13].

splits in two components which travel in the two directions ($X_1$ and $X_2$ here). Each LC circuit delays the signal of 2 ns. The time of arrival of the signal at one side of the plate is proportional to the distance from the hit strip (the one with the maximum charge collected). The reference of the axis is located at the centre strip of the plate. The time of the nearest end is proportional to $\frac{L}{2} - x$ with $L$ the length of the delay line. The time of the other side is proportional to $\frac{L}{2} + x$. To obtain $x$, we have to compute the time difference divided by two. The convention $T_1 - T_2$ is used for all the PPAC of the beam line. The X and Y positions are thus given by

$$
\begin{aligned}
X &= k_X \frac{T_{X_1} - T_{X_2}}{2} + X_{\text{offset}} \\
Y &= k_Y \frac{T_{Y_1} - T_{Y_2}}{2} + Y_{\text{offset}}
\end{aligned}
\tag{2.4}
$$

where $T_{X_i}$ and $T_{Y_i}$ are respectively the first and second cathode times of a PPAC plate. $k_X$ and $k_Y$ are calibration factors, they were calculated by the BigRIPS team before the experiment and are approximately equal to 1.25 mm/ns.

Three pairs of PPACs are positioned at F3, F5 and F7. From the X and Y positions of the two PPACs of a focal plane, one can also compute the horizontal and vertical angles of the ion trajectory between the detectors. They allow the trajectory reconstruction in the dipole pairs D3-D4 and D5-D6.

## 2.3   Decay setup

The results presented in this thesis come from the analysis of data taken during the $^{78}$Kr campaign. The setup EURICA-WAS3ABi was used (situated at F11) to full-fill the different goals of the campaign. It allows to study decays by emission of charged particles (protons and $\beta$ particles). With the three silicon detectors of WAS3ABi (Wide range Active Silicon-Strip Stopper Array for Beta and Ion detection), a large variety of isotopes is implanted and studied. The germanium detectors of EURICA enable spectroscopic studies with the detection of $\gamma$ rays. The full setup is shown in figure 2.9.

### 2.3.1   WAS3ABi

The nuclei selected by BigRIPS and the ZeroDegree spectrometer are implanted in WAS3ABi [Nis13]. It is constituted of multiple DSSSDs (Canberra PF-60CT-40CD-40*60) aligned along the beam axis. The setup can hold up to eight DSSSDs, but in our experiment WAS3ABi was composed of three silicon detectors. The picture in figure 2.10 shows the full device.

Each DSSSD is a 1-mm thick segmented silicon detector composed of 60 vertical strips on one side for X position, and 40 horizontal strips for Y position on the other side of the detector.
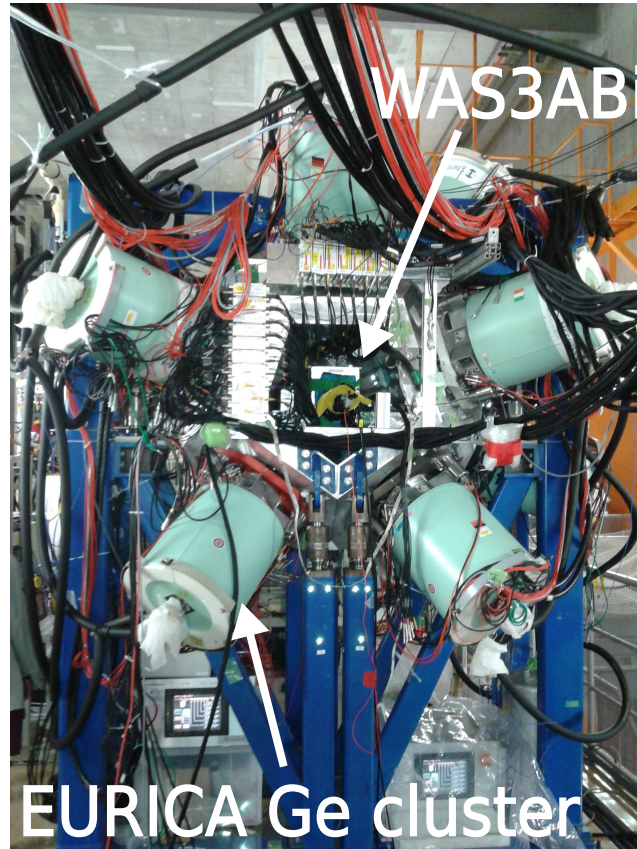
Figure 2.9:  Photograph of the whole decay setup:  the DSSSDs of WAS3ABi in the center surrounded by the EURICA $\gamma$-ray array.
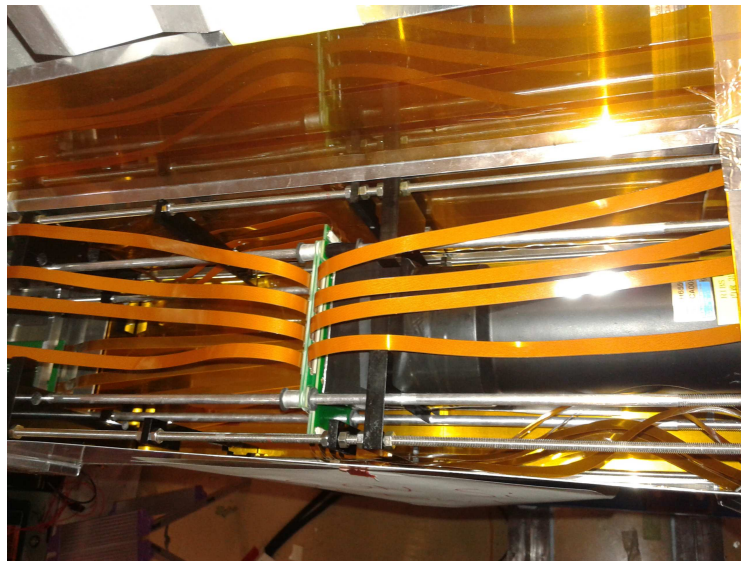


Figure 2.10:  Photograph of the WAS3ABi setup.  One sees at the center the three aligned DSSSDs and on the right the photo-multiplier tube of the veto plastic scintillator.

A high voltage of 250 Volts is applied to bias the detectors. Each strip is 1 mm wide thus the detector is divided in 7200 pixel of 1 mm$^2$ to correlate the implantation events (ions) with decays. WAS3ABi is inside an aluminium chamber of 0.2 mm thickness maintained at a temperature of 10 degrees Celsius by a N$_2$ gas cooling system. A scintillator (Bicron BC-400) of $60 \times 40$ mm$^2$ wide and 50 mm thick is placed 3 mm downstream the last DSSSD. This scintillator is used as veto for the implantations and also charged particles escaping from the last DSSSD.
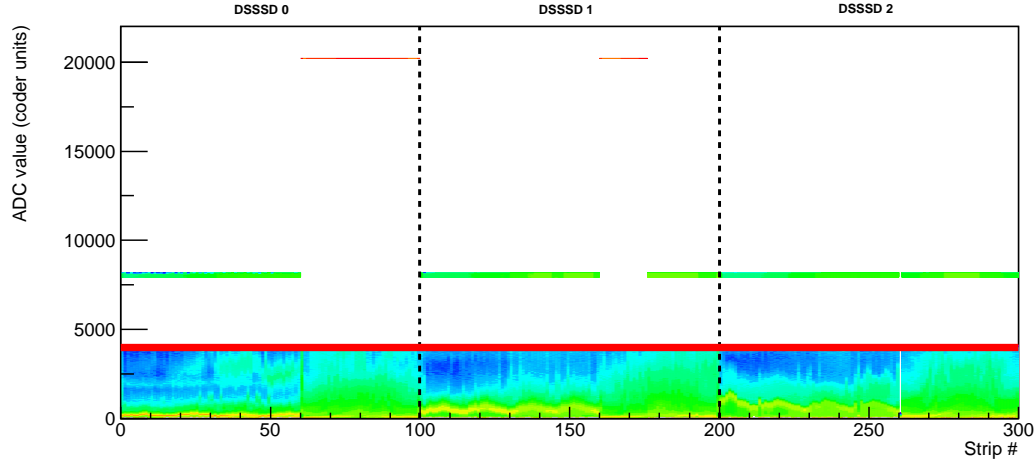


Figure 2.11: All ADC raw values (not aligned to pedestals) registered during runs of the RIBF4R1 experiment. The strips are numbered from 0 to 299, covering the three DSSSDs. The first 60 strips correspond to the X side of the DSSSD, the last 40 to the Y side. One can see the coders overflowing at 8000 and the others at 20000 in data files. The saturation threshold used in the WAS3ABi analysis is set to 4000 (horizontal red line).

For each strip, the charge signal is treated by a charge-sensitive preamplifier and a shaping amplifier, giving a high efficiency, even below 100 keV. The inverted signal of the shaping amplifier is sent into a leading-edge discriminator for trigger and timing information. The energy signal coding is performed by peak-sensing ADCs from two types: Mesytec MADC-32 and Caen V785. These 12-bit ADCs return values from 0 to 4095. The value written in the data file when an overflow occurs is different depending on the module. The value for the Mesytec MADC-32 is 20000 and 8000 for the Caen V785. The limit to separate implantation from decay events is set at 4000 in the analysis procedure (cf. figure 2.11). The same behaviour is observed on the ADC of the veto scintillator with a saturation value at 8000. This detector also saturates with ion slowing down.

Moreover this setup is tuned for low-energy signals with a range up to 8-10 MeV. With an average deposit energy of 1 GeV, the ion implantation saturates ADCs of strips near the implantation one. At least 3-4 contiguous strips are hit and return an overflow value. Consequently it is impossible to know which strip was hit first with the ADC information. It is nevertheless possible to determine the strip of implantation by using the timing information. The TDC signals of the hit strips are compared and the fastest one gives the first hit strip and thus the implantation one [Nis13] (cf. section 3.2.1 for details).

### 2.3.2   EURICA

EURICA (EUROBALL-RIKEN Cluster Array) [Söd13] allows to study the $\beta$ decay of exotic nuclei and perform high-resolution $\gamma$-ray spectroscopy. Mounted at RIBF in the end of 2011, the device was removed in September 2016.

Twelve EUROBALL IV detectors constitute EURICA. They were used in the past for the RISING campaign at GSI [Pie07]. Each detector is composed of seven hexagonal crystals of high-purity Germanium (HPGe) with an average energy resolution of 1.99(8) keV at 1332.5 keV [Söd13]. Six crystals are placed in a ring surrounding a central crystal (see figure 2.12). Distant on average of 22 cm from the center, the detectors are arranged in three rings at three different

angles relative to the beam axis: five at 51 and 90 degrees, two others at 129 degrees. Three empty positions are available for ancillary detectors (NaI or LaBr$_3$). These positions were not used during the campaign. Additionally, 9 crystals out of 84 were damaged and not used for the calibration and analysis.

To read the signals, each crystal has two outputs from the preamplifier: one for energy and the other for timing. The energy is read by digital $\gamma$-finder modules (DGF). These latter are tuned to register events over a 100-$\mu$s gate. The timing circuit is situated after the second preamplifier output. This analogue chain is composed of a timing filter amplifier (TFA), followed by a constant fraction discriminator (CFD) and a time-to-digital converter (TDC).
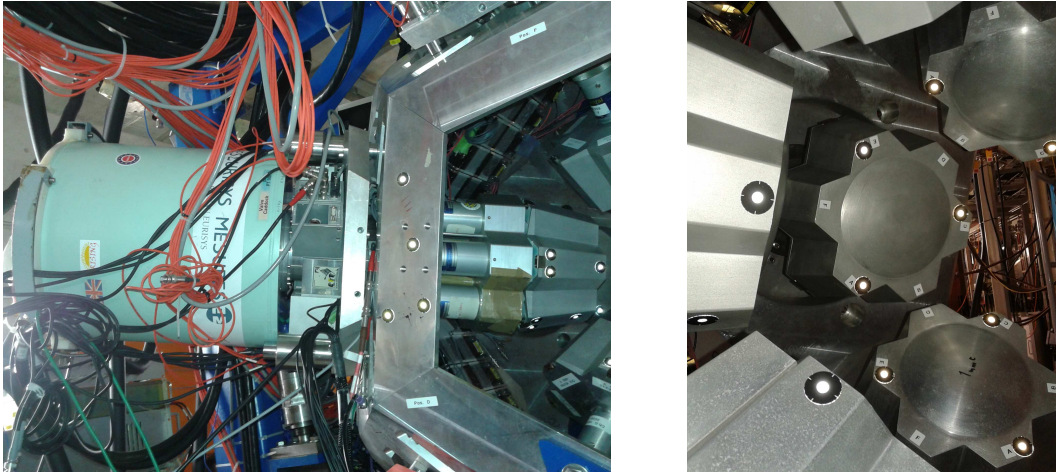


Figure 2.12: Photograph of the EURICA array. A cluster detector with its cryostat is shown on the left. On the right one can see the arrangement of the detectors on the holding structure.

A lot of interactions in the germanium crystals are Compton scattering instead of photo-electric effect. An add-back algorithm is implemented in the software to process EURICA data. It allows to recover the total energy of events from Compton scattering in contiguous clusters. When a signal is seen in three or more neighbouring crystals in a 400-ns time window, the energies are added and treated as one single event. Otherwise each energy is considered as a different $\gamma$ event. Using a $^{60}$Co source, the peak-to-total ratio is 16.3% for the 1173-keV and 1333-keV peak. The add-back algorithm increases this value to 25.8% and therefore improves thes detection efficiency. However, the add-back algorithm degrades a little the total energy resolution (3.17 keV against 2.89 keV at 1333 keV) [Söd13].

## 2.4 Data acquisition system

Each part of the experiment uses a different data acquisition system (DAQ). The BigRIPS, EURICA and WAS3ABi setups have own DAQ with data coming from their respective detectors. As an example, to identify a nucleus which triggered all the BigRIPS detectors (MUSIC, scintillator and PPAC) of the line, the data of the detectors for this nucleus have to be tagged as a single event on BigRIPS. WAS3ABi and EURICA have also an absolute tag for each event. Moreover the events of the different setups have to be correlated to analyse the data.

Each event is tagged with an absolute timing information named time-stamp. Each DAQ is connected to a Logic Unit for Programmable Operation (LUPO) developed by RIBF [Bab10, Bab15]. Two types of LUPO are used at RIBF depending on the electronics standard of the DAQ. This system uses a Field Programmable Gate Array [1] (FPGA) commercialised by XILINX, a Spartan 3E 500.

FPGA are mounted on the two types of modules used for the RIBF DAQs: CAMAC and VME modules (cf. figure 2.13). VME (Versa Module Eurocard) is a bus system with interrupt

---

[1]A FPGA can be reprogrammed to achieve the desired application. It is different from an Application Specific Integrated Circuit (ASIC) which is a custom device manufactured for a specific tasks and without the great versatility of a FPGA.

management and multiprocessor capability. A VME bus is a computer bus standardized by the IEC as ANSI/IEEE 1014-1987. It was first developed in 1981 and is largely utilised in the world of experimental nuclear physics but also in industry.

CAMAC stands for Computer Aided Measurement And Control. CAMAC was introduced in 1971 with the standards EUR4100 and EUR4600. The CAMAC modules are dedicated to computer based experiment control and data acquisition. The main fields of CAMAC are nuclear and high energy physics experiments. These two types of module can use the NIM (Nuclear Instrument Module) standard of logic input/output. Developed in 1964 it defines mechanical and electrical specifications for electronics modules used in experimental particle and nuclear physics. The CAMAC standard was then designed to overcome the limitations of NIM in the processing of large amounts of digital data.
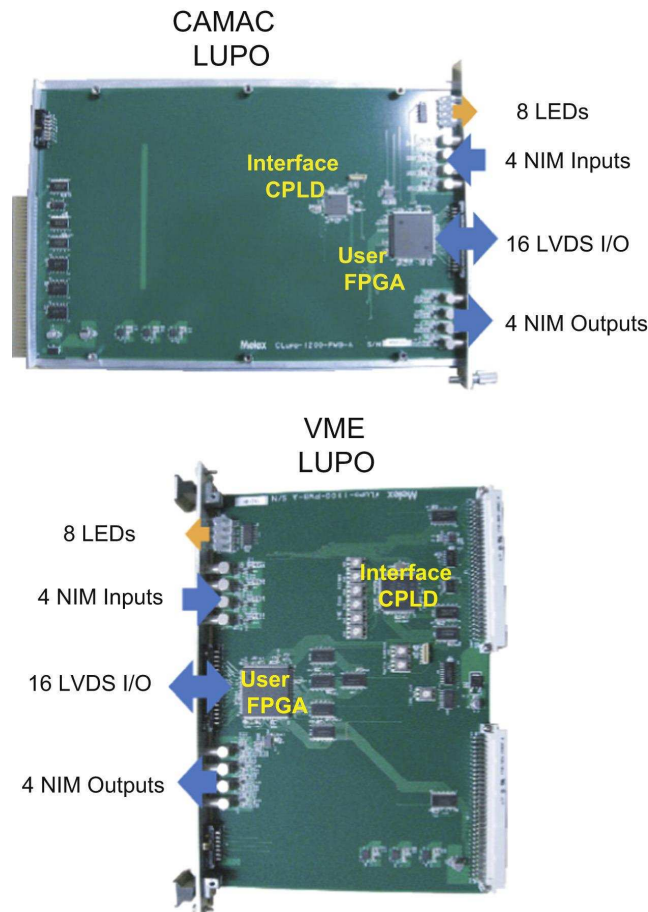


Figure 2.13: Photographs of the two LUPO system varieties: CAMAC and VME modules. A FPGA is integrated on each module, communicating with the interface bus via a CPLD interface. The modules are connected to the detector circuits by NIM and LVDS ports. Taken from [Bab15].

The two available LUPO module types shown in figure 2.13 are interfacing by a CPLD (Complex Programmable Logic Device) interface. Two kinds of input/output are used: the NIM (Nuclear Instrumentation Module) and LVDS (Low Voltage Differential Signaling) standards, a transmission norm for high-frequency electric signal (several hundreds of MHz). The FPGA provides a intern clock at 100 MHz coded on 48 bits (one month of coding). This clock gives the event time-stamp when a trigger is received from the acquisition.

Each detection system (BigRIPS, EURICA and WAS3ABi) has its own master trigger to register an event. The BigRIPS DAQ covers all beam-line detectors with a master trigger taken from the plastic scintillator at F7. The WAS3ABi DAQ is triggered by a logic *OR* between the F11 plastic scintillator and the sum of front and back signals of the three silicon detectors. The EURICA DAQ uses the same trigger as WAS3ABi.

Although two DAQs can have the same trigger (EURICA and WAS3ABi for example), the

time-stamps can be delayed because all the cables of the acquisitions do not have the same length. The DAQ merging is done "by hand", by analysing the average difference between two DAQ time-stamps. The procedure used in the experiment analysis is described in section 3.3.

## 2.5 Settings of the experiment

During the experiment, five settings were used (summarised on table 2.1). The first setting, optimised for the production of $^{51}$Ni, was used for calibration purposes. The exotic setting tuned on $^{65}$Br was dedicated to produce and implant the $2p$ candidates $^{67}$Kr, $^{63}$Se and $^{59}$Ge. Two other settings, respectively optimised for $^{64}$Se and $^{66}$Se production, were dedicated to study less exotic nuclei by $\gamma$ spectroscopy. The last setting, and the most exotic was tuned on $^{62}$Se to search for the isotopes $^{58}$Ge and $^{62}$Se.

| Setting | Effective data taking (h) |
|---|---|
| A ($^{51}$Ni) | 10.5 |
| B ($^{65}$Br) | 156 |
| C ($^{64}$Se) | 52 |
| D ($^{66}$Se) | 13 |
| E ($^{62}$Se) | 48 |

Table 2.1: The settings used during the experiment and their duration of data taking. They are optimised respectively for the production of $^{51}$Ni, $^{65}$Br, $^{64}$Se, $^{66}$Se and $^{62}$Se.

All these settings were used with the $^{78}$Kr$^{36+}$ primary beam presented in section 2.1.1. The beam energy is 345 MeV/u and a maximum intensity of 250 pnA [2].

Also $^{207}$Bi source runs were acquired in order to calibrate the WAS3ABi silicon detector with conversion electrons. Runs with $\gamma$-ray sources ($^{152}$Eu, $^{133}$Ba and Cm-C) were acquired independently for EURICA calibration (cf. section 3.2).

---

[2] 1 pnA $= 6.24 \times 10^9$ particles/s

# Chapter 3

# Analysis procedure

The procedures used to analyse the data of the RIBF4R1 experiment are detailed here. First the fragments are separated and identified by the BigRIPS fragment separator presented in chapter 2. The particle identification procedure is described here.

The main part of this chapter is then dedicated to the analysis of the decays with the setup EURICA-WAS3ABi, which was introduced in chapter 2. Before analysing the decay data, these detectors were calibrated in time (TDC data) and in energy (ADC data). The energy calibration is performed with known energy transitions and radioactive sources. Then analysis methods are used to perform the ion-decay correlations and study the decays. Indeed the implantation signals are discriminated from the decay ones in WAS3ABi because of their energy. Moreover, by merging the DAQs of BigRIPS and the decay setup detectors, the implanted nuclei are identified. Position and time correlations between implantations and decays allow to make energy and time spectra to study the properties of the decays: their half-lives, proton branching ratios for direct and $\beta$-delayed proton emissions, absolute intensities of proton transitions.

## 3.1   BigRIPS particle identification

The analysis procedure described below is the one developed by the BigRIPS team [Fuk13]. The technique used to separate and identify the produced fragments is the $\Delta E$-$B\rho$-$ToF$ method.

Thanks to the detectors introduced in section 2.2, it is possible to determine the $A/Q$ ratio with the trajectory reconstruction in the dipoles between F3 and F7. This reconstruction is performed from the time of flight measured with the plastic scintillators and the trajectory vectors from the PPAC detectors. Then the charge number $Z$ of the fragments is deduced from the energy loss in the F7 MUSIC and from the time of flight between F3 and F7.

### 3.1.1   Determination of $A/Q$ ratio

The $A/Q$ ratio is computed using equation 2.1 presented in chapter 2. The value of $\beta$ is computed from the time of flight measurement (plastic scintillators) and $B\rho$ from the trajectory reconstruction (PPACs).

The time of flight (ToF) is extracted from timing information of the plastic scintillators at F3 and F7. Because of the presence of a degrader at F5, the velocity of the ions is modified so the time of flight depends on two velocities: $\beta_{35}$ between F3-F5 and $\beta_{57}$ between F5-F7. The time of flight is equal to the difference between F3 and F7 times:

$$ToF = \frac{t_{F7} - t_{F3}}{2} + T_{\text{offset}} \tag{3.1}$$

by averaging the left and right timing informations where $t_{Fi} = t_{Fi}^{\text{right}} + t_{Fi}^{\text{left}}$ is the sum of left and right times recorded in the plastic scintillator, calibrated in $ns$. The calibrations were performed by the BigRIPS team.

The relation between the time of flight and the F3-F5 ($\beta_{35}$) and F5-F7 ($\beta_{57}$) velocities ($v/c$) is the following:

$$ToF = \frac{L_{35}}{\beta_{35}c} + \frac{L_{57}}{\beta_{57}c} \tag{3.2}$$

where $L_{35}$ and $L_{57}$ are, respectively, the F3-F5 and F5-F7 distances.

$A/Q$ values are the same for F3-F5 and F5-F7 because the produced nuclei are fully stripped ($Z = Q$) and their charge state is not modified by the degrader. Thus, according to equation 2.1, one gets:

$$\frac{A}{Q} = \frac{B\rho_{35}}{\beta_{35}\gamma_{35}}\frac{c}{u} = \frac{B\rho_{57}}{\beta_{57}\gamma_{57}}\frac{c}{u} \tag{3.3}$$

As a consequence:

$$\frac{B\rho_{35}}{B\rho_{57}} = \frac{\beta_{35}\gamma_{35}}{\beta_{57}\gamma_{57}} \tag{3.4}$$

By a substitution method, one obtains the $\beta_{35}$ expression:

$$\left(ToF^2c^2 + L_{57}^2(R_{12}^2 - 1)\right)\beta_{35}^2 - 2L_{35}ToFc\beta_{35} + L_{35}^2 - R_{12}^2L_{57}^2 = 0 \tag{3.5}$$

where $R_{12} = \frac{1}{R_{21}} = \frac{B\rho_{35}}{B\rho_{57}}$. By solving this equation, one finds:

$$\beta_{35} = \frac{2L_{35}ToFc + \sqrt{(2L_{35}ToFc)^2 - 4\left(ToF^2c^2 + L_{57}^2(R_{12}^2 - 1)\right)\left(L_{35}^2 - R_{12}^2L_{57}^2\right)}}{2\left(ToF^2c^2 + L_{57}^2(R_{12}^2 - 1)\right)} \tag{3.6}$$

$\beta_{57}$ is found with:

$$\left(ToF^2c^2 + L_{35}^2(R_{21}^2 - 1)\right)\beta_{57}^2 - 2L_{57}ToFc\beta_{57} + L_{57}^2 - R_{21}^2L_{35}^2 = 0 \tag{3.7}$$

and:

$$\beta_{57} = \frac{2L_{57}ToFc + \sqrt{(2L_{57}ToFc)^2 - 4\left(ToF^2c^2 + L_{35}^2(R_{21}^2 - 1)\right)\left(L_{57}^2 - R_{21}^2L_{35}^2\right)}}{2\left(ToF^2c^2 + L_{35}^2(R_{21}^2 - 1)\right)} \tag{3.8}$$

The last parameter necessary to compute $A/Q$ is the magnetic rigidity value (cf. equation 3.3). This latter is deduced from the positions measured by the PPACs and the transfer matrices between the focal planes. These matrices are determined experimentally by the BigRIPS team [Fuk13]. Indeed each dipole-quadrupoles set behaves as an optical system and can be modelled by a transfer matrix. The transfer matrix between F3 and F5 has this expression:

$$\begin{pmatrix} x_{F5} \\ x'_{F5} \\ y_{F5} \\ y'_{F5} \\ l_{F5} \\ \delta_{F5} \end{pmatrix} = \begin{pmatrix} (x|x) & (x|x') & 0 & 0 & 0 & (x|\delta) \\ (x'|x) & (x'|x') & 0 & 0 & 0 & (x'|\delta) \\ 0 & 0 & (y|y) & (y|y') & 0 & 0 \\ 0 & 0 & (y'|y) & (y'|y') & 0 & 0 \\ (l|x) & (l|x') & 0 & 0 & 0 & (l|\delta) \\ 0 & 0 & 0 & 0 & 0 & 1 \end{pmatrix} \begin{pmatrix} x_{F3} \\ x'_{F3} \\ y_{F3} \\ y'_{F3} \\ l_{F3} \\ \delta_{F3} \end{pmatrix} \tag{3.9}$$

where

- $x$ and $y$ are the horizontal and vertical positions at F3 and F5,

- $x' = tan(\theta)$,

- $y' = tan(\phi)$,

- $l = vt$,

- $\delta$ the deviation from the reference magnetic rigidity as $B\rho = B\rho_0(1 + \delta)$ with $B$ the magnetic field and $\rho_0$ the central curvature of the dipole.
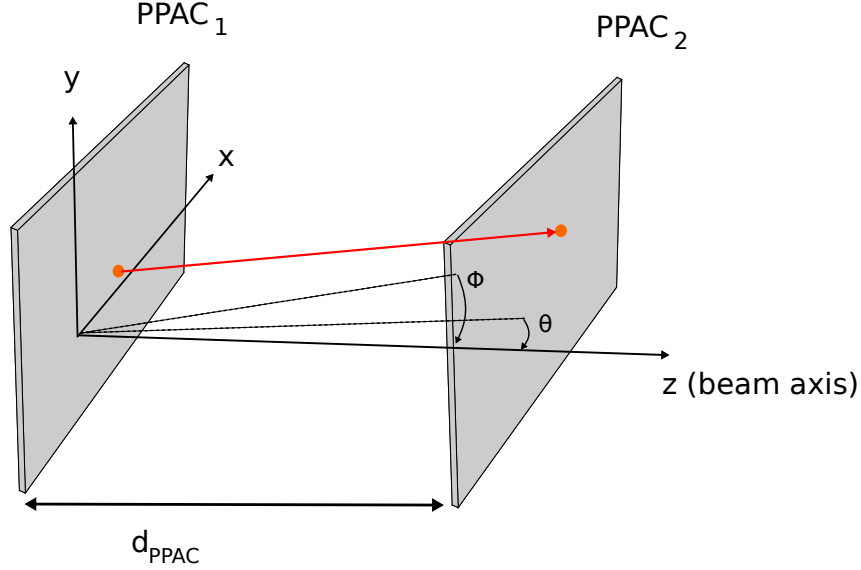
Figure 3.1: Scheme of a PPAC pair of the BigRIPS separator. The beam line is aligned on the $z$ axis. The measurement of the $(x, y)$ position of an event (orange point) in the two PPACs (PPAC$_1$ and PPAC$_2$) allows to calculate the horizontal and vertical angles ($\phi$ and $\theta$) of the trajectory vector (orange arrow) between the positions measured in the two PPACs. $\phi$ is the angle between the projection of the vector in the $yz$ plane and the $z$ axis. $\theta$ is the angle between the projection on the $zx$ plane and the $z$ axis.

The reference frame associated with the trajectory is defined along the beam line. The beam propagates along $z$, $x$ is the horizontal axis and $y$ the vertical axis. The vertical angle $\phi$ is defined between the projection of the trajectory vector on the $yz$ plane and the $z$ axis, the horizontal angle $\theta$ between the projection on $zx$ and $z$. The reference frame and the PPAC positions at a focal point are represented in figure 3.1.

The first line of the matrix product of equation 3.9 gives the relation:

$$x_{F5} = (x|x)x_{F3} + (x|x')x'_{F3} + (x|\delta)\delta_{F3} \tag{3.10}$$

$x_{F3}$ and $x'_{F3}$ are calculated from measurements of the PPAC pair at F3 (see figure 3.1):

$$\begin{aligned} x'_{F3} &= \frac{x_{\text{PPAC}_2} - x_{\text{PPAC}_1}}{d_{\text{PPAC}}} \\ x_{F3} &= \frac{x_{\text{PPAC}_2} - x_{\text{PPAC}_1}}{d_{\text{PPAC}}} d_{\text{PPAC}_2 - F3} + x_{\text{PPAC}_2} \end{aligned} \tag{3.11}$$

where

- $x_{\text{PPAC}_1}$ and $x_{\text{PPAC}_2}$ are the positions measured on PPAC 1 and 2,

- $d_{\text{PPAC}}$ the distance between the two PPACs,

- $d_{\text{PPAC}_2 - F3}$ the distance between PPAC$_2$ and F3 (negative or positive depending on the PPAC position).

In the same manner, $x'_{F5}$ and $x_{F5}$ are found thanks to the PPAC pair at F5. Thus one obtains with equation 3.10 the value of $\delta$ at F3:

$$\delta_{F3} = \frac{x_{F5} - (x|x)x_{F3} - (x|x')x'_{F3}}{(x|\delta)} \tag{3.12}$$

By combining the first term of equations 3.3, 3.12 and $B\rho_{35} = (1 + \delta_{F3})(B\rho_0)_{35}$, one obtains the expression:

$$\frac{A}{Q} = \frac{1}{\beta_{35}\gamma_{35}} \frac{c}{u} (1 + \frac{x_{F5} - (x|x)x_{F3} - (x|x')x'_{F3}}{(x|\delta)})(B\rho_0)_{35} \tag{3.13}$$

where $\beta_{35}$ (and $\gamma_{35}$) are computed with equation 3.6.

### 3.1.2  $Z$ determination

The $Z$ value of the nuclei is determined from the MUSIC at F7 and the time of flight measured by the plastic scintillators. From the time of flight between F3 and F7, we deduce from equation 3.8 the velocity $\beta_{57}$ at the entrance of the MUSIC. The energy loss inside the MUSIC comes from the integration of the Bethe-Bloch equation 2.2 over the length of the chamber [1]:

$$-\frac{\Delta E_{\mathrm{MUSIC}}}{L_{\mathrm{MUSIC}}} = \frac{4\pi e^4}{m_e c^2} \frac{\mathcal{N}_{\mathcal{A}} \rho Z_m}{A_m} \frac{Z^2}{\beta_{57}^2} \left[ \ln \left( \frac{2 m_e c^2 \beta_{57}^2 \gamma_{57}^2}{I} \right) - \beta_{57}^2 \right] \tag{3.14}$$

with

- $L_{\mathrm{MUSIC}} = 48$ cm the active volume length of the MUSIC,

- $\rho = 1,562$ g.cm$^{-3}$ the gas density,

- $e$ the electron charge,

- $m_e$ the electron mass,

- $N_A$ the Avogadro's number,

- $Z_m = 18$ the atomic number of the gas,

- $A_m = 39,948$ g.mol$^{-1}$ the molar mass of the gas,

- $Z$ the atomic number of the ion,

- $I = 16 Z_m^{0,9}$ eV the mean ionisation potential.

The $Z$ expression as a function of the energy loss in the MUSIC is deduced by [Fuk13]

$$Z = A \beta_{57} \sqrt{\frac{-\Delta E_{\mathrm{MUSIC}}}{\ln \left( \frac{2 m_e \beta_{57}^2 c^2}{I} \right) - \ln \left( 1 - \beta_{57}^2 \right) - \beta_{57}^2}} + B \tag{3.15}$$

where $A$ and $B$ are the calibration parameters measured on the MUSIC by the BigRIPS team before the experiment.

### 3.1.3  Cleaning procedures

Background events remain in the particle identification procedure. Reactions with the detector or diffusions induce wrong events. It is necessary to check some correlations between different detectors of the beam line and different variables to constrain them. Correlations between plastic scintillator, MUSIC events and also between optical vector variables are constrained.

**Plastic scintillators**

The position $x$ of the interaction in the plastic material is given by the difference between the timing information of each photo-multipliers. One has:

$$x = -\frac{V}{2}(t_{\mathrm{right}} - t_{\mathrm{left}}) \tag{3.16}$$

with $V$ the propagation speed of light in the plastic material.

  Background events are generally far from the plastic center. Thus a condition on the time difference between the TDCs of the right and left scintillators performs a selection of the events according to $x$, as shown in equation 3.16. To remove the background events, we keep only events with similar left and right times for F3, F5 and F7 scintillators. This selection is shown on the left plot of figure 3.2.

---

[1]N.B. a $-$ sign is here because $\Delta E_{\mathrm{MUSIC}}$ is negative, the ion losing energy in the chamber.
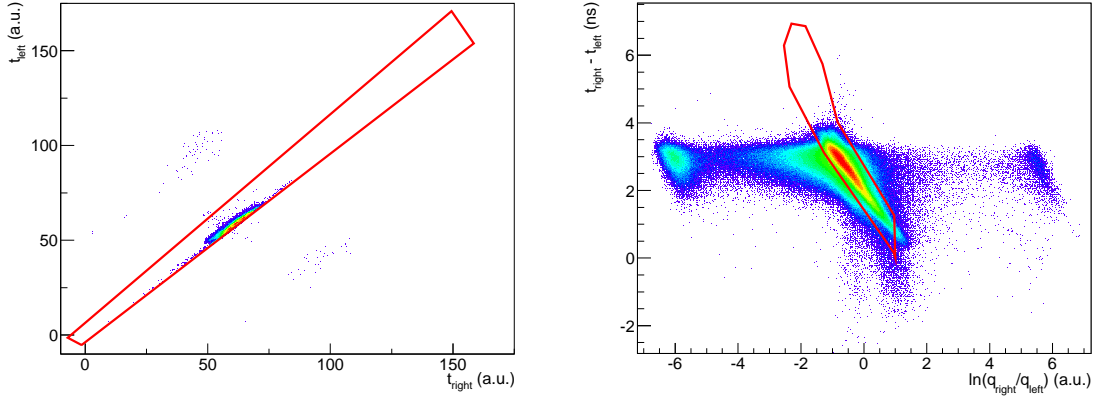
Figure 3.2: Background subtraction on the plastic scintillator at F3. The plot on the left represents correlations between the left and right times. The good events are close to the diagonal inside the red contour. On the plot on the right, one discriminates good events by selecting those having a similar time and charge difference (acceptance window in red).

The position $x$ of interaction can also be expressed as a function of the charges collected by the two photo-multipliers. The intensity of the light in the plastic material follows an exponential law with the distance from the interaction position. Thus the collected charges on the right and left photo-multipliers are [Fuk13]:

$$q_{\text{right}} = q_0 \exp\left(-\frac{L+x}{\lambda}\right) \text{ and } q_{\text{left}} = q_0 \exp\left(-\frac{L-x}{\lambda}\right) \tag{3.17}$$

where $x$ is the position of the interaction, $q_0$ the charge deposit at the interaction point, $L$ the length of the scintillator and $\lambda$ the attenuation length of light. The combination of these two charge expressions leads to:

$$x = -\frac{\lambda}{2} \ln\left(\frac{q_{\text{left}}}{q_{\text{right}}}\right) \tag{3.18}$$

$x$ follows the relations of the equations 3.16 and 3.18, so we can apply the following condition to remove background events from plastic scintillators:

$$\lambda \ln\left(\frac{q_{\text{right}}}{q_{\text{left}}}\right) = -V(t_{\text{right}} - t_{\text{left}}) \tag{3.19}$$

This second condition is illustrated on the right plot of figure 3.2.

### MUSIC events

Background subtraction procedures are also applied on the F7 MUSIC. Firstly, only events with correlated signals between two following anode pairs are kept, i.e. $\Delta E_i \simeq \Delta E_{i+1}$ (see left plot in figure 3.3). It removes the background caused by reactions with the gas or the electrodes of the detector. Indeed, if a reaction happens in the chamber, the energy loss is greatly different for this event. A selection in averaged charge of the F7 plastic scintillator and averaged energy of the F7 MUSIC is also preformed (illustrated on the right plot of figure 3.3).

### Coordinate vectors

Background events are also removed by using the coordinate vectors $(x, x', y, y', l, \delta)$ at F3, F5 and F7 (cf. equation 3.9), computed by the corresponding PPACs. Too diverging events in angle and position are rejected. For each focal point, events satisfying the $x$-$\theta$ condition are kept (cf. figure 3.4). Since the beam was vertically focused (on $y$) and diverging on $x$, only a selection in the horizontal plane is done.
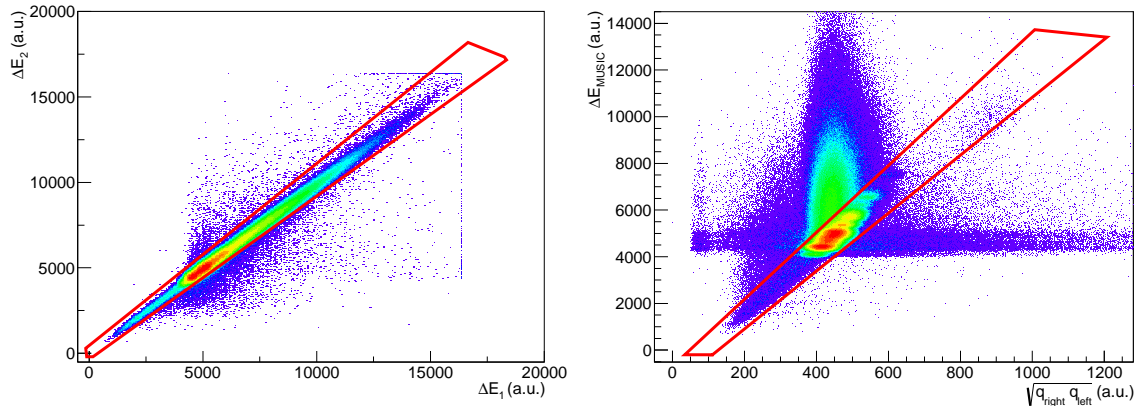
Figure 3.3: Background subtraction by correlations implying the F7 MUSIC. Left: correlation between first and second anode energy signals. The plot on the right shows the correlation between the average charge collected by the F7 plastic scintillator and the energy loss in the MUSIC at F7. In each case, good events are close to the diagonale. The applied cuts are represented by a red line.
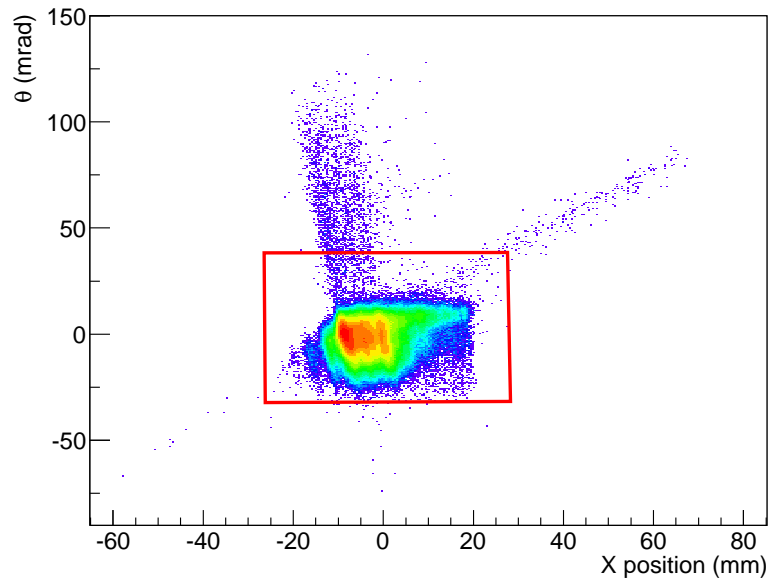


Figure 3.4: Correlation between the horizontal angle $\theta$ and the $x$ position measured by the PPAC at F7. The cut used to reject the background events is represented in red.

### 3.1.4  Identification matrices

The procedures described above provide an identification matrix of the fragments in $Z$ and $A/Q$. The isotopes are gathered in wide spots due to the separation power of the separator, as shown on figure 3.5. They are "aligned" according to their $Z$ value (horizontal) and their isospin projection $T_z$. The effects of the procedures presented in section 3.1.3 to subtract background events are visible. Indeed, background events create tails on the identification plot. Their subtraction give a clearer plot with a best separation of the nuclei.
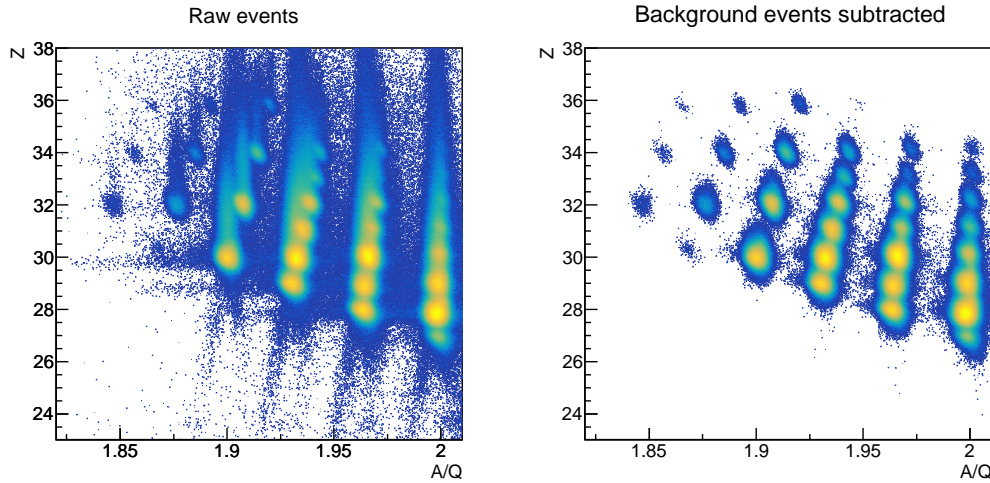


Figure 3.5: Identification matrices of isotopes produced on the BigRIPS fragment separator during the setting optimised for $^{65}$Br production. The plot obtained from all BigRIPS events (left) is compared with the matrix subtracted from background events (right).

The analysis of the identification plots obtained from the RIBF4R1 experiment are detailed in chapter 4.

## 3.2  Detector calibrations

A coder gives only numerical values of the detector signal, depending on the gain of the channel. Peak-sensing ADC give the maximum value of the charge deposit in the detector. The calibrations for the BigRIPS and ZDS detectors were performed by the BigRIPS team. Concerning EURICA and WAS3ABi, calibrations have to be performed for the analysis of the experiment.

### 3.2.1  WAS3ABi

WAS3ABi needs to be calibrated in time and energy. The timing calibration is crucial to compare contiguous strips and determine the implantation strip. The energy calibration is necessary to obtain the energies of the proton transitions involved in the decay events.

**Timing**

When an ion stops in one of the DSSSDs, 3.4 X strips and 4.3 Y strips saturate on average because of the high energy deposit. One can identify the strip of implantation by comparing the TDC signals of the saturated strips. The fastest one gives the exact position of the implantation event [Nis13].

As presented in figure 3.6, the TDC values corresponding to overflowed ADC values are divided in three peaks. The first one gives the relative offset to the origin of the timing spectrum. We align the first peak of each strip to this origin to be able to compare them. For every channel, this component was fitted by a Gauss function to obtain the central value of the peak. This value is the offset of the channel. For each channel this offset value is subtracted from the TDC value in order to align the channels of the three DSSSDs.
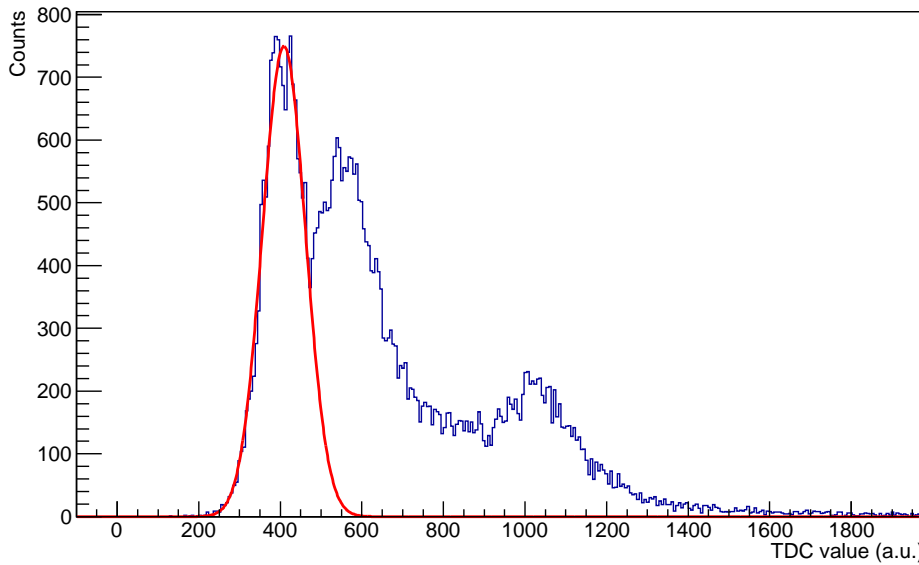
Figure 3.6: Distribution of TDC values for implantation events (overflow of the ADC signal) on one strip. The fastest component is fitted by a Gauss function (in red) to give the offset value of this channel.

**Energy**

The energy calibration was performed on the spectra obtained from the analysis procedure described in section 3.4. It is done in two steps: first, a low-energy calibration using a radioactive source; then a high-energy one with known proton transitions of nuclei produced during the experiment. The calibration was performed strip by strip as for the timing calibration. Before the calibration, the ADC of all strips were aligned according to their respective pedestal values.

For low energies, a $^{207}$Bi source producing conversion electrons was placed in front of several areas of each DSSSD to cover the entire surface of the detector. This source gives four peaks for a calibration up to 1 MeV. The reference values are taken from table 3.1.

| Transition | Energy (keV) | Number of $e^-$ per 100 disint. |
|------------|--------------|---------------------------------|
| $ec_{1,0K}$ | 481.694(2) | 1.548(22) |
| $ec_{1,0L}$ | 553.838 - 556.664 | 0.429(7) |
| $ec_{3,1K}$ | 975.655(3) | 7.11(17) |
| $ec_{3,1L}$ | 1047.798 - 1050.624 | 1.84(5) |

Table 3.1: Values of the four electron emissions used to calibrate WAS3ABi in energy below 1 MeV. Taken from [Bé04].

The four peaks are fitted from the spectra obtained strip by strip (see spectrum in the left of figure 3.7). Each peak was fitted by a Gauss function added to a linear left-right function for the background:

$$f(x) = Ae^{-\frac{(x-\mu)^2}{2\sigma^2}} + b(x)$$
$$\text{with } b(x) = \begin{cases} p_0 x + p_1 & \text{if } x < \mu \\ q_0 x + q_1 & \text{else.} \end{cases} \quad (3.20)$$

$x$ is the ADC channel, $A$ the amplitude factor, $\mu$ and $\sigma$ the average and standard deviation of the Gauss function, $p$ and $q$ the parameters of the two background functions. All the parameters of the fit are free.

In order to get a better uncertainty at high energy (above 1 MeV), proton peaks from known and highly produced $\beta p$ emitters are used with the reference energies in table 3.2. These proton peaks allow a calibration up to 4.6 MeV, the proton transition of the highest energy in this

| Nucleus | Energy (keV) |
|---------|--------------|
| $^{57}$Zn | 1900(60) |
|         | 2560(50) |
|         | 3130(60) |
|         | 4590(50) |
| $^{61}$Ge | 3220(60) |
| $^{65}$Se | 2620(30) |
|         | 3510(20) |

Table 3.2: Values of proton peaks used to calibrate WAS3ABi at high energy. These reference values are taken from [Bla07] for $^{57}$Zn and $^{61}$Ge, [Rog11b] for $^{65}$Se.

experiment. On each strip, each identifiable peak was fitted by the procedure presented in section 3.7. The function used is similar to equation 3.20 but the function is convoluted with a decreasing exponential to take into account the contribution of the $\beta$ particles:

$$f(x) = Ae^{-\frac{(x-\mu)^2}{2\sigma^2}} * e^{-\frac{x}{p\sigma}} + b(x) \tag{3.21}$$

where $x$ is the ADC channel and $p$ the tail parameter of the fit. The background $b(x)$ is the same as used for the fits of the $^{207}$Bi electron spectra. All parameters are free except the tail. This latter was empirically fixed for each proton peak of each nucleus. The value giving the best $\chi^2/ndf$ value on a reference spectrum is used for the fits of the same proton peak. The parameter $\mu$ corresponds to the proton energy and it is used to obtain the calibration point. An example of a fit of a $\beta$-delayed proton peak is illustrated in figure 3.7 (right).
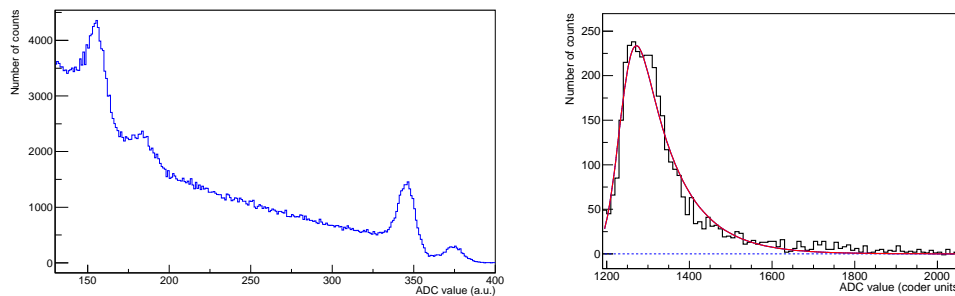


Figure 3.7: Fits of $^{207}$Bi and $^{61}$Ge energy spectra for WAS3ABi calibration. Left: a $^{207}$Bi conversion electrons spectrum for one DSSSD strip. Right: a $^{61}$Ge energy spectrum of a strip with the fit of the 3220-keV peak used for the calibration (red curve).

The strips were calibrated in energy with the $^{207}$Bi and proton peaks by a linear fit as presented in figure 3.8. Then the calibration uncertainty was estimated by the covariance matrix computed by the fit procedure. The calibration curve is defined by:

$$\begin{cases} E(x) = p_0 + p_1 x \\ \Delta E^2(x) = \sigma_{p_0}^2 + \sigma_{p_0 p_1} x + \sigma_{p_1 p_0} x + \sigma_{p_1}^2 x^2 \end{cases} \tag{3.22}$$

where $x$ is the ADC channel, $\sigma_{p_0}^2$, $\sigma_{p_0 p_1}$, $\sigma_{p_1 p_0}$ and $\sigma_{p_1}^2$ the elements of the covariance matrix of the fit.

Because it was difficult to find highly produced nuclei covering the three DSSSDs, most of the strips of the first DSSSD were only calibrated with the $^{207}$Bi source. The energy of the $^{61}$Ge peak saturates very often the X strips so it could not be used for most of these strips. Indeed the Y strips saturate at around 8 MeV on each DSSSD. X strips have the same dynamics as the Y ones on the first DSSSD, but the two last detectors saturate at 3 MeV on X side. $^{61}$Ge and $^{57}$Zn were mostly implanted in the two last DSSSD, $^{65}$Se in the two first DSSSDs. Moreover these nuclei were mostly implanted in half of the DSSSD surface, with very few statistics on the other half. The strips $X = 0$ and $Y = 46$ of the last DSSSD were not working during the experiment thus they were not calibrated and therefore not used for the analysis.
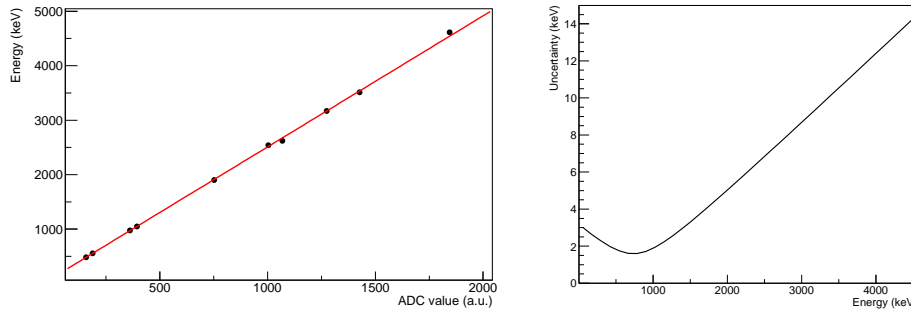
Figure 3.8: Calibration curve and uncertainty for the strip 76 of the second DSSSD. The calibration curve is represented on the left. The curve on the right is the calibration uncertainty curve.

### 3.2.2 EURICA

The EURICA cluster array was calibrated in energy according to well-known $\gamma$-ray sources ($^{133}$Ba and $^{152}$Eu). These same sources were also used to compute the $\gamma$-detection efficiency. The energy calibration used in the analysis is provided by P.-A. Söderström from the EURICA team at RIBF. The efficiency computations were performed by A. I. Morales from IFIC in Valencia. The procedures used to achieve the calibration of the detectors are presented in here.

**Energy**

The energy calibration is performed for each crystal by using $^{133}$Ba and $^{152}$Eu sources. They allow a calibration from 80 keV to 1.4 MeV. The peaks as used for the calibration are summarised in table 3.3. $^{133}$Ba and $^{152}$Eu spectra with the energies of the peaks are presented in figure 3.9.

| Nucleus | Transition energy (keV) | Emission probability per decay |
|---------|------------------------|-------------------------------|
| $^{133}$Ba | 80.9979(11) | 0.329(3) |
| | 276.3989(12) | 0.0716(5) |
| | 302.8508(5) | 0.1834(13) |
| | 356.0129(7) | 0.6205(19) |
| | 383.8485(12) | 0.0894(6) |
| $^{152}$Eu | 121.7817(3) | 0.2841(13) |
| | 244.6974(8) | 0.0755(4) |
| | 344.2785(12) | 0.2658(12) |
| | 411.1165(12) | 0.02237(10) |
| | 778.9045(24) | 0.1296(6) |
| | 867.380(3) | 0.04241(23) |
| | 964.072(18) | 0.1462(6) |
| | 1212.948(11) | 0.01415(9) |
| | 1299.142(8) | 0.01632(9) |
| | 1408.013(3) | 0.2085(9) |

Table 3.3: Transition energies used for the EURICA energy calibration. Taken from [Int07].

For high-energy calibration, a $^{244}$Cm-$^{12}$C source extends the calibration up to 5 MeV. There is a double escape peak of the 6.13-MeV transition of $^{16}$O originating from the $\alpha$-particle capture (from $^{244}$Cm $\alpha$-decay) by the carbon nuclei of the source.

Each peak was fitted by a function composed of a sum of a Gauss, step and constant function as:

$$f(x) = Ae^{-\frac{(x-\mu)^2}{2\sigma^2}} + \frac{B}{1 + e^{\frac{x-\mu}{\sigma}}} + C \qquad (3.23)$$

where $x$ is the ADC channel, $A$, $B$, $C$, $\mu$ and $\sigma$ the fit parameters. The energy calibration
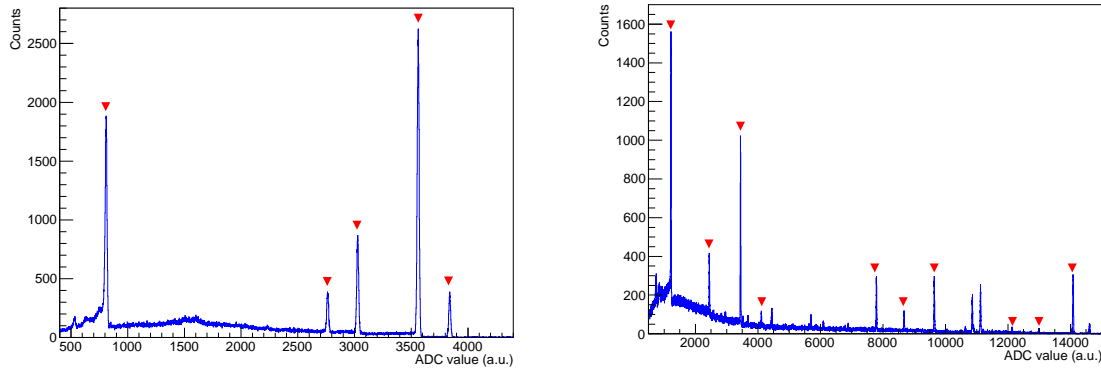
Figure 3.9: Gamma spectra of $^{133}$Ba (left) and $^{152}$Eu (right) obtained for a EURICA cluster. The peaks fitted are those with a red marker above.

was then obtained by a linear fit, as for WAS3ABi calibration, with the equation 3.22. The associated calibration uncertainty was obtained in the same manner.

**Gamma-detection efficiency**

The $\gamma$-detection efficiency was determined with the $^{133}$Ba and $^{152}$Eu sources. For the calibration runs, the DAQ of EURICA is triggered by a 1-kHz clock generator (1 ms between two triggers). A gate of 100 $\mu$s width is generated at each trigger to register the events. The activity of the source is constantly monitored and communicated by RIBF, thus its value is known at the time of data acquisition. The absolute efficiency for each $\gamma$-ray peak is given by:

$$\varepsilon_\gamma = \frac{N_\gamma}{A I_\gamma N_{\text{triggers}} T_{\text{gate}}} \tag{3.24}$$

where

- $N_\gamma$ is the number of counts in the peak at a given energy,

- $N_{\text{triggers}}$ the total number of triggers during the calibration runs,

- $A$ the activity of the source,

- $I_\gamma$ the absolute intensity of the $\gamma$ transition,

- $T_{\text{gate}}$ the width of the time gate generated at each trigger.

The experimental points were then fitted by the RadWare [Rad17] function:

$$\varepsilon_\gamma(E_\gamma) = \exp\left(\left(\left(A + B\frac{E_\gamma}{100} + \left(C\frac{E_\gamma}{100}\right)^2\right)^{-G} + \left(D + E\frac{E_\gamma}{1000} + F\left(\frac{E_\gamma}{1000}\right)^{-G}\right)^{-\frac{1}{G}}\right) \tag{3.25}$$

where $A$, $B$, $C$, $D$, $E$, $F$, $G$ are the six parameters of the fit. The fit curve is shown in figure 3.10. It gives the $\gamma$ detection efficiency up to 1.4 MeV, a sufficient energy to study $\gamma$ rays originating from the $\beta p$ decays presented in this thesis.

## 3.3 Data acquisition merging

As it is presented in section 2.4, each acquisition is driven by a different LUPO module with its own 48-bit clock (10 ns). Data files are independently generated for BigRIPS, WAS3ABi and EURICA.

Time windows were defined for each DAQ combination and experiment setting to match coincident events. To achieve this, all time-stamps between two acquisitions are compared for
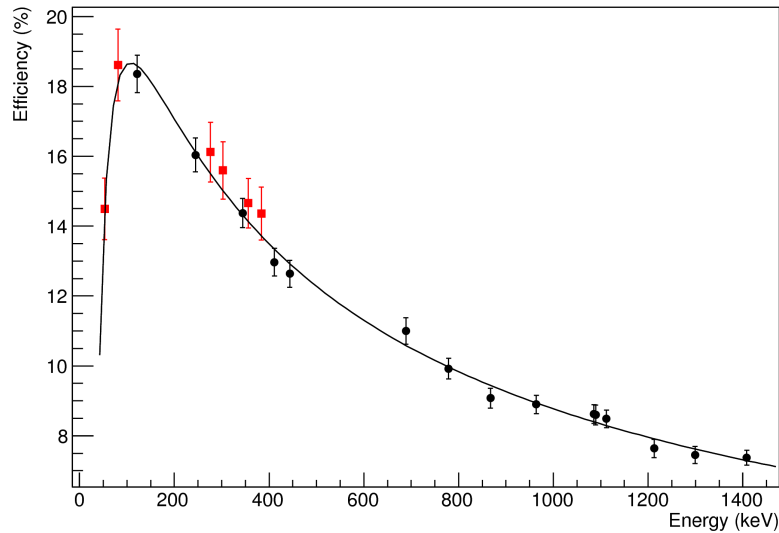
Figure 3.10: EURICA efficiency curve for the add-back spectra. The red dots correspond to the
$^{133}$Ba energies, the black dots to the $^{152}$Eu ones.

runs of each setting (cf. figure 3.11 for $^{65}$Br setting). A predominating peak indicates the most
common shift between the events and thus the average time shift between the two clocks.

A coincidence time-stamp window was defined for the three correlations useful for the analysis:

- BigRIPS - WAS3ABi: identification of the implantations,

- WAS3ABi - EURICA: $\gamma$-ray emissions in coincidence with charged particles from decay
  events in WAS3ABi.

All event couples in these time window are considered in coincidence. Thus every WAS3ABi
implantation event is correlated with its coincident BigRIPS event to identify the implanted
nucleus. Every WAS3ABi decay event is correlated with its coincident EURICA event (if it
exists).
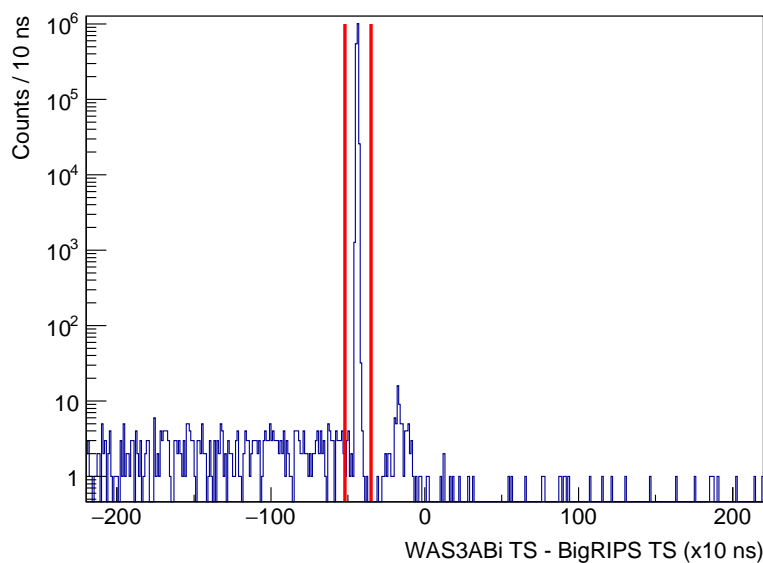


Figure 3.11: Distribution of time-stamp difference between the BigRIPS and WAS3ABi acqui-
sitions over the first five runs of the $^{65}$Br setting. The time window of this setting is between
the two vertical red lines.

## 3.4 Decay spectra construction

The energy and time spectra are built by correlating all decay and implantation events in a given time window. An energy spectrum associated to a nucleus is a histogram of all decay events correlated to the implantations identified as belonging to this isotope. A time spectrum is constructed in the same way but the events are represented by the difference between the WAS3ABi time-stamp of the decay and the correlated implantation one. There is a lot of fortuitous correlations since we work with a continuous beam. A correlation in position is thus performed to decrease the background, otherwise all triggered strips of a DSSSD at a same time could be correlated with a same implantation event. Moreover the background can be removed from the energy spectrum, this procedure is presented in this section.

### 3.4.1 Position determination of implantations

WAS3ABi ADC channels are tuned in this experiment to measure an energy up to 8 MeV, so they saturate when an ion is slowed down in the DSSSD. The implantation events are recognised by matching the saturated strips. For an event with a signal at the F7 and F11 plastic scintillators, the last fired DSSSD (or veto scintillator) with at least one saturated strip on each side is the one of implantation. The saturation condition on both X and Y is required to match an implantation. Unfortunately, an ion implantation saturates on average 3.4 strips on the X side and 4.3 on the Y side. To locate the strip of implantation, we retain the fastest fired strip with the TDC coders as it is explained in section 3.2.1.

Positions of all implantation events (fastest saturated strip) are shown in figure 3.12. One observes an abnormal number of saturation events, especially for $(X = 0, Y = 0)$ and $(X = 59, Y = 39)$ pairs. These events may be caused by ions hitting the detector holding structure. To avoid having wrong implantation positions, the strips on the edges are completely removed from the analysis. Also the strips $Y = 0$ and $X = 46$ of the last DSSSD are not taken into account because they were damaged for the calibration runs.
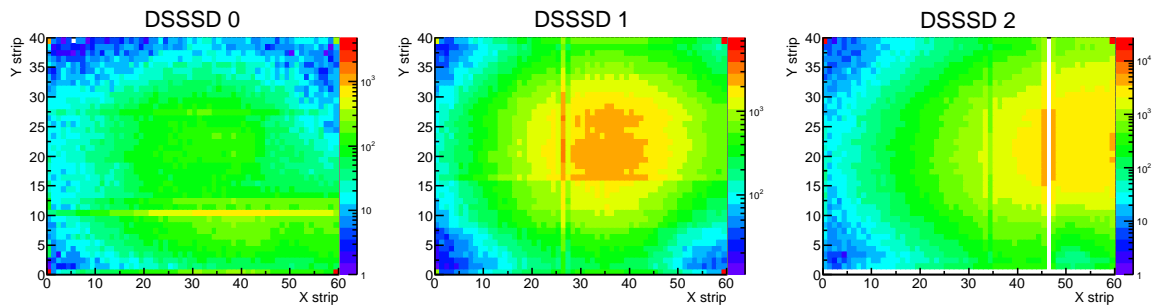


Figure 3.12: Positions of all implantation events in the three DSSSDs during the RIBF4R1 experiment. The first Y strip of the DSSSD2 was out during the whole experiment, the 46th X strip of the same DSSSD was damaged at the end of the experiment. These two strips are rejected from data analysis.

### 3.4.2 Decay correlation and background subtraction method

A decay event is defined as an event without any saturation on the Y side of the DSSSD (because of their high gain, X strips can saturate even for decay events). It is then correlated in position with an implantation event, i.e. located in the same DSSSD and strip. All decay events happening in a time window of 2 s at the same position can be correlated with the corresponding implantation. A method is described here to subtract fortuitous correlations. The method can also be applied to EURICA in order to clean the γ-ray spectra.

The background subtraction method is illustrated in figure 3.13. Many decay events happening at the same position as an implantation are wrongly correlated to this one. These fortuitous correlations induce a constant background in time. The correlations are done in positive and negative time difference with the implantation to suppress the background from energy spectra.
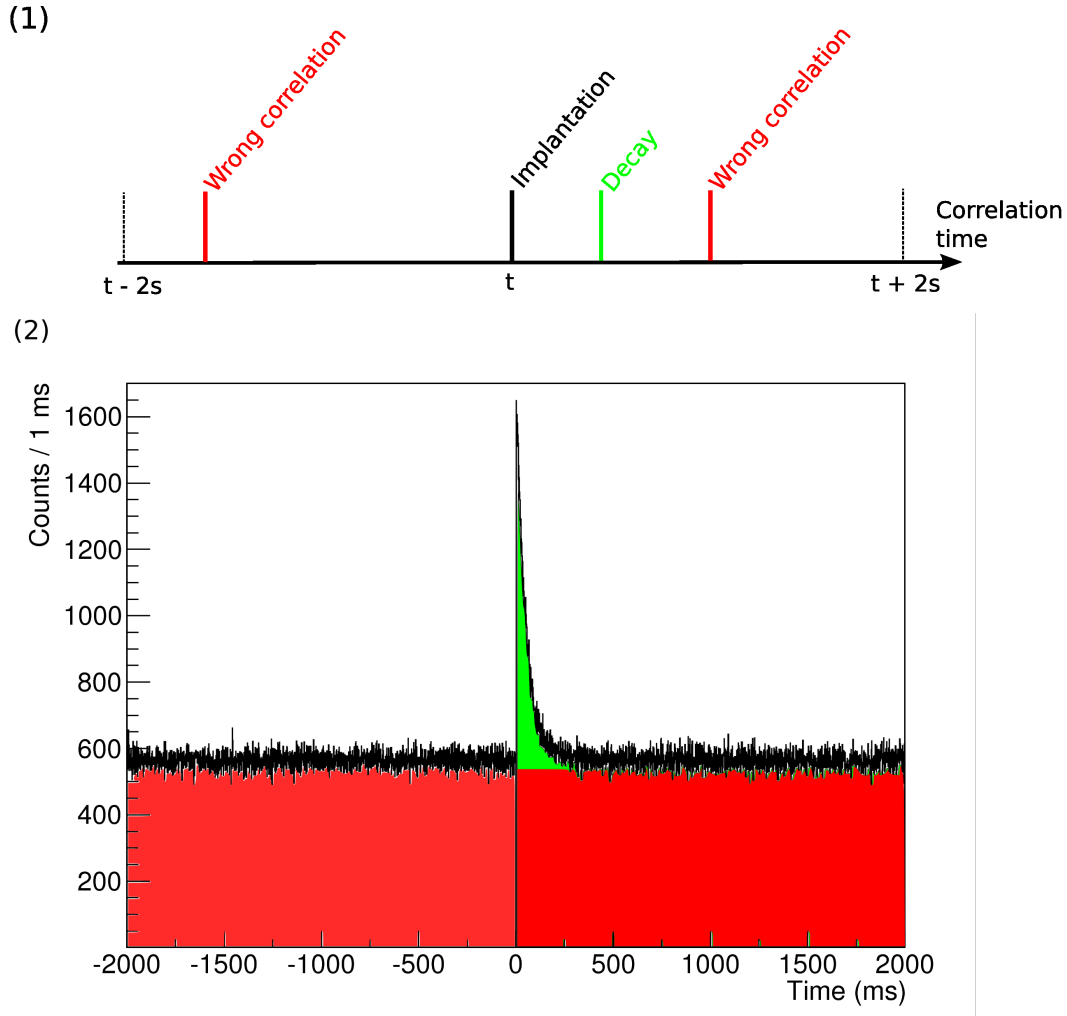
Figure 3.13: Illustration of the background subtraction method.  Each implantation event is correlated with all decay events occurring at the same position (DSSSD number, X and Y strips) in a time window of 2 s before and after this latter.  This procedure is illustrated on part (1) of the figure.  Despite the position correlation, a lot of decays are wrongly correlated. The corresponding time spectrum on part (2) is thus composed of rightly correlated events in green.  The fortuitous correlations in red are suppressed from the positive-time energy spectrum by subtracting the negative-time one.

The positive-time energy spectrum contains the decay events related to the nucleus (in green in figure 3.13) and the events coming from other decays (in red in figure 3.13).  Thus the energy spectrum $S_{\text{raw}}$ obtained from the events correlated in a $T$-second gate (2 s here) is composed of the decay events from the selected nucleus (and its filiation) and events of the other nuclei wrongly correlated to the implantation (background). The background is uniformly distributed in time, so it can be suppressed by subtracting the energy spectrum corresponding to a window of same width and only composed of background events. This spectrum $S_{\text{bg}}$ is generated from events correlated in a negative-time window with the same width as set for the positive-time one.  The background subtraction procedure gives the clean spectrum by subtracting the spectra bin by bin:

$$S_{\text{clean}} = S_{\text{raw}} - S_{\text{bg}} \tag{3.26}$$

And the associated statistical uncertainty is obtained with:

$$\Delta S_{\text{clean}} = \sqrt{S_{\text{raw}} + S_{\text{bg}}} \tag{3.27}$$

An example of a clean energy spectrum is illustrated in figure 3.14.

The background subtraction procedure removes on a statistical basis all events from fortuitous correlations. These energy spectra are thus more convenient to compute branching ratios
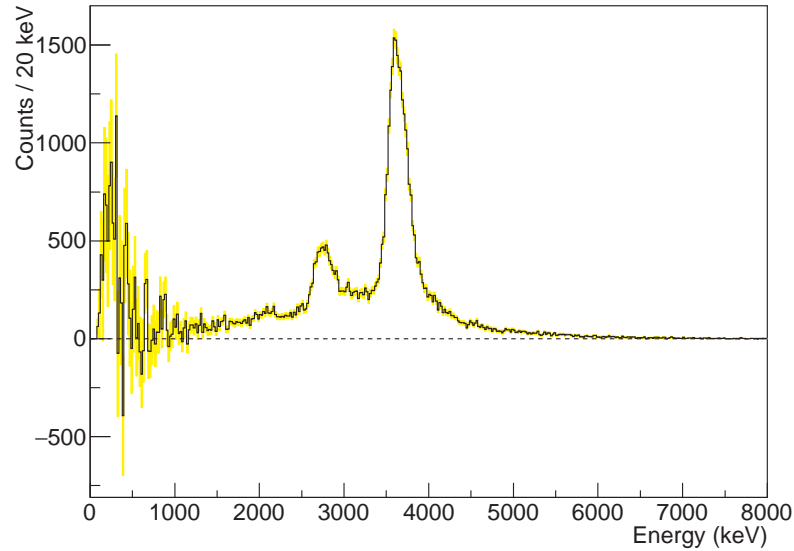
Figure 3.14: $^{65}$Se decay spectrum obtained with the background-subtraction procedure. The associated uncertainty is represented bin by bin in yellow. The distribution at low energy (below 900-1000 keV) is the contribution of $\beta$ particles. The high-energy peaks come from $\beta$-delayed proton emissions.

of the proton peaks and determine their energies. Unfortunately this method induces uncertainties, especially on the $\beta$-decay part of the spectrum, below 900-1000 keV (see figure 3.14). These uncertainties strongly increase with lower statistics spectra.

Events belonging to the first or last 2 s of each run are also excluded from the spectra in order to avoid having a no-time-constant background in the spectra because 2 s is the size of the correlation window.

## 3.5 Dead time

The dead time is an important issue to determine the proton branching ratio and the intensity of a proton peak. Because of the dead time, events are missed and therefore the count numbers extracted from the spectra are biased and need to be corrected. We deal with two dead times in this experiment.

The first one is the global dead time depending on the WAS3ABi DAQ and affects all the events. The second dead time is the dead time per event. It is the time while the DAQ is treating an implantation event and during which a decay event can be missed.

### 3.5.1 Global dead time

It is a ratio between rejected and all triggers of the acquisition scalers. Even if we abusively call it a dead time, it is actually directly linked to the dead time of the acquisition (the time while the acquisition is not available because it is treating an event). This dead time fraction was computed setting by setting by reading the scalers of the WAS3ABi acquisition. It is equal to:

$$\begin{cases} DT = \frac{N_{\text{triggers}}^{\text{rejected}}}{N_{\text{triggers}}^{\text{total}}} \\ \Delta DT = \frac{\sqrt{N_{\text{triggers}}^{\text{rejected}}}}{N_{\text{triggers}}^{\text{total}}} \end{cases} \quad (3.28)$$

The computed global dead times and their uncertainties for each setting are summarised below in table 3.4.

| Setting | Dead time (%) |
|---------|---------------|
| B ($^{65}$Br) | 22(3) |
| C ($^{64}$Se) | 27(3) |
| D ($^{66}$Se) | 27(4) |
| E ($^{62}$Se) | 11(3) |

Table 3.4: Global dead times associated to the different settings of the RIBF4R1 experiment. The settings are respectively optimised for the production of the isotope in parenthesis.

### 3.5.2   Dead time per event

The second dead time of the acquisition is the time of treatment of an implantation. During this time, no decay event is registered, resulting in a loss of amplitude in the correlated energy spectra. This dead time was determined from decay time spectra as illustrated in figure 3.15.



| Entries | 5103569 |
|---------|---------|
| Mean | 2.072 |
| RMS | 0.4582 |
| Underflow | 0 |
| Overflow | 5.032e+06 |
| Integral | 1.4e+04 |
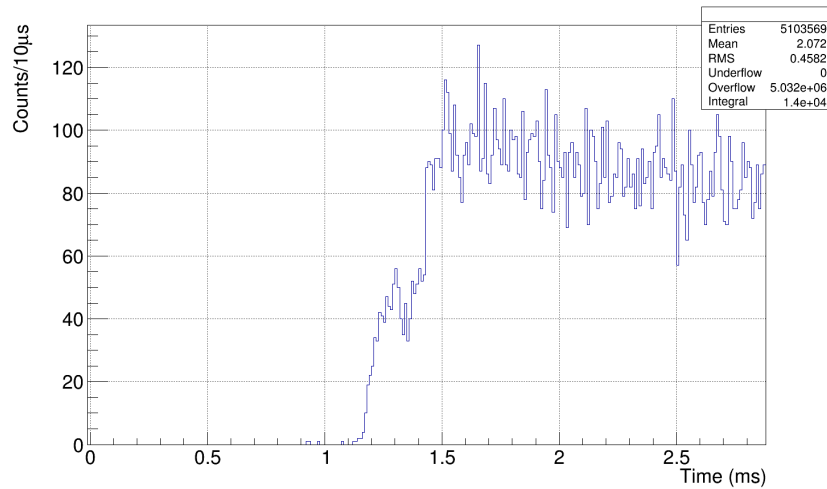
Figure 3.15: Decay time spectrum of the $^{61}$Ge nuclei implanted in the three DSSSDs. The maximum amplitude of the decay curve is at approximately 1.5 ms after the implantation because of the dead time per event.

At the beginning of the time spectrum, one can see that very few events are situated in a window of 1.5 ms after the implantation. This is due to the treatment of the implantation by the WAS3ABi DAQ. This duration of 1.5 ms is the dead time per event. The event loss associated to this dead time depends on the half-life of the nucleus. A fraction $1 - e^{-\frac{DT \ln(2)}{T_{1/2}}}$ of the decay events is lost during the dead time. The smaller the half-life is, the greater is the loss of events. This dead time correction is thus crucial for short-lived nuclei as $^{67}$Kr or $^{63}$Se, because one can lose up to 20% of the events with a half-life lower than 10 ms. In order to avoid rate-dependent dead-time contributions due to the electronics processing of the implantation, events between 0 and 1.5 ms after implantation are excluded from the energy spectra.

## 3.6   Determination of half-lives and proton branching ratios

The half-life and the proton branching ratio of a nucleus are determined from the time spectra presented in section 3.4.2. $\beta$ and $\beta p$ decays are the only possible decays which can be observed in this experiment. The typical decay chain is represented in figure 3.16, a nucleus $^{A}_{Z}X_{N}$ of half-life $T^{1}_{1/2}$ decays by $\beta$ decay to a nucleus $^{A}_{Z-1}X_{N+1}$ and by $\beta p$ emission to $^{A-1}_{Z-2}X_{N+1}$ with a proton branching ratio $P_{p1}$. The daughters can also decay by $\beta$ or $\beta p$ decay and have respectively the proton branching ratios $P_{p2}$ and $P_{p3}$.

This scheme enables the calculation of the decay function that is used for the fit of the half-life. The contribution of the daughters is estimated from the computation of the proton

Figure 3.16: Typical decay chain for a proton-rich nucleus $^A_ZX_N$. Except if it is a direct proton emitter ($p$ or $2p$), $\beta$ and $\beta p$ decays dominate. The corresponding daughters can decay also via the same processes. To fit the decay curve, it is necessary to take into account the entire filiation. In all the cases studied in the following, $^{A-1}_{Z-3}X_{N+2}$ and $^A_{Z-2}X_{N+2}$ have very long half-lives so they are negligible in the decay equation. $P_{p1}$, $P_{p2}$ and $P_{p3}$ are the proton branching ratios for the corresponding nuclei.

branching ratio and the $\beta$-detection efficiency. These latter are detailed in this section. An add back was implemented to solve issues of the calculations of proton branching ratios.

### 3.6.1 Half-life estimate

For the half-life fit, the daughters of $^A_{Z-1}X_{N+1}$ and $^{A-1}_{Z-2}X_{N+1}$ do not required to be taken into account because their half-lives are long compared to the duration of correlation (2 s) and the half-life of the studied nucleus. Indeed their half-lives are higher than a few tens seconds. Considering the decay chain presented previously in figure 3.16, the decay rates of $^A_ZX_N$, $^{A-1}_{Z-2}X_{N+1}$ and $^A_{Z-1}X_{N+1}$ nuclei behave as:

$$\begin{cases} \frac{dN_1}{\lambda_1 dt}(t) = -N_1(t) \\ \frac{dN_2}{\lambda_2 dt}(t) = -N_2(t) + N_1(t) \\ \frac{dN_3}{\lambda_3 dt}(t) = -N_3(t) + N_1(t) \end{cases} \quad (3.29)$$

The contributions of the three nuclei are present in a time spectrum. The total count rate fitting the spectrum is $N(t) = N_1(t) + N_2(t) + N_3(t)$. Each contribution is given by the solution of a Bateman equation [Bat10] with a daughter fed by a single mother nucleus. We assume that at time $t = 0$ there are no daughter nuclei produced and the decay rates $N_2(0)$ and $N_3(0)$ are equal to zero. Thus the evolution in time of the decay rate is:

$$N(t) = \lambda_1 \left[ N_1^0 e^{-\lambda_1 t} + N_2^0 (e^{-\lambda_2 t} - e^{-\lambda_1 t}) + N_3^0 (e^{-\lambda_3 t} - e^{-\lambda_1 t}) + N_{\text{bg}} \right] \quad (3.30)$$

with $\lambda_1 = \frac{\ln 2}{T^1_{1/2}}$, $\lambda_2 = \frac{\ln 2}{T^2_{1/2}}$, $\lambda_3 = \frac{\ln 2}{T^3_{1/2}}$ and $N_{\text{bg}}$ a constant for the background.

The disintegration rates at time $t = 0$, $N_1^0$, $N_2^0$ and $N_3^0$ require to consider the probabilities of detecting the $\beta$ particles and the protons. Thus $N_1$, $N_2$ and $N_3$ are expressed as

$$\begin{cases} N_1^0 = N_0' \\ N_2^0 = N_0' \frac{\lambda_2}{\lambda_1 - \lambda_2} \frac{P_{p1}\varepsilon_p(P_{p2}\varepsilon_p + (1-P_{p2})\varepsilon_\beta)}{P_{p1}\varepsilon_p + (1-P_{p1})\varepsilon_\beta} \\ N_3^0 = N_0' \frac{\lambda_3}{\lambda_1 - \lambda_3} \frac{(1-P_{p1})\varepsilon_\beta(P_{p3}\varepsilon_p + (1-P_{p3})\varepsilon_\beta)}{P_{p1}\varepsilon_p + (1-P_{p1})\varepsilon_\beta} \end{cases} \quad (3.31)$$

$\varepsilon_p$ is the proton detection efficiency. With a thickness of 1 mm for each DSSSD, the detection efficiency of protons is assumed to be 100% in this analysis (protons of 11 MeV have a range of 1 mm [Sup09]). That is not the case for $\beta$ particles which have a longer range in silicon (1 mm for 520 keV [Sup09]). Their detection efficiency is not 100% and has to be determined experimentally (cf. section 3.6.2 for details). $N_0'$ is the number of detected decays of $^A_Z X_N$ at time 0 (extracted from the fit of the time distribution). $N_0$ is the number of the nuclei $^A_Z X_N$ which actually decay but they are not all detected. To evaluate the numbers $N_2^0$ and $N_3^0$, one has $N_0 = \frac{N_0'}{P_{p1}\varepsilon_p + (1-P_{p1})\varepsilon_\beta}$ to take into account the decays which are not detected.
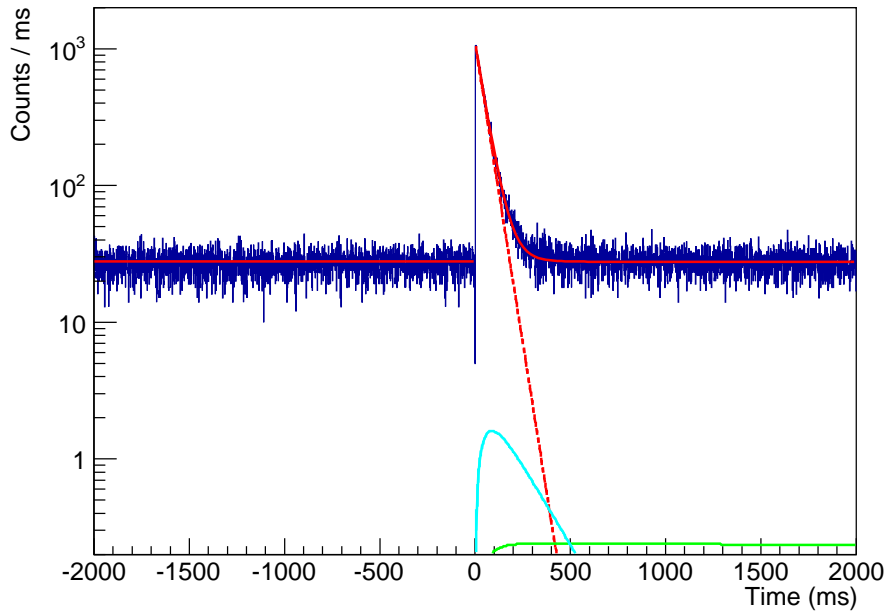


Figure 3.17: Half-life fit of $^{65}$Se. The result is the red curve. The dashed red curve is the decay component of $^{65}$Se. The contribution of the $\beta$ decay daughter $^{65}$As ($T_{1/2} = 128$ ms) is represented by the blue curve. The $\beta p$ daughter $^{64}$Ge ($T_{1/2} = 63.7$ s) is the green curve.
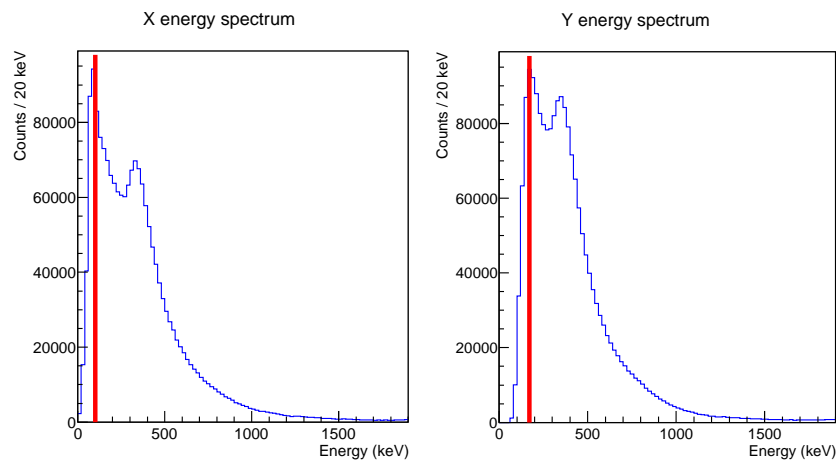


Figure 3.18: Software threshold applied to energy spectra to generate the time distributions. This example shows the X and Y energy spectra of $^{61}$Ge with the software threshold illustrated by a vertical red line (100 keV for X, 150 keV for Y).

The background constant is extracted from a fit on the negative time part of the spectrum (this part of the spectrum is only composed of wrong correlations). The decay contributions of the mother and the daughters are fitted on the positive part. The half-lives of the daugh-

ters and proton branching ratios are fixed to avoid that contributions were overestimated or underestimated. The proton branching ratios of the daughters are taken from literature and the mother ones are computed from decay spectra as presented in section 3.6.3. An example of fit is shown in figure 3.17. To reduce the noise in the time spectra, these latter are generated from events with both X and Y energies above a threshold of 100 keV for X and 150 keV for Y. This threshold is fixed according to the noise peak of the energy spectra as it is illustrated for $^{61}$Ge in figure 3.18.

### 3.6.2   Beta-detection efficiency

The detection efficiency of $\beta$ particles ($\varepsilon_\beta$) is deduced from time spectra of known nuclei, only decaying by $\beta$ decay or with a negligible proton branching ratio. The same conditions as the time spectra for half-life measurements are used (X and Y energies above a given threshold). The time spectra are fitted by taking into account the daughter half-life and fixing it with the literature values. The decay of the other nuclei in the decay chain are negligible. The nuclei used and the daughter half-lives are summarised in table 3.5.

| Nucleus | $T_{1/2}$ | $T_{1/2}^{\text{daughter}}$ | $P_p$ (%) |
|---------|-----------|------------------------------|-----------|
| $^{56}$Cu | 93(3) ms | 6 d | 0 |
| $^{58}$Zn | 86.7(24) ms | 3.204(7) s | 0 |
| $^{60}$Ga | 70(13) ms | 2.38(5) min | 1.6(7) |
| $^{62}$Ge | 129(35) ms | 116.121(21) ms | 0 |
| $^{63}$Ge | 150(9) ms | 32.4(5) s | 0 |
| $^{65}$As | 128(16) ms | 30.9(5) s | 0 |
| $^{66}$As | 95.77(23) s | 2.26(6) h | 0 |
| $^{66}$Se | 42(12) ms | 95.77(23) ms | 0 |

Table 3.5: List of the chosen nuclei for the $\beta$-detection efficiency estimate. Data taken from [Ens17].
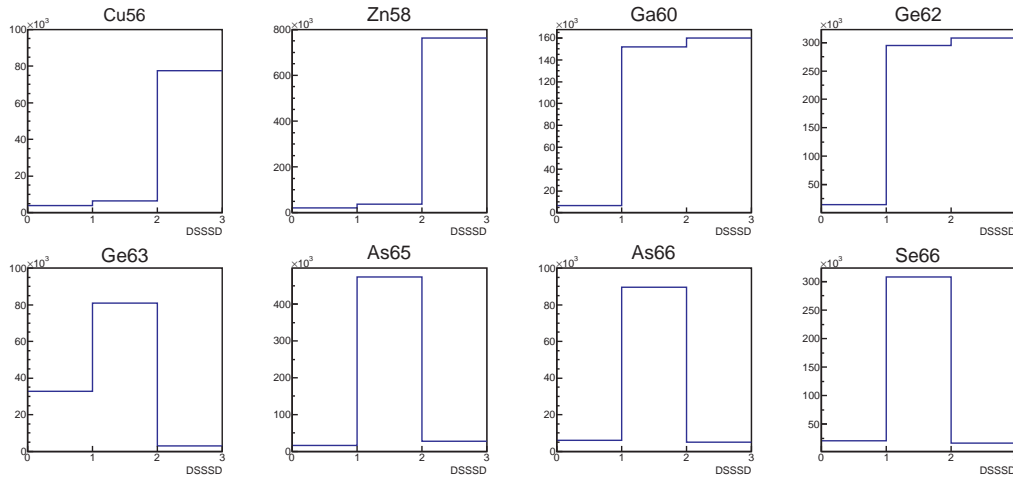


Figure 3.19: Distribution of the implantation events on the three DSSSD detectors for the nuclei used to evaluate the $\beta$-detection efficiency.

The efficiency $\varepsilon_\beta$ is the probability of detecting a $\beta$ particle from a decay in the same DSSSD as the implantation. This efficiency is hence equal to the number of detected $\beta$ decays $N_\beta$ divided by the number of implanted nuclei (for a given DSSSD). If the detection efficiency is 100%, one should detect a number of decays equal to the number of implantations. The fit procedure is performed by the function presented at the beginning of section 3.6 by taking into

account the contribution of the daughter. One has:

$$\begin{cases} \varepsilon_\beta = \frac{N_\beta}{N_{\text{imp}}} \\ \Delta\varepsilon_\beta = \frac{\Delta N_\beta}{N_{\text{imp}}} \end{cases} \qquad (3.32)$$

The discrepancy of the number of implantation events can be very high between the detectors. As illustrated in figure 3.19, the considered $\beta$ emitters are mainly implanted in the two last DSSSDs. The degrader at the entrance of the WAS3ABi setup was tuned to implant the most exotic nuclei in the first DSSSD. For $\varepsilon_\beta$ estimate, only $^{63}$Ge is implanted at an acceptable rate in the first DSSSD.

The computed efficiencies are highly dependent to the implantation profile. To compare them, the implantation barycentre of each nucleus is computed. As shown on the right plot of figure 3.20, the efficiency increases (and the uncertainty decreases) for the DSSSD with a higher number of implantations. The DSSSD0 which has the lowest number of implantations has computed efficiencies 2-3 times lower. A simulation was performed with the GEANT4 framework [Ago03]. A Gaussian implantation profile over the three DSSSDs for a nucleus (fit with three experimental points) was assumed and no such difference of efficiency was seen between the detectors.
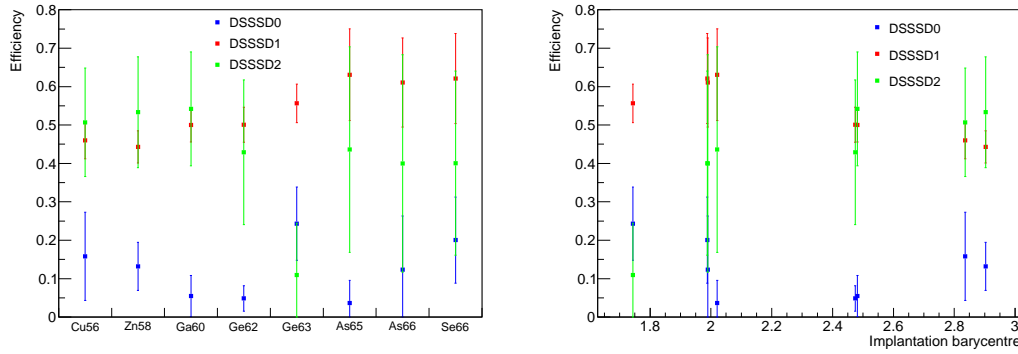


Figure 3.20: Estimated $\beta$-detection efficiency for each nucleus and DSSSD. The comparison between the nuclei is on the left plot. The plot on the right shows the efficiency as a function of the implantation barycentre of the nucleus. The uncertainties are multiplied by the square root of the $\chi^2$ value of the corresponding DSSSD.

The $\beta$-detection efficiency is evaluated for each DSSSD by the weighted average between the nuclei. The uncertainty is multiplied by the reduced $\chi^2$ value to take into account the large discrepancies between the nuclei (cf. appendix D for the values). The global $\beta$-detection efficiency for a DSSSD is estimated by:

$$\begin{cases} \varepsilon_\beta = \sqrt{\dfrac{\sum\limits_{i=1}^{N}\left(\dfrac{\varepsilon_i}{\Delta\varepsilon_i}\right)^2}{\sum\limits_{i=1}^{N}\dfrac{1}{(\Delta\varepsilon_i)^2}}} \\ \Delta\varepsilon_\beta = \sqrt{\dfrac{\chi^2}{N-1}\dfrac{1}{\sum\limits_{i=1}^{N}\dfrac{1}{(\Delta\varepsilon_i)^2}}} \end{cases} \qquad (3.33)$$

Here $N$ is the number of nuclei used for the computation (i.e. 8). The evaluated $\beta$-detection efficiencies are summarised in the table 3.6. The values of the two last DSSSDs are similar. They are calculated from high statistics time spectra. The value found for the first DSSSD is probably underestimated because no nucleus is in majority implanted in this latter. Thus they must be mostly implanted with a low depth in this DSSSD, leading to higher losses of counts. Nevertheless, others causes than the implantation profile may affect this result, and are not understood here. The $\beta$-detection efficiency of the first DSSSD (DSSSD 0) is not used in this

| DSSSD | $\varepsilon_\beta$ |
|-------|----------|
| 0 | 8(3)% |
| 1 | 50(2)% |
| 2 | 41(7)% |

Table 3.6: Estimated values of the $\beta$-detection efficiencies of WAS3ABi.

analysis. Only the most exotic nuclei are mostly implanted in the first detector: $^{69}$Kr, $^{68}$Kr and $^{67}$Kr which decay only by $\beta$-delayed or direct proton emission.

   This method is not completely rigorous since the uncertainties should be asymmetrical and estimated from a binomial statistical law (especially for the efficiencies close to zero), because the values of the efficiencies are bounded between 0 and 1. Regarding the values of the uncertainties corrected by the $\chi^2$ value, the changes of the results are negligible.

### 3.6.3   Proton branching ratio estimate

The proton branching ratio $P_p$ is estimated from a fit of the time spectrum of the given nucleus composed of events with energies above 1 MeV. Below this value, proton transitions are very unlikely and proton peaks can not be separated from the contribution of the $\beta$ decay branch (cf. figure 3.14 as an example). The number of decays in the spectrum is compared with the number of implantations $N_{\mathrm{imp}}$ for the given nucleus.

   Nevertheless, differences are seen between time distributions of X and Y strips. To solve this issue, an add-back procedure is implemented. Although $\beta$ particles have a mean energy loss of 400 keV, some events are seen above 1 MeV. This proportion has to be taken into account to correct the branching ratio and evaluate its uncertainty.

**Definition of the proton branching ratio**

The estimate of the proton branching ratio is obtained by the number of decay events above 1000 keV divided by the number of implantations of the nucleus:

$$\begin{cases} P_p = \frac{N_p}{N_{\mathrm{imp}}} \\ \Delta P_p = \frac{\Delta N_p}{N_{\mathrm{imp}}} \end{cases} \tag{3.34}$$

The number of proton decays $N_p$ is determined by a time spectrum composed of events above 1000 keV and $N_{\mathrm{imp}}$ is the number of identified ions implanted in the DSSSDs. The spectrum is fitted by an exponential decay and a background constant. No nucleus studied here has a $\beta p$ daughter with a proton branching ratio above 0.5%. Thus the daughters are not taken into account in the fits of the nuclei studied in this work. The integral value of the nucleus component of the fit function gives the value of $N_p$ and the associated uncertainty.

   The computed $N_p$ is biased because decay events are missed in the global dead time. A correction of this dead time has to be applied to $N_p$. $N_p$ is corrected by the global dead time as follow:

$$\begin{cases} N_p^{\mathrm{cor}} = \frac{N_p}{1-DT} \\ (\Delta N_p^{\mathrm{cor}})^2 = \frac{1}{(1-DT)^2}(\Delta N_p)^2 + \frac{N_p^2}{(1-DT)^4}(\Delta DT)^2 \end{cases} \tag{3.35}$$

This computation is done separately for every nucleus. The global dead time $DT$ has to take into account the implantation distribution over the different settings with different dead times, as presented in section 3.5. This dead time for a nucleus is defined as

$$\begin{cases} DT = \sum_i \frac{N_{imp}^i}{N_{imp}} DT^i \\ (\Delta DT)^2 = \sum_i \frac{(N_{imp}^i)^2}{N_{imp}^2}(\Delta DT^i)^2 \end{cases} \tag{3.36}$$

with $N_{imp}^i$ the number of implantations during the setting $i$, $DT^i$ the global dead time computed for this setting and its uncertainty $\Delta DT^i$ presented in section 3.5.

**Energy add back**

Many decay events have an energy value above thresholds on a side of the DSSSD but with noise on the implantation strip of the other side. To minimise the number of lost events in the proton branching ratio computation, an energy add back is used. Thus the branching ratio computation is the only part of the analysis using add-back energies. The energies of strips neighbouring to the implantation one $(+/-1)$ and above the energy threshold (100 keV for X, 150 keV for Y) are added. This enables the reduction of events for which the decay occurs between two strips. The results of the add back are illustrated in figure 3.21. The number of inter-strip events is reduced (more events are gathered near the $E_Y = E_X$ line) but still many events remain with a good energy on only one DSSSD side.
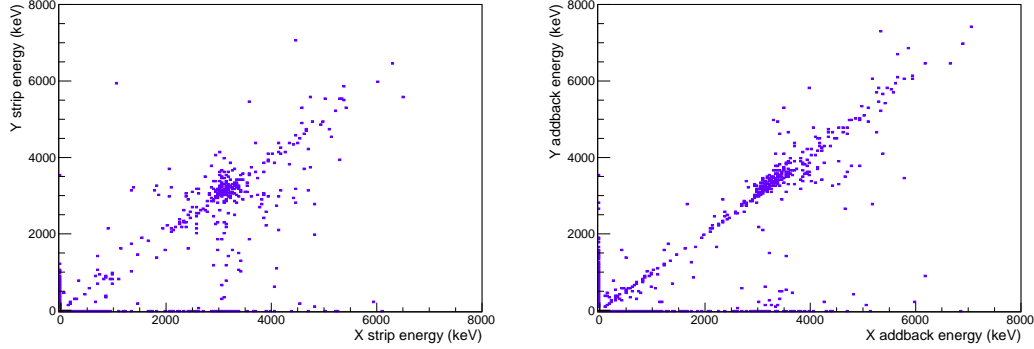


Figure 3.21: Bi-dimensional histogram of the X and Y decay energies correlated with $^{69}$Kr implantation events within a time window of 500 ms. The plot on the left is composed of the energies of the same strip as the implantation one. The plot on the right is composed of add-back energies.

The add back logically increases the background in the time spectra as it is shown in figure 3.22 especially for low energy events ($\beta$ particles). That is why the time spectra without add back will be used to estimate the half-lives for a better uncertainty.

The proton branching ratio estimates are improved by the add-back procedure. It improves the value found as it is shown in table 3.7 for the $^{69}$Kr. The values are found with the procedure described in section 3.6.3. As one can see in figure 3.21, many events remain with an X energy above 1 MeV and Y energy below. The fit of the time spectra with X or Y above 1 MeV increases the proton branching ratio. This latter is compatible with literature and 100%. This result is much more realistic since the $^{69}$Br is a proton-unbound nucleus. Nuclei with higher statistics (and thus lower uncertainties) are less sensible to the use of the add-back procedure.
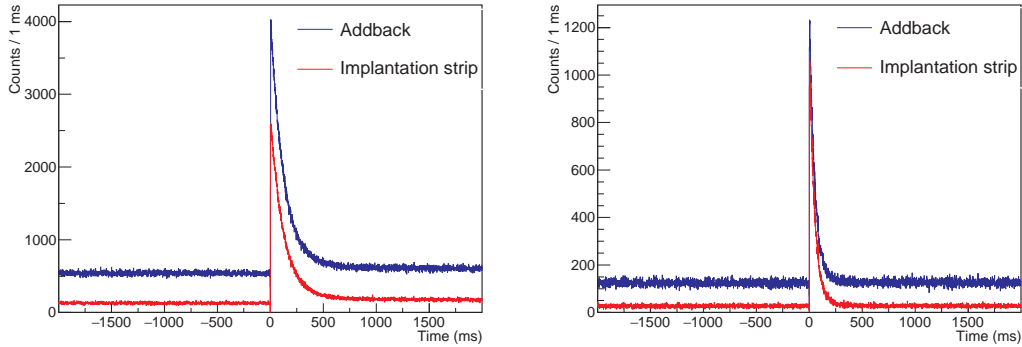


Figure 3.22: Comparison between the time spectra obtained with and without add-back procedure. These decay events have X and Y energies above their respective thresholds. The left plot is the time spectrum of $^{58}$Zn, a pure $\beta$ emitter. The plot on the right is the $^{65}$Se one, dominated by $\beta p$ decay.

| Correlation | $P_p$ | |
| --- | --- | --- |
| | Implantation strip | Addback |
| X and Y | 69(5)% | 73(5)% |
| X or Y | 88(5)% | 93(6)% |
| Lit. [Rog11b] | $99^{+1}_{-11}$% | |

Table 3.7: Proton branching ratio of $^{69}$Kr for various strip correlations. The values are extracted from the fit of the time spectra of the first DSSSD. These spectra are generated with events for which X and/or Y strip energies are above 1 MeV. The add-back and implantation strip energies are compared.

**Correction of the proton branching ratio**

The computation method of the proton branching ratio (equation 3.34) assumes that no $\beta$ particle deposes an energy higher than 1 MeV in the DSSSD. It was seen on energy spectra of $\beta$ emitters that there is a fraction $x$ of the $\beta$ particles with an energy loss above 1 MeV. Instead of measuring the number of protons $N_p$, we obtain a overestimated number $N_p + xN_\beta$ (contributions of daughters are neglected) with $xN_\beta$ the fraction of $\beta$ particles detected above 1 MeV. In fact, the measured proton branching ratio is

$$P_p^{\text{meas}} = \frac{N_p + xN_\beta}{N_{\text{imp}}} = P_p + x\left(1 - P_p\right) \tag{3.37}$$

with $P_p$ the true branching ratio without the high-energy $\beta$ particles. This latter can be expressed as a function of $P_p^{\text{meas}}$:

$$P_p = \frac{P_p^{\text{meas}} - x}{1 - x} \tag{3.38}$$

The ratio $x$ was estimated from the same nuclei as those used for the $\beta$-detection efficiency. The time spectra for add-back events (X or Y above 1 MeV) were fitted as for proton branching ratios. The daughters are also taken into account in the fit procedure. For a given nucleus and DSSSD, the ratio $x$ of the previous equations is the integral of the decay function divided by the number of implantations. As for the $\beta$-detection efficiency presented in section 3.6.2, the $x$ ratio is dependent on the implantation distribution and the DSSSD (cf. figure 3.23). Indeed for each nucleus, the ratio $x$ is higher for the DSSSD with the highest number of implantations. Because the nuclei used to estimate the $\beta$-detection efficiency and this ratio are mostly implanted in the two last DSSSDs, values for the first DSSSD are always underestimated.
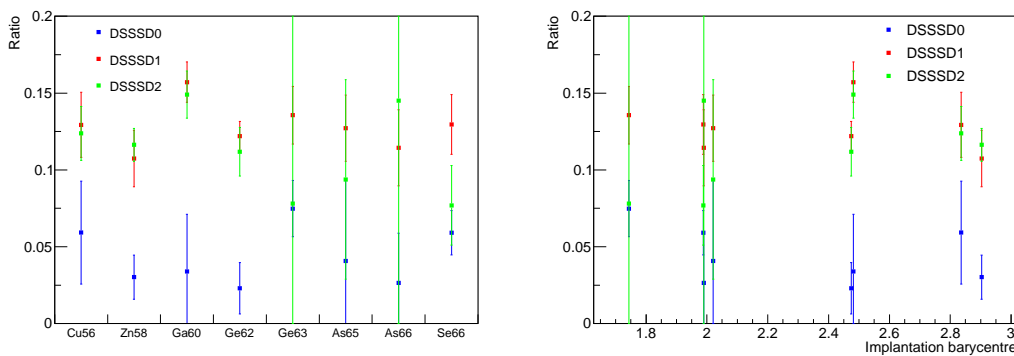


Figure 3.23: Estimated ratios of events above 1 MeV for nuclei decaying by $\beta$ radioactivity. The comparison between the nuclei is on the left. The plot on the right shows the ratio as a function of the implantation barycentre of the nucleus. The uncertainties are multiplied by the square root of the reduced $\chi^2$ value of the corresponding DSSSD.

The fraction $x$ of $\beta$ particles above 1 MeV was estimated as for the $\beta$-detection efficiencies by multiplying the uncertainty square root of the reduced $\chi^2$ to take into account the discrepancies

between the nuclei. The results found are presented in the table 3.8. As for the $\beta$-detection efficiency, the ratio of the first DSSSD is still difficult to estimate since only the most exotic nuclei are mainly implanted in it.

| DSSSD | Fraction of $\beta$ decay events $> 1$ MeV |
|-------|---------------------------------------------|
| 0     | 4.5(8)%                                      |
| 1     | 13.0(6)%                                     |
| 2     | 12.0(7)%                                     |

Table 3.8: Estimated fraction of $\beta$ decay events above 1 MeV with WAS3ABi add back.

One has to notice that this correction is not applied on values compared in table 3.7. Nevertheless the correction is negligible for nuclei which have a high total proton branching ratio above 80-90%, as $^{69}$Kr, because they are dominated by $\beta$-delayed proton decay.

## 3.7   Study of the proton peaks

The energy peaks originating from the $\beta$-delayed emission of protons were fitted to study the energy and the absolute branching ratio of the proton transitions. Because X strips saturate at around 3 MeV, all the fits are performed on Y-strip energy spectra. All spectra presented in chapter 4, except for the 2p candidates, are composed of the energies of Y strips only.

As presented in chapter 1, the energy peak of a $\beta$-delayed proton decay is a summation of the proton energy deposit and the $\beta$ particle energy loss contributions of the $\beta$ particle and the proton. The energy distribution of the peak is fitted by a Gauss function for the proton contribution, and a tail for the contribution of $\beta$ particles (pileup). The function used for the fits is:

$$f(E) = Ae^{-\frac{(E-\mu)^2}{2\sigma^2}} * e^{-\frac{E}{p\sigma}} \tag{3.39}$$

where $E$ is the energy released by the decay in the DSSSD and $p$ the tail parameter for the $\beta$-particle pileup. In this function, the proton energy of the peak is the value of $\mu$. This latter is the one referenced in literature. Because the spectrum is cleaned from background events, the background should be zero. A constant background or no background is used for the fit in order to extract the number of counts in the peak. The squared total uncertainty on the proton energy is obtained by adding the squares of the statistical uncertainty and the calibration uncertainty. All the parameters of the fit function are free. For the tail parameter, it is better to fix it for low-statistics peaks otherwise the fit does not converge or the resulting values are abnormal. All the uncertainties obtained from the fit are multiplied by $\sqrt{\chi^2/ndf}$ when the $\chi^2/ndf$ value is greater than 1.

The absolute branching ratio of a proton peak is the integral of the fit function divided by the number of implantation events. This number has to be corrected from the global dead time fraction of the acquisition as it is presented in section 3.6.3 for the branching ratio. The branching ratio (also named intensity) of a peak is

$$\begin{cases} I_p = \frac{N_p}{(1-DT)N_{\text{imp}}} \\ (\Delta I_p)^2 = \frac{1}{(1-DT)^2 N_{\text{imp}}^2}(\Delta N_p)^2 + \frac{N_p}{(1-DT)^4 N_{\text{imp}}^2}(\Delta DT)^2 \end{cases} \tag{3.40}$$

Moreover, the branching ratio above has to be corrected from the dead time per event presented in section 3.5. For half-lives below 10 ms, as $^{67}$Kr, losses reach 20%, but for half-lives around 30-40 ms, as $^{61}$Ge or $^{57}$Zn, 2-3% of decay events are lost. This correction is applied on the peaks presented in chapter 4, by using the $\beta$-delayed proton decay half-life (extracted from time-distribution fits used to estimate the total proton branching ratios).

# Chapter 4

# Results

This chapter is dedicated to the results obtained from the analysis of the RIBF4R1 experiment. The identifications were performed using the procedure described in chapter 2. The first indirect observation of the $^{67}$Kr 2p radioactivity is discussed here and compared with the calculations of the di-proton and three-body models.

The second aspect of the results is dedicated to $\beta$-delayed proton emitters with the two others 2p candidates, $^{59}$Ge and $^{63}$Se, for which no evidence of 2p decay was found but a measurement of their half-life was carried out for the first time. The first observation of the decay of $^{68}$Kr is reported. A new study of the decay of the $T_z = -\frac{3}{2}$ nuclei $^{69}$Kr, $^{65}$Se, $^{61}$Ge and $^{57}$Zn is also presented with new estimates of proton branching ratios and the half-lives.

New half-life measurements of exotic $\beta$ emitters, $^{55}$Cu, $^{56}$Cu, $^{60}$Ga, $^{63}$Ge, $^{64}$As and $^{65}$As, are also reported. A better measurement of these nuclei and the $\beta p$ emitters cited above have a direct effect on $rp$-process calculations.

The analysis of these nuclei is performed according to the procedure presented in chapter 3. However, some aspects of the analysis are different for the three 2p candidates $^{59}$Ge, $^{63}$Se and $^{67}$Kr because their analysis was performed prior to the analysis of the other $\beta$ and $\beta$-delayed proton emitters.

## 4.1    Identification results

Figure 4.1 shows the identification plot resulting from the RIBF4R1 experiment. It clearly indicates the successful production of many exotic nuclei, including the 2p candidates.

$^{59}$Ge was produced for the second time following the first identification by [Cie15] with only four counts. In the RIBF4R1 experiment, 1221 $^{59}$Ge were identified at the focal plane F7. The other 2p candidates $^{63}$Se and $^{67}$Kr were produced and identified for the first time with respectively 348 and 82 counts at F7. $^{68}$Kr was also measured for the first time with 479 counts at F7. Before [Cie15] and the RIBF4R1 experiment, the most exotic nuclei known in this mass region were $^{60}$Ge, $^{64}$Se [Sto05] and $^{69}$Kr [Bla95]. The work of [Cie15] enabled to reach the proton drip line at $Z = 32$. With the discovery of new Kr and Se isotopes at RIBF, the proton drip line was reached for $Z = 34$ and 36. These results are reported in [Bla16]. One sees on the plot (figure 4.1) the other nuclei presented in this chapter, the $T_z = -\frac{3}{2}$ nuclei and the $\beta$ emitters $^{56}$Cu, $^{60}$Ga, $^{63}$Ge, $^{64}$As and $^{65}$As.

The last setting of the experiment, optimised for $^{62}$Se production (cf. section 2.5), was dedicated to the investigation of the $^{58}$Ge and $^{62}$Se isotopes. As can be seen in figure 4.1, these isotopes could not be identified probably to their short predicted half-life in conjunction to the time of flight of BigRIPS (410 ns) [Bla16]. This aspect of the experiment will not be discussed here, to focus on the results of $^{67}$Kr and the less exotic nuclei noted in figure 4.1.

The transmission between F7 and F11 was about 90% because of the losses in the ZeroDegree Spectrometer. Less than 50% of the identified fragments at F7 were successfully implanted in the silicon detectors of WAS3ABi. The degrader located before WAS3ABi was tuned to optimise the implantation in the three DSSSDs. Because a large number of different isotopes (more or less exotic) had to be covered for the campaign, high losses were inevitable.
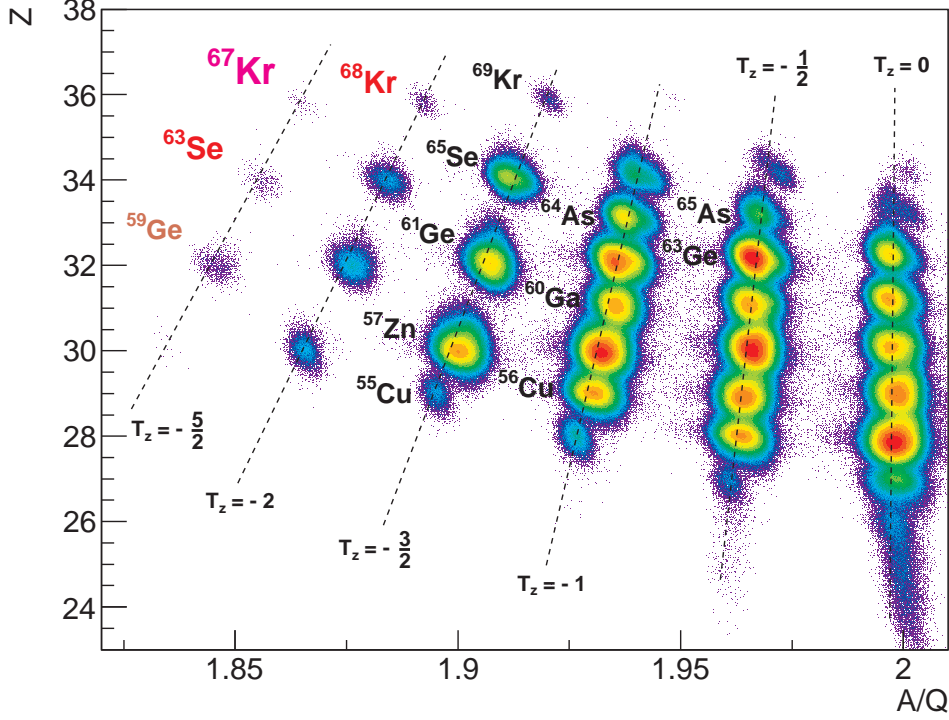
Figure 4.1: Z versus A/Q plot given by the BigRIPS identification procedure of the RIBF4R1 experiment. Each dashed line gathers nuclei of the same isospin projection $T_z$. The newly discovered 2p emitter $^{67}$Kr is notified in purple. This latter and the nuclei $^{63}$Se and $^{68}$Kr were produced and identified for the first time. $^{59}$Ge was produced and identified for the second time after [Cie15]. The isotopes of the $T_z = -\frac{3}{2}$ line ($^{69}$Kr, $^{65}$Se, $^{61}$Ge, $^{57}$Zn and $^{55}$Cu), $^{56}$Cu, $^{60}$Ga, $^{63}$Ge, $^{64}$As and $^{65}$As are also discussed in this work. The other nuclei of the $T_z = -2$ line are not presented here, they are analysed by other members of the collaboration.

## 4.2 $^{67}$Kr two-proton radioactivity

As already mentioned, $^{67}$Kr was implanted in the two first DSSSDs of WAS3ABi. From the 36 implantation events, 21 nuclei were found in the first DSSSD and 15 in the second one. The nuclei were produced with the $^{65}$Br and $^{64}$Se settings, the details are given in table 4.1.

| Setting | F7 | DSSSD 0 | DSSSD 1 | DSSSD 2 |
|---|---|---|---|---|
| B ($^{65}$Br) | 72 | 18 | 15 | 0 |
| C ($^{64}$Se) | 10 | 3 | 0 | 0 |
| Total | 82 | 21 | 15 | 0 |

Table 4.1: Identification and implantation distributions of the $^{67}$Kr nuclei. They were produced with the two settings B and C optimised for $^{65}$Br and $^{64}$Se production, respectively.

From the decay events correlated with these implantations over a time window of 100 ms we obtain the energy and time spectra. The properties and the decay scheme are presented here.

### 4.2.1 Decay energy

The energy spectrum of $^{67}$Kr was obtained by correlating all the decay events subsequent to an implantation, both on X and Y sides. Some decays were missed on X or Y because the right decay is in a strip contiguous to the implantation one (thus not correlated) or one side of the DSSSD that did not fire. To overcome this problem and obtain a spectrum with a maximum number of correlated decay events, the maximum energy between the X and Y strip ones is

taken. Thus we keep events with an inter-strip decay or a signal below the ADC threshold on one of the DSSSD sides. Moreover it is required for each event that the veto plastic scintillator does not saturate to avoid signals induced by high energy particles or ions crossing the DSSSDs.

The signal threshold was set above 200 keV in at least one of the neighbouring DSSSD or in the veto scintillator in order to discriminate the $\beta$-delayed proton events from direct proton emission (the $\beta$ particles escape from the detector most of the time). The two resulting spectra are shown in figure 4.2, one with the condition mentioned above (red curve) and the other without this condition (blue curve).
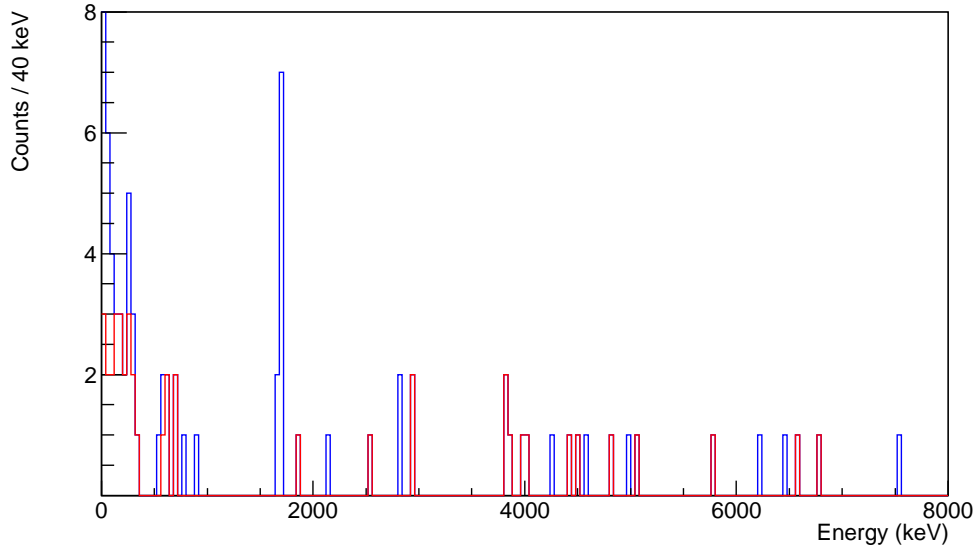


Figure 4.2: Energy spectrum of $^{67}$Kr decay events correlated with implantation events over a time gate of 100 ms. The blue spectrum is the distribution of events without any condition on the neighbouring detectors except the non-saturation of the veto scintillator. The red one shows events with a coincident signal in at least one of the other DSSSDs or the veto scintillator. For this curve, a $\beta$ particle is detected and the event is due to a $\beta$-delayed proton emission. The prominent peak at 1690(17) keV is exempt of $\beta$-particle coincidence and assigned to the 2p decay of $^{67}$Kr.

One notices a narrow peak without coincident events in the neighbouring detectors. The energy corresponds to the expected $Q_{2p}$ value, around 1.7 MeV according to theoretical predictions (cf. details in section 4.2.4). Moreover, no $\beta$ particle was observed in coincidence with this peak and, this peak is very sharp contrary to $\beta p$ decay peaks which are broadened because of the contribution of the $\beta$ particles.

The spectrum of the events registered in the neighbouring DSSSDs for those outside the supposed 2p peak is compared with the spectrum obtained under the same conditions for the 3220-keV peak of the well-known $\beta p$ emitter $^{61}$Ge (cf. figure 4.3). One notices that the shapes of the two spectra are similar. The probability of missing all the $\beta$ particles of this peak was evaluated with the 3220-keV and the 3510-keV peaks of the $\beta p$ emitters $^{61}$Ge and $^{65}$Se, respectively. For decay events of each DSSSD, the percentage of counts above 200 keV (the maximum energy of the DSSSD has to be above this threshold) in each neighbouring detector was evaluated, for both the X and Y sides. The average result is a $\beta$-detection efficiency in the neighbouring detectors of 53(1)%, 92(1)% and 51(1)% for the decay events in the first, second and third DSSSD, respectively. According to the distribution of the events of the peak (in table 4.2), 3 events in DSSSD1 and 6 in DSSSD0, the $\beta$-detection efficiency is 67(1)% for this peak. Thus, the probability of missing all $\beta$ particles of the 9 events of the peak is smaller than $5.5 \times 10^{-6}$.

In addition, if the decay is not a direct proton emission, a $\beta$-delayed proton decay happens with a positron emitted. In this case, two $\gamma$ rays (511 keV) from the positron anihilation are emitted and may be observed. Here, no 511-keV $\gamma$ ray from electron-positron annihilation was

seen in coincidence with the peak at 1.7 MeV. Its detection efficiency is 12% at 511 keV (cf. section 3.2). It leads to a probability of 8% of missing all annihilations. From these evidences, we undoubtedly claim that $^{67}$Kr is a new ground-state 2p emitter.
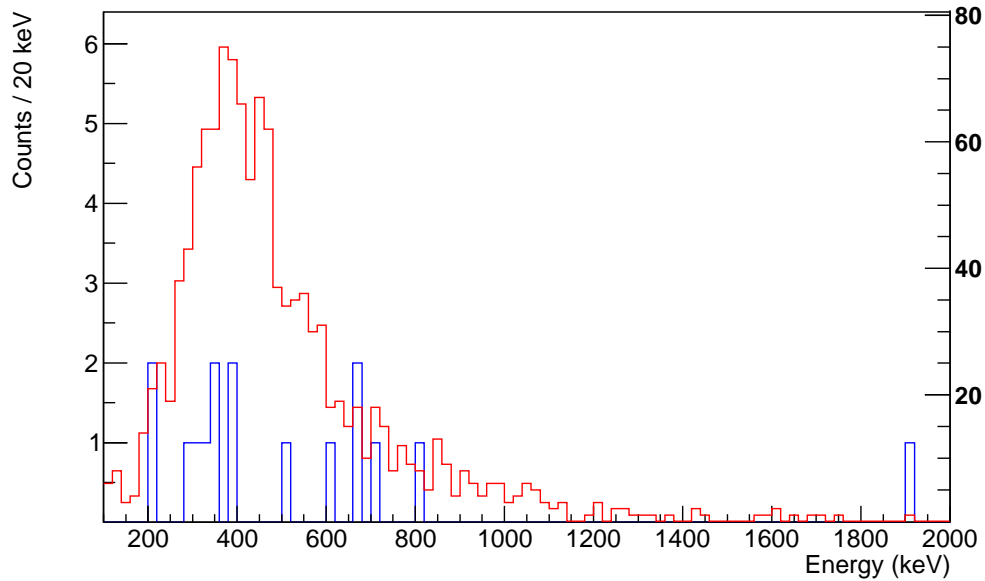


Figure 4.3:  Maximum energy of the neighbouring DSSSDs for the decay events.  This blue distribution (left axis labels) is obtained from the proton events above 1 MeV outside the 2p peak of $^{67}$Kr. The red one (right axis labels) is produced from events inside the peak of $^{61}$Ge at 3220 keV (3100-3600 keV gate). It shows that the events of $^{67}$Kr outside the 1.7-MeV peak are $\beta$-delayed proton emissions. The same shape of the $^{61}$Ge curve (red) proves the consistency of the method.

The details of the events of the 2p peak are gathered in table 4.2. One sees that sometimes, one of the decay energies of the implantation strips is abnormal or missing (X or Y). Moreover, some decay events are in the neighbouring strip to the implantation one as shows the position of the strip with the maximum energy of the DSSSD. The energy taken for the spectrum of figure 4.2 is the maximum between the X and Y energies of the strips.  The arithmetical average of the energies of the peak events is 1694 keV. The Y energies were found in average around 8 keV greater than the X ones. 4 keV are retrieved to the value of 1694 keV to take into account this effect. The standard deviation of the peak energies is 16 keV, and the calibration uncertainty is 5 keV at 1690 keV. The total uncertainty is thus 17 keV. The reference energy of the peak is 1690(17) keV.

### 4.2.2  Two-proton branching ratio

The 2p branching ratio of $^{67}$Kr is simply the number of counts belonging to the 2p peak (9 events), divided by the number of $^{67}$Kr implantation events (36 events). Besides, the number of measured 2p events has to be corrected for the dead times presented in section 3.5. With the distribution of the implantation events over the $^{65}$Br and $^{64}$Se settings, we computed a global dead time of 22(2)%. The number of decays corrected by the global dead time is 11.5(39) events instead of 9 observed.

The dead time per event (due to the processing of the implantation event) of 1.5 ms is also taken into account.  To correct the branching ration from it, the 2p half-life extracted from the fit of the time spectrum composed of the events of the 1690-keV peak is used, 6.5(33) ms (discussed in the next section 4.2.3). The loss factor due to the dead time per event is $13^{+8}_{-3}\%$. One finally obtains 13.3(45) events. The 2p branching ratio is thus estimated to 37(14)%.

| DSSSD | X side | | | | Y side | | | | Time (ms) |
| | Imp. strip | | Max. strip | | Imp. strip | | Max. strip | | |
| | Pos. | Energy | Pos. | Energy | Pos. | Energy | Pos. | Energy | |
|---|---|---|---|---|---|---|---|---|---|
| 0 | 36 | 1662 | 36 | 1662 | 12 | - | - | - | 2.90 |
| 0 | 42 | 1678 | 42 | 1678 | 28 | 1668 | 28 | 1668 | 22.71 |
| 0 | 28 | 1699 | 28 | 1699 | 22 | 1688 | 22 | 1688 | 10.44 |
| 0 | 18 | 1251 | 18 | 1251 | 19 | 1693 | 19 | 1693 | 8.17 |
| 0 | 39 | 1670 | 39 | 1670 | 34 | 1697 | 34 | 1697 | 4.71 |
| 0 | 34 | 1720 | 34 | 1720 | 23 | - | 38 | 85 | 23.84 |
| 1 | 17 | 1707 | 17 | 1707 | 24 | 1246 | 24 | 1246 | 5.64 |
| 1 | 20 | 1695 | 20 | 1695 | 15 | 1687 | 15 | 1687 | 5.94 |
| 1 | 26 | 40 | 25 | 1682 | 21 | 1691 | 21 | 1691 | 5.56 |

Table 4.2: Decay events of the $^{67}$Kr 2p peak (1.7 MeV). The energies (in keV) of the implantation strip and the strip with the highest decay signal in the DSSSD are listed. An absence of value means the coder value was below the threshold (TDC for implantation or ADC for decay events).

### 4.2.3   Half-life

The half-life was estimated with the time distribution of the events above 1 MeV and from the 2p peak alone. The threshold at 1 MeV excludes the $\beta$ particles which have a mean energy of 400 keV in the detector (see section 3.6.3) and decreases the background in the time distribution. Indeed $^{67}$Kr can only decay by 2p radioactivity to $^{65}$Se or by $\beta$ decay to the proton-unbound nucleus $^{67}$Br ($S_p = -1581$ keV [Ens17]). Thus the only possible decays are via proton emission. The schematic decay scenario is represented in figure 4.4.
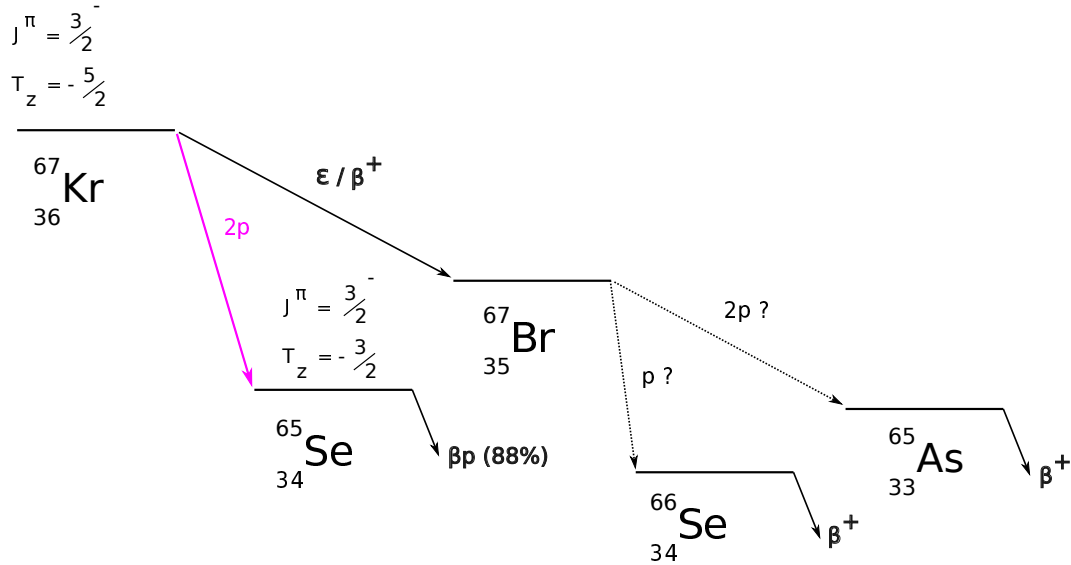


Figure 4.4: Proposed decay scheme for $^{67}$Kr. The 2p branch decays to $^{65}$Se that have a half-life of 33(4) ms and a $\beta$-delayed proton branching ratio of $88^{+12}_{-13}\%$ [Rog11b]. The other possible decay is the $\beta$ decay to proton-unbound $^{67}$Br leading to a delayed proton emission. The $\beta p$ daughter $^{66}$Se is a $\beta$ emitter [Rog14]. The $\beta xp$ ($x > 1$) daughters have too long half-lives to be taken into account in our analysis.

Two time spectra are represented in figure 4.5. The first is composed of all events above 1 MeV and the second is composed only of the events belonging to the 2p peak. They are fitted with an exponential function and a constant background by a likelihood minimisation method. The fit limits are 3 ms and 100 ms. The half-life from the fit of the 2p events curve (right plot in figure 4.5) is found to be 6.5(33) ms. Because there is a very poor statistics here (9 events), the fit method developed by K.-H. Schmidt [Sch84] was also used for the 2p events. This method

proposes to compute the lifetime by:

$$\begin{cases} \tau = \frac{1}{n}\sum_{i=1}^{n}(t_i - DT) \\ \tau_u = \frac{\tau}{1-n^{-\frac{1}{2}}} \\ \tau_l = \frac{\tau}{1+n^{-\frac{1}{2}}} \end{cases} \qquad (4.1)$$

where $\tau$ is the lifetime which is estimated as the average value the event times minus the 1.5-ms dead time, $n$ the number of events and $\tau_{u/l}$ the high and low uncertainty bounds of the estimation. The computed half-life by this method is found to be $5.9^{+3.0}_{-1.5}$ ms, a value consistent with the previous one.

The total half-life was estimated from the time spectrum on the left in figure 4.5. We take into account the 2p daughter $^{65}$Se with a half-life of 33 ms [Rog11b] and the 2p branching ratio of 37%. We assume a proton detection efficiency of 100% and the spectrum with the 1-MeV cut to avoid to deal with $\beta$ decays of the daughters. The decay rate is fitted by the equation

$$N(t) = \lambda_{\text{Kr}} N_0^{\text{Kr}} e^{-\lambda_{\text{Kr}}t} + P_{2p} N_0^{\text{Kr}} \frac{\lambda_{\text{Kr}}\lambda_{\text{Se}}}{\lambda_{\text{Kr}} - \lambda_{\text{Se}}} (e^{-\lambda_{\text{Se}}t} - e^{-\lambda_{\text{Kr}}t}) + B \qquad (4.2)$$

with $N_0^{\text{Kr}}$ the total number of $^{67}$Kr decays in the spectrum, $P_{2p}$ the 2p branching ratio of $^{67}$Kr, $B$ the background constant and $\lambda$ the decay constants. The half-life found by the fit procedure is 7.4(29) ms. A dispersion of 0.65 ms was found on the results due to the upper fit limit when it moves from 90 to 110 ms. By adding it as a systematic uncertainty, we propose 7.4(30) ms as a first half-life measurement of $^{67}$Kr. We adopt this value because it is a global half-life of $^{67}$Kr, considering all possible decay branches of $^{67}$Kr. With the branching ratio of 37(14)%, $^{67}$Kr has a partial 2p half-life $\frac{T_{1/2}}{P_{2p}} = 20(11)$ ms.
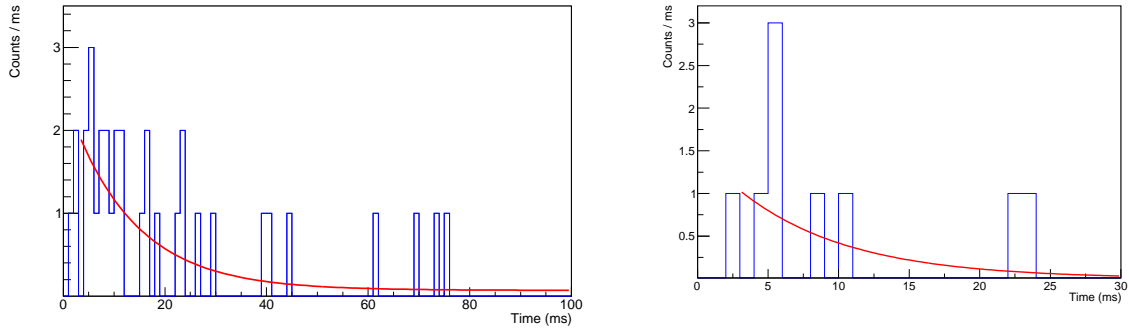


Figure 4.5: Time spectra of $^{67}$Kr. The distribution on the left is obtained from all correlated decays with an energy above 1 MeV. The right spectrum is exclusively composed of the events belonging to the 2p peak. The red curves are the results of the fits. The first 3 ms are excluded from the fits because of the acquisition dead time. 7.4(30) ms was found for the left spectrum, 6.5(33) ms for the peak-gated spectrum. The Schmidt method [Sch84] gives $5.9^{+3.0}_{-1.5}$ ms for the 2p events (spectrum on the right).

### 4.2.4   Comparison with theoretical models

The experimental half-life and $Q_{2p}$ values obtained for $^{67}$Kr are compared to the models to get information on the nuclear structure. We assume a $^{67}$Kr ground state with $J^{\pi} = \frac{3}{2}^{-}$, being the same as its mirror nucleus $^{67}$Ga. $^{67}$Kr decays to the ground state ($J^{\pi} = \frac{3}{2}^{-}$) of $^{65}$Se. As for the other 2p emitters, the valence protons are in the $pf$ shells. The valence shells related to proton emission are $1f_{5/2}$ and $2p_{3/2}$ for $^{67}$Kr (cf. figure 4.6). Depending on the $pf$ mixing configurations, our experimental result is compared to the half-lives calculated with the three-body and shell models. The decay energy is also compared to local mass model predictions.
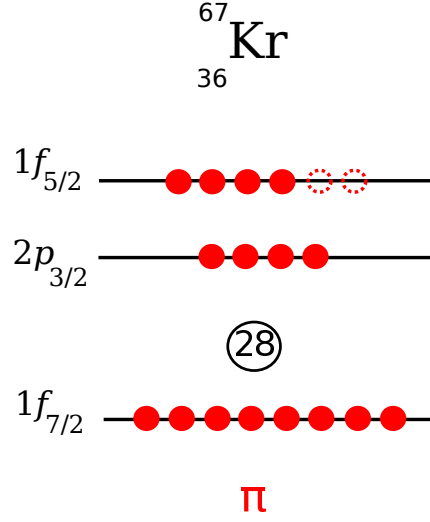
Figure 4.6: Proton shell occupancies for $^{67}$Kr in a simple shell model framework.
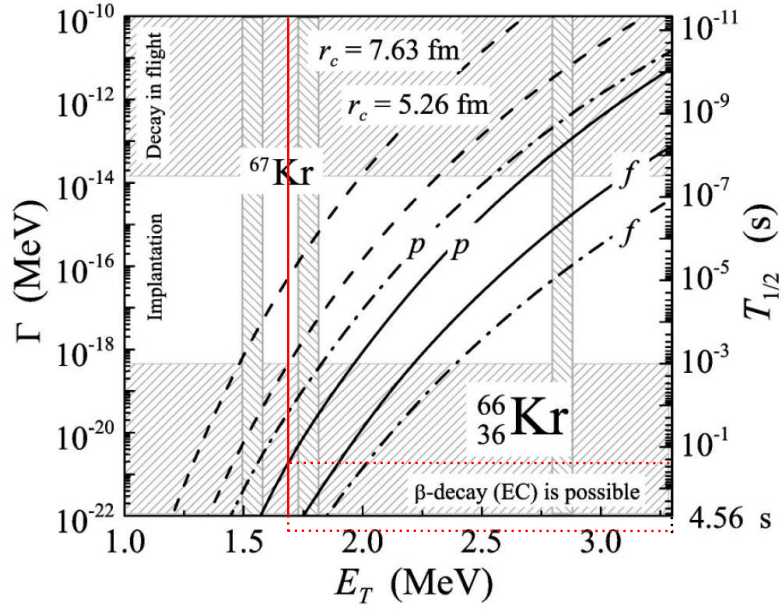


Figure 4.7: Half-life (decay width) versus decay energy of $^{66}$Kr according to the three-body calculations. Horizontal hatched areas represent lifetime regions with the accessible experimental techniques for 2p radioactivity study. The vertical hatched bands show the possible decay energies for $^{66}$Kr and $^{67}$Kr. The curves are the lifetime-energy correlations calculated for $^{66}$Kr, assumed to be the same as $^{67}$Kr. The solid curves correspond to a case of pure $l^2$ components. The dashed curves are the di-proton estimates with different channel radii. The dashed-dotted curves describe a simultaneous emission for different $l$ values. The vertical red line is the experimental $Q_{2p}$ value found in this work (1.7 MeV). The dashed red lines show the half-life values corresponding to the two half-life limits (the black solid curve $f$ had to be extrapolated). Taken from [Gri03].

The plot in figure 4.7 from [Gri03] provides the three-body model calculations for $^{66}$Kr, assumed to be the same as for $^{67}$Kr. The calculated half-life is 13.5 s for a pure $f^2$ configuration (extrapolation of the solid curve named $f$ on the plot) and 0.28 s for a pure $p^2$ configuration (solid curve named $p$ on the plot), at an energy of 1.690 MeV. There is a factor 14 between the smallest three-body half-life (280 ms) and the experimental partial 2p half-life (20(11) ms).

We correct the three-body half-lives with the shell model removal amplitudes as it was done for $^{45}$Fe in [Aud12] and $^{54}$Zn in [Asc11b]. Calculations with a 2p shell model GXPF1A Hamiltonian [Hon05] gave good results. The two-nucleon decay amplitudes for this transition are calculated in a $1p$-$0f$ shell-model space with up to two proton holes in $0f_{7/2}$ orbital. The calculated $L = 0$ 2p decay amplitudes are 0.156 for the $0f_{7/2}$, 0.820 for the $0f_{5/2}$, 0.419 for the $1p_{3/2}$ and 0.371 for the $1p_{1/2}$ orbitals (results given by B. A. Brown from NSCL). The $L = S = 0$ removal amplitudes are 0.655 and 0.556 for the $f^2$ and $p^2$ configurations respectively. The three-body half-lives presented above for $p^2$ and $f^2$ configurations are corrected by the decay amplitudes to calculate the "shell model corrected" half-lives $T_{1/2}(f^2) = 13.5/(0.655)^2 = 31$ s and $T_{1/2}(p^2) = 0.28/(0.556)^2 = 0.90$ s. Then the total half-life by adding coherently the two configurations is

$$\frac{1}{[T_{1/2}]^{\frac{1}{2}}} = \frac{1}{[T_{1/2}(f^2)]^{\frac{1}{2}}} + \frac{1}{[T_{1/2}(p^2)]^{\frac{1}{2}}} \tag{4.3}$$

leading to a half-life of 660 ms, a factor 30 greater than the experimental one (20 ms).

On the contrary, the $\beta$-decay partial half-life obtained with the $\beta$ branching ratio $1 - P_{2p} = 63(14)\%$, 10(6) ms is in accordance with the Gross theory [Jae14] (11.1 ms). It shows that our half-life and branching ratio measurements are consistent with $\beta$ decay calculations.

| $T_{1/2}$ (ms) | Exp. | 3-body $p^2$ | 3-body $f^2$ | Shell-mod. cor. | R matrix | Gross th. |
|---|---|---|---|---|---|---|
| 2p decay | 20(11) | 280 | 13500 | 660 | 2 | |
| $\beta$ decay | 10(6) | | | | | 11.1 |

Table 4.3: Experimental half-lives (in ms) for the different decay processes of $^{67}$Kr and the theoretical calculations given by the three-body model [Gri03], the GXPF1A shell model [Hon05] and the R-matrix [Orm97] model for proton emission, and the Gross theory for $\beta$ decay [Jae14].

Our experimental 2p half-life is in strong disagreement with the calculations. It was not the case for $^{45}$Fe [Aud12] and $^{54}$Zn [Asc11b]. For $^{67}$Kr, even if we compare with the smallest three-body value (see table 4.3) there is an overestimate of a factor 10. The R-matrix value calculated by Ormand [Orm97] (2 ms) underestimates with a factor 10.

A possible reason for this discrepancy could be the absence of deformation effects in calculations. The models used here consider spherical nuclei that is true for the emitters near the doubly-magic $^{48}$Ni, but $^{67}$Kr is in a region far from magic numbers where more deformation effects are expected. Indeed, calculations from FRDM (cf. [Mö16]) predict deformation in the mass region of $^{67}$Kr.

On the contrary to the half-life predictions, the experimental $Q_{2p}$ is in good agreement with the calculations as it is shown for values in table 4.4 and figure 1.15 of chapter 1.

| Sep. energy | [Bro02] | [Col99] | [Orm97] | Exp. (this work) |
|---|---|---|---|---|
| $S_p$ | $-0.05(14)$ | $0.017(53)$ | $0.155(288)$ | - |
| $S_{2p}$ | $-1.76(14)$ | $-1.779(98)$ | $-1.538(262)$ | $-1.690(17)$ |

Table 4.4: Theoretical and experimental proton separation energies of $^{67}$Kr (in MeV).

New three-body calculations of the $^{67}$Kr case were proposed by Grigorenko [Gri17]. They are based on an improved model of 2p decay developed by [Gol16]: the IDDM (improved direct decay model). This latter relies on R-matrix decay amplitudes and provides a description of the transition between direct and sequential 2p decay for $s$-$d$ shell nuclei. It studies the width of the ground-state resonance of the core+p subsystem. On figure 4.8 are compared calculations between IDDM (figure 4.8(a)) and the three-body model with two types of Woods-Saxon potential (P3 and P5 in figure 4.8(b), see [Gri17] for details). The variable $E_r$ is the resonance
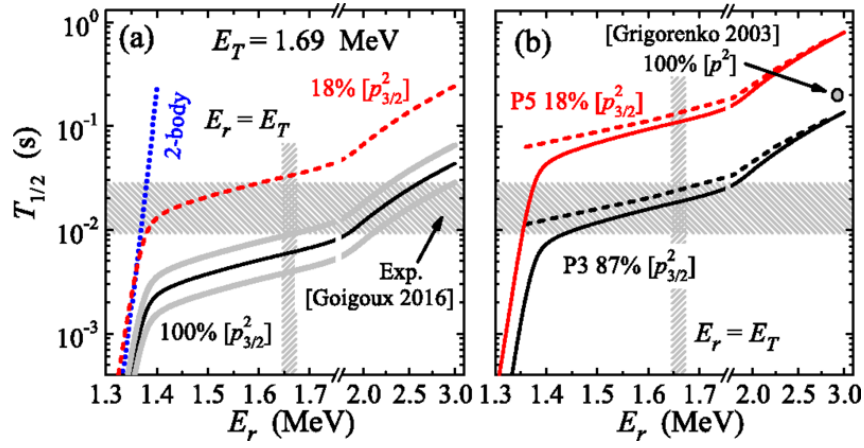
Figure 4.8: Correlation between lifetime and resonance energy in $^{66}$Br ($E_r$) for $^{67}$Kr 2p decay. A fixed decay energy of 1690 keV (experimental value) is used. Because the one-proton separation energy of $^{67}$Kr is close to zero, one can assume $E_r = E_T$. The part (a) of the figure shows calculations from IDDM for different $p^2$ configurations. The solid grey curves correspond to the black one with $\pm 0.5$ fm modified channel radius. The dotted blue line shows a two-body R-matrix estimate. The part (b) shows three-body calculations with different mixing configurations and Woods-Saxon potentials named P3 and P5 (not discussed here). The hatched areas are the experimental results presented in this PhD work. The calculation from [Gri03] is indicated by the grey dot. Taken from [Gri17].

energy of the $^{66}$Br+p system ($E_r = -S_p$ of $^{66}$Br). $E_T$ is the 2p decay energy of $^{67}$Kr, fixed to 1690 keV, the experimental value presented in this PhD work. According to shell model calculations from Brown [Goi16], a realistic mixing configuration for $^{67}$Kr is 18% of $p^2$ configuration. For example, the experimental values of the $p^2$ contribution in $^{45}$Fe (30(10)% [Mie07c]) and $^{54}$Zn ($30^{+33}_{-21}$% [Asc11b]) 2p decay are small. For a 18% of $p^2$ configuration in $^{67}$Kr 2p decay, the three-body model is in disagreement with the experimental value as the comparisons done previously in this section. The IDDM, better tuned phenomenologically to take into account low-lying states of $^{66}$Br, agrees in a narrower energy range with the experimental value. But this narrower range could indicate a "transitional dynamics" between true and sequential 2p decay according to [Gri17]. Moreover, one can notice on table 4.4 that the $S_p$ value of $^{67}$Kr could be weakly negative because of the large uncertainties on the predictions, making possible a sequential 2p decay.

The value of $E_r$ given by IDDM depends on the position of the $^{66}$Br ground state, i.e. the $S_p$ of $^{67}$Kr. Distribution of energy sharing between the two protons was calculated by [Gri17] with the IDDM for various $E_r$ values. If a dominance of $p^2$ configuration is assumed, model calculations are closer to the experimental results, the true 2p decay is expected for $E_r \in [1.45, 2.0]$ MeV ($^{67}$Kr $S_p \in [-240, 310]$ keV). The energy distribution between the two protons is composed of one peak in this case (black line in figure 4.9). If a 18% $p^2$ configuration mixing is assumed, a more realistic structure according to [Gri17], different decay possibilities are expected. $E_r \in [1.35, 1.42]$ MeV ($S_p \in [-340, -270]$ keV) values corresponds to a transitional dynamics on the borderline between true 2p and sequential 2p emission. A lower value of $E_r$ (higher value of $S_p$) gives a pure sequential decay, not compatible with the experimental value.

Further experiments with proton energy correlation measurements, as it was done for $^{45}$Fe [Mie07c] (cf. figure 1.14 in chapter 1) and $^{54}$Zn [Asc11b], could very simply clarify the nature of the 2p decay of $^{67}$Kr. The energy sharing between the two protons is different according to the decay. An energy distribution with two other peaks corresponds to a sequential 2p decay, with one central peak to a true 2p decay.
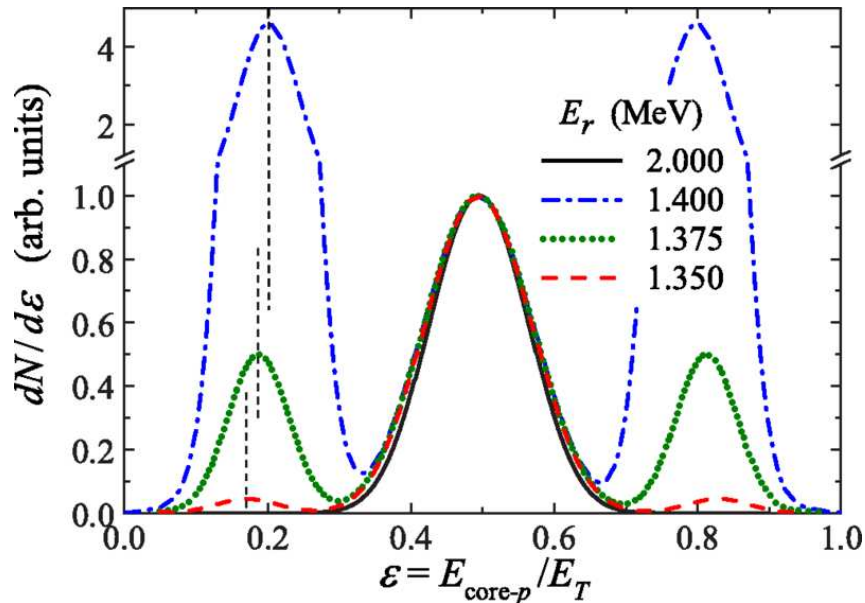
Figure 4.9: Example of energy correlations between the two protons of the $^{67}$Kr decay according to IDDM for different energy sharings between the two protons. Calculations were performed for different resonance energy values $E_r$ corresponding to different dynamics (see text). The vertical dashed lines are the centroids of the decay peaks. Taken from [Gri17].

## 4.3   Study of beta-delayed proton emitters

In the RIBF4R1 experiment, many other exotic nuclei near the proton drip-line were produced at high rates. At first the other 2p candidates, $^{63}$Se and $^{59}$Ge, are presented with an estimate of their half-lives. $^{68}$Kr decay was also observed for the first time with a first estimate of its proton branching ratio and half-life. New half-life and proton branching ratio values for the $T_z = -\frac{3}{2}$ nuclei $^{69}$Kr, $^{65}$Se, $^{61}$Ge and $^{57}$Zn are presented. The production and implantation statistics for these nuclei are gathered in table 4.5.

The decay structure analysis of the $\beta$-delayed proton emitters was performed by using the procedures presented in chapter 3. The energies and branching ratios of the identified proton peaks were computed as it is described in section 3.7 from the energy spectra subtracted from background by the method introduced in section 3.4.2. The half-lives were computed from distribution of the time difference between decays and implantations with the fit function in section 3.6 by estimating the $\beta$-detection efficiency and the total proton branching. It allows to fix all contributions of the daughters ($\beta$ and $\beta p$ decay) for the fit.

### 4.3.1   The 2p candidates $^{63}$Se and $^{59}$Ge

The most promising candidates for 2p radioactivity which were reached at RIBF are $^{67}$Kr, $^{63}$Se and $^{59}$Ge. The first was proven as a new 2p emitter (see section 4.2) while no evidence was found for the two other candidates. The possibility of a 2p decay is discussed here and their half-life measurements is presented.

#### $^{63}$Se study

From the 348 produced nuclei of $^{63}$Se with the $^{65}$Br and $^{64}$Se settings, 189 were implanted in the WAS3ABi setup (see table 4.5 for details), mostly in the central DSSSD.

The implantation-decay correlations were studied as for $^{67}$Kr in section 4.2. These events were correlated with possible $\beta$ particles detected in the neighbouring detectors. As shown on the figure 4.10, no clear peak can be distinguished without coincident $\beta$ particle in the energy spectrum. Every peak of the spectrum overlaps with coincident events in the neighbouring DSSSDs (red histogram). Thus we can not establish that this nucleus decays by 2p radioactivity.

| Nucleus | $T_z$ | Setting | F7 | DSSSD 0 | DSSSD 1 | DSSSD 2 |
|---------|-------|---------|------|---------|---------|---------|
| $^{63}$Se | $-5/2$ | B ($^{65}$Br) | 303 | 12 | 135 | 26 |
| | | C ($^{64}$Se) | 45 | 0 | 12 | 4 |
| | | Total | 348 | 12 | 147 | 30 |
| $^{59}$Ge | $-5/2$ | B ($^{65}$Br) | 934 | 5 | 30 | 349 |
| | | E ($^{62}$Se) | 287 | 8 | 163 | 7 |
| | | Total | 1221 | 13 | 193 | 356 |
| $^{68}$Kr | $-2$ | B ($^{65}$Br) | 477 | 198 | 42 | 3 |
| $^{69}$Kr | $-3/2$ | B ($^{65}$Br) | 1287 | 616 | 23 | 7 |
| $^{65}$Se | $-3/2$ | B ($^{65}$Br) | 63592 | 16758 | 20065 | 755 |
| | | C ($^{64}$Se) | 155079 | 2133 | 58749 | 1592 |
| | | D ($^{66}$Se) | 63 | 1 | 9 | 0 |
| | | Total | 218734 | 18892 | 78823 | 2347 |
| $^{61}$Ge | $-3/2$ | B ($^{65}$Br) | 607585 | 5108 | 169078 | 131066 |
| | | C ($^{64}$Se) | 32180 | 172 | 1013 | 5283 |
| | | E ($^{62}$Se) | 387 | 91 | 140 | 3 |
| | | Total | 640152 | 5371 | 170231 | 136352 |
| $^{57}$Zn | $-3/2$ | B ($^{65}$Br) | 1084955 | 7120 | 3052 | 201869 |
| | | E ($^{62}$Se) | 21374 | 347 | 10317 | 938 |
| | | Total | 1106329 | 7467 | 13369 | 202807 |

Table 4.5: Identification and implantation distributions of the $\beta$-delayed proton emitters studied in this work.



Figure 4.10: Energy spectrum of $^{63}$Se decay events correlated with implantation events over a time gate of 100 ms. The blue spectrum is the distribution of events without any condition. The red one shows events with a coincident signal in a neighbouring DSSSD or the veto scintillator. Two narrow peaks are seen around 2 and 6 MeV, respectively.

$\beta$-delayed proton peaks are seen at around 2.5 and 6 MeV. They do not seem to be $\beta$-delayed proton peaks (should be broaden because of the $\beta$-particle pileup). The data files were checked and no correlation artefact was found (same event counted many times). Three events are compatible with the theoretical $Q_{2p}$ at 1.5 MeV. Only one count without coincident $\beta$ particle (blue spectrum) belongs to this peak. If we suppose that this event comes from 2p radioactivity of $^{63}$Se, the 2p branching ratio is $1/189 \sim 0.5\%$. According to this observation, the 2p branch of $^{63}$Se should not exceed 0.5%.



Figure 4.11: Time spectrum of $^{63}$Se. The distribution is obtained from all correlated decays with an energy above 1 MeV. The red line is the fit of the decay function. The first 3 ms are excluded from the fit because of dead time losses. A half-life of 13.2(39) ms was found, including systematic uncertainties.

The half-life was also estimated from the time spectrum in figure 4.11. As seen above, $^{63}$Se mainly decays by $\beta p$ emission, the $\beta$-decay daughter $^{63}$As is a proton-unbound nucleus ($S_p = -951$ keV [Ens17]) thus the only possible decay for $^{63}$Se is the $\beta$-delayed emission of protons (or maybe $\alpha$ particles). We study the time spectrum of events with an energy above 1 MeV to reduce background and reject $\beta$ particle emissions without delayed protons. As for $^{67}$Kr, their contribution above 1 MeV is neglected. The $\beta p$ daughters have half-lives greater than 100 ms, they are neglected for the half-life estimation. This latter is performed by a fit considering an exponential decay and a constant background. The resulting half-life is 13.2(34) ms with a systematic uncertainty of 2 ms due to the upper fit limit. That gives a half-life estimate of 13.2(39) ms. The $\beta$-decay half-life given by the Gross theory is 13.4 ms [Jae14]. It is very close to the experimental measurement, showing that $\beta$ decay (i.e. $\beta p$) is highly dominating for $^{63}$Se.

### $^{59}$Ge study

The energy spectrum of $^{59}$Ge is similar to the $^{63}$Se one (cf. figure 4.12). The decays are dominated by $\beta$-delayed proton emission. Indeed the spectrum conditioned by signal detection in one of the neighbouring DSSSDs (red histogram in figure 4.12) covers all energies. No peak without coincident $\beta$ particle is seen. There is a prominent peak at around 6 MeV. At the expected $Q_{2p}$ value around 1.5 MeV, no pronounced peak is observed. One count without detected $\beta$ particle is seen at this energy. If it comes from a 2p decay of $^{59}$Ge, the branching ratio should be $1/562 \sim 0.2\%$. From this observation, we propose an upper limit of 0.2% for the 2p branch of $^{59}$Ge.

The half-life was estimated by a fit with a likelihood minimisation method (see figure 4.13) between 3 and 100 ms. The fit function is composed of an exponential decay and a constant background. As for the other nuclei, the $\beta$-decay daughter of $^{59}$Ge is a proton-unbound nucleus:
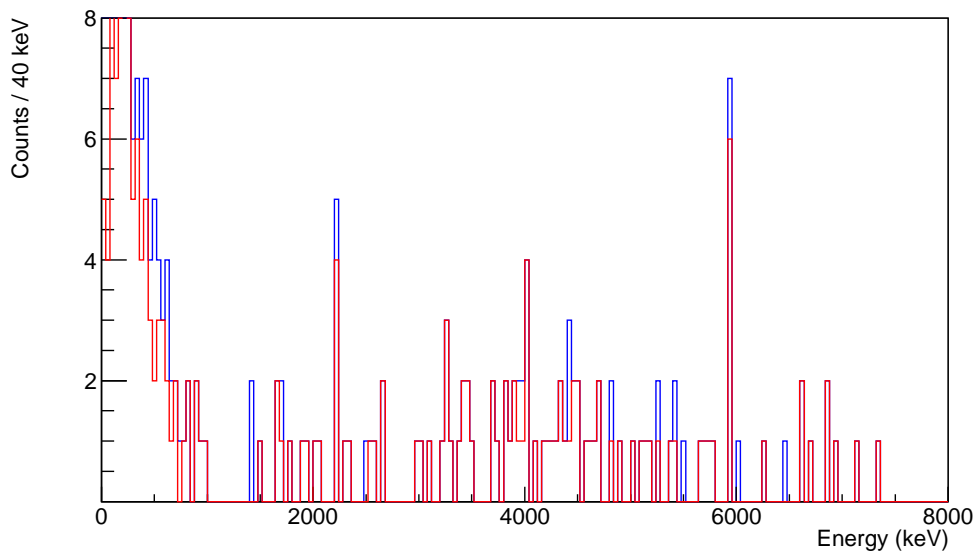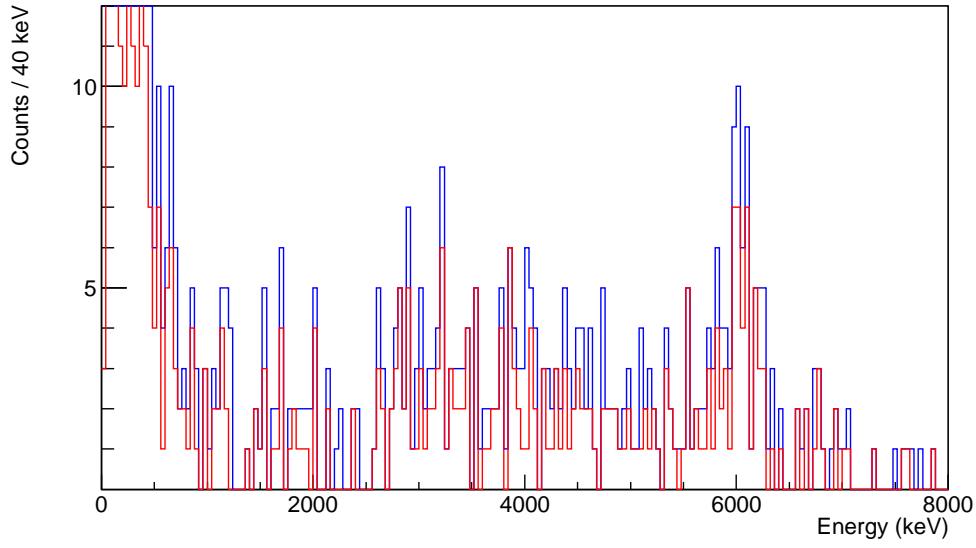
Figure 4.12: Energy spectrum of $^{59}$Ge decay events correlated with implantation events over a time gate of 100 ms. The blue spectrum is the distribution of events without any condition. The red one shows events with a coincident signal in a neighbouring DSSSD or the veto scintillator.
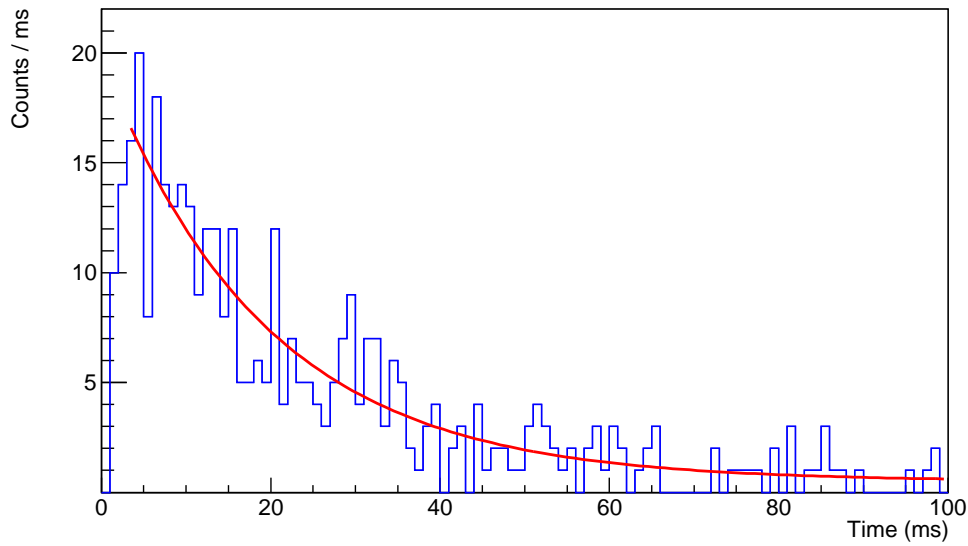
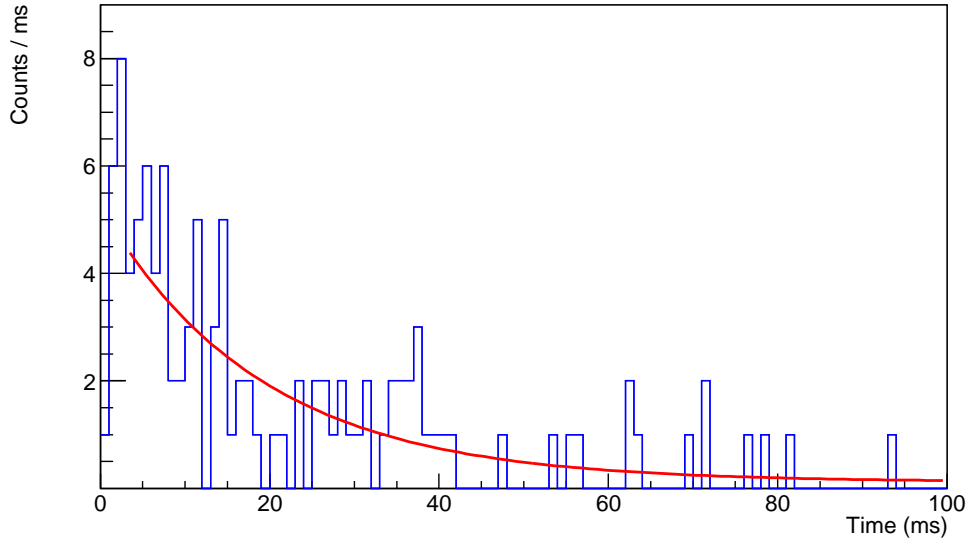

Figure 4.13: Time spectrum of $^{59}$Ge. The distribution is obtained from all correlated decays with an energy above 1 MeV. The fit of the decay function is plotted in red. The first 3 ms are excluded from the fit because of dead time losses. A half-life of 13.3(17) ms was found, including systematic uncertainties.

$^{59}$Ga ($S_p = -1250$ keV [Ens17]). The time spectrum of events above 1 MeV was fit to reduce background because the only possible decay for $^{59}$Ge is a $\beta$-delayed proton emission (2p branch is negligible if it exists). No daughter contribution was considered for the fit. The $\beta p$ daughter $^{58}$Zn decays mainly by $\beta$ decay so it does not appear in the spectrum. The other daughters of possible more exotic processes as $\beta 2p$ or $\beta 3p$ emission have half-lives greater than 200 ms. The fit gives a half-life of 13.3(15) ms, a systematic uncertainty of 0.6 ms was found due to the fit upper limit variation. The estimate of the $^{59}$Ge half-life is thus 13.3(17) ms. This value is close to the Gross theory value which is 10.9 ms [Jae14]. Therefore the $\beta$ decay (i.e. $\beta$-delayed proton emission) dominates for $^{59}$Ge.

### 4.3.2  $^{68}$Kr study

$^{68}$Kr is the other nucleus produced and identified for the first time. It was exclusively produced during the setting optimised on $^{65}$Br. The highest number of implantations is in the first DSSSD as it is shown in table 4.5. The results presented here are the computations made with the spectra of the first DSSSD. The procedures presented in chapter 3 are used.
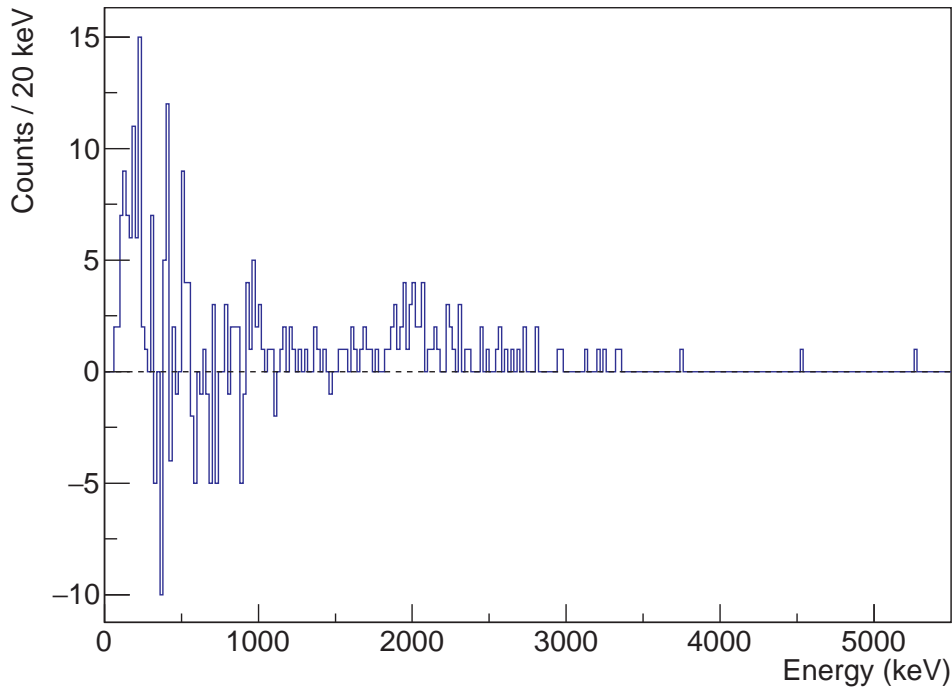


Figure 4.14: Energy spectrum of $^{68}$Kr decays correlated with implantation events in the DSSSD 0. The background is subtracted from the spectrum.

As shown in figure 4.14, the energy spectrum of $^{68}$Kr displays a peak around 1 MeV and a second around 2 MeV. The proton branching ratio was evaluated as $89^{+11}_{-10}\%$. This high value, compatible with 100%, is coherent with the fact that the $\beta$-decay daughter $^{68}$Br is a proton-unbound nucleus ($S_p = -500$ keV [Ens17]).

Because the $\beta$-decay daughter is a proton-unbound nucleus, the half-life was estimated from the time distribution of events above 1 MeV since only $\beta$-delayed proton emission is expected. The contribution of daughters is neglected because they are pure $\beta$ emitters. The fit shown in figure 4.15 gives a half-life of 21.6(33) ms. The statistical uncertainty of the fit is 3.2 ms. A systematic uncertainty of 0.5 ms was seen by moving the upper limit of the fit from 2000 ms to 200 ms ($\times 10$ half-lives).

This value is the first measurement of the $^{68}$Kr decay, no experimental value is available to compare it. The $\beta$-decay half-life of the Gross theory is 17.2 ms [Jae14]. It is in agreement with the value measured here.
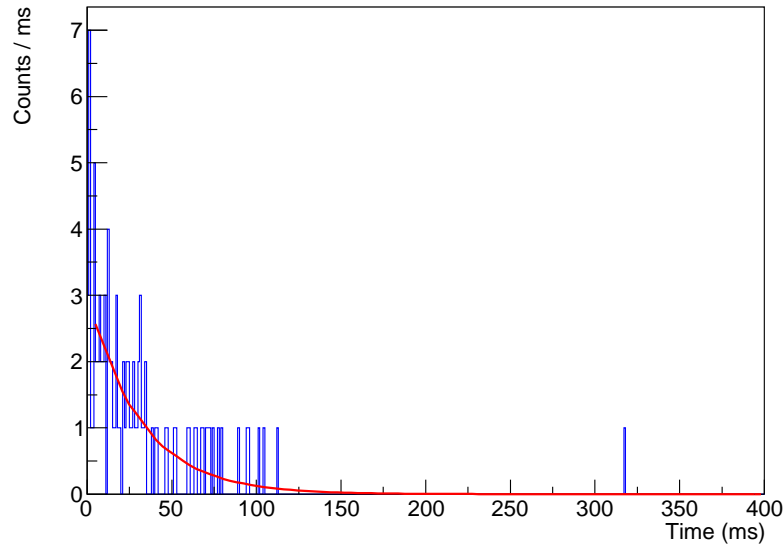
Figure 4.15: Time distribution of $^{68}$Kr decays correlated with implantation events in the DSSSD 0. The decay events with an energy above 1 MeV are represented. The red curve is the fit result. The resulting half-life is 21.6(33) ms.

### 4.3.3  $^{69}$Kr study

This nucleus was produced in the setting optimised for $^{65}$Br. The implantation events are mainly in the first DSSSD (cf. table 4.5). The analysis was thus performed only on this detector.
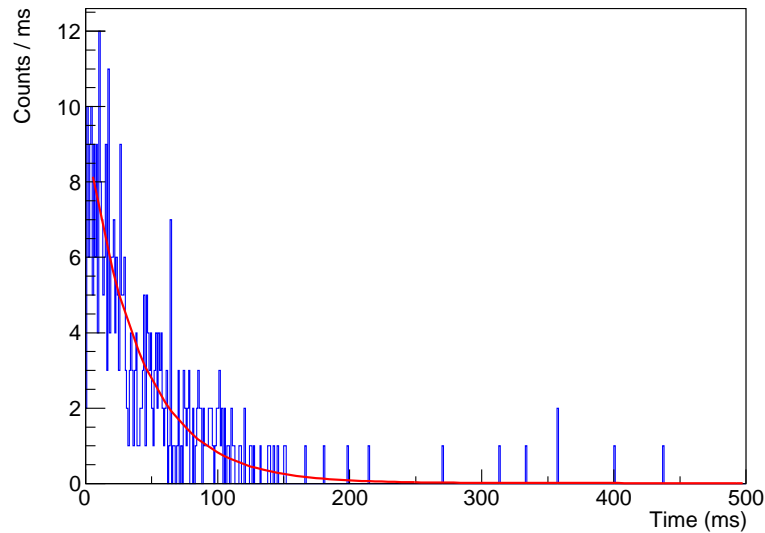


Figure 4.16: Time distribution of $^{69}$Kr decays correlated with implantation events in the DSSSD 0. The decay events with an energy above 1 MeV are represented. The red curve is the fit result. The resulting half-life is 27.8(16) ms.

$^{69}$Kr should decay only by $\beta p$ emission because the $\beta$-decay daughter $^{69}$Br is proton unbound ($S_p = -641$ keV [Ens17]). The proton branching ratio resulting from this work is $93^{+7}_{-6}\%$. This value is in agreement with the literature value $99^{+1}_{-11}\%$ [Rog11b]. The statistics was not high enough during the experiment to increase the precision of the value. Because of the branching ratio near 100% and the proton-unbound daughter, the half-life was estimated from the time distribution of events with an energy above 1 MeV. The contribution of the daughter $^{68}$Se is therefore neglected because this nucleus only decays by $\beta$ emission. No significant systematic

uncertainty compared to the statistical one was seen due to the variation of the upper limit of the fit. The resulting half-life is 27.8(16) ms. This value is in agreement with the values from 32(10) ms [Xu97], 27(3) ms [Rog11b] and 28(1) ms [DS14]. The statistics of the results presented here is similar to [Rog11b].

### 4.3.4    $^{65}$Se study

$^{65}$Se was produced with the settings optimised on $^{65}$Br, $^{64}$Se and $^{66}$Se. The nuclei were mainly implanted in the central DSSSD (cf. table 4.5). This latter was used to study this nucleus.

This observation of the $\beta p$ decay of $^{65}$Se is the third one after [Bat93] and [Rog11b]. New evidences about the decay scheme and new estimate of the half-life are reported here.

**Decay scheme**

A proton branching ratio of $94^{+6}_{-4}\%$ was estimated for $^{65}$Se. This value is more precise than the literature one from [Rog11b] ($88^{+12}_{-13}\%$) and compatible with 100%.

The energy spectrum presented in figure 4.17 shows the two peaks observed by [Rog11b]. Another proton transition is visible around 2.2 MeV but the statistics is too low to estimate its energy by a fit. The two highest proton peaks are estimated at energies of 2642(15) keV and 3532(16) keV, in agreement with the values of [Rog11b] at 2620(30) keV and 3510(20) keV. The value of [Bat93] at an energy of 3550(30) keV is also in agreement. We found an absolute branching ratio of 18(2)% and 44(2)% for the two peaks leading to a total branching ratio of 63(2)% for these two proton groups. This value is in agreement with the measurement of [Rog11b], 62(13)%, and the uncertainty is divided by a factor 6.
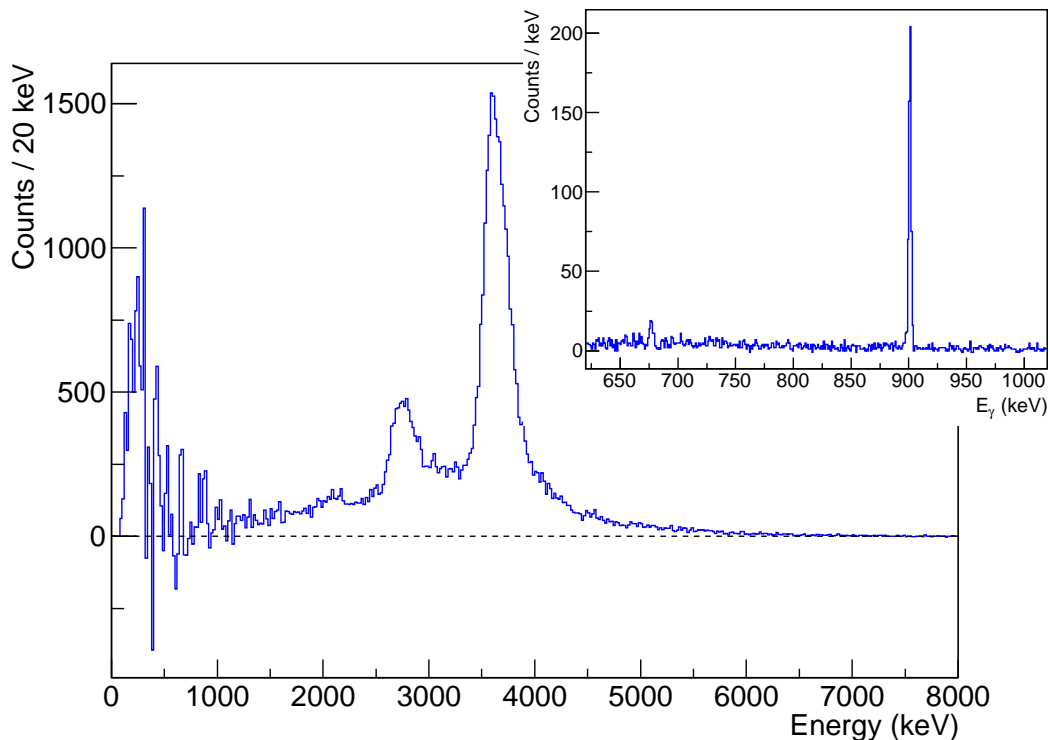


Figure 4.17: Energy spectrum of $^{65}$Se in DSSSD1. The inset shows the $\gamma$-ray spectrum coincident with the 2.6-MeV proton peak. It shows the $\gamma$ ray from the decay of the first excited state in $^{64}$Ge at 901.1(3) keV. The background is subtracted from the two energy spectra (charged particles and $\gamma$ rays).

The 2.6-MeV proton peak was found in coincidence with a $\gamma$-ray peak, measured at 901.1(3) keV (fit with a Gauss function). The energy found is in agreement with the first excited state of $^{64}$Ge evaluated at 901.7(3) keV [Ens17]. It shows that the 2.6-MeV proton peak feeds the

$2^+$ state of $^{64}$Ge. The absolute intensity of this transition is measured at 9.1(6)%. This $\gamma$-ray transition was not seen in the previous study of [Rog11b]. The intensity is surprising since it should be equal to the branching ratio of the 2.6-MeV proton peak. Possible explanations could be an underestimate of the $\gamma$-detection efficiency or that all events of this proton peaks do not come from the same $^{65}$As state. Moreover the structure of $^{65}$As is partially known.

By using the proton separation energy of $^{65}$As from [Ens17] ($S_p = -90(85)$ keV ) and the proton energy found for the 2.6-MeV peak, we find a total energy of 3453(82) keV between the $^{64}$Ge ground state and the excited state of $^{65}$As feeding the 901-keV transition. This value is compatible with [Rog11b] who computed 3420(87) keV. This value of 3453(82) keV is compatible with the energy of the second peak, 3532(16) keV. Thus this latter feeds the ground state of $^{64}$Ge. A more elaborated scheme of the $\beta p$ decay of $^{65}$Se is brought by these new results. This latter is shown in figure 4.18. The $Q_\beta$ value is taken from Coulomb displacement energy calculations of [Rog11b]. The assumed proton separation energy of $^{65}$As is taken from the data evaluation from [Ens17].
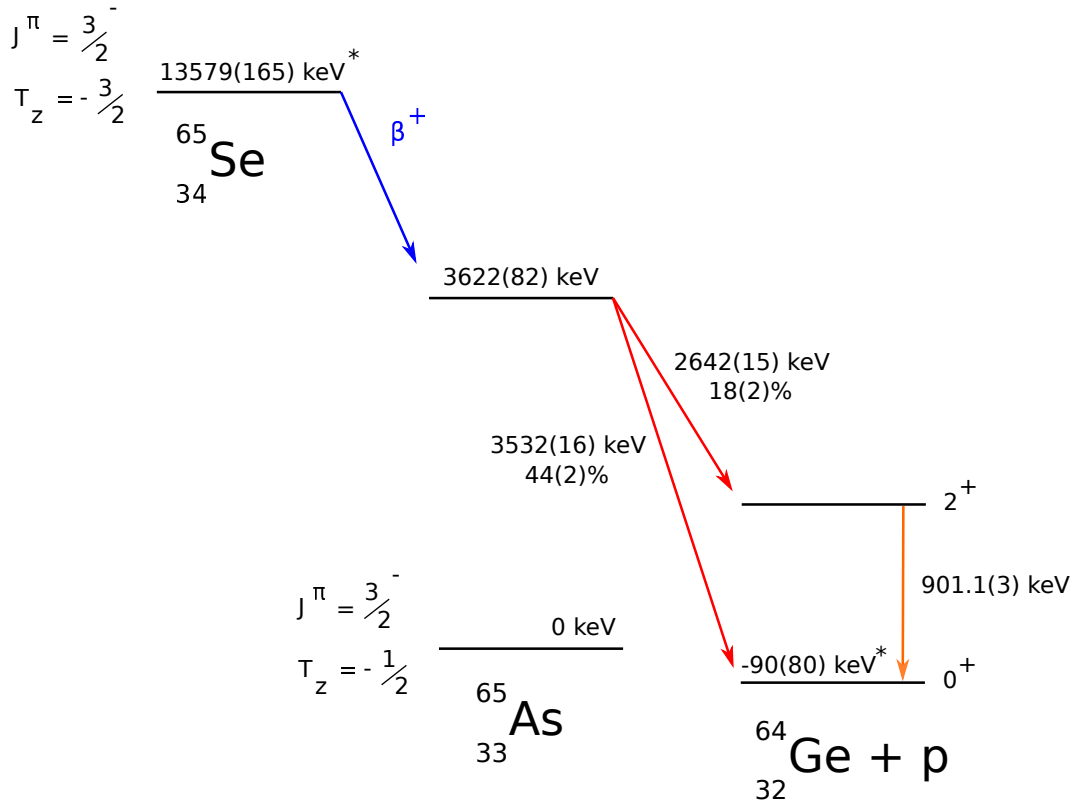


Figure 4.18: Proposed decay scheme of $^{65}$Se. The reference of the energy scale is set on the ground state of $^{65}$As The values with a * are taken from literature ($Q_\beta$ value from [Rog11b] and $S_p$ of $^{65}$As from [Ens17]), the others are calculated from the present work. The $2^+ \rightarrow 0^+$ transition of $^{64}$Ge is fed by the 2.6-MeV proton peak from $^{65}$As.

**Half-life**

The half-life was fitted from the time distribution represented in figure 4.19. There is no certitude that the proton branching ratio is 100% because the $\beta$-decay daughter $^{65}$As is weakly proton-unbound ($S_p = -90(85)$ keV [Ens17]). Thus the contributions of $^{65}$As ($T_{1/2} = 128(16)$ ms [Ens17]) and the $\beta p$ daughter $^{64}$Ge ($T_{1/2} = 63.7(25)$ s [Ens17]) are both considered for the fit. They decay only by $\beta$ radioactivity. The result of the fit is represented in figure 4.19. The resulting half-life is 34.2 ms with a statistical uncertainty of 0.2 ms. The fixed parameters of the fit were tested according to their uncertainties to search for possible systematic uncertainties. These parameters are the proton branching ratio, the $\beta$-detection efficiency and the half-lives of the two daughters. Their influence on the half-life is presented in figure 4.20. An asymmetric uncertainty of $-0.4$ and $+0.6$ ms was found. The upper limit of the fit was moved from 2000

to 300 ms (×10 half-lives). No significant systematic uncertainty was seen due to the fit limit. With all the systematic uncertainties, the resulting half-life is 34.2(7) ms (total uncertainty symmetrised). This value is three times more precise than the literature value (33(4) ms [Rog11b]).
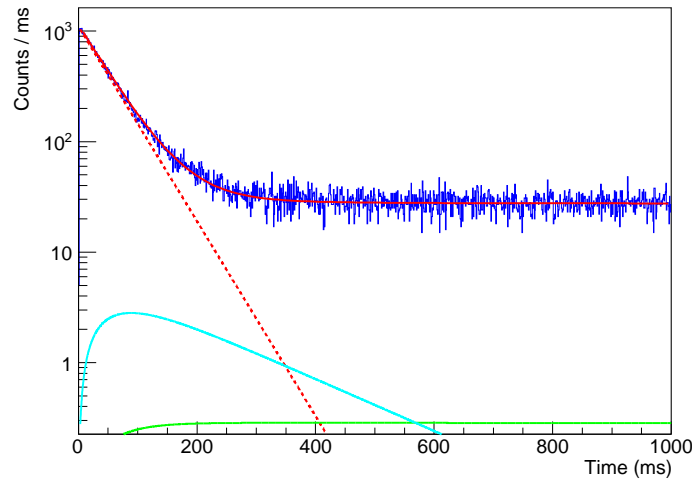


Figure 4.19: Time distribution of $^{65}$Se decays correlated with implantation events in the DSSSD 1. The red curve is the fit result. The dashed red line is the $^{65}$Se contribution, the blue one is the contribution of the $\beta$-decay daughter $^{65}$As and the green one the contribution of the $\beta p$ daughter $^{64}$Ge . A half-life of 34.2(7) ms was found, including systematic uncertainties.
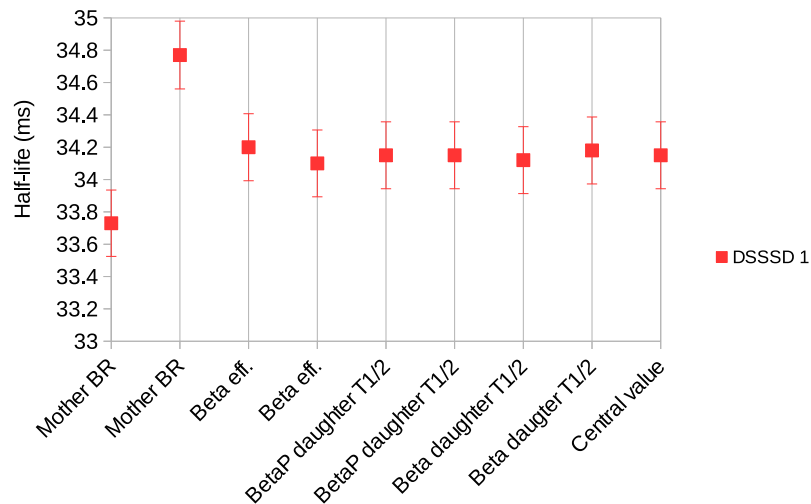


Figure 4.20: Systematic variations of the half-life extracted from the fit of $^{65}$Se time distribution (DSSSD 1) with lower and upper values for various parameters that are fixed in the fit procedure. These parameters are the experimental proton branching ratio of the mother ($^{65}$Se), the $\beta$-detection efficiency and the half-life of the two daughters $^{64}$Ge ($\beta p$ daughter) and $^{65}$As ($\beta$-decay daughter). The central value is the adopted half-life for this nucleus with all fixed parameters at their respective central values.

### 4.3.5　$^{61}$Ge study

$^{61}$Ge was produced with the settings optimised for $^{65}$Br, $^{64}$Se and $^{62}$Se production. The DSSSDs with the highest number of implantations are the two last ones with nearly the same numbers (cf. table 4.5). These two detectors were analysed. The values computed from the spectra are a weighted average between the results of the two DSSSDs.

A new estimate of the total proton branching ratio is presented. Energies and branching ratios of the proton transitions are also estimated in this work. The high statistics of this experiment allowed to have a more accurate estimate of the half-life of $^{61}$Ge. It is the third measurement after [Bla07] and [Hot87].

**Proton emission**

The total proton branching ratio was measured at 89(3)% for the DSSSD 1 and 85(3)% for the DSSSD 2. By averaging these values, we find a proton branching ratio of 87(3)%. The value is in disagreement with the literature as a value of 62(4)% was found in [Bla07]. The result computed here is the second evaluation of the proton branching ratio.

The energy spectrum of $^{61}$Ge obtained from the RIBF4R1 experiment is shown in figure 4.21. In addition to the known 3.2-MeV peak, many unresolved proton transitions are seen at low energy, between 1000 keV and this peak. This complex structure does not appear in the spectrum from [Bla07], shown in figure 4.22. This difference of counts between the two energy spectra explains the underestimate of [Bla07].
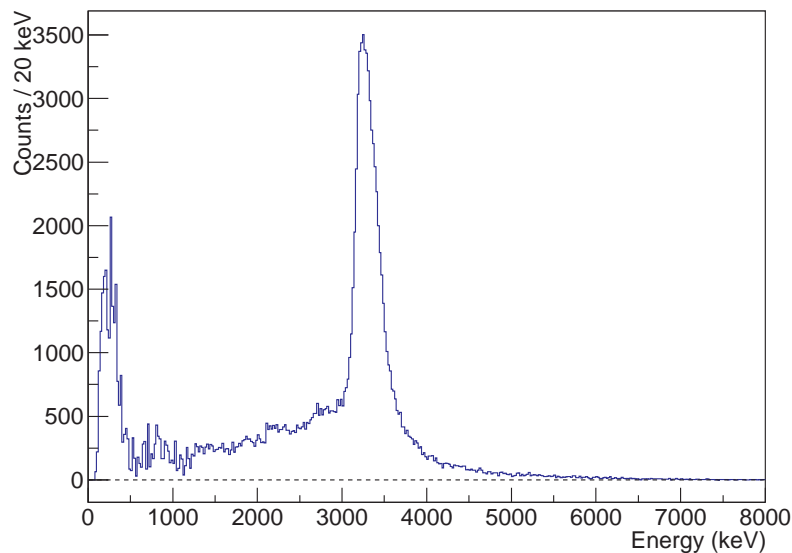


Figure 4.21: Energy spectrum of $^{61}$Ge (background subtracted) of DSSSD 1. One sees clearly the known 3.2-MeV peak. Many proton transitions with a complex structure are seen at lower energy.
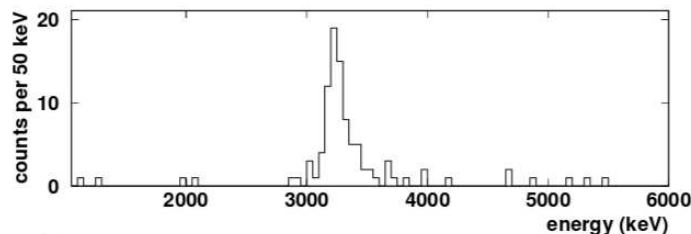


Figure 4.22: Energy spectrum of $^{61}$Ge from [Bla07].

The energy and the branching ratio of the proton peak were estimated by a fit. A value of 3162(17) keV for the DSSSD 1 and 3174(13) keV for the DSSSD 2 was measured. The error-weighted average value between the two detectors gives an energy of 3169(11) keV. This result is in agreement with the estimates of [Hot87], 3160(30) keV, and [Bla07], 3170(30) keV. The branching ratio of this peak was computed at 50(2)% for the DSSSD 1 and 49(2)% for the DSSSD 2. The error-weighted average of these two values is 50(2)%. This value is in agreement with [Bla07], 55(6)% for this single peak.

**Half-life**

The half-life was estimated for the two DSSSDs separately. The proton branching ratio is fixed with the value estimated for the corresponding detector. The half-lives of the two daughters $^{60}$Zn ($\beta p$ daughter, $T_{1/2} = 2.38(5)$ min [Ens17]) and $^{61}$Ga ($\beta$-decay daughter, $T_{1/2} = 167(3)$ ms [Ens17]) are also fixed for the fit. A result of the fit is illustrated in figure 4.23. For the DSSSD 1, a half-life of 40.7 ms was found. The statistical uncertainty is 0.2 ms. A systematic uncertainty of 0.4 ms was found due to the variation of the fixed parameters of the fit (cf. figure 4.24). No significant systematic uncertainty due to the limit of the fit was seen. The value of DSSSD 1 is thus 40.7(5) ms. The DSSSD 2 half-life is 40.8(6) ms with a statistical uncertainty of 0.3 ms and a systematic one of 0.5 ms. The average half-life of the two DSSSD values is 40.7(4) ms. This resulting half-life is compatible with the previous values 45(6) ms [Bla07] and 40(15) ms [Hot87].
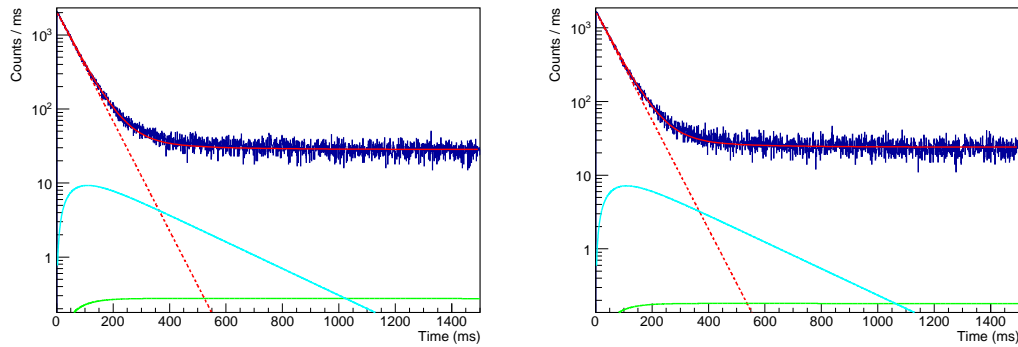


Figure 4.23: Time distributions of $^{61}$Ge decays correlated with implantation events in the DSSSD 1 (left) and 2 (right). The red curve is the fit result. The dashed red line is the $^{61}$Ge contribution, the blue one is the contribution of the $\beta$-decay daughter $^{61}$Ga and the green line the contribution of the $\beta p$-decay daughter $^{60}$Zn. The resulting half-lives are 40.7(5) ms for DSSSD 1 and 40.8(6) ms for DSSSD 2, including systematic uncertainties. The error-weighted average of these two values is 40.7(4) ms.



Figure 4.24: Systematic variations of the half-life extracted from the fit of the $^{61}$Ge time distribution with lower and upper values for various parameters that are fixed in the fit procedure. These parameters are the experimental proton branching ratio of the parent ($^{61}$Ge), the $\beta$-detection efficiency and the half-life of the two daughters $^{60}$Zn ($\beta p$ daughter) and $^{61}$Ga ($\beta$-decay daughter). The central value is the adopted half-life for this nucleus with all fixed parameters at their respective central values.

### 4.3.6 $^{57}$Zn study

The highest number of implantations is in the last DSSSD with an enormous disequilibrium in favour of this detector. There are nearly 200000 implantations in DSSSD 2 against 20 times fewer in the two other detectors (cf. table 4.5). The analysis of this nucleus was performed on the DSSSD 2 only.

In this section is presented a new evaluation of the proton transitions observed for $^{57}$Zn with their energy and branching ratios. A new value of the half-life is also proposed. This measurement of $^{57}$Zn decay is the third after [Bla07] and [Jok02].

**Proton emission**

The total proton branching ratio was measured at 86(3)%. It is the second evaluation of this ratio after [Bla07] who found 78(17)%. The two values are in good agreement. The present work improves the uncertainty by a factor 6.
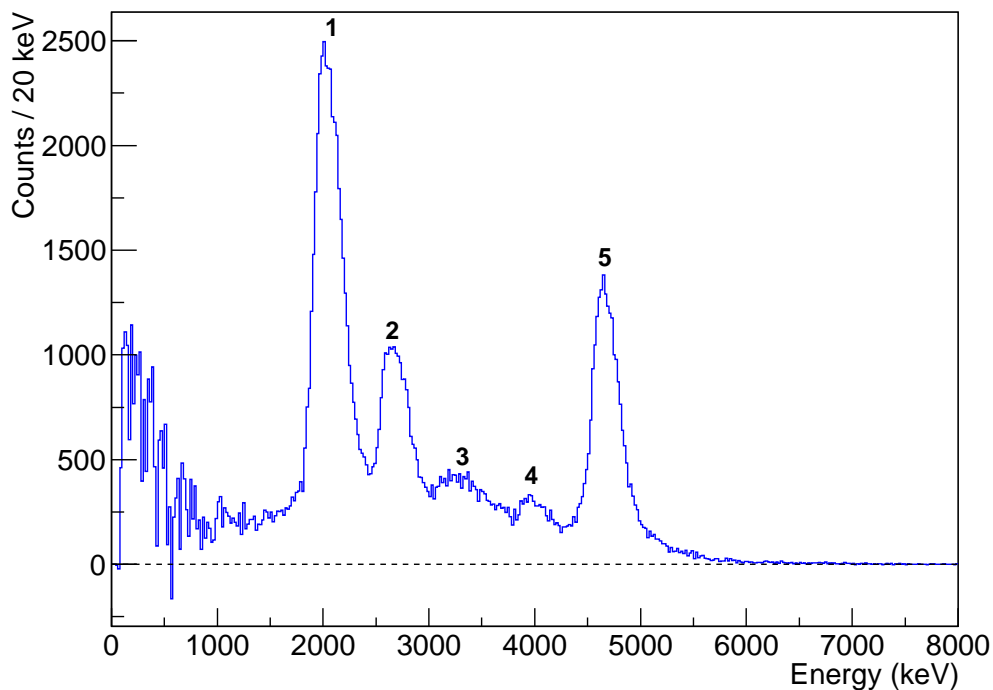


Figure 4.25: Energy spectrum of $^{57}$Zn (subtracted from background) in DSSSD 2. The five proton peaks numbered on this figure are evaluated in this work.

| Peak | This work | | [Bla07] | | [Jok02] | [Vie76] |
|------|-----------|--------|-----------|--------|-----------|-----------|
| | $E_p$ (keV) | $I_p$ (%) | $E_p$ (keV) | $I_p$ (%) | $E_p$ (keV) | $E_p$ (keV) |
| 1 | 1939(9) | 30(2) | 1900(60) | 14(2) | 1902(12) | 1950(50) |
| 2 | 2567(10) | 14(2) | 2560(50) | 13(2) | 2531(16) | 2580(50) |
| 5 | 4570(21) | 15(1) | 4590(50) | 19(2) | 4595(29) | 4650(50) |

Table 4.6: Energy values of the identified proton peaks of $^{57}$Zn with their absolute branching ratios and the probable corresponding values in literature.

The energy spectrum of $^{57}$Zn in figure 4.25 shows five proton groups. The first two peaks at 1939(9) keV and 2567(10) keV together with the highest energy at is estimated at 4570(21) keV (number 5) correspond to an absolute branching ratio of 30(2)%, 14(2)% and 15(1)%, respectively. The properties of groups 3 and 4 could not be evaluated. Indeed the previous measurements of [Bla07] and [Jok02] in figure 4.26 show that many proton peaks are visible
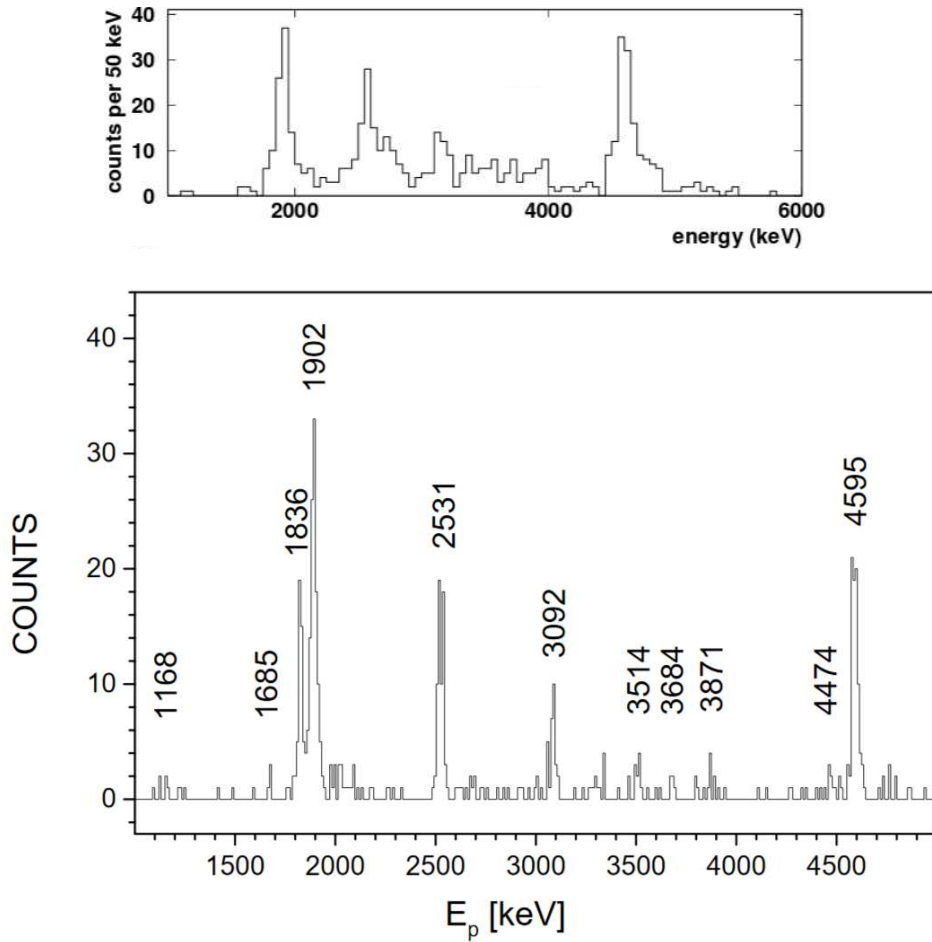
Figure 4.26: Energy spectra of [Bla07] and [Jok02] for $^{57}$Zn. Top: energy spectrum of [Bla07]. Bottom: energy spectrum of [Jok02] with the estimated energies of the proton peaks.

between 3 and 4 MeV. The two proton groups (3 and 4) visible in figure 4.25 have a more complex structure and the energy resolution is not high enough in order to distinguish the different proton peaks.

The known proton energies found in literature are compared with the values of this work in table 4.6. The energy values of peaks number 1 and 2 are in disagreement with [Jok02]. These disagreements are understandable if one compares our spectrum (cf. figure 4.25) with the one from [Jok02] on figure 4.26 which has a better energy resolution.

By comparing the spectrum of this experiment with the [Bla07] one in figure 4.26 (top), one notices that the peak 1 is higher compared to [Bla07]. Thus our values of the branching ratios are in disagreement with [Bla07], except for the peak 2. For the low-energy peak, the value of [Bla07] is biased because of the cut-off from the trigger threshold according to the authors.

**Half-life**

The total half-life was estimated with the estimated proton branching ratio and by fixing the daughter half-lives and the $\beta$-detection efficiency. The $\beta p$ daughter $^{56}$Ni is a $\beta$ emitter with a half-life of 6.075(10) days [Ens17]. The $\beta$-decay daughter $^{57}$Cu is also a $\beta$ emitter with a half-life of 196.3(7) ms [Ens17]. The result of the fit is shown in figure 4.27. A half-life of 45.7 ms was found. The statistical uncertainty is 0.2 ms. The parameters fixed for the fit were modified according to their respective uncertainties to search for systematic biases (cf. figure 4.28). The resulting systematic uncertainty is asymmetric with $-0.3$ ms and $+0.6$ ms. No systematic error was seen due to the variation of the limit of the fit. The resulting half-life with the total uncertainty is thus 45.7(6) ms (total uncertainty symmetrised). It is compatible with the previous measurements of 40(10) ms [Vie76] and 48(3) ms [Bla07].
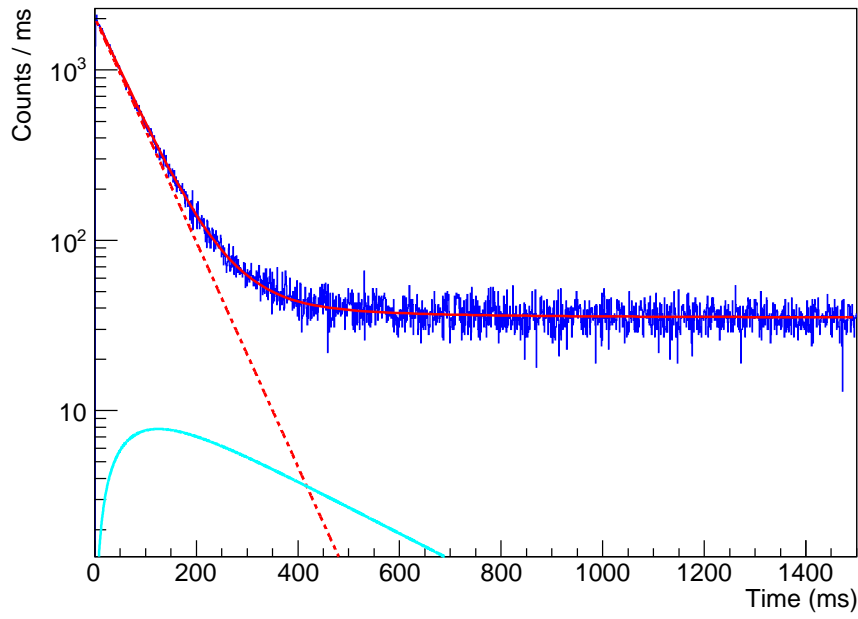
Figure 4.27: Time distribution of $^{57}$Zn decays correlated with implantation events in the DSSSD 2. The red curve is the fit result. The dashed red line is the $^{57}$Zn contribution, the blue one is the contribution of the $\beta$-decay daughter $^{57}$Cu. The resulting half-life is 45.7(6) ms.
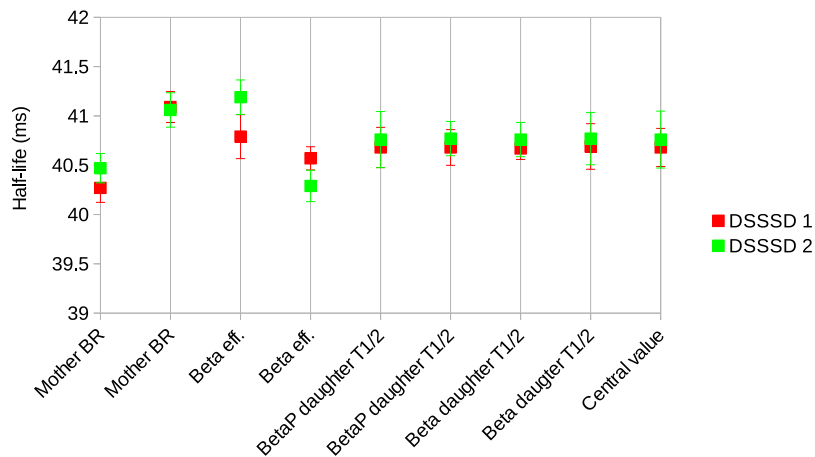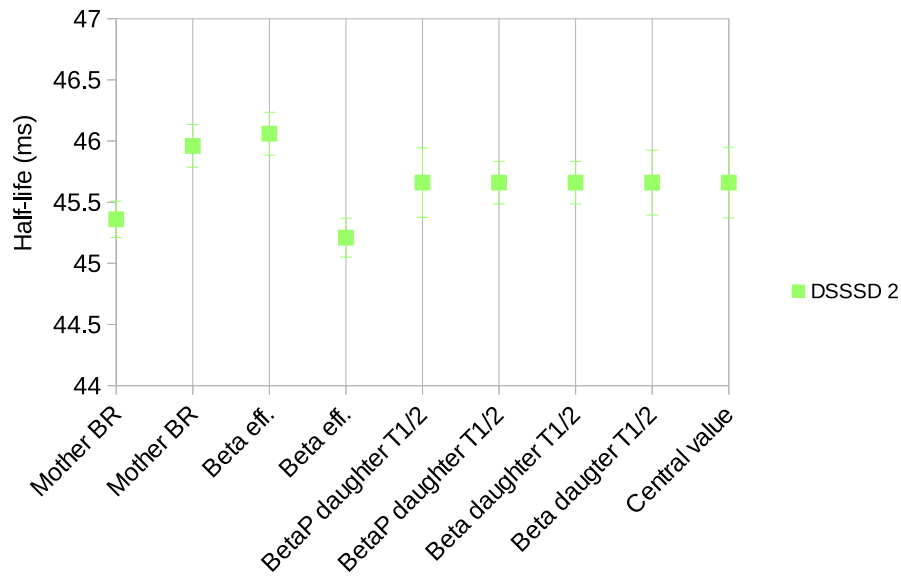


Figure 4.28: Systematic variations of the half-life extracted from the fit of the $^{57}$Zn time distribution of the DSSSD 2 with lower and upper values for various parameters that are fixed in the fit procedure. These parameters are the experimental proton branching ratio of the parent ($^{57}$Zn), the $\beta$-detection efficiency and the half-life of the two daughters $^{56}$Ni ($\beta p$ daughter) and $^{57}$Cu ($\beta$-decay daughter). The central value is the adopted half-life for this nucleus with all fixed parameters at their respective central values.

## 4.4    Half-life determination of beta-decaying nuclei

In this section are detailed the new half-life results of the $\beta$ decay of the exotic nuclei $^{55}$Cu, $^{56}$Cu, $^{60}$Ga, $^{63}$Ge, $^{64}$As and $^{65}$As. The fit of the time spectra was performed according to the function in section 3.6 by neglecting the contribution of the $\beta p$ daughter of these nuclei. Except for $^{60}$Ga and $^{56}$Cu with a proton branching ratio of around or below 1%, the other nuclei have no $\beta p$ branch. The production and implantation distributions of the isotopes presented in this this section are summarised in table 4.7.

| Nucleus | $T_z$ | Setting | F7 | DSSSD 0 | DSSSD 1 | DSSSD 2 |
|---------|-------|---------|-----|---------|---------|---------|
| $^{55}$Cu | $-3/2$ | E ($^{62}$Se) | 7359 | 166 | 494 | 3905 |
| $^{64}$As | $-1$ | B ($^{65}$Br) | 29365 | 6023 | 10229 | 428 |
|  |  | D ($^{66}$Se) | 463 | 3 | 133 | 12 |
|  |  | Total | 29828 | 6026 | 10362 | 440 |
| $^{60}$Ga | $-1$ | B ($^{65}$Br) | 642690 | 6581 | 151644 | 159832 |
| $^{56}$Cu | $-1$ | B ($^{65}$Br) | 647961 | 3740 | 1313 | 76742 |
|  |  | E ($^{62}$Se) | 11049 | 202 | 5208 | 704 |
|  |  | Total | 659010 | 3942 | 6521 | 77446 |
| $^{65}$As | $-1/2$ | D ($^{66}$Se) | 1568050 | 16352 | 474419 | 27116 |
| $^{63}$Ge | $-1/2$ | B ($^{65}$Br) | 202912 | 32803 | 80445 | 2860 |
|  |  | D ($^{66}$Se) | 2189 | 13 | 514 | 37 |
|  |  | Total | 205101 | 32816 | 80959 | 2897 |

Table 4.7: Identification and implantation distributions of the $\beta$ emitters studied in this work.

### 4.4.1    $^{55}$Cu study

The largest implantation rate was measured in DSSSD2. Whereas the two others were almost not counting (cf. table 4.7). For this reason, the latest were not included in the following analysis.



Figure 4.29: Energy spectrum of $^{55}$Cu decays correlated with implantion events in the DSSSD 2. The background is subtracted from the spectrum.

The energy spectrum of $^{55}$Cu is presented in figure 4.29. No proton peak can be distinguished

from the $\beta$ particles. The method used previously to determine the proton branching ratio is uncertain. Even by performing all the corrections presented in section 3.6.3, a branching ratio of only a few percents is found. The time distributions conditioned by events of energy above 1 MeV are difficult to fit and dominated by background. On the energy spectrum one sees clearly that the branching ratio is very small, close to zero. The results of the literature are contradictory. The proton branching ratio announced by [Dos07] is 15.0(43)% while [Tri13] did not observe any proton in the reported experiment. The results presented here are in favour of [Tri13].

The fit of the time distribution of $^{55}$Cu provides the resulting half-life of 55.4 ms (cf. figure 4.30). The contribution of the daughter $^{55}$Ni is taken into account ($T_{1/2} = 204.7(37)$ ms [Ens17]). No $\beta p$ decay branch is considered. A statistical uncertainty of 1.8 ms was found. No significant systematic uncertainty was found due to the half-life of the daughter or the upper limit of the fit. The resulting half-life is 55.4(18) ms. The literature values are 27(8) ms [Dos07] and 57(3) ms [Tri13]. This new result confirms the value of [Tri13]. As it is shown in figure 4.31, the very low statistics available to estimate the half-life in [Dos07] is the most logical explanation to the underestimate of the half-life.
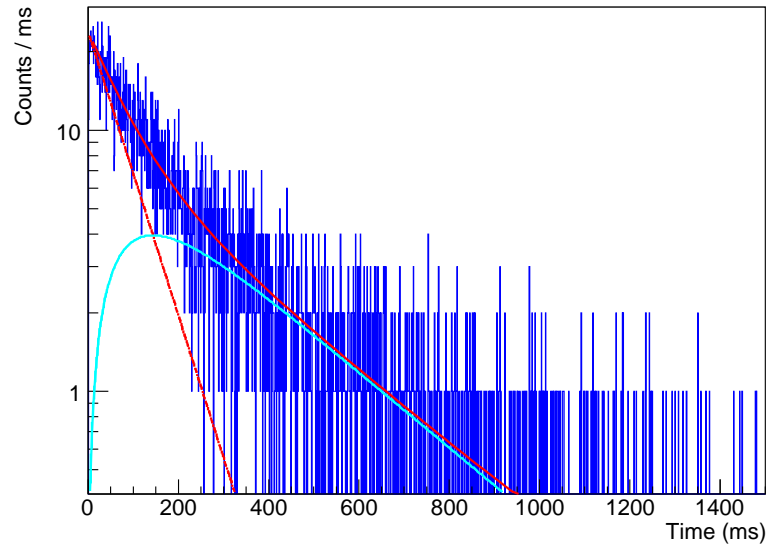


Figure 4.30: Time distribution of $^{55}$Cu decays correlated with implantation events in the DSSSD 2. The red curve is the fit result. The dashed red line is the $^{55}$Cu contribution, the turquoise one the contribution of the $\beta$-decay daughter $^{55}$Ni. A half-life of 55.4(18) ms was found, including systematic uncertainties.
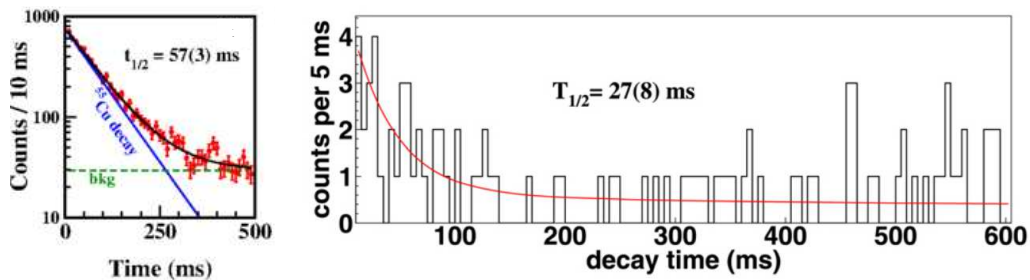


Figure 4.31: Time distributions of $^{55}$Cu decays from previous studies of [Tri13] and [Dos07]. Left: time distribution and half-life estimate from [Tri13]. Right: time distribution and half-life estimate from [Dos07].

### 4.4.2   $^{56}$Cu study

$^{56}$Cu was produced by the settings optimised for $^{65}$Br and $^{62}$Se production. This nucleus was largely implanted in the last DSSSD (cf. table 4.7). Thus it was studied for this detector.

$^{56}$Cu is a known $\beta$ emitter. Its $\beta p$ branch, estimated at 0.40(12) [Bor01] is negligible. The half-life was estimated from the time distribution of decay events of the DSSSD 2. The value extracted from the fit in figure 4.32 is 80.2(7) ms. The contribution of the daughter $^{56}$Ni (6 days [Ens17]) was neglected. No systematic uncertainty was seen due to the fit limit on the time spectrum. If we compare the resulting value with the literature, one notices that it is in agreement with [Ram98] (78(15) ms), [LJ02] (82(9) ms) and [Kuc17] (80(2) ms) but in contradiction with the value from [Bor01] (93(3) ms).



Figure 4.32: Time distribution of $^{56}$Cu decay events in the DSSSD 2. The red curve is the fit result. The dashed red line is the $^{56}$Cu contribution. A half-life of 80.2(7) ms was found.

### 4.4.3   $^{60}$Ga study

$^{60}$Ga was produced in the setting optimised for $^{65}$Br. As it is shown in table 4.7, the nuclei were mostly implanted in the DSSSDs 1 and 2 with a similar number in each one. The results presented here are computed from the spectra of these two detectors.

The $\beta p$ branching ratio of $^{60}$Ga is estimated to 1.6(7)% [Maz01]). The energy spectrum in figure 4.33 shows counts above 1 MeV which are proton groups, their amplitudes (around 80 counts / 20 keV) is very low compared to the amplitude of the $\beta$ particle distribution (around 7000 counts / 20 keV, not shown in figure). The statistics is too low here to determine a total proton branching ratio as it is done for $\beta$-delayed proton emitters in section 4.3. Indeed, the $\beta p$ branching ratio is estimated to 1.6(7)% [Maz01]). The energy spectrum of $^{60}$Ga in figure 4.33 shows counts above 1 MeV which could be proton groups. The statistics is too low here to determine an total proton branching ratio as it was done for $\beta$-delayed proton emitters in section 4.3.

Regarding the negligible proton proton branching ratio of $^{60}$Ga, the contribution of the $\beta p$ branch is not taken into account to determine the half-life. The fit of the $^{60}$Ga half-life is shown in figure 4.34 for the DSSSDs 1 and 2. The half-life of the daughter $^{60}$Zn was fixed for the fit at 2.38(5) min [Ens17]. Values of 69.9(4) ms and 71.8(4) ms were found for the detectors 1 and 2, respectively. No systematic uncertainty was seen due to the half-life of the daughter or the upper limit of the fit. However, these two values are not in agreement and a difference of 1.9 ms is seen. The error-weighted average of the two DSSSD values is 70.8(3) ms. By taking into account as a systematic uncertainty the difference between the DSSSDs, a total uncertainty of
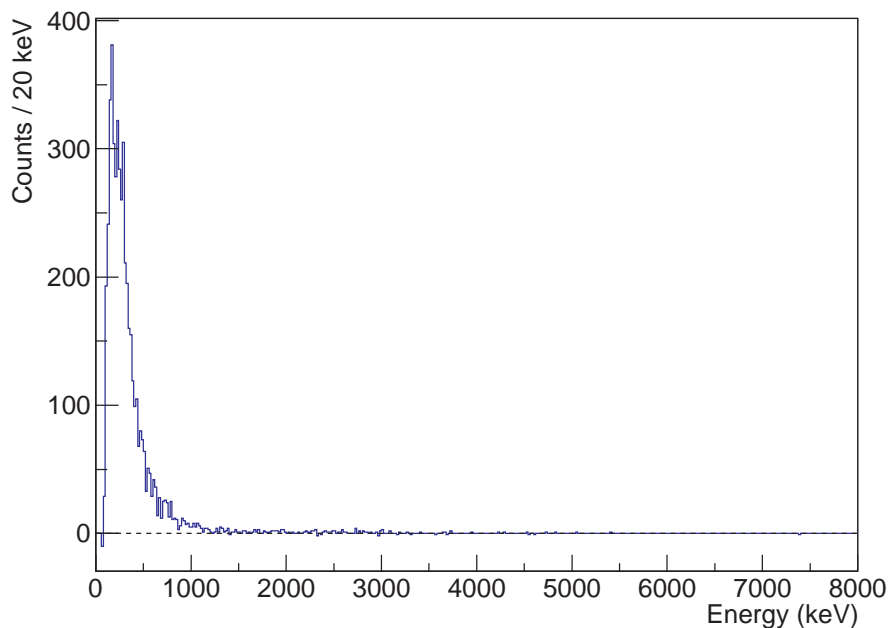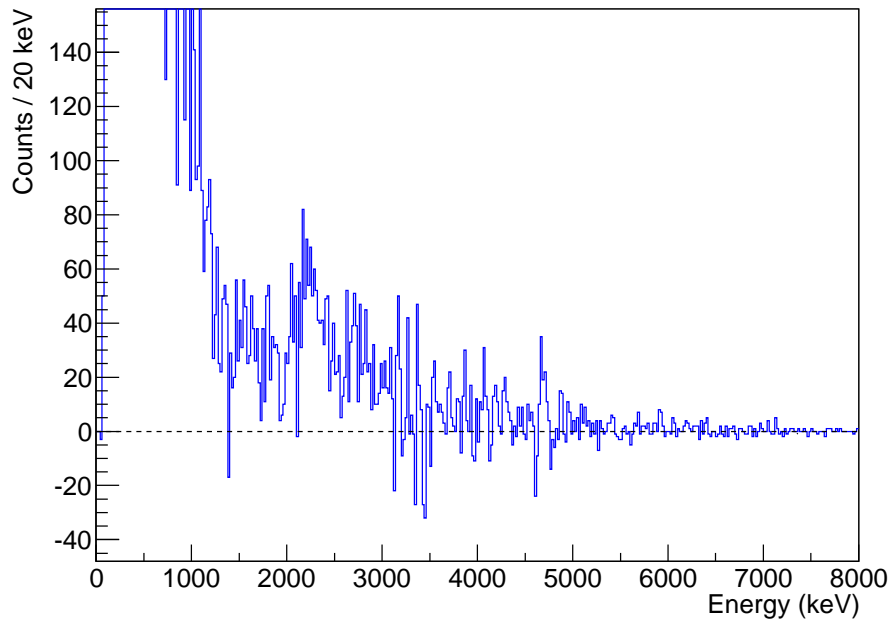
Figure 4.33: Energy spectrum of $^{60}$Ga decays correlated with implantation events in the DSSSD 2. The background is subtracted from the spectrum. Peaks above 1 MeV, with a prominent one at around 2.2 MeV, are assigned to $\beta$-delayed proton emission.

2 ms is found. The half-life from this work is 70.8(20) ms. This value is compatible with the previous measurements of [Maz01], 70(15) ms, [LJ02], 70(13) ms, and [Kuc17], 76(3) ms.
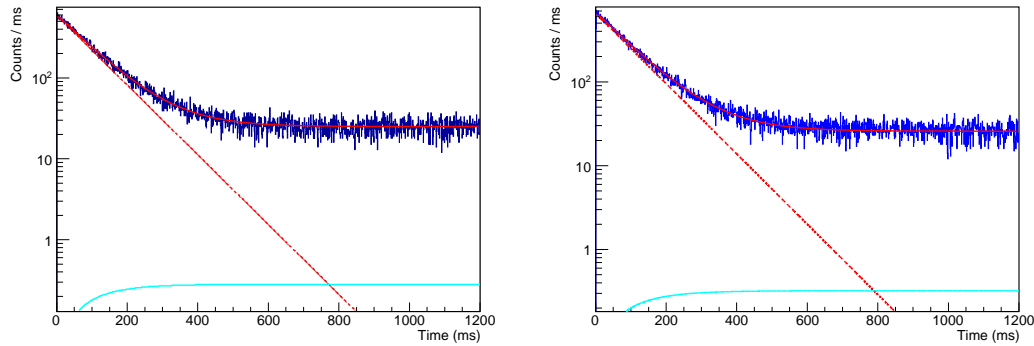


Figure 4.34: Time distributions of $^{60}$Ga decays correlated with implantation events in the DSSSD 1 (left) and 2 (right). The red curve is the fit result. The dashed red line is the $^{60}$Ga contribution, the blue one the contribution of the daughter $^{60}$Zn. Half-lives of 69.9(4) ms and 71.8(4) ms were found for the detectors 1 and 2, respectively. A half-life of 70.8(20) ms was found (weighted average of the two detector values), including systematic uncertainties.

### 4.4.4   $^{63}$Ge study

$^{63}$Ge was produced in the two settings optimised for $^{65}$Br and $^{66}$Se, respectively. As it is shown in table 4.7, the largest number of nuclei was implanted in the DSSSD 1. The results presented here are computed from the spectra of this DSSSD.

The nucleus $^{63}$Ge is a known $\beta$ emitter, its half-life was estimated from the fit of the time distribution of decay events in DSSSD 1. The contribution of the daughter $^{63}$Ga was fixed for the fit with a half-life of 32.4(5) s [Ens17]. The result of the fit is shown on 4.35, the half-life found is 153.6 ms with a statistical uncertainty of 1 ms. A systematic uncertainty of 0.1 ms due
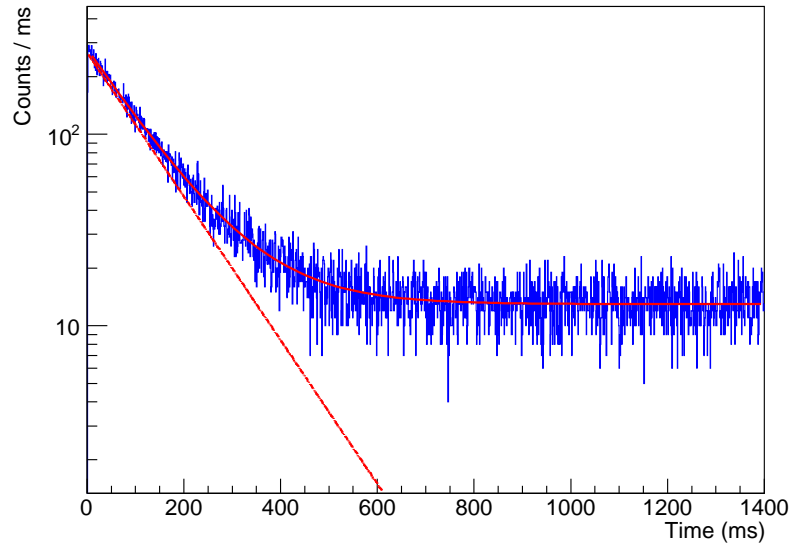
Figure 4.35: Time distribution of $^{63}$Ge decay events in the DSSSD 1. The red curve is the fit result. The dashed red line is the $^{63}$Ge contribution and the blue line the contribution of the daughter $^{63}$Ga. A half-life of 153.6(11) ms was found, including systematic uncertainties.

to the uncertainty on the daughter half-life was found. The variation of the upper limit of the fit leads to another systematic uncertainty of 0.4 ms. By taking into account these values, the measured half-life is 153.6(11) ms. This measurement of $^{63}$Ge is in agreement with the previous values of [Bla02], 150(9) ms [Rog14], 149(4) ms and [Kuc17], 156(11) ms. The estimated half-life is approximately ten times more accurate than the previous values.

### 4.4.5    $^{64}$As study

$^{64}$As was produced in the two settings optimised for $^{65}$Br and $^{66}$Se, respectively. As it is shown in table 4.7, the largest number of nuclei was implanted in the DSSSD 1. The results presented here are computed from the spectra of this DSSSD.

To fit the time distribution of the $\beta$ decay of $^{64}$As, the half-life of the daughter $^{64}$Ge (63.7(25) s [Ens17]) was fixed. The result is shown in figure 4.36 for the DSSSD 1. A half-life of 69.0(14) ms was found without significant systematic uncertainty due to the half-life of the daughter or the upper limit of the distribution used for the fit. This value is in agreement with literature. [LJ02] found a result of $18^{+43}_{-7}$ ms and [Rog14] 72(6) ms. The value resulting from the present work is four times more accurate than the [Rog14] one.

### 4.4.6    $^{65}$As study

$^{65}$As was produced in the setting optimised for $^{66}$Se. As it is shown in table 4.7, the largest number of nuclei was implanted in the DSSSD 1. The results presented here are computed from the spectra of this detector.

The $^{65}$As time distribution was fitted by taking into account the $\beta$-decay daughter $^{65}$Ge with a half-life of 30.9(5) ms [Ens17], fixed for the fit procedure. The result of the fit for DSSSD 1 is illustrated in figure 4.37. A half-life of 130.3(6) ms was found without any systematic uncertainty observed by varying the daughter half-life or the upper limit of the interval of the fit. The value presented here is in agreement with the previous values of [Rog14] (126(5) ms) and [Bro10] (128(16) ms).

Figure 4.36: Time distribution of $^{64}$As decay events in the DSSSD 1. The red curve is the fit result. The dashed red line is the $^{64}$As contribution and the blue line the contribution of the daughter $^{64}$Ge. A half-life of 69.0(14) ms was found.
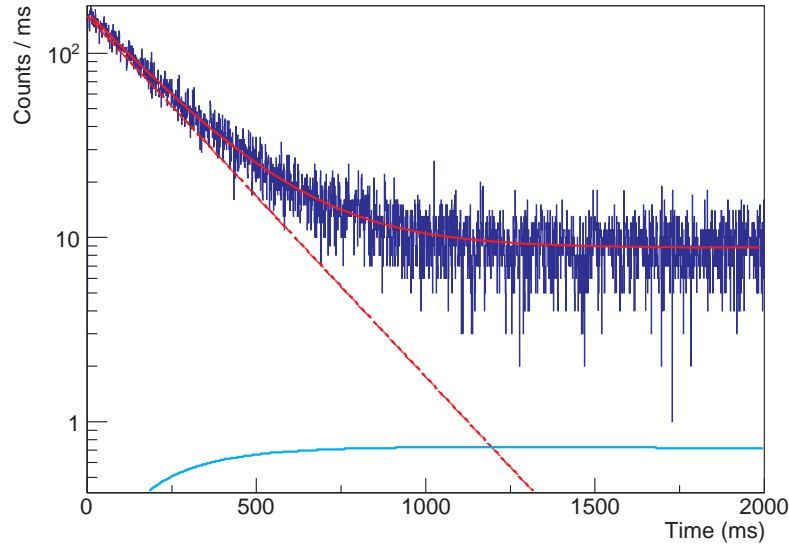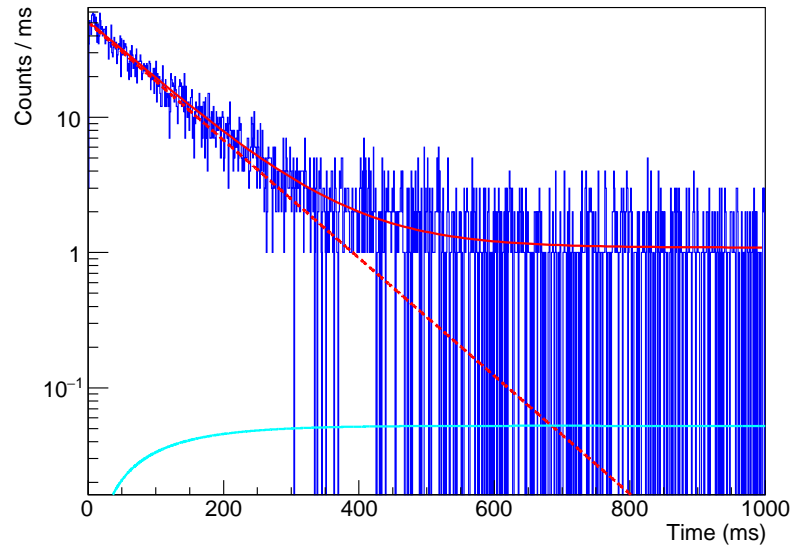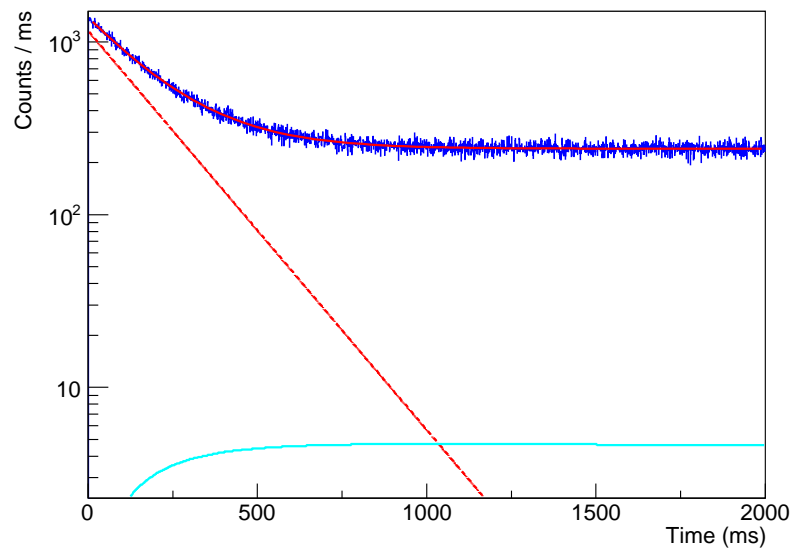


Figure 4.37: Time distribution of $^{65}$As decay events in the DSSSD 1. The red curve is the fit result. The dashed red line is the $^{65}$As contribution and the blue line the contribution of the daughter $^{65}$Ge. A half-life of 130.3(6) ms was found.

## 4.5　Conclusion and perspectives

The RIBF4R1 experiment lead at the BigRIPS fragment separator allowed to perform a new study beyond the proton drip line with the discovery of the 2p decay of $^{67}$Kr. Proton-rich nuclei in the vicinity of krypton were also produced, allowing an improvement of the knowledge of their decay properties: half-life, proton branching ratio and, in few cases, the decay structure ($^{61}$Ge and $^{65}$Se). Indeed first observation of the decay of $^{59}$Ge, $^{63}$Se and $^{68}$Kr was possible through the measurement of their half-lives. New measurements of the $\beta$-delayed proton emitters $^{65}$Se, $^{61}$Ge and $^{57}$Zn give more accurate values of their half-lives and their proton branching ratios. In particular, the $\beta p$ decay scheme of $^{65}$Se was clarified. The $\beta$ decay of $^{55}$Cu, $^{56}$Cu, $^{60}$Ga, $^{63}$Ge, $^{64}$As and $^{65}$As was studied. The new half-life estimates of these nuclei are more accurate. The properties measured here are ingredients to the $rp$-process calculations, influencing their precision. The half-lives and proton branching ratios of these nuclei are summarised in table 4.8.

| Nucleus | $T_z$ | $T_{1/2}$ (ms) | | $P_p$ (%) | |
|---|---|---|---|---|---|
| | | Lit. | This work | Lit. | This work |
| $^{63}$Se | $-5/2$ | | 13.2(39) | | 100 |
| $^{59}$Ge | $-5/2$ | | 13.3(17) | | 100 |
| $^{68}$Kr | $-2$ | | 21.6(33) | | $89^{+11}_{-10}$ |
| $^{69}$Kr | $-3/2$ | 28(1) [DS14] | 27.8(16) | $99^{+1}_{-11}$ [Rog11b] | $93^{+7}_{-6}$ |
| | | 27(3) [Rog11b] | | | |
| $^{65}$Se | | 33(4) [Rog11b] | 34.2(7) | $88^{+12}_{-13}$ [Rog11b] | $94^{+6}_{-4}$ |
| $^{61}$Ge | | 45(6) [Bla07], | 40.7(4) | 62(4) [Bla07] | 87(3) |
| | | 40(15) [Hot87] | | | |
| $^{57}$Zn | | 48(3) [Bla07] | 45.7(6) | 78(17) [Bla07] | 86(3) |
| | | 40(10) [Vie76] | | | |
| $^{55}$Cu | | 57(3) [Tri13] | 55.4(18) | 0 [Tri13] | |
| | | 27(8) [Dos07] | | 15.0(43) [Dos07] | |
| $^{64}$As | $-1$ | 72(6) [Rog14] | 69.0(14) | | |
| | | $18^{+43}_{-7}$ [LJ02] | | | |
| $^{60}$Ga | | 76(3) [Kuc17] | 70.8(20) | 1.6(7) [Maz01] | |
| | | 70(13) [LJ02] | | | |
| | | 70(15) [Maz01] | | | |
| $^{56}$Cu | | 80(2) [Kuc17] | 80.2(7) | 0.40(12) [Bor01] | |
| | | 82(9) [LJ02] | | | |
| | | 93(3) [Bor01] | | | |
| | | 78(15) [Ram98] | | | |
| $^{65}$As | $-1/2$ | 126(5) [Rog14] | 130.3(6) | | |
| | | 128(16) [Bro10] | | | |
| $^{63}$Ge | | 156(11) [Kuc17] | 153.6(11) | | |
| | | 149(4) [Rog14] | | | |
| | | 150(9) [Bla02] | | | |

Table 4.8: Experimental half-life and total proton branching ratios of the $\beta$ and $\beta$-delayed proton emitters studied in this work. These values are compared with the previous works. Nuclei without proton branching ratio value decay only by $\beta$ radioactivity.

### 4.5.1　Two-proton radioactivity

$^{67}$Kr is the heaviest 2p emitters observed until now. It is also the lowest 2p branching observed, 37(14)% against more than 50% for the other emitters (cf. table 1.5). The decay energy of 1690(17) keV is in agreement with calculations based on local mass models. The 2p partial half-life of 20(11) ms is in disagreement with the three-body calculations from [Gri03].

New estimates with the IDDM model [Gri17] show that the 2p decay of $^{67}$Kr could be a transitional case between sequential and true 2p decay. The nature of this decay depends on the position of the $^{66}$Br ground state with respect to $^{67}$Kr one and the orbital configuration of the $^{67}$Kr valence protons. A measurement of the distribution of the energy sharing between the two protons will clarify the $^{67}$Kr case (one peak for true 2p radioactivity, two peaks for sequential decay). An experiment with a time projection chamber is forseen in the coming years. The ACTAR TPC described in chapter 5 will be used to perform a new measurement of $^{67}$Kr decay at RIBF.

### 4.5.2 Astrophysical implications

The study of the $\beta p$ and $\beta$ decays of nuclei in the vicinity of 2p emitters cited before and the proton drip line has astrophysical applications with $rp$ process calculations in X-ray bursts on the surface of accreting neutron stars [Sch04]. These bursts are powered by successive thermonuclear reactions represented in figure 4.38 with the concerned elements. The reactions are triggered by processes between the lightest isotopes powering these stars. A mix of helium and hydrogen are first burned via $3\alpha$ reaction. This latter produces beryllium from the fusion of two helium nuclei and carbon from fusion between helium and beryllium. The breakout from hot HCNO cycle occurs via the $\alpha p$ process producing nuclei for the $rp$ process. This latter consists in successive rapid-proton captures $(p, \gamma)$ and slower $\beta^+$ decays. These two reactions are in competition, the $\beta^+$ decay slowing the proton capture. Some nuclei involved in the process have particularly long $\beta$-decay half-lives or low proton capture rate, they are called "waiting points". The waiting points in our region of interest are $^{64}$Ge, $^{68}$Se and $^{72}$Kr [Sch98].
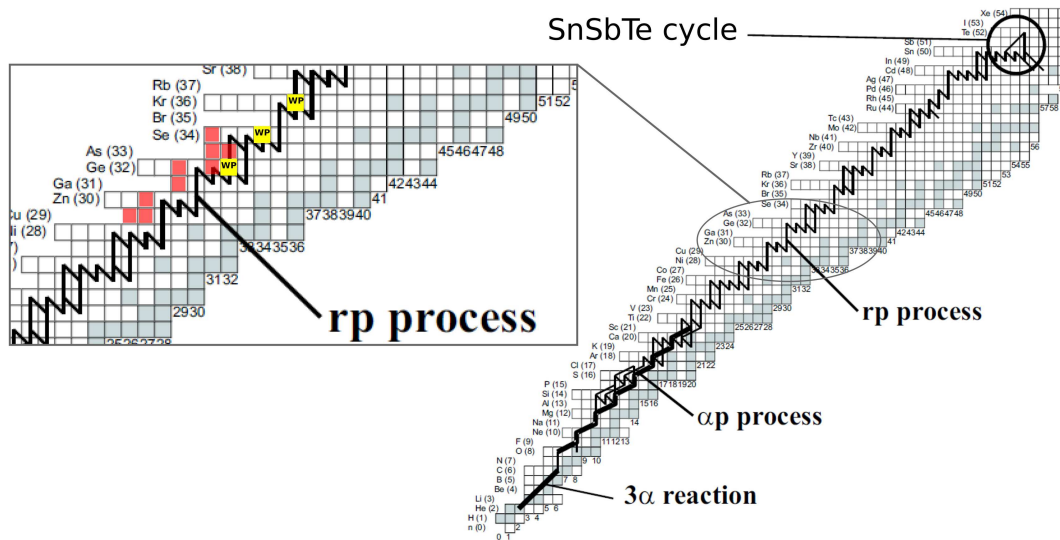


Figure 4.38: Reaction flow integrated over time of an x-ray burst with the triple-$\alpha$ reaction, $\alpha p$ and $rp$ processes. The endpoint of the $rp$ process is the SnSbTe cycle (depending on the models). The inset shows the region of interest with the nuclei measured in this work marked by red squares. The waiting points are shown in yellow. Figure adapted from [Sch04].

The mass region studied in this work is illustrated in the inset of figure 4.38. The nuclei represented by a red square were measured in this work with a better precision of their decay half-lives or proton branching ratio. As one can see in figure, the $\beta$ decay of $^{64}$As and $\beta p$ decay of $^{65}$Se directly feed the waiting point $^{64}$Ge. The half-life of $^{63}$Ge has a direct effect on the $rp$ path to reach this waiting point. The half-life values from the present work can be used for new $rp$-process calculations with a better precision.

# Chapter 5

# The ACTAR time projection chamber at CENBG

The next step to study the 2p radioactivity of $^{67}$Kr presented in chapter 4 will be an experiment with a time projection chamber (TPC) as it was performed in the past for the other 2p emitters presented in chapter 1, $^{45}$Fe and $^{54}$Zn.

Many other TPCs are used in nuclear physics around the world. As an example, for the 2p radioactivity study, an optical TPC (OTPC) [Mie07b] was also used (cf. chapter 1). The two TPCs developed in France for nuclear physics were the CENBG TPC [Bla08b, Bla10] and MAYA [Dem03, Dem07]. The latter was used as an active target (the detector is used as the target).

A new generation of TPC in France is under development, gathering the common interests of the MAYA and the CENBG TPC collaborations. It satisfies the physics studies of the two former detectors (2p radioactivity and active target). This next generation is developed in the ACTAR TPC (ACtive TARget for TPC) collaboration. This new TPC is developed within an ERC (European Research Council) Starting Grant funding. The collaboration is composed of people from various laboratories in Europe:

- Centre d'Etudes Nucléaires de Bordeaux Gradignan (CENBG)

- Grand Accélérateur National d'Ions Lourds (GANIL)

- Institut de Physique Nucléaire d'Orsay (IPNO)

- Institut de Recherche Fondamentale sur les lois de l'Univers (IRFU/CEA)

- Katholieke Universiteit Leuven (KU Leuven)

- Universidade de Santiago de Compostela (USC)

The project consists in the development of two new chambers using the same technology, with different geometries, a square one (development at GANIL), for reaction studies (with large transverse particle tracks), and a rectangular one (development at CENBG) for 2p radioactivity studies (short transverse tracks and larger implantation depth). These detectors are equipped with a new detection plane technology to reduce the number of connections due to the high number of channels. The pads are connected to the General Electronics for TPCs (GET) [Pol12, Pol17], a customisable electronics.

In this work, we will focus only on the development of CENBG chamber. Tests of the pad plane were performed to evaluate the energy resolution and validate the used technology. To compute the charge deposit on the pads, the energy loss of the particles and reconstruct the trajectories, the input signal in each hit pad needs to be reconstruct from the output signal. The characterisation of the GET electronics and the first results of the demonstrator are also presented in this chapter.

## 5.1   Characteristics of time projection chambers

A TPC is a gaseous detector functioning in proportional mode. An electric field is created between a cathode and an anode. The charged particles ionise the gas of the active volume and the electrons drift along the electric field to a position sensitive detector (micro-strips as an example), named the collection plane. An amplifier can also be used with this plane. The sensitive detector thus provides a 2D projection of the signal of energy loss in the active volume. From the drift time of this signal, one can extract the third dimension.

The generalities of a TPC are presented here, with the active volume and the amplification device.

### 5.1.1   Active volume

The active volume is composed of a mixture of a noble gas and a hydrocarbon. A common gas mixture is P10 (90% Ar - 10% $CH_4$). The advantage of a noble gas is a weak diffusion coefficient of the electrons in the gas which gives a better spatial resolution. The mixture with a hydrocarbon also dissipates the UV photons produced by the electron avalanches.

The drift velocity of the electrons is a function of the pressure $p$ and the electric field $\|\overrightarrow{E}\|$ [Kno10]:

$$v_d = \mu \frac{\|\overrightarrow{E}\|}{p} \tag{5.1}$$

The mobility of the electrons $\mu$ is constant over wide ranges of pressure and electric field strength. Typical values are between 1 and $10^{-4}$ $m^2.atm.V^{-1}.s$. Contrary to a pure hydrocarbon gas, a mixture with a noble gas reduces the variation of the drift velocity with the electric field and pressure as shown in figure 5.1. Additionally, the track length is sensitive to the gas pressure: lower pressure will result longer tracks.
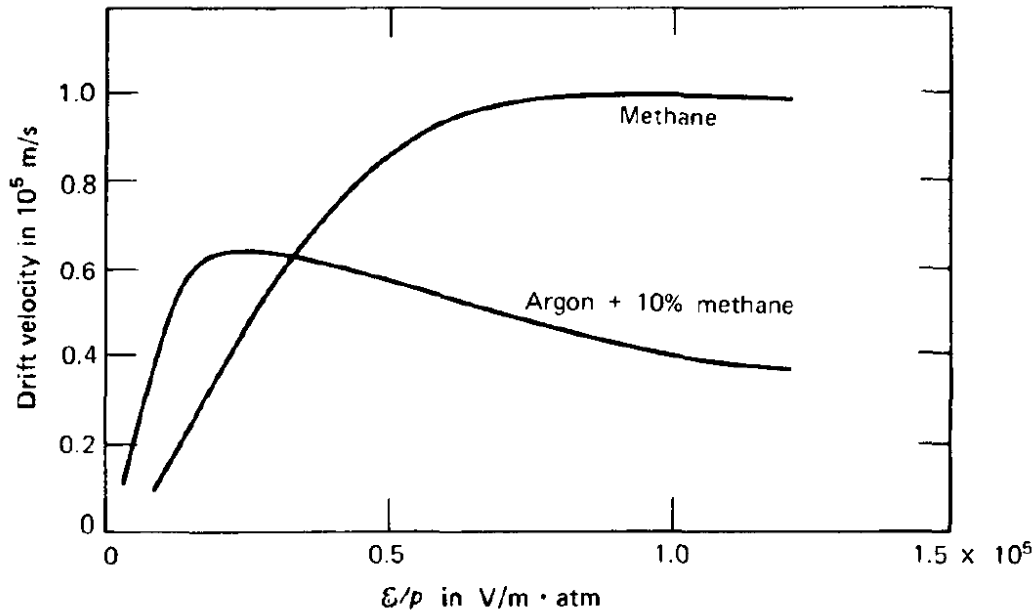


Figure 5.1: Electrons drift velocity dependence with the ratio of the electric field strength over the gas pressure. The behaviours for pure methane ($CH_4$) and P10 gas are drawn. Taken from [Kno10].

The signal collected on the position sensitive detector gives a two-dimensional projection of the energy loss of the particle. With the position-sensitive detection plane, one has also a projection of the trajectory of the charged particle on X and Y. The third dimension can be extracted from the timing signal of the position patterns of the detection plane (strips or pads for ACTAR TPC). The knowledge of the drift velocity of the ionisation electrons and the time

of the hit pattern gives a relative Z value. Here, the drift velocity $v_d$ is deduced from simulations or calibration sources. With the difference of time between two positions on the detection plane, one obtains the difference:

$$\Delta z = v_d(t_{\text{ref}} - t_i) \tag{5.2}$$

### 5.1.2 Signal amplification

The TPC is composed of drift region, drifting the ionisation electrons to the collection plane. The field of this drift region is generally a few kV/cm. At the level of the detection plane, the electrons can be amplified before the signal collection. An amplification region is created between the plane and an amplification device. The two main technologies are the GEM (Gas Electron Multiplier) and the micromegas (MICRO-MEsh-GAseous Structure).

**GEM** This system was introduced in 1997 [Sau97, Sau16]. A GEM is an isolating plate of kapton (typically 50 $\mu$m thick) with copper deposited on its two faces (a few $\mu$m). This plate is drilled with holes of 70-$\mu$m diameter, distant 100 $\mu$m from each others typically. A microscopic view is shown on the left of figure 5.2. One applies a high voltage between the two copper faces, typically around 300 V. The field strength is increased along the central field line as illustrated on the right of figure 5.2. This high-field region inside each hole (up to 40 kV/cm) causes electron avalanches, amplifying the signal. The applied voltage and also the gas pressure defines
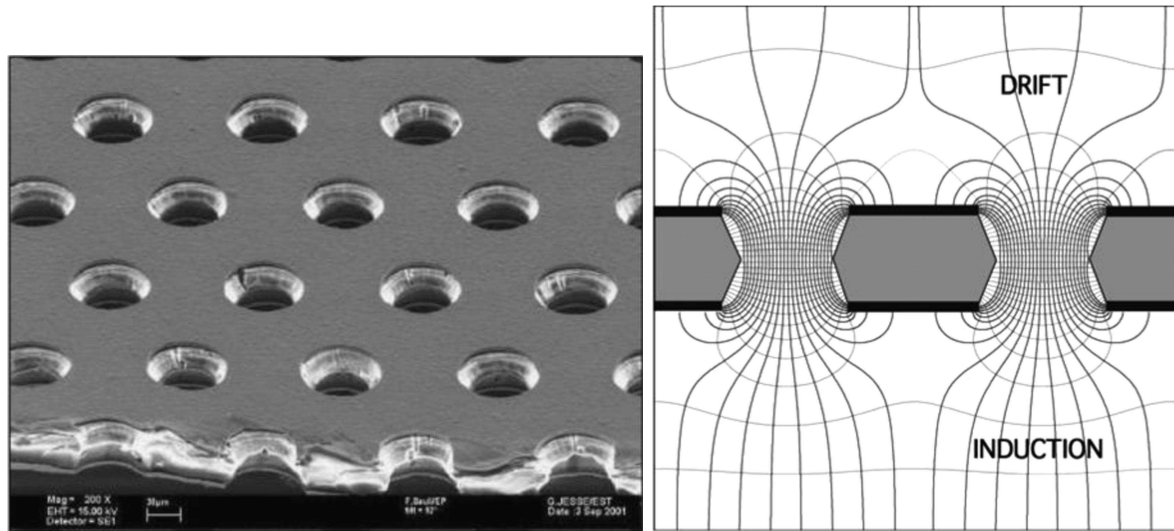


Figure 5.2: Illustration of a GEM. Left: microscope picture of a GEM. Right: electric field map of a GEM. Because of the applied voltage between the two faces, the field strength is increased inside the holes, causing electron avalanches. Adapted from [Sau16].

the amplification gain. Moreover, stacking many GEMs multiplies the gain (typically a few tens per GEM).

**Micromegas** The micromegas technology was developed in 1996 [Gio96, Gio98]. A micromegas is a two-stage parallel plate detector. The first designed prototype of micromegas is illustrated on the left part of the figure 5.3.

Anode micro-elements (strips or pads) are maintained distant from a cathode by small insulating pillars. This gap of a hundred of $\mu$m is subject to a high electric field of tens kV/cm to produce electron avalanches and amplify the collected signal (right part of figure 5.3). The charge collection of a micromegas is fast, allowing higher counting rates up to $10^5$-$10^6$ part/mm$^2$/s.

A micromegas is composed of the elements shown in figure 5.3. The main part of the micromegas, the micromesh, is metallic grid openings of a few $\mu$m diameter. Made of nickel, the mesh has generally a transparency of the order of 45%. This mesh is maintained by spacers (pillars) made of quartz fibres, glued on the frame.
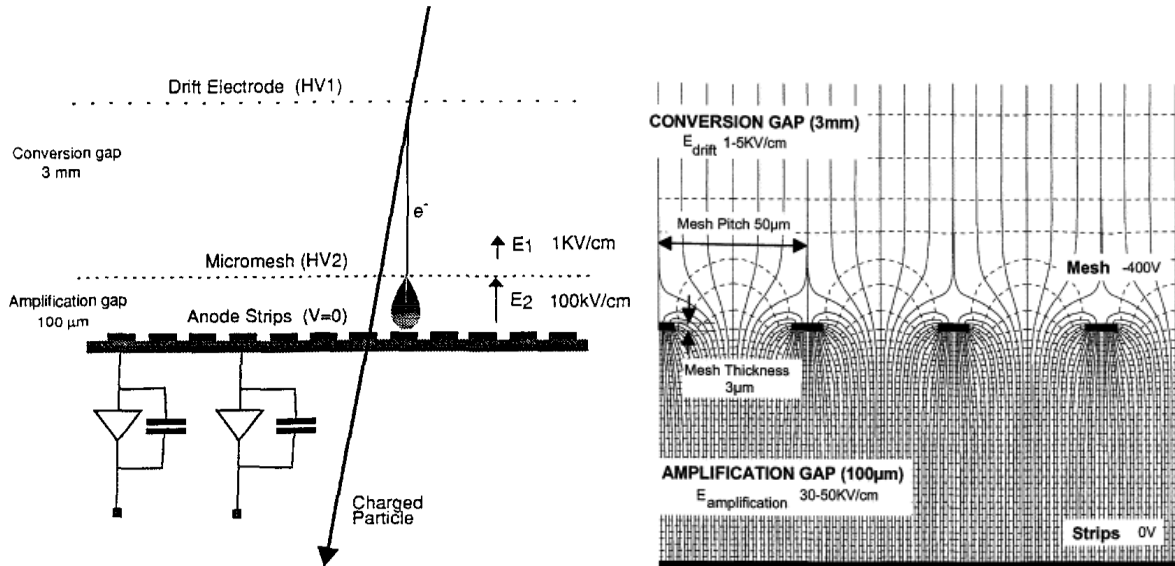
Figure 5.3: Scheme of the micromegas principle. On the left part is shown the general principle. The electrons originating from ionisation of the gas are drifted by an electric field between a drift electrode and a micromesh. Then they are amplified by a high-strength electric field between this mesh and strips at a zero electric potential. Preamplifiers collect the strip signals. The strength of the electric field is simulated on the right part of the figure. Its intensity highly increases in the amplification gap causing electron avalanches. Left part taken from [Gio96], right part taken from [Gio98].

A good test of a micromegas is the measurement with a $^{55}$Fe source which produces X rays at 5.9 keV. The average resolution of a micromegas is usually 14% (FWHM) [Gio96].

In order to reduce production and material costs and industrialise the process to face large amounts of detectors required by big experiments at LHC in CERN, micromegas on PCB (Printed Circuit Board) was developed in the early 2000s [Gio06]. This solution is used for the chambers of ACTAR TPC.

## 5.2  Time projection chambers preceding the ACTAR TPC

The ACTAR TPC project has emerged from the two former TPC and active target projects developed in France in the 2000s: the MAYA chamber from GANIL [Dem03, Dem07] (active target) and the 2p radioactivity study TPC from CENBG [Bla08b, Bla10]. These two detectors are both micro-pattern gaseous detectors (MPGD). Their detection planes are composed of detectors with sizes of the order of mm and cm (pads for MAYA, strips for CENBG TPC). MPGD have the advantages of being robust, cost effective and can be produced in a variety of shapes and sizes. In this section, the main highlights of these two detectors are presented.

### 5.2.1  MAYA

MAYA was developed in GANIL in the 2000s. Its active volume of 28x25x20 cm$^3$ is filled with gaseous hydrogen or helium, most of the time mixed with $C_4H_{10}$ or $CF_4$. The other parts of the detectors are shown in figure 5.4. The amplification zone is a Frish grid located above a plane of anode wires. Below this plane, there is a segmented cathode composed of hexagonal pads. MAYA is segmented in $33 \times 32$ pads with sides of 5 mm each (see right part of figure 5.4). Ancillary detectors can be mounted on the exit side of the chamber to detect charged particles escaping from the active volume. Usually, additional CsI crystals and silicon or diamond detectors are placed on the sides of the active volume to detect particles escaping from the active volume.

MAYA allows to reconstruct in three dimensions the trajectories of the particles and the vertices of the interactions [Rog11a]. Transfer reactions ([Tan08]) and resonance studies (as an
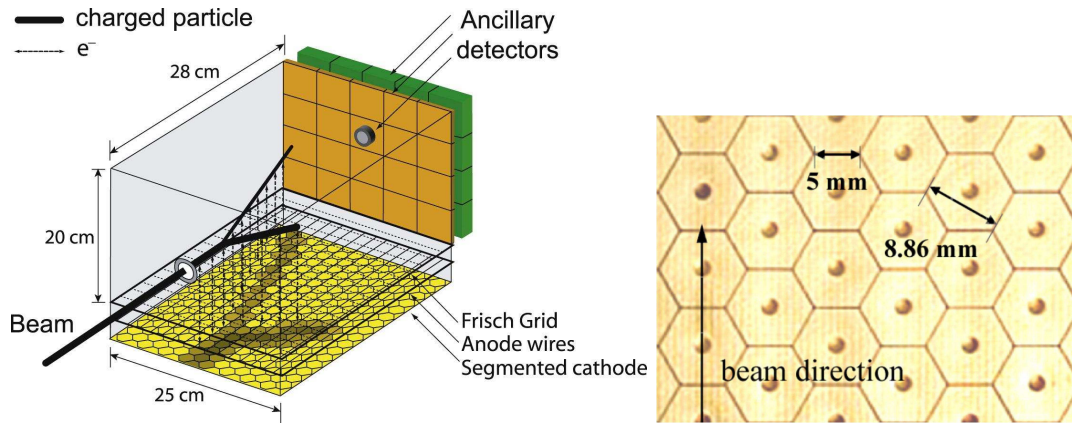
Figure 5.4: On the left is shown a schematic view of the MAYA active target. CsI detectors are situated behind the active volume to detect charged particles leaving the gas. Taken from [Rog11a]. The detection plane represented on the right is composed of hexagonal pads. Taken from [Dem07].

example [Caa07]) were performed with the MAYA detector.

### 5.2.2 The CENBG time projection chamber

The CENBG TPC was also developed in the 2000s [Bla08b, Bla10] but its purpose was the 2p and $\beta p$ decay studies. The view of the chamber and its inside is shown in figure 5.5.

The active volume is surrounded by drift electrodes maintained by four pillars (see right picture in figure 5.5). These electrodes create equi-potential surfaces to have homogeneous vertical electric field along the height of the volume. The active volume is $15 \times 15 \times 15$ cm$^3$ filled with P10 gas. The amplification is performed by GEMs stacked above the detection plane, composed of two perpendicular sets of horizontal strips.
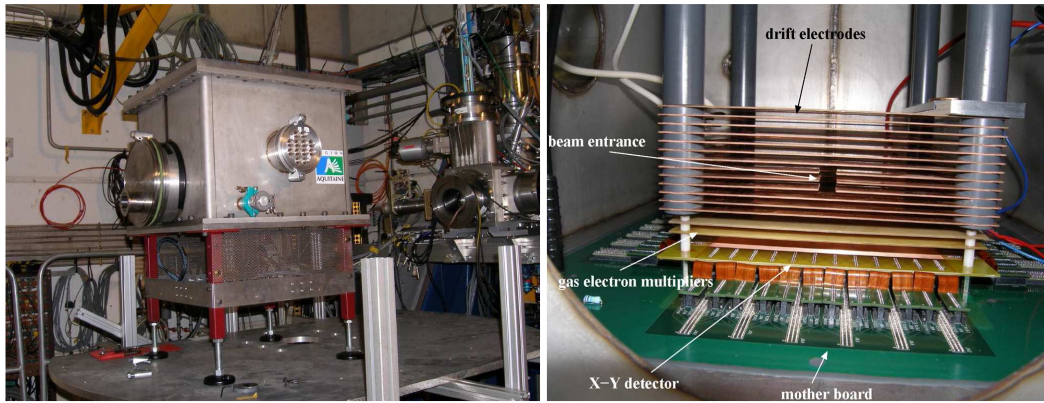


Figure 5.5: CENBG TPC installed at the exit of the LISE3 beam-line (GANIL) on the left picture. The picture on the right is a view of the inside of the chamber. The drift electrodes maintain a constant vertical electric field. The electrons are amplified by the GEMs (two for this test) at the bottom of the chamber before being collected by the XY detection strips. Adapted from [Bla10].

The detection matrix of the TPC gives two projections of the particles trajectories along X and Y axis respectively. It is composed of $2 \times 768 = 1536$ strips covering a $15.36 \times 15.36$ cm$^2$ area (cf. figure 5.6). These strips are made of copper. The upper strips are the anodes and the lower the cathodes. These two sides are separated by 50 $\mu$m of kapton. The strips are 50-$\mu$m wide with a 100 $\mu$m pitch. The cathodes are 150-$\mu$m wide with a pitch of 200 $\mu$m. The anodes are connected two by two to have the same pitch on X and Y i.e. 200 $\mu$m. The energy resolution achieved by this detection matrix is 150 keV (FWHM) at 5 MeV (three-alpha source) [Bla08b].
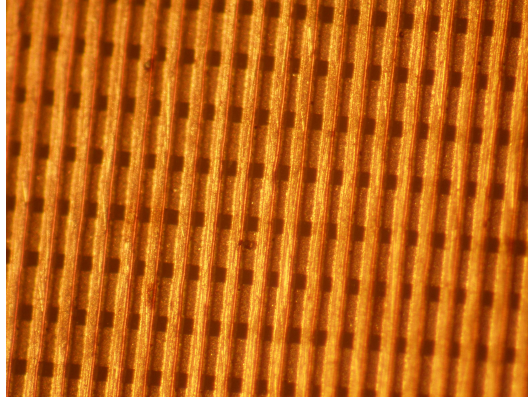
Figure 5.6: Photograph of the XY detection matrix of the CENBG TPC. This detection plane is composed of two perpendicular copper-coated kapton foils. Taken from [Bla10].

The channels are readout by ASICs developed for this TPC, each ASIC managing 64 channels. One out of two channel is read by the ASICs, thus 12 ASICs read $2 \times 384$ channels. The signal amplitude and timing is read on each channel. The amplitude of timing signals are multiplexed and treated by a VME module that digitises the signals. The dead time of the acquisition is 1.4 ms.

### 5.2.3   The next generation: ACTAR TPC

The two TPCs presented above have limitations. That is why a new TPC project (ACTAR TPC) is under development to succeed them.

The MAYA detector does not give a timing information from the pads. Time is measured on the wires. This information is thus obtained only transversely because the wires are placed along the length of the detector. The spatial resolution for the energy and time is not the same.

For the CENBG TPC, there is no real three-dimension reconstruction of the trajectories since the detection plane is in fact two one-dimension projections instead of a real two-dimension projection. Moreover the signal deposited on a strip is not fully coded but only its amplitude. Thus there is not a full digitisation on the Z axis. Furthermore this TPC has a high dead time (1.4 ms). It leads to a lot of event losses because the 2p emitters have half-lives of a few ms.

The ACTAR TPC solves these problems. The detection plane is composed of pads to have a true 2D projection of the signal. The pads are connected to the GET electronics which samples in time the collected signal on each pad. As a result, it allows a full digitisation in three dimensions of the charge deposit along the particle tracks (voxels). A dedicated 2p mode of this electronics allows to achieve a dead time of a few $\mu$s instead of ms.

## 5.3   Demonstrator tests at CENBG

The ACTAR TPC collaboration aims to develop two TPCs. They will be both equipped with a high-density detection plane composed of 16384 pads of $2 \times 2$ mm$^2$ (25 pads/cm$^2$). The active volume is inside a chamber built from a stainless steel skeleton. The electric field is generated by a drift cage and the amplification by a micromegas.

A TPC with a square pad plane is built by GANIL: the reaction chamber. With a $128 \times 128$ pads collection plane, it allows the measurement of large transverse tracks.

A TPC with a rectangular pad plane, the decay chamber, is built at CENBG. This TPC is dedicated to the 2p radioactivity study. The size of the detection plane, $256 \times 64$ pads, allows a larger implantation depth but short transverse tracks. This latter is not a limiting parameter for 2p radioactivity studies since the two protons have a small mean path in the active volume. As the MAYA detector, these TPCs can be equipped by ancillary detectors on each side: Si or CsI detectors for escaping particles, LaBr3 or HPGe for $\gamma$ rays.

Currently two demonstrators of the TPCs are available at GANIL and CENBG respectively. They are composed of $32 \times 64 = 2048$ pads. Test experiments were already performed with the GANIL demonstrator at IPNO in 2015: a first with the $^{12}C(\alpha, \alpha')^{12}C$ reaction to study Hoyle states of $^{12}C$ and a second with $^{6}Li(\alpha,^{10}B)$ to study the $\alpha$ clustering of $^{10}B$. Experiments are scheduled with the final detectors in the following years including a 2p radioactivity study of $^{54}Zn$ or $^{48}Ni$ at GANIL in 2018. The two final detectors should be produced by the end of 2017.

The CENBG demonstrator currently under test at Bordeaux is shown in figure 5.7. The detection plane of the demonstrator (called FAKIR) allowed to test the feasibility of the production process and its performances. The TPC is equipped by the GET electronics, a four-stage electronics acquisition for TPCs. This electronics is composed of boards named AsAd (front-end board), CoBo (data collection) and MUTANT (trigger and timing), visible in figure 5.7. Their description is available in section 5.3.4.
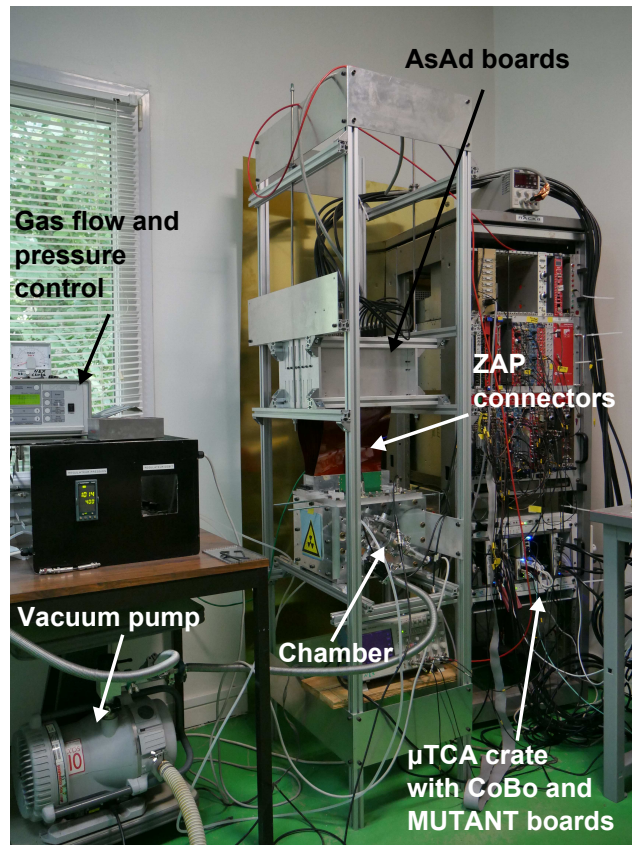


Figure 5.7: TPC demonstrator with GET electronics at CENBG. The chamber (middle) is fed by P10 gas with a gas regulation unit that maintains a constant pressure and flow. The chamber is connected to the first stage of GET, 8 AsAd cards, by the ZAP connectors developed at CENBG. The AsAd cards are connected to the $\mu$TCA crate, housing the GET modules CoBo and MUTANT. The vacuum pump allows to empty the chamber and circulate the gas.

### 5.3.1 Pad plane technology

The signal amplification is performed by a Micromegas glued on a PCB board (cf. section 5.1.2). Two technical solutions are used on the two demonstrators. The chamber from GANIL utilises a standard building process. The micromegas is on a standard PCB glued on the metallic flange. The connectors are extracted through it. But the connectors are fragile and one has to route the signal from the pads. This includes additional possibilities of perturbations. Moreover, non-negligible deformations and sealing problems were observed at GANIL on this technology. Another solution, based on metal-core PCB, was developed for the detection plane of the demonstrator of CENBG. The pads are directly connected through the PCB avoiding problems with fragile connections and routing. Thus the PCB is used as the interface between

the inner and outer sides of the gas volume. The use of a metal core PCB significantly increases the robustness of the circuit to handle mechanical constraints due to pressure difference between inside and outside the chamber: it reduces deformation of the plane (and avoids its destruction).

Three prototypes of 2048 pads were made in collaboration with the PCB workshop at CERN and the FEDD company (Fabrique Electronique De Dordogne) between 2013 and 2016. A first pad plane prototype was manufactured in 2012 with only two lines of pads to test the soldering process at CERN. A second was made in 2013 with the 2048 pads to test the process improvements and perform first measurements at CENBG. The last prototype built in 2015 equips the TPC demonstrator at CENBG. Now this technology is ready for the production of the pad plane for the final detector. The main aspects of its manufacturing are explained here.

## Manufacturing

At first an aluminium plate (3.8 mm thick) is drilled with 2048 holes of 1.5 mm diameter. Their centers are 2 mm distant (first photograph in figure 5.8). A stainless steel plate of 7 mm thick will be used for the final pad plane. The holes are filled with an epoxy resin and the aluminium plate is placed in an epoxy frame. Then a Krempel adhesive with polyimide (a type of polymer) are fixed on it. A new drilling is performed and the holes are metallized (nickel-gold) to insert and solder the connectors. The PCB is laminated and the micromesh deposited. Finally an chemical etching builds the pillars of the micromegas. The value of the gap is 130 $\mu$m. The pad plane after manufacturing is shown on the central picture of the figure 5.8. The connectors are visible at the back side of the PCB in figure 5.8 (picture on the right). The main layers of the PCB are represented in figure 5.9.
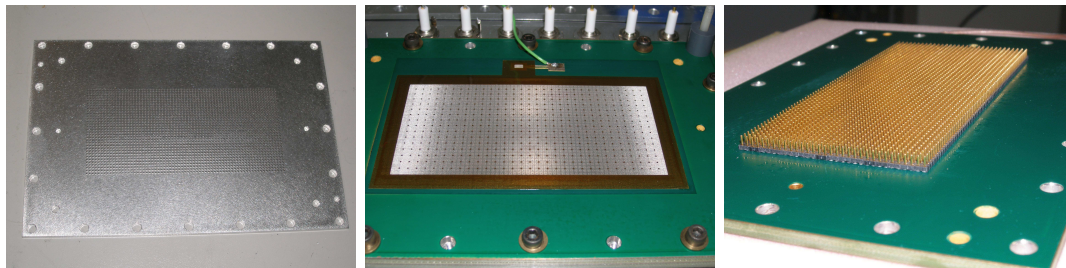


Figure 5.8: Conception of the pad plane (FAKIR) of the TPC demonstrator at CENBG. The aluminium plate on the left is drilled of 2048 holes at the beginning of the process. The resulting detector after the building process is on the middle photograph. At the back of the PCB, one can see the pins used for connection to GET (right photograph).
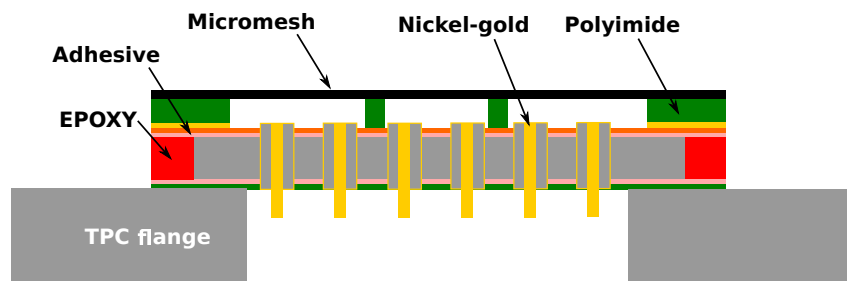


Figure 5.9: Illustration (simplified) of the pad plane (FAKIR) mounted on the TPC demonstrator at CENBG (not at scale). The micromesh is located above it. This latter is supported by pillars in polyimide (green). The aluminium plate (grey) is in an epoxy frame (red). The connectors made of nickel-gold are directly in contact with the pads (yellow). The flange of the TPC is screwed to the aluminium plate of the PCB.

### 5.3.2  The field cage

A field cage is fixed above the pad plane to create the electric drift field. The cage developed by GANIL which is mounted on the CENBG demonstrator is shown in figure 5.10. This cage is composed of a top electrode (cathode). Its voltage is a few thousands Volts (-2 kV during the tests at CENBG). Wires (copper) of 20 $\mu$m diameter and 1 mm spacing are maintained by four pillars. The optical transparency of the cage is around 98% allowing to put a radioactive source on it for test measurements. The wires are at a decreasing voltage with resistances connecting neighbouring wires. They create a gradient of electrical potential to have a homogeneous vertical electric field. The last wire before the pad plane is at a voltage slightly higher than the micromesh one (around 5 V more).
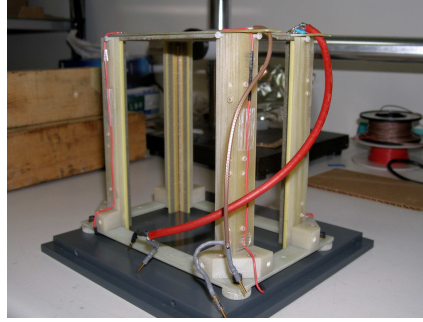


Figure 5.10: Field cage equipping the TPC demonstrator of the CENBG. Copper wires create a gradient of electric potential to reduce electric field inhomogeneities. A voltage a little higher than the micromesh one is applied on the last wire (bottom here) before the pad plane.

### 5.3.3  Pad plane characterisation

Before assembling the full demonstrator, the micromegas of the pad plane FAKIR composed of 2048 pads was tested with radioactive sources to evaluate the resolution of this latter. A metallic mesh was put above the pad plane (around 5 cm) to create an electric field between the electrode and the micromesh. The device is represented on the figure 5.11. A high voltage
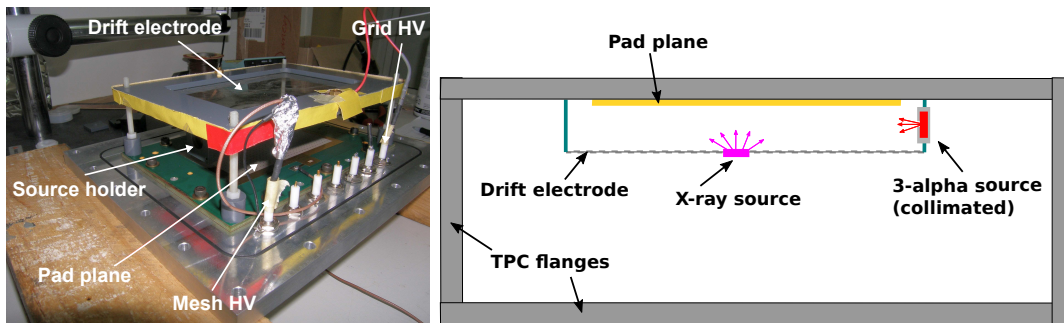


Figure 5.11: Photograph and scheme of the test setup of the pad plane characterisation. A drift electrode made of a metallic mesh is mounted 5 cm above the pad plane. Two SHV connectors are used for the high voltages: the micromesh and the drift electrode (top grid). The third connector is dedicated to the high voltage of the bottom of the drift cage and thus is not used here. As shown on the scheme, the source holder is placed on a side of the active volume for three-alpha source tests because of the long mean path of $\alpha$ particles in the gas. The $^{55}$Fe source was put directly on the drift electrode because of the low mean path of X rays. All the pad connectors are connected to the ground for the tests.

around -1 kV is applied on the drift electrode. The voltage on the mesh depends on the used source because the required amplification is not the same. Resolution test were made with a collimated three-alpha source ($^{239}$Pu/$^{241}$Am/$^{244}$Cm) and a $^{55}$Fe X-ray source (non collimated). For the three-alpha source with energies around 5-6 MeV, the voltage was set to -350 V to have

low amplification of the signal. For the $^{55}$Fe X-ray source with a peak at a few keV, the voltage was rather higher at -500/-600 V. The P10 gas used for these tests was at a pressure of 1 bar for $^{55}$Fe and 400 mbar for the three-alpha source. Capacitors and resistors are mounted at the high-voltage inputs to filter signals. The electric scheme of the test device is represented in figure 5.12. The electron signal collected on the micromesh is extracted through a charge preamplifier (gain of 20 mV/MeV) connected to the mesh with a decoupling capacitor from the high voltage. During these test measurements all the pads were connected to the ground. The RC circuits in figure have the following values:

- $R_d = R_m = 1$ MΩ

- $C_d = C_m = 4.7$ nF

- $R_{dec} = 51$ kΩ

- $C_{dec} = 2 \times 4.7$ nF

The signal is then treated by an ORTEC 579 fast filter amplifier and a threshold discriminator CAEN N147. The signal is shaped by a spectroscopic amplifier ORTEC 572A. The signal is digitised by a CAEN V875 ADC module. A VME GANIL acquisition system was used to register data.
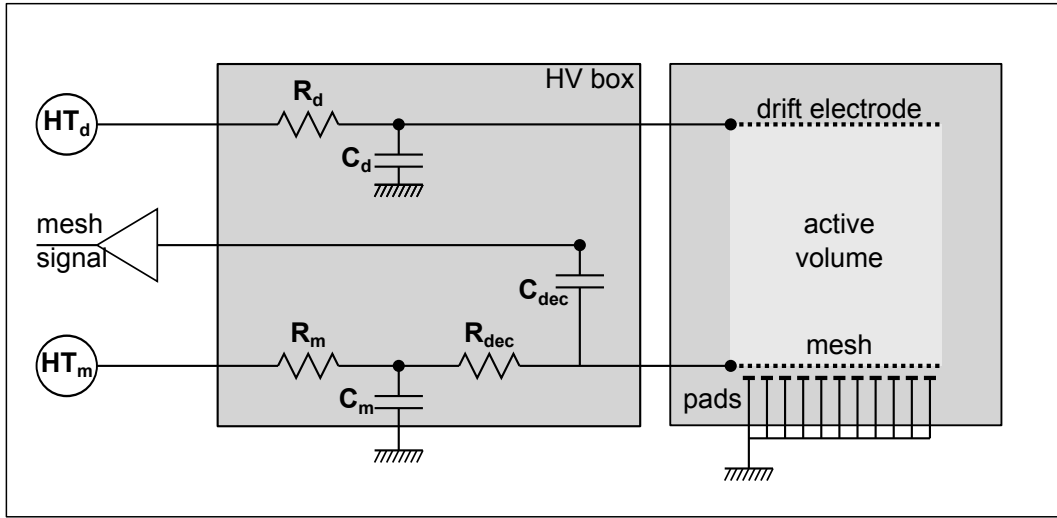


Figure 5.12: Electric scheme of the test phase of the pad plane prototype at CENBG. The high-voltage inputs (for the drift electrode $HT_d$ and for the mesh $HT_m$) are connected through RC circuits for filtering. The micromesh signal is extracted through a capacitor by a charge preamplifier.

The first tests were performed with a three-alpha source emitting three principle peaks at 5.2 MeV ($^{239}$Pu), 5.5 MeV ($^{241}$Am) and 5.8 MeV ($^{244}$Cm) [Kno10]. The source was collimated and placed in the active volume as it is represented in figure 5.11. The same tests were also performed with the field cage but are not presented here. The histogram in figure 5.13 is the total charge collected on the micromesh. The three $\alpha$ peaks are clearly visible. They were fitted by a Gauss function and a constant background. With values of the three peaks and the literature energies we determined the slope of the calibration curve to evaluate the resolution of the central peak at 5.5 MeV ($^{241}$Am). Because of the dead layers between the source and the pad plane, the alpha particles lose energy and the collected energy by the pads is not 5.5 MeV. A Geant4 simulation of the setup allowed to find the energy shift due to this dead zone. The corrected alpha energy of this peak was estimated at 4.8 MeV. The resolution of this peak (FWHM) $w_m$ found from the fit of the three peaks of the spectrum in figure 5.13, can be expressed with the intrinsic resolution $w_d$ and the deposited energy $w_\alpha$ of the alpha particle (around 40 keV here, determined from simulation). One has $w_m = \sqrt{w_d^2 + w_\alpha^2}$. For the 4.8-MeV peak, we found an intrinsic resolution of 150(5) keV (FWHM).
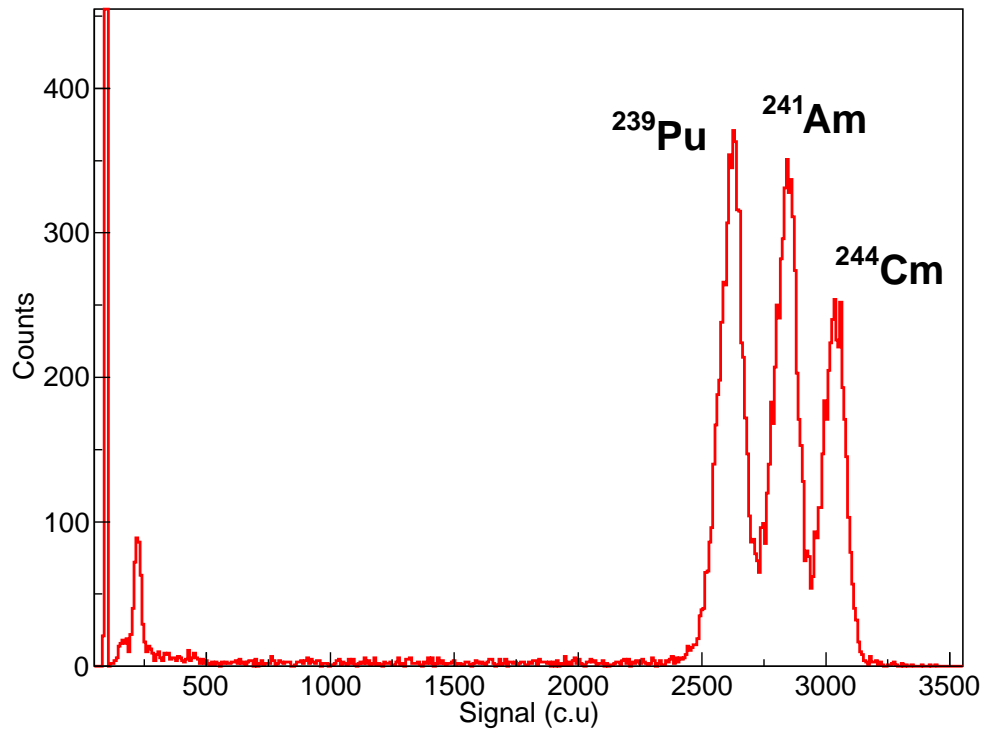
Figure 5.13: Spectrum of the collected charge on the micromesh with a collimated three-alpha source $^{239}$Pu/$^{241}$Am/$^{244}$Cm. The first peak comes from the $\alpha$ decay of $^{239}$Pu at 5.2 MeV, the second from $^{241}$Am at 5.5 MeV and the third from $^{244}$Cm at 5.8 MeV. The origin of the energy peak at 250 c.u. was not investigated.
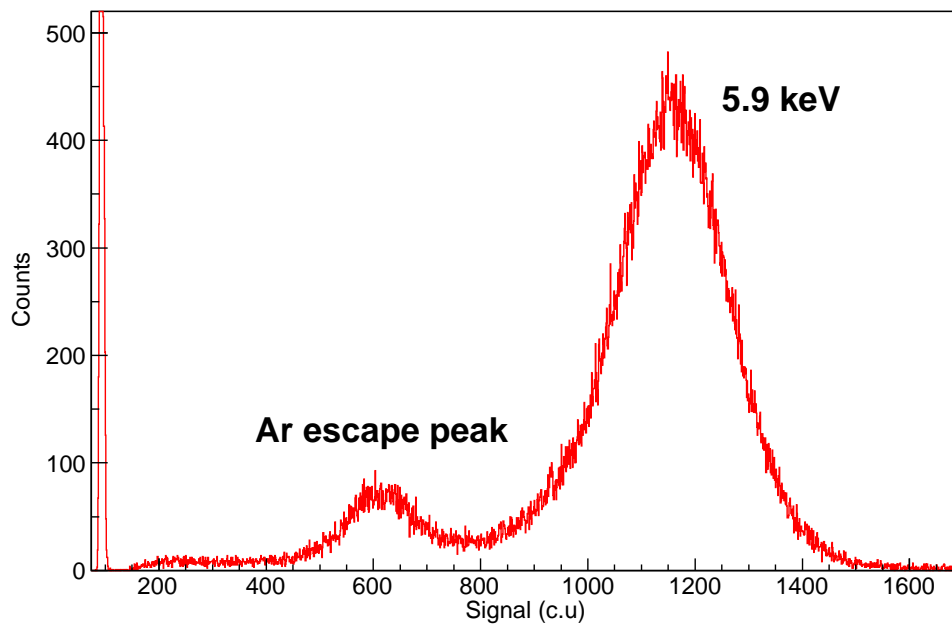


Figure 5.14: Spectrum of the collected charge on the micromesh with a $^{55}$Fe source (non collimated). The X-ray peak at 5.9 keV is seen and the peak from diffusion on the argon K-shell at 3.2 keV.

The resolution test of the micromegas was done with a $^{55}$Fe source. This latter was not collimated and put on the drift electrode on the top of the active volume. The most intense transition of $^{55}$Fe is the X-ray emission from the electronic K-shell at 5.9 keV [Bé04]. A second peak is expected in the energy spectrum since we measure the energy deposit with a P10 gas composed of argon. X rays are diffused on the argon K shell giving electrons at around 3.2 keV. The spectrum obtained on the micromesh is in figure 5.14. The first peak at low energy is the electronics noise. The two others are respectively at 3.2 and 5.9 keV. They were fitted with a Gauss function and a constant background. With the ratio between the centroids and the literature values difference, the slope of the calibration curve is determined and also the resolution is deduced from the peak widths. The FWHM at 5.9 keV is 21.5(5) %, an acceptable resolution for a micromegas.

### 5.3.4   Description of the General Electronics for TPCs

The GET (General Electronics for TPCs) [Pol12, Pol17] is a generic acquisition system developed to equip a variety of TPC experiments around the world as AT-TPC [Suz12], S$\pi$RIT [Sha15] or ACTAR TPC. This system is based on ASIC, FPGA and $\mu$TCA technologies. The general scheme of a GET acquisition is illustrated in figure 5.15.
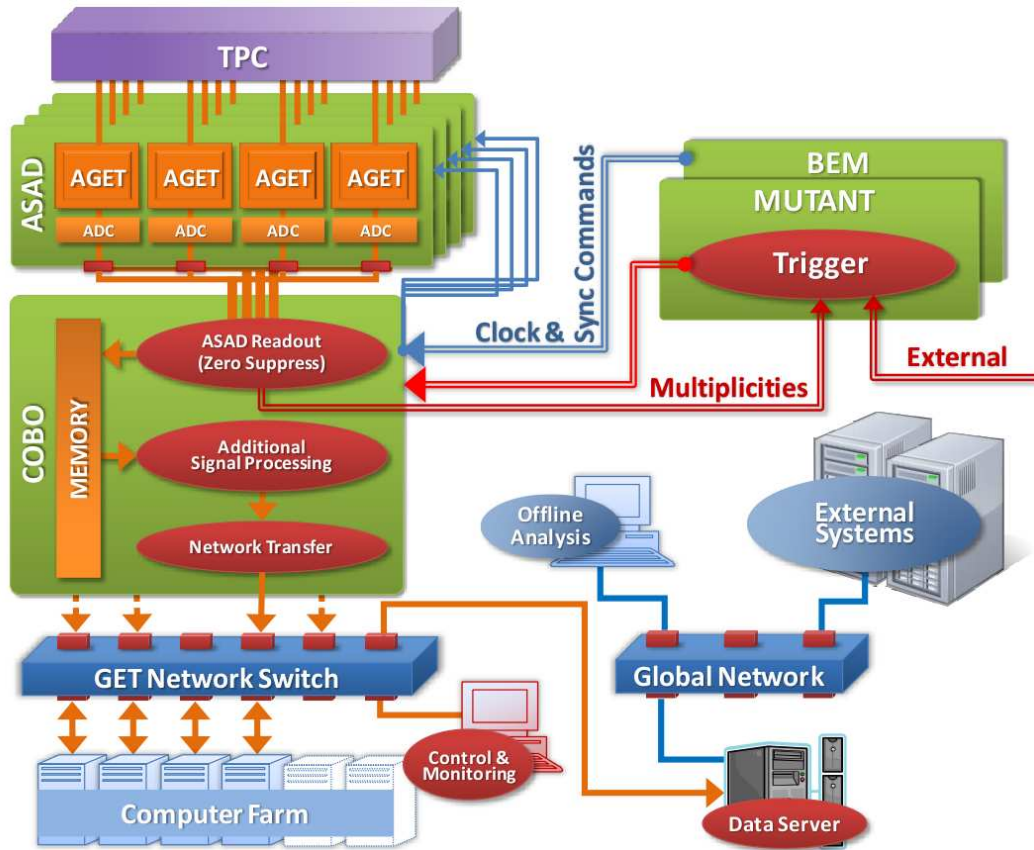


Figure 5.15: Overview of the GET system. The detector is connected to AGET chips (64 channels). They pre-amplify and sample the signal. The signals are then registered and digitised by ADC placed on the AsAd boards (4 AGETs per board). CoBo manages the AsAd readout and data transfer to a storage farm. The module MUTANT synchronises the boards, manages the triggers and time-stamping.

Three main levels compose the GET electronics. At first the signal from each pad of the detection plane of the TPC is treated by AGET (Asic for GET). It performs a pre-treatment of the signal. An AGET can handle 64 channels. These chips are gathered four by four on AsAd boards (Asic Support and Analogue-Digital conversion) performing the digitisation of the signal. CoBo cards (COcentration BOard) manage the readout of AsAd for the storage server transfer. A CoBo card can handle four AsAd. The trigger of CoBo and the absolute clock (time-

stamping) is managed by the MUTANT module (MUltiplicity ANd Trigger). All the CoBo and the MUTANT boards are housed in a $\mu$TCA crate (11 CoBos and one MUTANT per crate).

The final detector (16384 channels) will be composed of the 256 AGETs on 64 AsAd cards with 16 CoBo boards and 2 MUTANT modules. Two $\mu$TCA crates will be necessary. Currently the TPC demonstrator (2048 pads) is composed of 32 AGETs on 8 AsAd cards with 2 CoBo modules and a MUTANT. One $\mu$TCA is necessary for this demonstrator (cf. figure 5.7).

### AGET architecture and parameters

The AGET chip is an ASIC dedicated to the pre-treatment and sampling of the signal. It was designed by the IRFU at CEA Saclay. A general view of the AGET treatment chain is represented in figure 5.16. The main parameters of the AGET chip readout are summarised in table 5.1. They are explained in the text below.

An AGET can manage 64 channels. For each channel, the input signal is amplified by a CSA (Charge Sensitive Amplifier). Four charge dynamic ranges (called gain) values are available: 120 fC, 240 fC, 1 pC and 10 pC. This dynamics depends on the capacitance $C_g$ of the CSA (120 fF, 240 fF, 1 pF and 10 pF). The collected charges induce a current $i_e$. The voltage at the output of the CSA is $v_s(t) = -\frac{G}{C_g}q(t)$ for a charge $q(t)$ created by the ionisation and $G$ the gain of the micromegas.
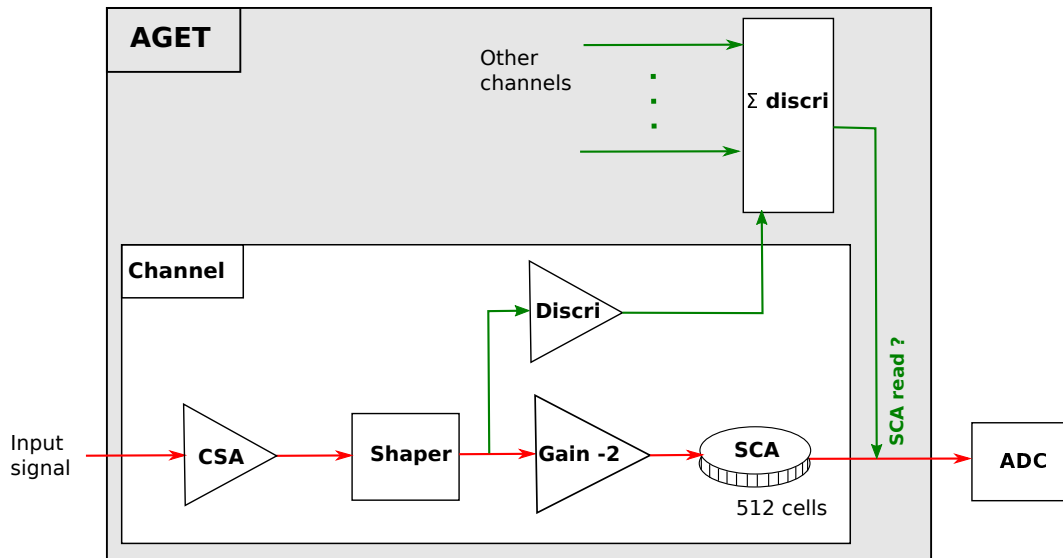


Figure 5.16: Simplified block diagram of AGET. Each channel signal is pre-amplified by a CSA (Charge Sensitive Amplifier) and filtered by a shaper. Then the signal is sampled in time by a SCA (Switched Capacitor Array) made of capacitors which are charged continuously one after each other. Each capacitor stores a sample of the signal. Discriminators of the channels are summed per AGET (64 channels) to command the readout of the SCA. If the SCA is read, the signal is digitised by the ADC of AsAd. The summations of the discriminators also provides a multiplicity signal per AGET to know the number of hit channels.

After this stage, the signal is filtered by a shaper. The peaking time of this latter can be tuned with 16 values from 70 to 1024 ns. The signal is then multiplied by an inverted $\times 2$ gain. Indeed by injecting a negative signal, this latter will give a positive output.

The signal is continuously written in an analogue circular memory named SCA (Switched Capacitor Array). Capacitors are successively loaded to sample the signal in time. The written frequency of this memory defines the sampling frequency of the signal. 512 capacitors (cells) compose it, thus each signal is sampled over 512 points maximum. The number of read cells (named "time buckets") can be set from 1 to 512. The readout of the SCA can be delayed by the parameter named "trigger delay". The write stop and readout of the SCA is managed by CoBo (see dedicated subsection for details). Different trigger modes are available. The readout of the SCA can be issued by an external trigger, internal parameters of the chips (*slow control*)

| Test modes | calibration, functional, test |
|---|---|
| Test mode range | 120 fF, 240 fF, 1 pF, 10 pF |
| Channel gain | 120 fC, 240 fC, 1 pC, 10 pC |
| Channel readout | hit, selected, all |
| Peaking time | 16 values from 70 to 1014 ns |
| SCA writing frequency | from 1 to 100 MHz |
| SCA readout frequency | 25 MHz |
| SCA time buckets | from 1 to 512 |
| Trigger mode | slow control, external, periodically (internal), multiplicity |

Table 5.1: Main parameters of the AGET chip readout.

or on the multiplicity signal (defined by the summation of the discriminators).

Each channel has a discriminator to compare the signal with a programmable threshold. The outputs of these discriminators are summed over the AGET chip to obtain a multiplicity signal proportional to the number of hit channels (see the subsection dedicated to MUTANT). This latter allows the SCA readout if the trigger mode is based on multiplicity.

The sampled signal is finally digitised by the ADC of the AsAd board, housing the AGET chips (cf. the next subsection dedicated to AsAd).

Four additional channels are in the AGET chip: the FPN (Fixed Pattern Noise) channels. These test channels are not pre-amplified by AGET, they are directly connected to the inverted gain stage. They can be used to evaluate the coherent noise of the chip. On each AGET, the channels 11, 22, 45 and 56 are FPN channels. Physically, an AGET chip is composed of 68 channels (including the FPN).
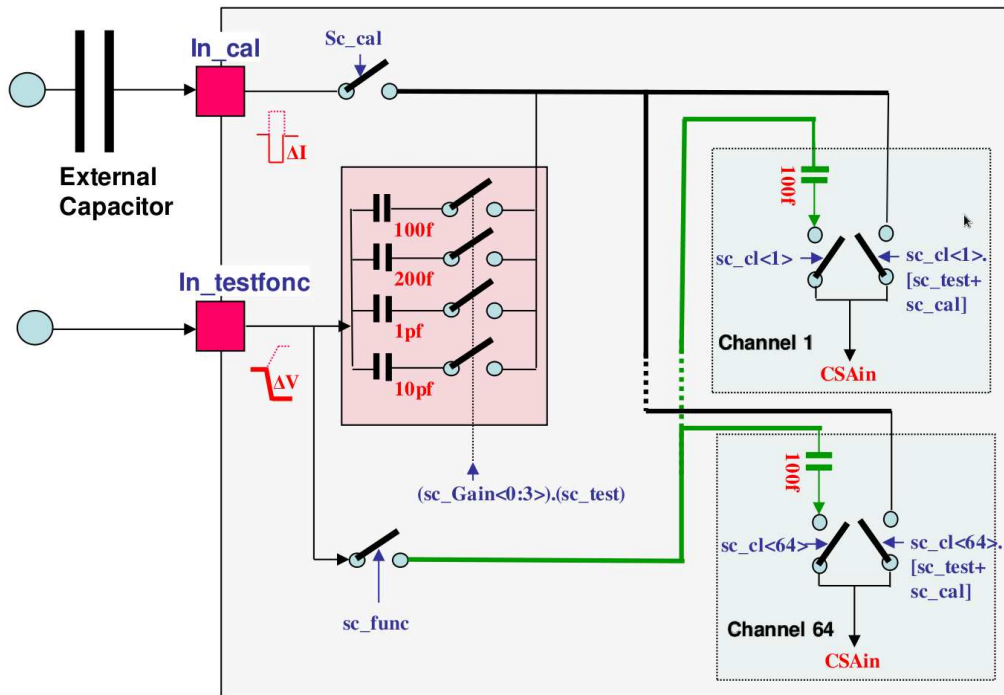


Figure 5.17: Schematic view of the test system of AGET. The circuit in the box is proper to each AGET. The external capacitor is located on AsAd. The test input voltage signal is generated by the AsAd internal pulser. Three modes are available. The calibration mode (black line) uses the "In_cal" input. The test mode (thin black line) uses the "In_testfunc" entrance with four possible capacitors. The functionality (green line) needs the same input as the test mode but the same injection capacitor of 100 fF is used for each channel.

Before the processing chain (CSA) in figure 5.16, each channel can be connected directly to the input signal or through an embedded test circuit, internal to each AGET. Three test modes

are available on the GET electronics: *calibration*, *test* and *functionality*. They are represented on the scheme of the figure 5.17. In all cases, a voltage is applied at the entrance of a channel of the AGET by the AsAd pulser (cf. subsection dedicated to AsAd). An internal capacitor converts the voltage to a current which is injected in the channel.

The calibration mode follows the thick black line on the scheme (input "In_cal"). The signal is injected by an external capacitor (embedded on AsAd) which has a value $C_i$ of $1(\pm 10\%)$ or $11 (\pm 1.82\%)$ pF known with a high precision. The input voltage is multiplied by a factor $\sim \frac{C_i}{C_g}$ with $C_i$ the external capacitance and $C_g$ the capacitance of the CSA. $C_g$ is set with a high uncertainty of around 20%, that is not the case of $C_i$. With a known voltage step at the channel inputs, this mode allows to compute accurately the capacitor $C_g$ of each channel to perform a calibration.

The test mode follows the thin black line of the scheme. An input capacitor is selected between four values known with an uncertainty of 20%.

The functionality mode (or functionality test mode) follows the green line on the scheme of the figure 5.17. The input capacitance has the same value for all channels, 100 fF ($\pm 20\%$). This test mode is the only one usable with the FPN channels.

### AsAd

The AsAd board houses four AGET chips and digitises the content of the SCA with a 12-bit ADC (coding from 0 to 4095). Four ADCs are used on an AsAd (one per AGET). The cards were designed by the electronics group of CENBG. One of the AsAd of the TPC is represented in figure 5.18.
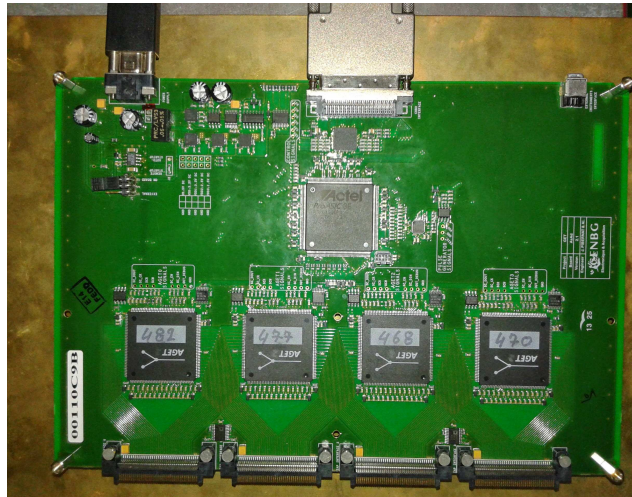


Figure 5.18: Photograph of an AsAd card used for the TPC demonstrator at CENBG. Four AGET chips are embedded on an AsAd with a 12-bit ADC each. The connector at the centre of the top of the card is the VHDCI connection to CoBo. The connector on the top left is the power supply of 5 V. An ASIC manages the card (chip at the centre).

AsAd sends the write stop to the SCA (AGET level) depending on the trigger mode. After this stop, the signal is digitised by the ADC and sent to CoBo.

When the SCA is continuously writing, AsAd codes the multiplicity signal by adding the multiplicity signals of each AGET of the card. It is proportial to the number of hit AGET and channels. This signal is sent to CoBo and the multiplicity signals of all the AsAd of the system are treated by MUTANT (cf. subsection dedicated to MUTANT).

A voltage generator is embedded on the card for test modes (cf. previous subsection on AGET). It produces square signals with amplitudes from $-1$ V at $+1$ V. The external two capacitors of the calibration mode are also on the card.

The connection between AsAd and the detector is done by "ZAP" connectors. They were also developed by the electronics group at CENBG. Each ZAP is made of two extremities (one for the pads, one for the AGETs connection) joined by a flexible PCB to adapt to the geometry

of the detector. The AsAd cards occupy more surface than the pad plane. Thus the ZAP provides a flexible geometry to put the AsAd cards on the holding structure. The ZAP is also shielded to prevent from electromagnetic perturbations.

Two ZAP prototypes were developed by CENBG. The first was produced to test the feasibility of this solution. To adapt the ZAP connector to the two geometries (cubic and rectangular chambers), a second prototype was made. They are represented in figure 5.19. A ZAP connects the four AGET of an AsAd card to two lines of 128 pads. The photograph on the left is the first prototype of ZAP tested at CENBG. The two flexible PCBs connect the pads and AsAd. The two layers are symmetric.

To adapt the ZAP to the cubic geometry of the pad plane of the GANIL chamber, the two parallel flexible PCBs were replaced by two asymmetric circuits: left and right (second demonstrator on the right picture of figure 5.19). This ZAP version also offer the possibility to polarise the pads by zone. This asymmetric ZAP will equip the final detector.
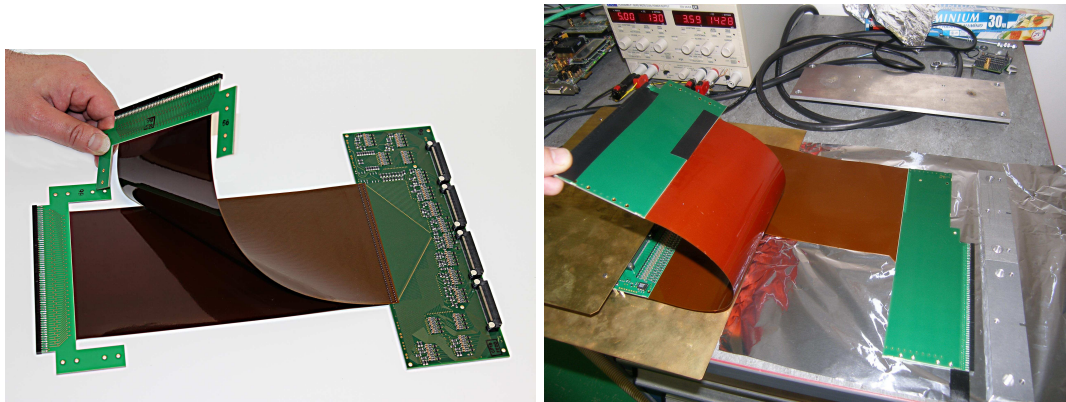


Figure 5.19: The two ZAP prototypes developed by CENBG to connect the pads to AsAd with flexible PCB circuits, one per line of 128 pads. The left photograph shows the first ZAP template with two parallel flexible circuits. The right photograph shows the last version of ZAP (the AsAd card is shielded) with left and right connectors, adapted to the geometry of the two ACTAR TPC chambers.

**CoBo**

CoBo (COncentration BOard) reads, reduces and concentrates the data coming from the AsAd to send it to the storage server. A CoBo manages 4 AsAd (1024 channels). This module is developed by NSCL for the GET collaboration.

A CoBo is made of a PCB embedding a Xilinx Virtex-5 FPGA. It is an Advanced Mezzanine Card (AMC) hosted in a $\mu$TCA chassis. AMC is a standard PCB card for $\mu$TCA architecture. $\mu$TCA (MICRO Telecommunications Computing Architecture) is an embedded architecture of electronics subsystems for data processing. This standard has the main advantages of using high-speed connections and the capability of fast processing the data. Indeed, new generation detectors in nuclear physics can have up to 30000 channels (16384 for ACTAR TPC).

The photograph of CoBo is shown in figure 5.20. The backplane connector at the back of the card (picture on the left of figure 5.20) allows the communication with MUTANT through the $\mu$TCA chassis and powers the card. They are connected to the AsAd by 68-pin VHDCI cables (four connectors on the front-end of the board). The communication with the controller/storage farm is done by 1 or 10 GbE (Gb Ethernet) connection. LEMO connectors send the triggers of the AsAd cards in NIM standard.

The $\mu$TCA chassis used for ACTAR TPC is a Vadatech VT893 represented in figure 5.21. It is composed of 12 slots for AMC. 11 can be used for the CoBo modules and one to house MUTANT. Two MCH slots ($\mu$TCA Carrier Hub) control the different modules of the system. They are responsible for data switching. The chassis is managed by a network interface accessed by the acquisition computer.

Figure 5.20: Photograph of a CoBo module of the TPC demonstrator at CENBG. The left picture shows the top-view of the card with the backplane connectors on the left. The right picture is the front view of CoBo. Four VHDCI connectors to the AsAd cards are here. The four LEMO connectors labelled L0, L1, L2 and L3 send the trigger signals (NIM) for each AsAd. A $\mu$USB port is available at the centre.



Figure 5.21: $\mu$TCA chassis installed at CENBG for the TPC demonstrator. Two CoBo boards and a MUTANT are hosted to manage the 2048 channels. The top and bottom of the chassis comprise the cooling units.
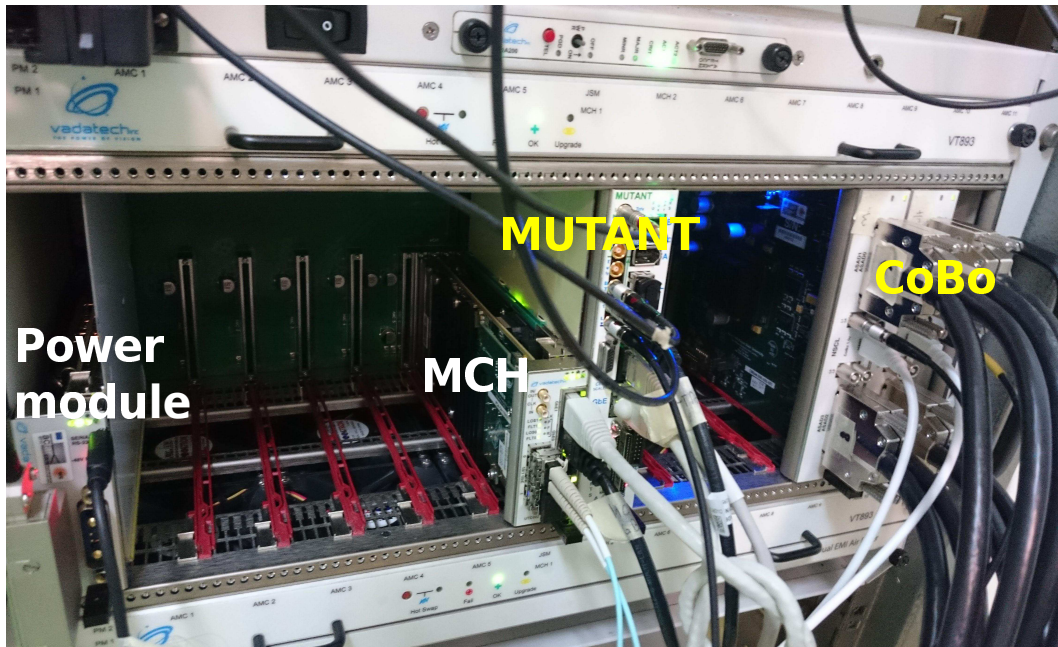
**Reduced CoBo**   A version called "reduced CoBo" (RCoBo) of the board was developed at IRFU to perform tests of the AsAd cards. It is implemented on a Xilinx Virtex-5 ML507 demonstration board (see photograph in figure 5.22).

RCoBo works in a standalone mode with only one AsAd card. Moreover it does not need $\mu$TCA chassis. It is simply connected to an AsAd board and a acquisition computer for the tests. A dedicated software was created by IRFU at CEA Saclay to load the parameters on CoBo and save the signals. This device was used to perform the analysis of GET presented in this work (section 5.3.5).
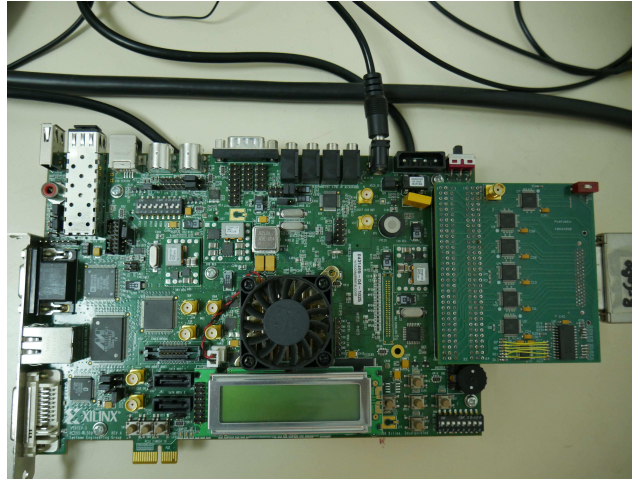


Figure 5.22: Photograph of the RCoBo used for the GET tests.

### MUTANT

MUTANT (MUltiplicity Trigger ANd Time) is an AMC of the $\mu$TCA chassis. It is developed by GANIL and manages the clock, trigger and time-stamp information for the acquisition. The global architecture of a GET system with MUTANT is represented in figure 5.15. The MUTANT module is shown on the photograph in figure 5.21.

MUTANT is made of two Xilinx Virtex-5 FPGAs. One is dedicated to trigger and time-stamp information. The other has an embedded Linux OS and is not used for the acquisition system here. MUTANT is fully programmable by TCP/IP protocol and all its logic signals are in NIM standard. Each MUTANT is equipped with a 200-MHz internal clock (Quartz).The time-stamp is defined with a 100-MHz clock and written on 48 bits. Moreover MUTANT codes the event number on a 32-bit counter.

The most important point is the trigger. Three levels of trigger are available: L0 (external), L1 (multiplicity) and L2 (hit pattern). For L0 (external), the system is triggered by a NIM signal sent by the user to the dedicated LEMO connector of the MUTANT module. It allows to do coincidences with ancillary detectors of the TPC.

The second trigger L1 uses the multiplicity. MUTANT triggers if the multiplicity signal is above the threshold set by the user. This signal is a total signal from multiplicities of each CoBo of the system. The system registers an event if this signal is above the defined threshold.

The third trigger L2 is based on the hit pattern. MUTANT gathers the hit pattern values of all pads (information if the pad is hit or not). This global pattern is analysed by an algorithm. The match of the desired pattern fires the acquisition.

The trigger modes L0 and L1 can be used at the same time. If a L0 trigger happens, the system waits for a L1 trigger in the time gate generated by L0. This mode is L0L1. The contrary can be done with L1L0 mode. The system waits for a L0 trigger in the time gate generated by a L1 trigger.

**Two-proton mode**

GET has a special mode, named 2p mode, dedicated to 2p radioactivity study. The SCA is split in two equal parts of 256 cells. The first part is used to register the signal of implantation, the second one for the decay event. The dead time is thus the time to fill the first part of the SCA and to switch between the stop of the first memory and the write of the second one, a few $\mu$s (depending on the writing frequency). It is a very low dead time compared to the CENBG TPC (1.4 ms).

The first part of the SCA is continuously fed. At the first trigger (ion implantation) this part is frozen. At the second trigger (decay) the second part is frozen. The full SCA content is read and sent to AsAd and CoBo.

Each trigger can be tuned separately in a different mode. A trigger delay for each half of the SCA with its own parameters is available. A trigger timeout sets the maximum duration during which the firmware waits for the second trigger. If this delay is exceeded, CoBo waits for a new trigger. A trigger dead time, specific to the 2p mode, sets the delay after which the second trigger can be issued.

At the MUTANT level, the L1 trigger is adapted to the 2p mode. The first part of the SCA (implantation phase) is treated as the normal L1 case. But a "write SCA" signal is sent to CoBo to switch the system in decay phase. The second L1 trigger conditions start for the decay. If the second trigger is not found, the system will be reset after a timeout defined by the user.

### 5.3.5   Estimate of GET response function

To estimate the response function of the GET signals and reconstruct the input signals, many parameters were tested at CENBG. The results of this analysis are published in [Gio16]. This section is focused on my contribution to this work with tests of GET parameters and the corrections on the signals.

The full charge deposit signal is registered over a time window depending of the sampling frequency. The signal is modified by the electronics thus the input signal is not measured directly. When a pulse (square signal) is injected to a channel, the output signal is different from the input as it is shown in figure 5.23. Moreover this signal depends on the GET parameters used (peaking time of the shaper or charge dynamic range of the CSA for instance). To reconstruct the charge deposited on a pad, one needs to characterise the system and know how it modifies the input signal.
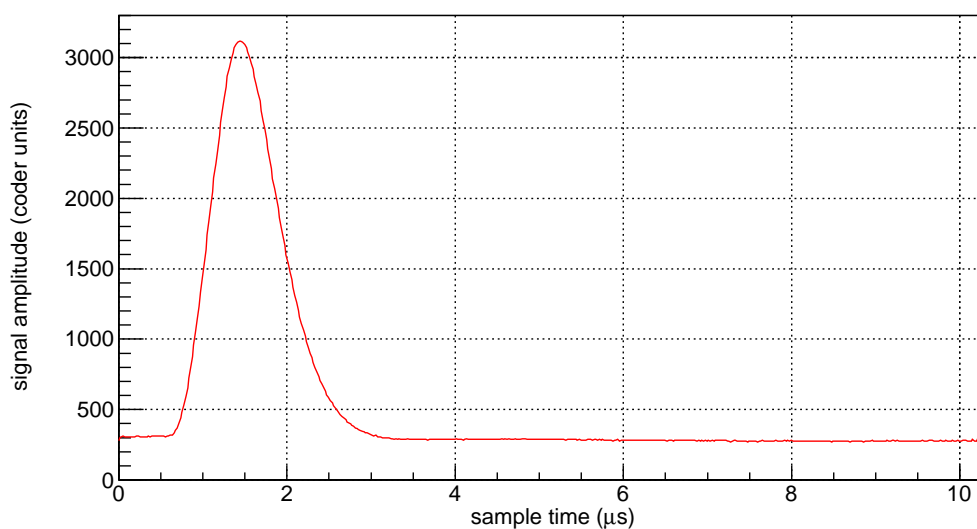


Figure 5.23: GET response to a square signal.

The reconstruction requires to know the impulse response $h(t)$ of the GET system, i.e. the output signal when a Dirac impulse is injected. Each linear time-invariant system is characterised

by its own response $h(t)$. When a signal $s_i(t)$ is treated by the system, the output signal is given by the convolution between the input and the impulse response:

$$s_{out}(t) = s_{in}(t) * h(t) \tag{5.3}$$

In Fourier space, this relation becomes a product, more convenient to manipulate:

$$S_{out}(f) = S_{in}(f).H(f) \tag{5.4}$$

with $S_{out}$, $S_{in}$ and $H$ the Fourier transforms of $s_{out}$, $s_{in}$ and $h$. In Fourier space, $H$ is the transfer function of the system. This transfer function has to be estimated for the signal reconstruction.

The more natural method to estimate $H$ is the calculation of the theoretical function because we know the electric dipoles which constitute the AGET chip. The calculated transfer function is [Sab13]:

$$H(f) = \frac{24A\tau}{(j2\pi f + 4)\left((j2\pi f \tau + 3)^2 + 7\right)} \tag{5.5}$$

with the time constant $\tau$ and the amplitude $A$, both determined by the components of the circuit. The use of this function was not conclusive with high disparity with the measured response [Sab13].

An empirical response function was also tested. It was elaborated by CEA (AGET chip designer P. Baron):

$$h(t) = Ae^{-\frac{3t}{\tau}} \left(\frac{t}{\tau}\right)^3 \sin\left(\frac{t}{\tau}\right) \tag{5.6}$$

This function gave better results than the theoretical transfer function but still far from the measurements [Sab13]. The chosen solution was to compute the transfer function by injecting
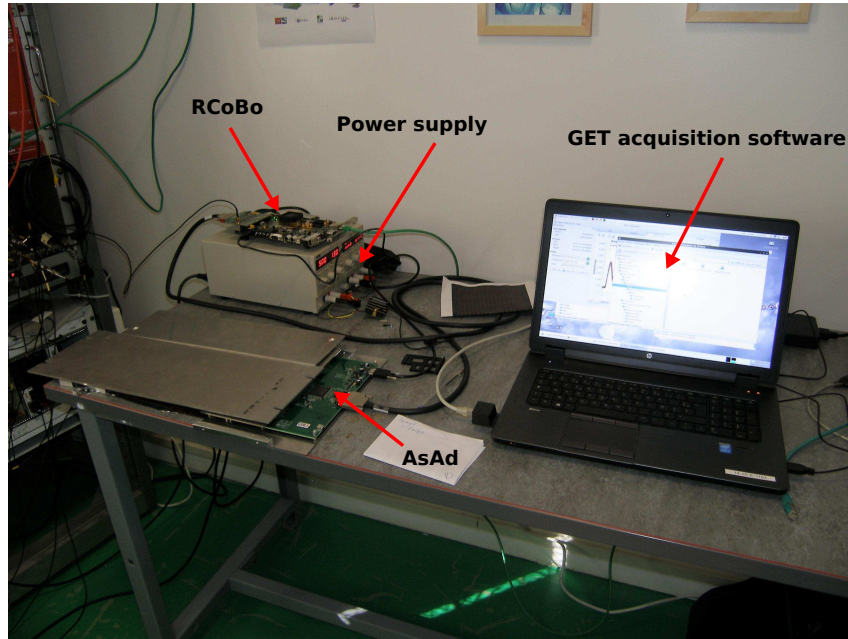


Figure 5.24: GET testbench made by the electronics group at CENBG. It is composed of an AsAd card, a RCoBo and an acquisition computer.

a known test signal in AGET. A known signal $s_{in}(t)$ is provided by a signal generator (external or AsAd pulser), then we measure the output signal $s_{out}(t)$. The transfer function is computed point by point in the Fourier space by:

$$H(f) = \frac{S_{out}(f)}{S_{in}(f)} \tag{5.7}$$

Since we manipulate digital signals, the Fourier transform is discrete. For a signal $s(t)$ sampled at a frequency $F_s$ and composed of $N$ samples, its Fourier transform is:

$$S(f) = \sum_{k=0}^{k=N-1} s\left(\frac{k}{F_s}\right) e^{-j\frac{2\pi k f}{F_s}} \tag{5.8}$$

This calculation is done by a Fast Fourier Transform algorithm (FFT).

The reconstruction tests were performed by a reduced CoBo or RCoBo (cf. section 5.3.4 for details) connected to one AsAd card and an acquisition computer. The GET testbench used to do these tests is represented on the figure 5.24.

The procedure proposed here to reconstruct the input signal of an event is shown in figure 5.25. A charged particle ionises the gas of the active volume, the signal collected on the pads is processed and stored by the GET electronics. The stored pad signals are corrected from the distortions presented in this section (baseline and phase or FPN correction). Then the input signal is reconstructed by using the transfer function of the system.
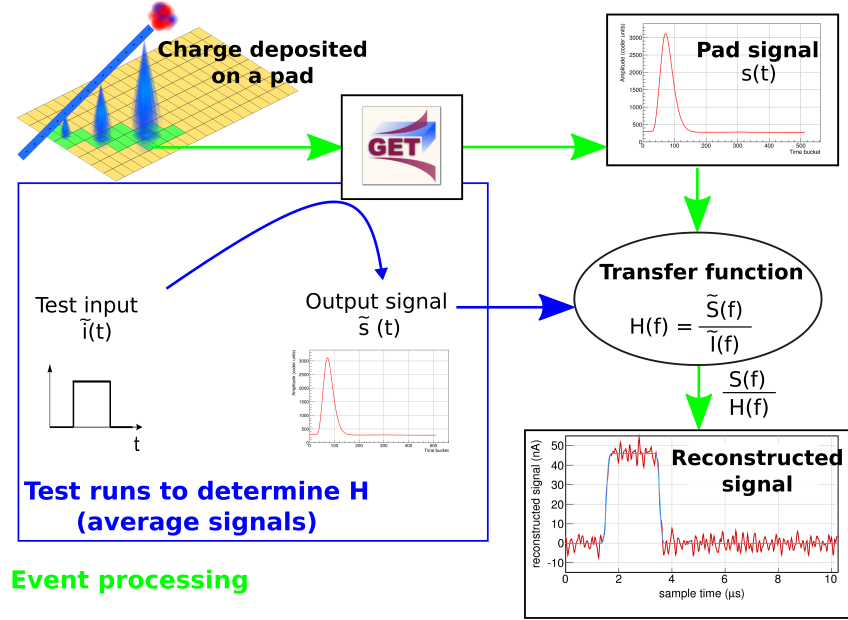


Figure 5.25: Illustration of the signal reconstruction with GET. The signals of the pads of the TPC are processed by the GET electronics. Then they are corrected from the distortions and reconstructed with the transfer function of the system. The transfer function is computed from test events with known input signals.

The distortions observed on the output signals are presented here. The proposed procedures to reduce these distortions and their characterisation are also presented, with their dependence on the parameters of the GET electronics. Indeed the settings used to determine the transfer function have to be the same as those used to estimate the transfer function and reconstruct the input signal.

**Noise reduction for response function estimate**

The estimated response function is the division of the output signal by the output in Fourier space. The noise of these signals induces noise on the response function estimate.

To reduce the noise of the estimated function, average signals are used. A test signal is injected $N_{evt}$ times in the GET system producing the same number of output signals. An average signal is defined by:

$$\langle s(k) \rangle = \frac{1}{N_{evt}} \sum_{n=0}^{N_{evt}} s_n(k) \text{ for } k \in [0, N-1] \tag{5.9}$$

for a signal composed of $N$ samples (typically 512). The standard deviation (RMS) signal of a GET signal is defined point by point as:

$$r_s(k) = \sqrt{\frac{1}{N_{evt}} \sum_{n=0}^{N_{evt}} (s_n(k) - \langle s(k) \rangle)^2} \text{ for } k \in [0, N-1] \tag{5.10}$$

An example of an average signal over 1000 realisations is represented in figure 5.26. One sees that a single signal is much more noisy than the average signal. The signal and also the estimate response are dependent on the parameters of GET. The RMS signal is used to compare the reduction of systematic distortions according to the electronics settings.
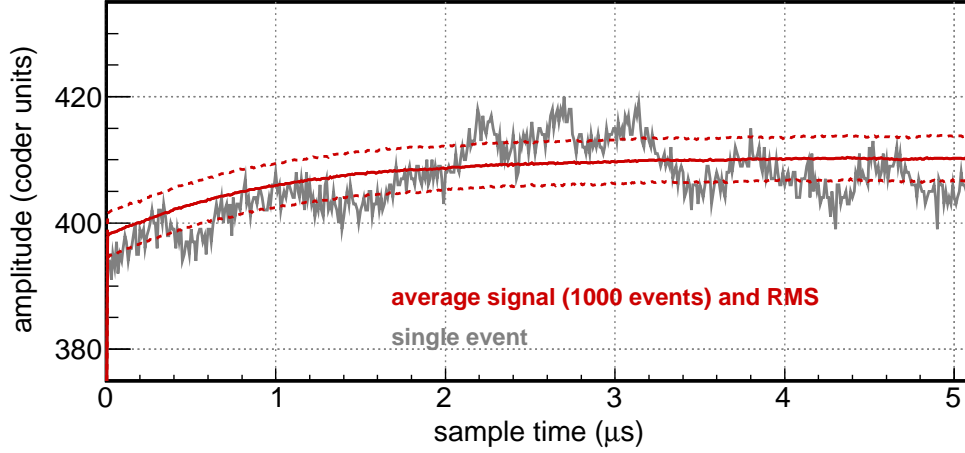


Figure 5.26: Signal realisation with the average and RMS over 1000 events (baseline events in this case). A single event is the grey curve. The average and RMS over the 1000 realisations are respectively the red continuous and dashed lines. The acquisition is done without input signal, thus this signal is the baseline of the electronics.

The question of the number of events used to have the best noise improvement on the signals is asked. The estimate of the noise of the signals is given by their power spectral density (PSD) which is the Fourier transform of the auto-correlation function of the signal. The PSD of a signal on an acquisition time window of width $T$ is computed by:

$$PSD(f) = \frac{1}{T}\langle|S(f)|^2\rangle \tag{5.11}$$

The PSD of an output signal is represented in figure 5.27. The signal frequencies are divided in two components: the signal itself at low frequencies and a white noise at high frequencies. The amplitude of this latter is decreased when the number of events increases. The noise of the average signal is almost the same for 1000 and 10000 events. The number of 1000 events was chosen for the analysis to spare computation time.
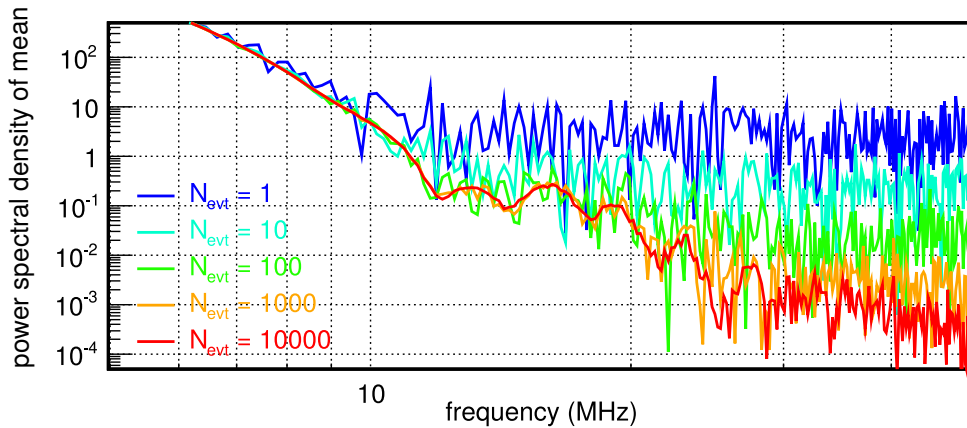


Figure 5.27: Power spectral density (PSD) of a GET output average signal computed over various numbers of events. In this example, the input signal is a pulse from AsAd pulse generator.

**Correction of the signal distortions**

Intrinsic distortions of the signal are observed. They have to be corrected before reconstructing the input signal or computing the transfer function. Systematic artefacts of the first and last samples of each signal are always seen. A non-constant pedestal (named baseline) is caused by the electronics on each signal. The third effect seen (named phase effect) is a readout effect due to the position of the signal in the SCA.

**First and last data artefacts** The first distortion is due to write/readout switching of the SCA memory. On the signal example of figure 5.28, there is systematically an aberrant value for the first and last sample of the signal. The signal is overestimated of about 50 coder units at concerned points. Each event has these effects, independently from the run conditions and the GET parameters.
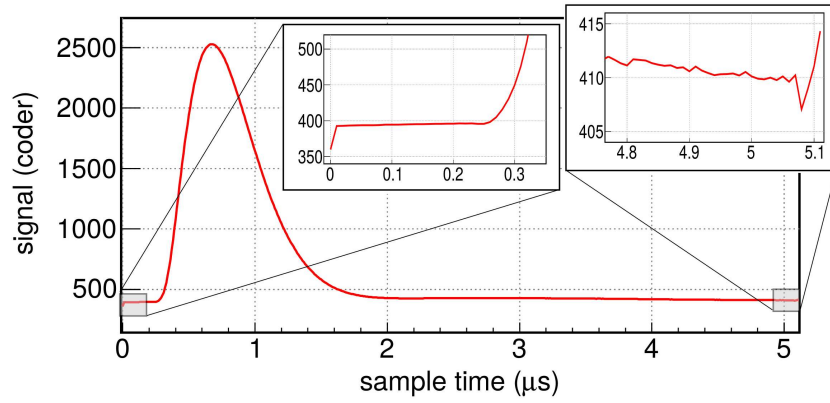


Figure 5.28: First and last data artefacts on an average signal. The write/readout effects are systematically seen on GET.

**Baseline** For the signal in figure 5.28, the input signal starts at 0 V but the output signal is shifted by a pedestal named baseline due to the chip itself. When a trigger is sent to the system without input signal, one obtains the baseline alone in the output data. A baseline signal is represented in figure 5.26. One notices that this baseline is not constant, complicating the correction of the signals. It has the same artefacts than the other test signals at the first and last sample. These distortions are corrected when the baseline is subtracted from a signal. The correction is performed on a signal $s(k)$ channel by channel by:

$$s^{cor1}(k) = s(k) - b(k) \text{ for } k \in [0, N-1] \tag{5.12}$$

where $b(k)$ is the average baseline computed over 1000 events.

To compare the effects of various GET settings on the baselines, one can compute their mean RMS defined by:

$$\begin{cases} R_s = \frac{1}{N} \sum\limits_{k=0}^{N-1} r_s(k) \\ \Delta R_s = \sqrt{\frac{1}{N} \sum\limits_{k=0}^{N-1} (r_s(k) - R_s)^2} \end{cases} \tag{5.13}$$

with $r_s$ the RMS signal of equation 5.10. $R_s$ is computed on the whole average signal with its standard deviation $\Delta R_s$.

The baseline was studied for an AsAd with various settings of GET especially different peaking times and gains. The average RMS of the baseline (defined in equation 5.13) is compared over a whole AsAd for various settings.

On figure 5.29, the average RMS is drawn for various peaking times of the shaper, at 120 fC and 10 pC of charge dynamic range of the CSA. The measurements were performed at 100 MHz, the maximum sampling frequency. For this value, the noise on the signals is the highest because
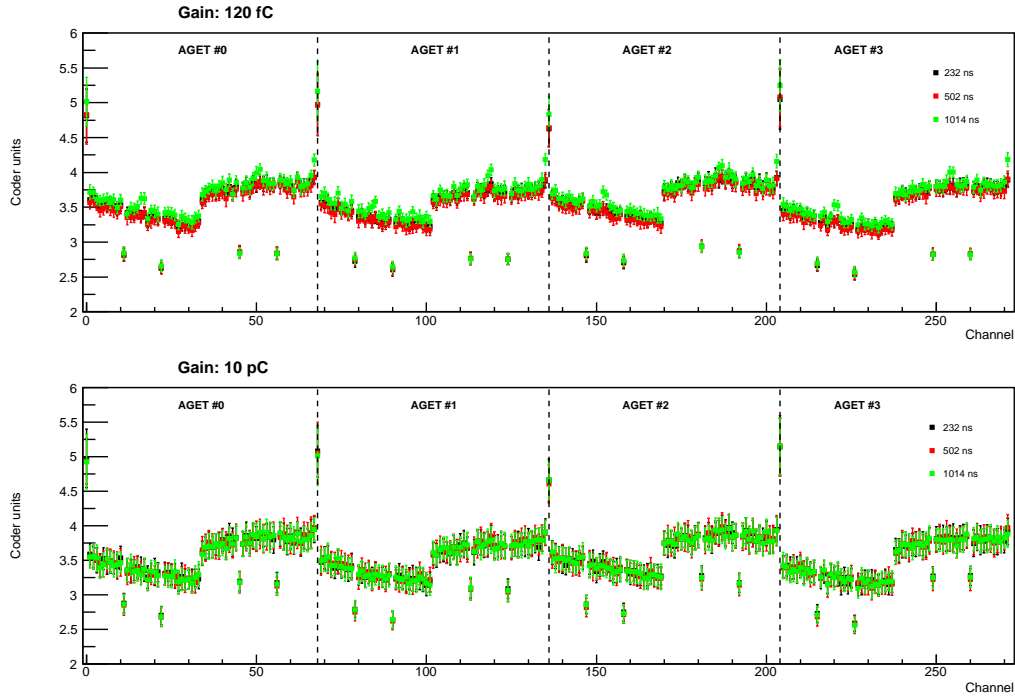
Figure 5.29: Mean RMS values ($R_s$) of the baseline channel per channel of an AsAd for various peaking times. The measurement was done for a sampling frequency of 100 MHz, a gain of 120 fC (the lowest) and 10 pC (the highest). The uncertainty bars are the standard variations around $R_s$. The FPN channels are also drawn on this plot.
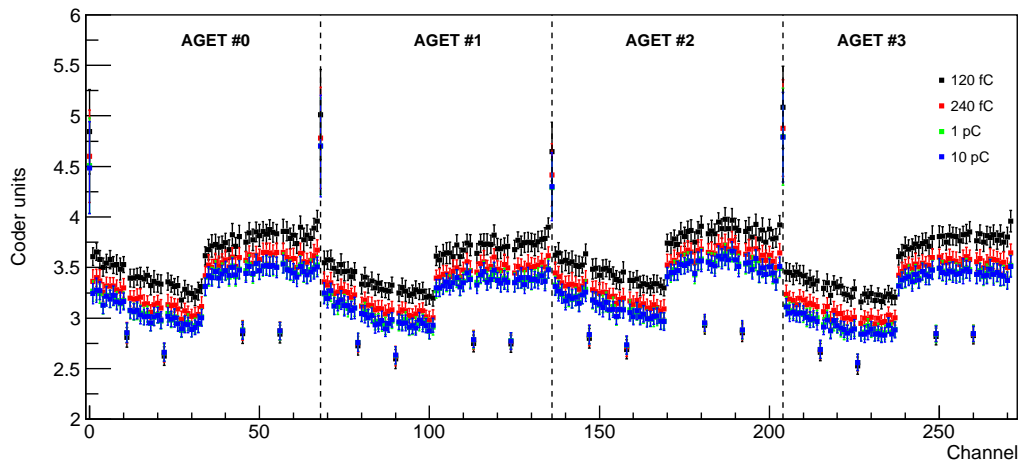


Figure 5.30: Influence of the gain on the external baseline noise. Signals are sampled at 100 MHz and a peaking time of 232 ns. The mean RMS and its standard deviation are represented.

the sampling period is the lowest. Fast variations of the signals are more likely to be visible. For each AGET, the behaviour of the baseline RMS is the same. The value is systematically lower on the 32 first channels with a difference of a half coder unit. No difference is seen on the baseline according to the peaking time. Even in the highest dynamic range (10 pC), the behaviour is the same and the RMS values are very similar to the case at 120 fC.

The gain was modified for a peaking time of 232 ns. Since the baseline is less sensible to the peaking time, the gain study can be generalised to the other peaking times. The figure 5.30 gives the variation with the gain value of the average RMS on an AsAd. The difference between the lowest (120 fC) and the highest dynamic range (10 pC) is around 0.5 coder unit. A gain of 10 pC improves by 15% the $R_s$ value compared to 120 fC.

**Phase effect**  For all the runs, the signal is continuously written in the SCA until a stop is sent to the SCA. The SCA is read from the memory cell following the last written one. This cell varies randomly from event to event because the buffer is circular. The position of the last read cell, named *LastCellRead* ($l_c$), induces a coherent distortion on the read signal as it is represented in figure 5.31. A fixed pattern which is named "phase effect" is superimposed to the signal. This pattern is associated to the physical positions of the cells in the SCA memory. Depending on the position of the last read cell, the pattern is moved according to the signal physical position in the memory. Thus the signal is not modified in the same manner for each event. The correction of this effect is different for each signal realisation.
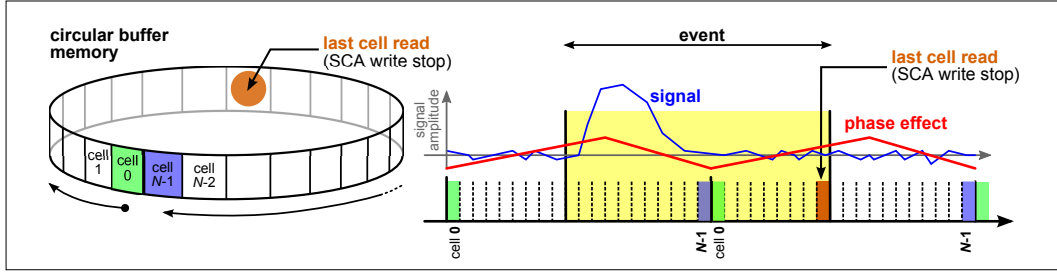


Figure 5.31: Illustration of the SCA memory and the phase effect on the signals. Left: the SCA is a circular buffer and the write stop varies between 0 and 511. The information of the write stop $l_c$ (and last cell read) is memorised. Right: a signal is biased according to the value of $l_c$ (phase effect). A phase pattern (red) characteristic of the SCA deformes the signal according to the position of $l_c$.

The information of the last read cell is stored in the data files. It is possible to force the readout from the first cell (cell 0). A regular baseline run with this supplementary condition provides an output signal different than usual (see red curve in figure 5.32). The difference between these two baseline signals (right plot in figure 5.32)) is the phase pattern associated to the SCA. It is obtained by:

$$\phi(k) = b^{D0}(k) - b(k) \text{ for } k \in [0, N-1] \tag{5.14}$$

where $b(k)$ is the regular average baseline (blue curve in figure 5.32) and $b^{D0}(k)$ the average baseline with the readout from cell 0. The signals have to be corrected from the phase pattern channel by channel. $\phi(k)$ is retrieved from baseline-corrected signal $s^{cor1}$ (cf. equation 5.12) according to:

$$s^{cor}(k) = s^{cor1}(k) - \phi(k + l_c + 1 - \epsilon N) \quad \text{for } k \in [0, N-1]$$
$$\text{with } \begin{cases} \epsilon = 0 \text{ if } k + l_c + 1 < N \\ \epsilon = 1 \text{ if } k + l_c + 1 \geq N \end{cases} \tag{5.15}$$

with $l_c$ the index of the last read cell. The phase pattern has to be shifted according to its value because a signal is not read from the cell 0 to 511 but from $l_c + 1$ to $l_c$ as it is illustrated in figure 5.31. Because the first/last data artefact is not suppressed from the phase pattern (cf.
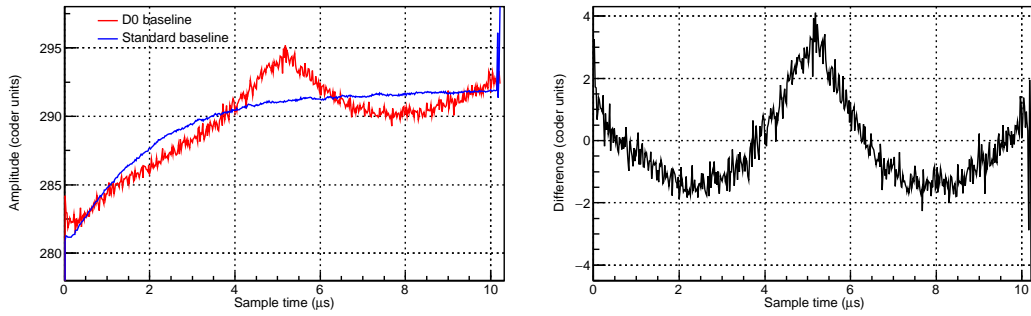
Figure 5.32: Baselines of the GET electronics. The plot on the left represents the baselines (average) for two different readout parameters. The blue curve is the regular baseline, the red curve is obtained from the same run conditions but the readout is forced to start from cell 0. The difference between the two baseline signals give the phase pattern of the SCA, represented on the right. The first data artefacts are on both baselines and thus absent from the phase pattern. It is not the case for the last data artefact.

figure 5.32), this latter has to be removed before the phase correction. It is done by filtering the phase pattern with a low-pass filter or by averaging the first/last points of the signal.

The complete correction of a signal from its distortions is performed by the subtraction of the baseline in a first time and the phase pattern in a second time.

**FPN channels** An alternative way to correct a signal from the distortions is the use of the FPN channels of the AGET chips (cf. section 5.3.4). They measure the coherent distortions after the amplification and shaping stages. For each event of a run, the FPN channels correct the signal for an event $i$ as:

$$s_i^{FPNcor}(k) = s_i(k) - s_i^{FPN}(k) \text{ for } k \in [0, N-1] \tag{5.16}$$

where $i$ is the event index. This remaining signal must then be corrected from the residual baseline, since the baseline presented previously is different for all channels (and thus different for a signal channel and for the FPNs). To choose the FPN channel to subtract, there are two possibilities. At first the closest FPN channel can be subtracted to the channel whose baseline is corrected. Secondly one can do an average of the four FPN channels of the AGET chip

To know what FPN correction is relevant, the different possibilities are compared in figure 5.33. The average baseline (uncorrected) is compared to the FPN-corrected one to see the effect of this correction on the intrinsic distortions. Computations with the closest FPN channel and the average of the four ones are compared. In both cases, the asymmetry between the two groups of 32 channels is corrected. This effect is thus due to systematic distortions related to the chip itself. The average of the four FPN signals gives the best result. In the following subsection, this FPN correction will be used.



Figure 5.33: Average RMS of the baseline and effects of the two FPN corrections on the intrinsic fluctuations: closest channel or average of the four channels of the chip.

**Comparison of the signal corrections**

As it was previously shown, a signal is distorted by the baseline (a non-constant pedestal) and the phase effect (distortion correlated to physical position of the samples in the SCA). The correction of these two effects was presented. An alternative correction with the FPNs was also described. Their effects on the intrinsic distortions are discussed here.

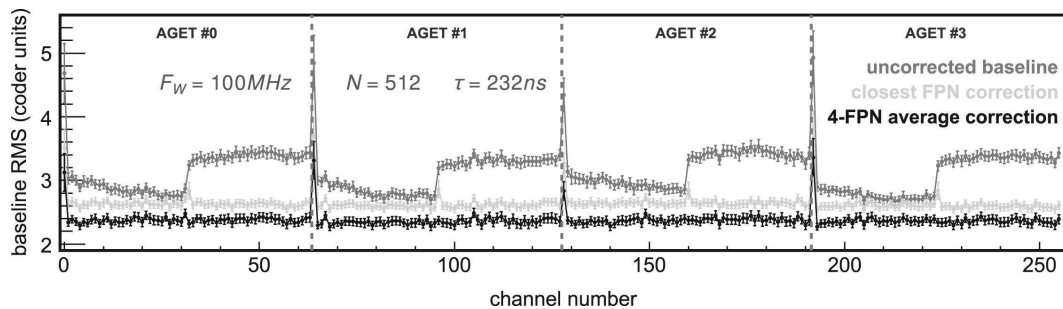The mean RMS of the average baseline is compared with the different corrections in figure 5.34: subtraction of the average phase pattern and the average of the four FPN channels. This plot shows the residual intrinsic fluctuations remaining after the corrections. The two corrections suppress the asymmetry between the two groups of channels and improve the RMS value from 1 to 1.5 coder units. One sees that the phase and FPN corrections have the same effect on the residual distortions. The improvement of the RMS value is 20% for the first half of the AGET channels and 30% for the second half.
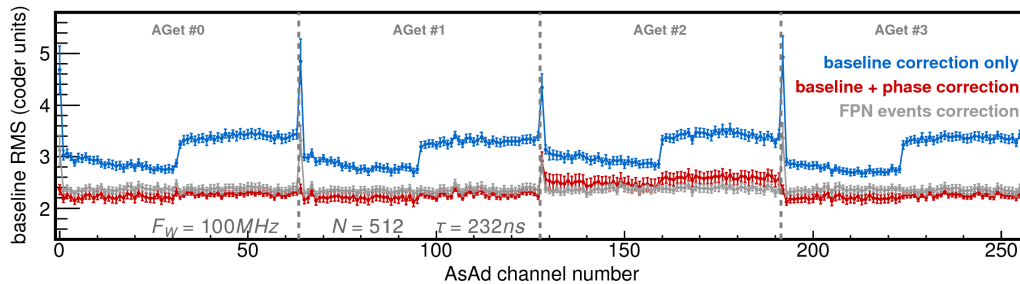


Figure 5.34: Baseline average RMS of the different corrections: phase effect and average of the four FPN channels. The runs were performed at 100 MHz with a peaking time of 232 ns and a gain of 120 fC. The phase and FPN corrections suppress both the fluctuations between the channels.

The baseline signals used for the corrections have to be readout from the electronics with the same parameters as the signals to correct. In the tests presented here, it was seen that the baselines are not sensitive to the peaking time. Nevertheless, they are modified by the gain of the CSA with a difference up to 15% of the RMS between the highest and lowest dynamic range (120 fC and 10 pC).

Practically, these two corrections have both disadvantages. Indeed to perform a baseline with a phase correction, only a single run without input signal on the detector should be required. The baseline and phase patterns of this run are then used to correct all the signals of the experiment. Ideally one should perform a baseline run as often as possible because the distortions induced by the electronics could be sensible to a lot of parameters (temperature, power voltage, etc...). Each time it generates a huge amount a data, up to 500 MB per channel (with runs of 1000 events on RCoBo testbench) i.e. 8 TB for a detector of 16384 channels.

The FPN correction requires to store all the FPN signals for each event of the experiment. With 4 FPN channels per AGET, it is 1024 signals to store for each event, even if a few tens of pads of the TPC are hit. With this method, a lot of useless information is stored by the acquisition. The more realistic solution is the baseline and phase correction by performing one baseline run per day or half-day. It was done during the test experiments of the GANIL demonstrator.

### 5.3.6 Two-proton mode characterisation

A mode dedicated to 2p radioactivity, the two-proton (2p) mode, was presented in section 5.3.4. The 2p mode is different than reading only half of the memory. The SCA is split in two contiguous parts of 256 cells, named *mem0* and *mem1* here. Each event (*mem0* or *mem1*) is labelled individually, thus a 2p mode data file has two times more events as a file in regular mode. In 2p mode, the last read cell $l_c$ of the first memory part is between 0 and 127 or 384 and 511, $l_c$ of the second part is comprised between 128 and 383 as illustrated in figure 5.35, showing the $l_c$ distribution for a set of events.
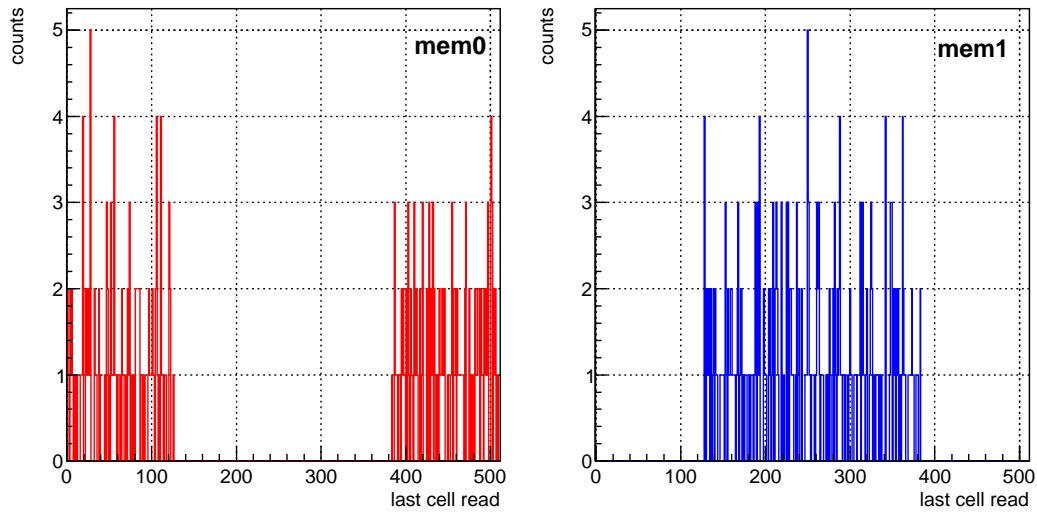
Figure 5.35: Distribution of the *LastCellRead* variable ($l_c$) for each memory part in 2p mode (*mem0* and *mem1*).

The baseline in 2p mode depends on the memory part as it is represented in figure 5.36. As it is expected, the baselines with 512 and 256 cells read in normal mode are nearly the same. However in 2p mode the baselines of the two parts of the SCA are different from 5 coder units. Therefore, contrary to the normal readout mode where no difference is seen regarding the number of read cells, the 2p mode requires a specific baseline correction. Indeed the mean baseline has to be stored for each memory part. The used phase pattern is the same as the study for 512 cells because this effect is related to the position of the read cells in the SCA memory. The phase correction is performed in function of the last read cell and the number of cells (256) for each part of the memory. The FPN correction also has to be performed for each parts of the memory independently.
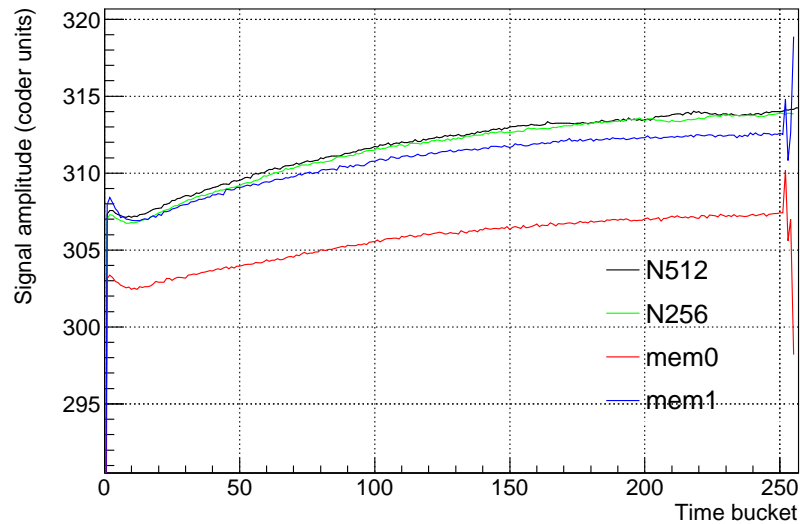


Figure 5.36: Baselines (average) of an AGET channel for various SCA readout modes: 512, 256 read cells in normal readout mode and the two buffer parts in 2p mode (mem0 and mem1).

An important behaviour to test is the output signal amplitude between the two parts of the memories. Two events (implantation and decay) can be distant from a few ms (lifetime of 2p
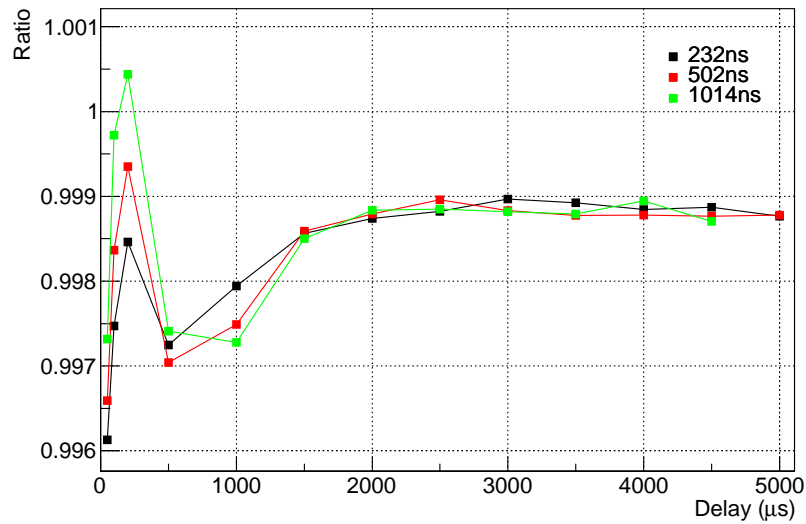
Figure 5.37: Ratio between the average amplitude of the *mem0* over *mem1* signals $\left(\frac{mem0}{mem1}\right)$ for various delays between two input pulses of same amplitude in 2p mode. The signals are not corrected.

emitter). While the acquisition is waiting for the second trigger, the first part of the memory is frozen and capacitors might lose charges, biasing the amplitude of the signal of *mem0*. A double pulse separated by a defined time is injected to a channel of AGET to compare the amplitudes of the two output signals. All the tests were performed at a sampling frequency of 50 MHz, a gain of 1 pC and various peaking times. The ratio between the average amplitude of the *mem0* signal and the *mem1* one was then compared for different times separating two successive pulses of -200 mV. The ratio (see figure 5.37) increases between 50 and 200 µs and stabilises for higher values of the delay between the two pulses. A strange behaviour is observed for the very short delays below 1000 µs. The amplitude ratio grows at around 500 µs and then decreases of the signal amplitude in *mem0* is greater than the *mem1* signal one at a shift around 250 µs. This problem with short times is probably due to the baseline. This latter does not come back to a stable value after the first event.

## 5.4 Perspectives

The correction methods presented in section 5.3.5 were applied to signals of the demonstrator. It was seen that the two corrections (baseline-phase and FPN) have the same effect and can be used either. It was seen that the output signals can be corrected in two ways: baseline and phase, or FPN correction alone. These two corrections have the same effect on the signals, correcting the intrinsic distorsions, and can be used either. The first tests and track reconstructions from the analysis of the pad signals on the demonstrator are reported here.

The CENBG demonstrator was tested with a collimated three-alpha source (as in section 5.3.3) by studying the pad signals instead of the micromesh signal. Events as the ones presented in figure 5.38 were obtained. A two-dimensional histogram of the amplitudes of the pad signals lets appear the trajectory projection on the pad plane of three $\alpha$ particles (left part of the figure). The signal amplitude is proportional to the energy loss of the particle in the chamber. The colour variation along the trajectory gives the Bragg curve of the particle. Moreover three-dimensional tracks of the charged particles were obtained with the demonstrator, as shown on the right part of figure 5.38. The drift time is the time of the maximum of the charge signal of the pad. This time is proportional to the Z position of the particle via the drift velocity of the ionisation electrons in the gas (cf. equation 5.2 in section 5.1). The drift velocity has to be estimated from simulations as the Garfield software [Gar17].
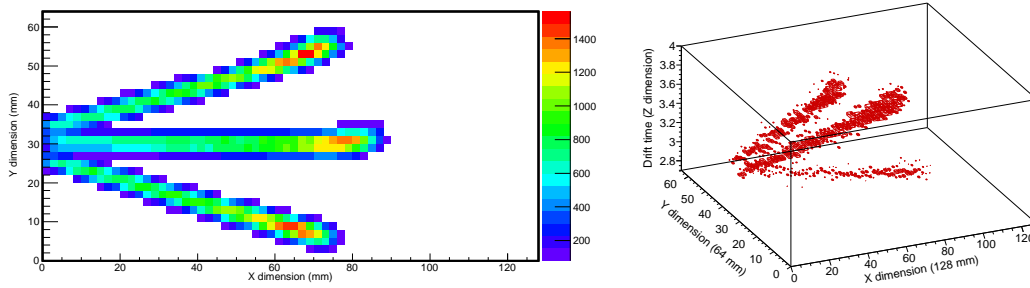
Figure 5.38: Events obtained with a three-alpha source in the CENBG demonstrator. Left: projection on the pad plane of three events obtained with a three-alpha source in the CENBG demonstrator. The trajectory projections of the three $\alpha$ particles are clearly visible. The colour scale is the amplitude of the pad signal in coder units. Right: three-dimensional view of three superimposed events with a three-alpha source in the CENBG demonstrator. The drift time (in $\mu$s on the Z axis) is the time of the maximum of the charge signal of the pad. This time is proportionnal to the Z dimension.

The total energy spectrum of the three-alpha source was obtained with the complete demonstrator as shown in figure 5.39. A summation of the signal amplitudes over all the pads gives this figure. For the first spectrum, all the pads of the pad plane with an amplitude above a threshold are added. For the second spectrum, the pads of selected tracks are added. The starting point of the tracks has to be in the first rows on the side of the TPC where the source is put. All tracks with pads in the edge rows are also excluded. Tracks with a short length are also excluded to avoid keeping events with a trajectory close to horizontal. The selection of tracks does not improve the resolution of the alpha-particle peaks but decreases the background in the energy spectrum. The intrinsic resolution (FWHM) was estimated for the central peak with the same procedure as in section 5.3.3. A value of 135(15) keV was measured. This value is in agreement with the computations from the micromesh signal in section 5.3.3 (150(5) keV).
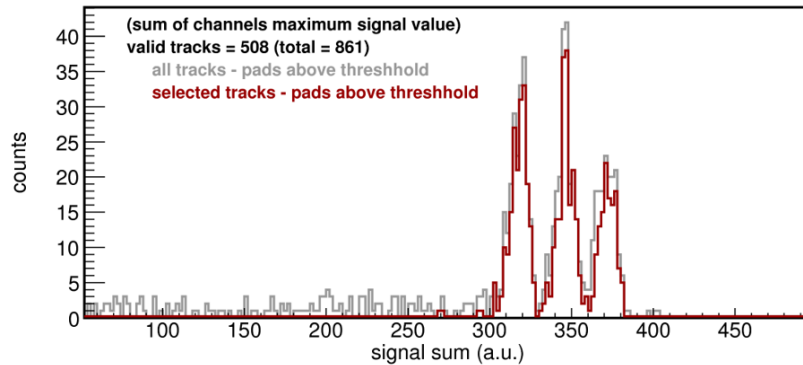


Figure 5.39: Energy spectrum of a collimated three-alpha source with the CENBG demonstrator. For each event, all the amplitudes of the pad signals are added. Different selections of pads are compared. All pads with the signal amplitude above a threshold or specific tracks are selected.

The next step is the reconstruction of the pads signals with the procedure presented in section 5.3.5 and apply it to the track reconstruction and measurement of energy loss. Tests of the two-proton mode with the full demonstrator will have to be performed: three-dimensional reconstruction, cases with simultaneous particle emissions.

# Conclusion

In this work were presented new perspectives in 2p radioactivity study, eleven years after the first observation of the heaviest 2p emitter $^{54}$Zn.

The different 2p emission models were presented in chapter 1. They allow to calculate the decay energy and half-life of the 2p emitter. After the discovery of the 2p radioactivity in 2002 with the observation of $^{45}$Fe, $^{48}$Ni and $^{54}$Zn were the three long-lived known ground-state 2p emitters. Study of the angular correlation of the emission with a time projection chamber allowed a comparison with the models and perform rough spectroscopic studies about their proton structure. For further studies, local mass models pointed out $^{67}$Kr, $^{63}$Se and $^{59}$Ge as the best 2p candidates of heavier mass.

With the RIBF4R1 experiment, presented in the chapter 2, the production and identification of these nuclei was performed. It was the second time for $^{59}$Ge but the first time for $^{63}$Se, $^{67}$Kr and also the $\beta$-delayed proton emitter $^{68}$Kr. The decay of the isotopes was studied by the setup EURICA-WAS3ABi. The ions were implanted in the segmented silicon detectors (DSSSD) of WAS3ABi to correlate the implantations of nuclei with their subsequent decay events. The high-purity germanium clusters of EURICA were used to detect gamma rays from the decays in the silicon detectors.

The analysis method described in chapter 3 allowed to obtain the energy spectra and time distributions of the studied nuclei. These proposed methods were used to compute the half-lives of the nuclei and the proton branching ratio of beta-delayed proton emitters. Issues were encountered to estimate the beta-detection efficiency required to estimate the half-lives and the branching ratios.

As presented in chapter 4, the experiment lead at RIBF allowed to produce exotic nuclei from the mass region $A \sim 70$ near the proton drip line with unprecedented production rates. It was the opportunity to measure with a better accuracy the decay properties of the $\beta$-delayed proton emission and $\beta$ radioactivity of nuclei of the region, relevant for $rp$-process calculations.

The main goal of this experiment was the search for 2p radioactivity in this mass region. No evidence was seen for $^{63}$Se and $^{59}$Ge. Nevertheless their decay spectra and a first estimate of their half-lives were done. On the contrary, a decay peak at 1690(17) keV composed of 9 events was seen for $^{67}$Kr with evidences that it comes from a 2p radioactivity. The 2p branching ratio of $^{67}$Kr was estimated at 37(14)%, a low value compared to the other 2p emitters with branching ratios above 50-60%. The half-life was estimated to be 7.4(30) ms, the highest one seen for a 2p emitter. This value is in contradiction with models. New calculations were performed presenting $^{67}$Kr as a transitional case between sequential and true 2p emission. A measurement of proton correlations should bring new evidences of the character of the $^{67}$Kr 2p decay.

A proposal of experiment with a time projection chamber to observe 2p radioactivity of $^{67}$Kr was accepted by the RIBF advisory committee. The facility and the beam-line will be the same as presented in chapter 2. A new generation of time projection chamber will be used for this experiment. Developed within the ACTAR TPC collaboration, this new detector allows a more efficient three-dimensional reconstruction of the tracks than the previous TPC. Chapter 5 summarises the tests preformed on the demonstrator used at CENBG. A new technology for the pad plane has been tested with radioactive sources. Procedures to reconstruct the signals read with the GET electronics are proposed and an evaluation of the different corrections of the signal intrinsic distortions are compared. Before performing experiments with this new detector, track reconstruction algorithms have to be made and tested with Monte Carlo simulations. The full characterisation of the demonstrator is ongoing, the final detector will be manufactured at

the end of 2017, and a 2p experiment at RIBF could be performed in 2018 or 2019.

Better observation techniques and higher production rates are required to study the 2p radioactivity deeper with accurate angular distributions. Theoretical models also need to be improved to include nuclear deformation. This radioactivity is a unique opportunity to study structure of nuclei beyond the proton drip line.

# Appendix A

# WAS3ABi implantation events

In this appendix are summarised the implantations in WAS3ABi of the nuclei identified in section 4.1 for all the settings of the experiment RIBF4R1.

| Nucleus | $T_z$ | PID at F7 | Implantations | | |
| | | | DSSSD 0 | DSSSD 1 | DSSSD 2 |
|---|---|---|---|---|---|
| $^{55}$Zn | $-5/2$ | 18 | 0 | 1 | 10 |
| $^{59}$Ge | $-5/2$ | 1221 | 9 | 189 | 332 |
| $^{63}$Se | $-5/2$ | 348 | 10 | 144 | 30 |
| $^{67}$Kr | $-5/2$ | 82 | 21 | 15 | 0 |
| $^{56}$Zn | $-2$ | 9817 | 155 | 932 | 4716 |
| $^{60}$Ge | $-2$ | 22564 | 166 | 2449 | 7219 |
| $^{64}$Se | $-2$ | 9090 | 397 | 4047 | 305 |
| $^{68}$Kr | $-2$ | 479 | 198 | 42 | 3 |
| $^{57}$Zn | $-3/2$ | 1106329 | 7467 | 13369 | 202807 |
| $^{61}$Ge | $-3/2$ | 640152 | 5371 | 170231 | 136352 |
| $^{65}$Se | $-3/2$ | 218734 | 18892 | 78823 | 2347 |
| $^{69}$Kr | $-3/2$ | 1289 | 616 | 23 | 7 |
| $^{56}$Cu | $-3/2$ | 659010 | 3942 | 6521 | 77446 |
| $^{58}$Zn | $-1$ | 2404933 | 20938 | 37588 | 762048 |
| $^{60}$Ga | $-1$ | 641690 | 6581 | 151644 | 159832 |
| $^{62}$Ge | $-1$ | 1548291 | 14928 | 294797 | 307824 |
| $^{64}$As | $-1$ | 29828 | 6026 | 10362 | 440 |
| $^{66}$Se | $-1$ | 996153 | 20914 | 308377 | 16832 |
| $^{55}$Cu | $-1/2$ | 7359 | 166 | 494 | 3905 |
| $^{61}$Ga | $-1/2$ | 821 | 70 | 217 | 52 |
| $^{63}$Ge | $-1/2$ | 205101 | 32816 | 80959 | 2897 |
| $^{65}$As | $-1/2$ | 1568050 | 16352 | 474419 | 27116 |
| $^{67}$Se | $-1/2$ | 8857 | 183 | 2438 | 169 |
| $^{66}$As | $0$ | 296237 | 6112 | 89608 | 5061 |

Table A.1: Implantation distributions of the nuclei identified during the RIBF4R1 experiment.

# Appendix B

# Details of the fit procedures

The most common approaches to estimate parameters from a histogram are the *chi-square* ($\chi^2$) and *maximum likelihood* methods. In both cases, one wants to estimate a distribution $\overrightarrow{x} = x_i$ ($x_i$ is the centre of the bin for an histogram fit) of $N$ values by a function $f(\overrightarrow{x}, \overrightarrow{p})$ defined by its free parameters $\overrightarrow{p}$.

The $\chi^2$ method consists in minimising the value

$$\chi^2(\overrightarrow{p}) = \sum_{i=1}^{N} \frac{(y_i - f(x_i, \overrightarrow{p}))^2}{\sigma_i^2} \tag{B.1}$$

with $y_i$ the value associated to $x_i$ with an uncertainty $\sigma_i$. This method supposes that each $y_i$ follows a Gauss distribution of mean $f(x_i, \overrightarrow{p})$ and standard deviation $\sigma_i$. Thus the $\chi^2$ variable introduced above follows a $\chi^2$ distribution which is defined by

$$f\left(\chi^2\right) = \frac{1}{2^{\nu/2}\Gamma\left(\frac{\nu}{2}\right)} e^{-\frac{\chi^2}{2}} \left(\chi^2\right)^{\frac{\nu}{2}-1} \tag{B.2}$$

with $\Gamma$ the Euler function [1] and $\nu$ the number of degrees of freedom defined by $\nu = N - r$. $N$ is the number of points fitted with a function of $r$ parameters. The mean value of this statistical distribution is $\nu$. A measurement of the goodness of the fit is given by the $\chi^2$ value for the parameters found. The most probable value is $\nu$. Thus a good fit result is characterised by a value $\chi^2/\nu \sim 1$. A value far from 1 is very unlikely and indicates a poor fit result with inconsistencies.

The $\chi^2$ procedure is a good approximation for high statistics (bin contents $y_i \geq 30$) since the assumption that each $y_i$ follows a Gauss distribution is right. For low statistics, the Gauss approximation is not correct anymore. A more realistic distribution is a binomial or Poisson law. The minimised estimator is the maximum likelihood which evaluates the probability density function from the bin values. The likelihood function is defined by

$$L(\overrightarrow{p}) = \prod_{i=1}^{N} F(x_i|\overrightarrow{p}) \tag{B.3}$$

For computational convenience, $-\ln(L(\overrightarrow{p}))$ is minimised instead. The probability density function $F(x_i|\overrightarrow{p})$ used in this work is a Poisson distribution of mean $\mu_i = f(x_i, \overrightarrow{p})$. It is usually a probability density function well reproducing low statistics cases:

$$\forall n \in \mathbb{N} , \ F(n|\mu) = \mu^n e^{-\frac{\mu}{n!}} \tag{B.4}$$

The maximum likelihood method does not give a goodness-of-fit measure contrary to the $\chi^2$ minimisation method. Besides the maximum likelihood and the $\chi^2$ methods give the same results for high statistics since the Poisson distribution converges to a Gauss distribution. Indeed for $F(x_i|\overrightarrow{p})$ a Gauss distribution, one has $\ln(L(\overrightarrow{p})) = -\frac{1}{2}\chi^2$.

---

[1] $\forall z \in \mathbb{C}, \Gamma(z) = \int_0^{+\infty} t^{z-1}e^{-t}dt$ and $\forall n \in \mathbb{N}, \Gamma(n) = n!$

For the fits presented in this work, a maximum likelihood method was used. Especially in the cases of the two-proton candidates $^{67}$Kr, $^{63}$Se and $^{59}$Ge, the statistics is low with only few tens of counts in the spectra. There are also empty bins which are not taken into account in the $\chi^2$ method because the uncertainty of the point is not defined. All the spectra presented in this work were fitted by using the MINUIT algorithm [Jam94] of the ROOT C++ framework [Bru97, Ant11].

# Appendix C

# Beta-detection efficiency

The computations of the $\beta$-detection efficiency, nucleus by nucleus and DSSSD by DSSSD, presented in section 3.6.2 are detailed here. The values with their uncertainties and the reduced $\chi^2$ value for each detector are in the table below.

| Nucleus | DSSSD | $\varepsilon_\beta$ (%) | $\Delta\varepsilon_\beta$ (%) | $\chi^2/ndf$ |
|---|---|---|---|---|
| $^{65}$As | 0 | 3.65 | 0.45 | 169.20 |
| $^{66}$As | | 12.35 | 1.07 | |
| $^{56}$Cu | | 15.82 | 0.88 | |
| $^{60}$Ga | | 5.50 | 0.41 | |
| $^{62}$Ge | | 4.85 | 0.26 | |
| $^{63}$Ge | | 24.33 | 0.73 | |
| $^{66}$Se | | 20.04 | 0.86 | |
| $^{58}$Zn | | 13.19 | 0.48 | |
| $^{65}$As | 1 | 63.09 | 3.51 | 11.53 |
| $^{66}$As | | 61.07 | 3.42 | |
| $^{56}$Cu | | 45.99 | 1.42 | |
| $^{60}$Ga | | 49.99 | 1.30 | |
| $^{62}$Ge | | 50.05 | 1.34 | |
| $^{63}$Ge | | 55.64 | 1.48 | |
| $^{66}$Se | | 62.09 | 3.45 | |
| $^{58}$Zn | | 44.28 | 1.24 | |
| $^{65}$As | 2 | 43.60 | 2.55 | 110.30 |
| $^{66}$As | | 39.99 | 2.69 | |
| $^{56}$Cu | | 50.70 | 1.34 | |
| $^{60}$Ga | | 54.20 | 1.41 | |
| $^{62}$Ge | | 42.92 | 1.79 | |
| $^{63}$Ge | | 10.98 | 1.28 | |
| $^{66}$Se | | 40.07 | 2.28 | |
| $^{58}$Zn | | 53.33 | 1.37 | |

Table C.1: Listing of the $\beta$-detection detection efficiency per nucleus and DSSSD for the RIBF4R1 experiment.

# Appendix D

# Beta fraction above the energy cut for protons

The computations of the total proton branching ratios presented in section **3.6.3** are corrected from an estimate of the ratio of $\beta$ particles detected above the arbitrary threshold of 1 MeV, used to discriminate $\beta$ particles from protons. The values of this ratio were computed for the same nuclei used to estimate the $\beta$-detection efficiency. The details of the computations for each nucleus and DSSSD, and the reduced $\chi^2$ value per DSSSD are reported in the table below.

| Nucleus | DSSSD | $\beta$ counts rate (%) | Uncertainty (%) | $\chi^2/ndf$ |
|---------|-------|-------------------------|------------------|--------------|
| $^{65}$As | 0 | 4.07 | 1.77 | 8.88 |
| $^{66}$As | | 2.65 | 1.09 | |
| $^{56}$Cu | | 5.92 | 1.12 | |
| $^{60}$Ga | | 3.40 | 1.25 | |
| $^{62}$Ge | | 2.29 | 0.56 | |
| $^{63}$Ge | | 7.48 | 0.61 | |
| $^{66}$Se | | 5.91 | 0.48 | |
| $^{58}$Zn | | 3.02 | 0.48 | |
| $^{65}$As | 1 | 12.72 | 0.83 | 6.78 |
| $^{66}$As | | 11.44 | 0.95 | |
| $^{56}$Cu | | 12.93 | 0.81 | |
| $^{60}$Ga | | 15.72 | 0.50 | |
| $^{62}$Ge | | 12.20 | 0.37 | |
| $^{63}$Ge | | 13.56 | 0.72 | |
| $^{66}$Se | | 12.96 | 0.75 | |
| $^{58}$Zn | | 10.74 | 0.70 | |
| $^{65}$As | 2 | 9.38 | 2.04 | 10.15 |
| $^{66}$As | | 14.51 | 6.03 | |
| $^{56}$Cu | | 12.37 | 0.55 | |
| $^{60}$Ga | | 14.90 | 0.48 | |
| $^{62}$Ge | | 11.18 | 0.50 | |
| $^{63}$Ge | | 7.82 | 6.62 | |
| $^{66}$Se | | 7.69 | 0.81 | |
| $^{58}$Zn | | 11.64 | 0.34 | |

Table D.1: Details of the estimate of the fraction of $\beta$ particles above 1 MeV in the add-back spectra. The values are given per nucleus and DSSSD. These values are used for proton branching ratio computation.

# Bibliography

[Ago03]   S. Agostinelli et al. *Nuclear Instruments and Methods in Physics Research Section A: Accelerators, Spectrometers, Detectors and Associated Equipment*, 506(3):250, 2003

[Alv38]   L. W. Alvarez. *Physical Review*, 54(7):486, 1938

[Ant86]   M. S. Antony, J. Britz and A. Pape. *Atomic Data and Nuclear Data Tables*, 34(2):279, 1986

[Ant97]   M. S. Antony, A. Pape and J. Britz. *Atomic Data and Nuclear Data Tables*, 66(1):1, 1997

[Ant11]   I. Antcheva et al. *Computer Physics Communications*, 182(6):1384, 2011

[Asc11a]  P. Ascher. *Etude de la radioactivité deux protons de 54Zn avec une chambre à projection temporelle*. Ph.D. thesis, Université Sciences et Technologies - Bordeaux I, 2011

[Asc11b]  P. Ascher et al. *Physical Review Letters*, 107(10):102502, 2011

[Aud11]   L. Audirac. *Etude de la radioactivité 2-protons de 45Fe avec une chambre à projection temporelle*. Ph.D. thesis, Université de Bordeaux1, 2011

[Aud12]   L. Audirac et al. *The European Physical Journal A*, 48(12):179, 2012

[Bab10]   H. Baba et al. *Nuclear Instruments and Methods in Physics Research Section A: Accelerators, Spectrometers, Detectors and Associated Equipment*, 616(1):65, 2010

[Bab15]   H. Baba et al. *Nuclear Instruments and Methods in Physics Research Section A: Accelerators, Spectrometers, Detectors and Associated Equipment*, 777(0):75, 2015

[Bar63]   R. Barton et al. *Canadian Journal of Physics*, 41(12):2007, 1963

[Bar01]   F. C. Barker. *Physical Review C*, 63(4):047303, 2001

[Bat10]   H. Bateman. *Cambridge Philosophical Society Proceedings*, 5:423, 1910

[Bat93]   J. C. Batchelder, D. M. Moltz, T. J. Ognibene, M. W. Rowe and J. Cerny. *Physical Review C*, 47(5):2038, 1993

[Bé04]    M. Bé et al. *Table of Radionuclides: A*, vol. 1. BIPM Sévres, 2004

[Bet30]   H. Bethe. *Annalen der Physik*, 397(3):325, 1930

[Bet36]   H. A. Bethe. *Reviews of Modern Physics*, 8(2):82, 1936

[Bla95]   B. Blank et al. *Physical Review Letters*, 74(23):4611, 1995

[Bla96]   B. Blank et al. *Physical Review Letters*, 77(14):2893, 1996

[Bla00]   B. Blank et al. *Physical Review Letters*, 84(6):1116, 2000

[Bla02]   B. Blank. *The European Physical Journal A*, 15(1):121, 2002

[Bla05]    B. Blank et al. *Physical Review Letters*, 94(23):232501, 2005

[Bla07]    B. Blank et al. *The European Physical Journal A*, 31(3):267, 2007

[Bla08a]   B. Blank and M. Borge. *Progress in Particle and Nuclear Physics*, 60(2):403, 2008

[Bla08b]   B. Blank et al. *Nuclear Instruments and Methods in Physics Research Section B: Beam Interactions with Materials and Atoms*, 266(19–20):4606, 2008

[Bla10]    B. Blank et al. *Nuclear Instruments and Methods in Physics Research Section A: Accelerators, Spectrometers, Detectors and Associated Equipment*, 613(1):65, 2010

[Bla16]    B. Blank et al. *Physical Review C*, 93(6):061301, 2016

[Bor01]    R. Borcea et al. *Nuclear Physics A*, 695(1–4):69, 2001

[Bro91]    B. A. Brown. *Physical Review C*, 43(4):R1513, 1991

[Bro02]    B. A. Brown, R. R. C. Clement, H. Schatz, A. Volya and W. A. Richter. *Physical Review C*, 65(4):045802, 2002

[Bro03]    B. A. Brown and F. C. Barker. *Physical Review C*, 67(4):041304, 2003

[Bro10]    E. Browne and J. K. Tuli. *Nuclear Data Sheets*, 111(9):2425, 2010

[Bru97]    R. Brun and F. Rademakers. *Nuclear Instruments and Methods in Physics Research Section A: Accelerators, Spectrometers, Detectors and Associated Equipment*, 389(1):81, 1997

[Caa07]    M. Caamaño et al. *Physical Review Letters*, 99(6):062502, 2007

[Cab83]    M. D. Cable. *Physical Review Letters*, 50(6):404, 1983

[Cie15]    A. A. Ciemny et al. *Physical Review C*, 92(1):014622, 2015

[Col96]    B. J. Cole. *Physical Review C*, 54(3):1240, 1996

[Col97]    B. J. Cole. *Physical Review C*, 56(4):1866, 1997

[Col99]    B. J. Cole. *Physical Review C*, 59(2):726, 1999

[Cow56]    C. L. Cowan, F. Reines, F. B. Harrison, H. W. Kruse and A. D. McGuire. *Science*, 124(3212):103, 1956

[Dem03]    C.-E. Demonchy. *Etude de réactions et d'états isobariques analogues dans le système 8He+p, à basse énergie, à l'aide de la cible active MAYA*. Ph.D. thesis, Université de Caen, 2003

[Dem07]    C. E. Demonchy et al. *Nuclear Instruments and Methods in Physics Research Section A: Accelerators, Spectrometers, Detectors and Associated Equipment*, 583(2–3):341, 2007

[Dos05]    C. Dossat et al. *Physical Review C*, 72(5):054315, 2005

[Dos07]    C. Dossat et al. *Nuclear Physics A*, 792(1-2):18, 2007

[DS14]     M. Del Santo et al. *Physics Letters B*, 738:453, 2014

[Ens17]    Evaluated Nuclear Structure Data File. https://www.nndc.bnl.gov/ensdf/, 2017

[Fan61]    U. Fano. *Physical Review*, 124(6):1866, 1961

[Fer34]    E. Fermi. *Il Nuovo Cimento (1924-1942)*, 11(1):1, 1934

[Fuk13]   N. Fukuda et al. *Nuclear Instruments and Methods in Physics Research Section B: Beam Interactions with Materials and Atoms*, 317, Part B(0):323, 2013

[Gar66]   G. T. Garvey and I. Kelson. *Physical Review Letters*, 16(5):197, 1966

[Gar17]   Simulation of gaseous detectors. `http://garfield.web.cern.ch/garfield/`, 2017

[Gee77]   D. F. Geesaman. *Physical Review C*, 15(5):1835, 1977

[Gio96]   Y. Giomataris, P. Rebourgeard, J. P. Robert and G. Charpak. *Nuclear Instruments and Methods in Physics Research Section A: Accelerators, Spectrometers, Detectors and Associated Equipment*, 376(1):29, 1996

[Gio98]   Y. Giomataris. *Nuclear Instruments and Methods in Physics Research Section A: Accelerators, Spectrometers, Detectors and Associated Equipment*, 419(2–3):239, 1998

[Gio02]   J. Giovinazzo et al. *Physical Review Letters*, 89(10):102501, 2002

[Gio06]   I. Giomataris et al. *Nuclear Instruments and Methods in Physics Research Section A: Accelerators, Spectrometers, Detectors and Associated Equipment*, 560(2):405, 2006

[Gio07]   J. Giovinazzo et al. *Physical Review Letters*, 99(10):102501, 2007

[Gio16]   J. Giovinazzo et al. *Nuclear Instruments and Methods in Physics Research Section A: Accelerators, Spectrometers, Detectors and Associated Equipment*, 840:15, 2016

[Goi16]   T. Goigoux et al. *Physical Review Letters*, 117(16):162501, 2016

[Gol60]   V. I. Goldansky. *Nuclear Physics*, 19(0):482, 1960

[Gol66]   V. I. Goldansky. *Nuclear Physics*, 78(1):233, 1966

[Gol16]   T. A. Golubkova et al. *Physics Letters B*, 762:263, 2016

[Gri00]   L. V. Grigorenko, R. C. Johnson, I. G. Mukha, I. J. Thompson and M. V. Zhukov. *Physical Review Letters*, 85(1):22, 2000

[Gri01]   L. V. Grigorenko, R. C. Johnson, I. G. Mukha, I. J. Thompson and M. V. Zhukov. *Physical Review C*, 64(5):054002, 2001

[Gri03]   L. V. Grigorenko and M. V. Zhukov. *Physical Review C*, 68(5):054005, 2003

[Gri07a]  L. V. Grigorenko and M. V. Zhukov. *Physical Review C*, 76(1):014008, 2007

[Gri07b]  L. V. Grigorenko and M. V. Zhukov. *Physical Review C*, 76(1):014009, 2007

[Gri10]   L. V. Grigorenko, I. A. Egorova, M. V. Zhukov, R. J. Charity and K. Miernik. *Physical Review C*, 82(1):014615, 2010

[Gri17]   L. V. Grigorenko, T. A. Golubkova, J. S. Vaagen and M. V. Zhukov. *Physical Review C*, 95(2):021601, 2017

[Hei32]   W. Heisenberg. *Zeitschrift für Physik*, 77(1-2):1, 1932

[Hof82]   S. Hofmann et al. *Zeitschrift für Physik A Atoms and Nuclei*, 305(2):111, 1982

[Hon05]   M. Honma, T. Otsuka, B. A. Brown and T. Mizusaki. *The European Physical Journal A*, 25(S1):499, 2005

[Hot87]   M. A. C. Hotchkis. *Physical Review C*, 35(1):315, 1987

[Int07]   *Update of X Ray and Gamma Ray Decay Data Standards for Detector Calibration and Other Applications.* International Atomic Energy Agency, Vienna, 2007

[Jae14]    Chart of the Nuclides 2014. `http://wwwndc.jaea.go.jp/CN14/`, 2014

[Jam94]    F. James. *Function Minimization and Error Analysis, Version 94.1*, 1994

[Jän88]    J. Jänecke and P. Masson. *Atomic Data and Nuclear Data Tables*, 39(2):265, 1988

[Jok02]    A. Jokinen et al. *EPJ direct*, 4(1):1, 2002

[Kam16]    O. Kamigaito et al. In *Proc. of International Particle Accelerator Conference (IPAC'16), Busan, Korea, May 8-13, 2016*, no. 7 in International Particle Accelerator Conference, 1281–1283. JACoW, Geneva, Switzerland, 2016

[Kel66]    I. Kelson and G. T. Garvey. *Physics Letters*, 23(12):689, 1966

[Kim05]    K. Kimura et al. *Nuclear Instruments and Methods in Physics Research Section A: Accelerators, Spectrometers, Detectors and Associated Equipment*, 538(1-3):608, 2005

[Kle82]    O. Klepper et al. *Zeitschrift für Physik A Atoms and Nuclei*, 305(2):125, 1982

[Kno10]    G. F. Knoll. *Radiation Detection and Measurement.* John Wiley & Sons, 2010

[Kon85]    T. Kondoh, T. Tachibana and M. Yamada. *Progress of Theoretical Physics*, 74(4):708, 1985

[Kry95]    R. A. Kryger et al. *Physical Review Letters*, 74(6):860, 1995

[Kub12]    T. Kubo et al. *Progress of Theoretical and Experimental Physics*, 2012(1):03C003, 2012

[Kuc17]    L. Kucuk et al. *The European Physical Journal A*, 53(6):134, 2017

[Kum01]    H. Kumagai, A. Ozawa, N. Fukuda, K. Sümmerer and I. Tanihata. *Nuclear Instruments and Methods in Physics Research Section A: Accelerators, Spectrometers, Detectors and Associated Equipment*, 470(3):562, 2001

[Kum13]    H. Kumagai et al. *Nuclear Instruments and Methods in Physics Research Section B: Beam Interactions with Materials and Atoms*, 317, Part B:717, 2013

[Lan58]    A. M. Lane and R. G. Thomas. *Reviews of Modern Physics*, 30(2):257, 1958

[Lis15]    A. A. Lis et al. *Physical Review C*, 91(6):064309, 2015

[LJ02]    M. J. López Jiménez et al. *Physical Review C*, 66(2):025803, 2002

[Lun03]    D. Lunney, J. M. Pearson and C. Thibault. *Reviews of Modern Physics*, 75(3):1021, 2003

[May48]    M. G. Mayer. *Physical Review*, 74(3):235, 1948

[Maz01]    C. Mazzocchi et al. *The European Physical Journal A - Hadrons and Nuclei*, 12(3):269, 2001

[Mie07a]    K. Miernik et al. *Physical Review C*, 76(4):041304, 2007

[Mie07b]    K. Miernik et al. *Nuclear Instruments and Methods in Physics Research Section A: Accelerators, Spectrometers, Detectors and Associated Equipment*, 581(1–2):194, 2007

[Mie07c]    K. Miernik et al. *Physical Review Letters*, 99(19):192501, 2007

[Mie09]    K. Miernik et al. *The European Physical Journal A*, 42(3):431, 2009

[Möl12]    P. Möller, W. D. Myers, H. Sagawa and S. Yoshida. *Physical Review Letters*, 108(5):052501, 2012

[Muk07]   I. Mukha et al. *Physical Review Letters*, 99(18):182501, 2007

[Muk08]   I. Mukha et al. *Physical Review C*, 77(6):061303, 2008

[Muk15]   I. Mukha et al. *Physical Review Letters*, 115(20):202501, 2015

[Mö16]    P. Möller, A. J. Sierk, T. Ichikawa and H. Sagawa. *Atomic Data and Nuclear Data Tables*, 109–110:1, 2016

[Nis13]   S. Nishimura et al. *RIKEN Accelerator Progress Report*, 46:182, 2013

[Oku12]   H. Okuno, N. Fukunishi and O. Kamigaito. *Progress of Theoretical and Experimental Physics*, 2012(1):03C002, 2012

[Orm96]   W. E. Ormand. *Physical Review C*, 53(1):214, 1996

[Orm97]   W. E. Ormand. *Physical Review C*, 55(5):2407, 1997

[Pap88]   A. Pape and M. Antony. *Atomic Data and Nuclear Data Tables*, 39(2):201, 1988

[Pat16]   C. Patrignani et al. *Chinese Physics C*, C40(10):100001, 2016

[Pfü02]   M. Pfützner et al. *The European Physical Journal A - Hadrons and Nuclei*, 14(3):279, 2002

[Pie07]   S. Pietri et al. *Acta Physica Polonica. Series B: Elementary Particle Physics, Nuclear Physics, Statistical Physics, Theory of Relativity, Field Theory*, 38(4):1255, 2007

[Pol12]   E. Pollacco et al. *Physics Procedia*, 37(Supplement C):1799, 2012

[Pol17]   E. Pollacco et al. *Nuclear Instruments and Methods in Physics Research Section A: Accelerators, Spectrometers, Detectors and Associated Equipment*, 2017. Submitted

[Pom11a]  M. Pomorski et al. *Physical Review C*, 83(6):061303, 2011

[Pom11b]  M. Pomorski et al. *Physical Review C*, 83(1):014306, 2011

[Pom14]   M. Pomorski. *Physical Review C*, 90(1):014311, 2014

[Rad17]   RadWare. `http://radware.phy.ornl.gov/`, 2017

[Ram98]   M. Ramdhane et al. *Physics Letters B*, 432(1–2):22, 1998

[Rik17]   RIKEN Nishina Center. `http://www.nishina.riken.jp/index_e.html`, 2017

[Rog11a]  T. Roger et al. *Nuclear Instruments and Methods in Physics Research Section A: Accelerators, Spectrometers, Detectors and Associated Equipment*, 638(1):134, 2011

[Rog11b]  A. M. Rogers et al. *Physical Review C*, 84(5):051306, 2011

[Rog14]   A. M. Rogers et al. *Nuclear Data Sheets*, 120(Supplement C):41, 2014

[Rot05a]  J. Rotureau. *Modèle en couches avec plusieurs particules dans le continuum : description de la radioactivité deux protons.* Ph.D. thesis, Université de Caen, 2005

[Rot05b]  J. Rotureau, J. Okołowicz and M. Płoszajczak. *Physical Review Letters*, 95(4):042503, 2005

[Rot06]   J. Rotureau, J. Okołowicz and M. Płoszajczak. *Nuclear Physics A*, 767(Supplement C):13, 2006

[Rut16]   S. E. Rutherford and A. B. Wood. *Philosophical Magazine Series 6*, 31(184):379, 1916

[Sab13]   L. Sabaut. *Caractérisation de l'électronique d'acquisition pour une TPC.* Master's thesis, École Centrale de Lyon, 2013

[Sau97]     F. Sauli. *Nuclear Instruments and Methods in Physics Research Section A: Accelerators, Spectrometers, Detectors and Associated Equipment*, 386(2):531, 1997

[Sau16]     F. Sauli. *Nuclear Instruments and Methods in Physics Research Section A: Accelerators, Spectrometers, Detectors and Associated Equipment*, 805(Supplement C):2, 2016

[Sch84]     K.-H. Schmidt, C.-C. Sahm, K. Pielenz and H.-G. Clerc. *Zeitschrift für Physik A Atoms and Nuclei*, 316(1):19, 1984

[Sch98]     H. Schatz et al. *Physics Reports*, 294(4):167, 1998

[Sch04]     H. Schatz. *Nuclear Physics A*, 746(Supplement C):347, 2004

[Sha15]     R. Shane et al. *Nuclear Instruments and Methods in Physics Research Section A: Accelerators, Spectrometers, Detectors and Associated Equipment*, 784:513, 2015

[Söd13]     P.-A. Söderström et al. *Nuclear Instruments and Methods in Physics Research Section B: Beam Interactions with Materials and Atoms*, 317, Part B:649, 2013

[Sto05]     A. Stolz et al. *Physics Letters B*, 627(1–4):32, 2005

[Sup09]     C. Suplee. Stopping-Power & Range Tables for Electrons, Protons, and Helium Ions. https://www.nist.gov/pml/stopping-power-range-tables-electrons-protons-and-helium-ions, 2009

[Suz12]     D. Suzuki et al. *Nuclear Instruments and Methods in Physics Research Section A: Accelerators, Spectrometers, Detectors and Associated Equipment*, 691:39, 2012

[Tac90]     T. Tachibana, M. Yamada and Y. Yoshida. *Progress of Theoretical Physics*, 84(4):641, 1990

[Tak69]     K. Takahashi and M. Yamada. *Progress of Theoretical Physics*, 41(6):1470, 1969

[Tan08]     I. Tanihata et al. *Physical Review Letters*, 100(19):192502, 2008

[Tri13]     V. Tripathi et al. *Physical Review Letters*, 111(26):262501, 2013

[Vie76]     D. J. Vieira, D. F. Sherman, M. S. Zisman, R. A. Gough and J. Cerny. *Physics Letters B*, 60(3):261, 1976

[Wei35]     C. F. v. Weizsäcker. *Zeitschrift für Physik*, 96(7-8):431, 1935

[Woo54]     R. D. Woods and D. S. Saxon. *Physical Review*, 95(2):577, 1954

[Xu97]      X. J. Xu et al. *Physical Review C*, 55(2):R553, 1997

[Zer35]     F. Zernike and H. Brinkman. In *Proc. Akad. Wet. Amsterdam*, vol. 38, 161–170. 1935

Un problème insoluble n'en est
pas un.

Isaac Asimov